De l'usage des protons hyperpolarisés pour augmenter la sensibilite de la RMN

THÈSE N^{O} 6581 (2015)

PRÉSENTÉE LE 22 MAI 2015

À LA FACULTÉ DES SCIENCES DE BASE
LABORATOIRE DE RÉSONANCE MAGNÉTIQUE BIOMOLÉCULAIRE
PROGRAMME DOCTORAL EN CHIMIE ET GÉNIE CHIMIQUE

ÉCOLE POLYTECHNIQUE FÉDÉRALE DE LAUSANNE

POUR L'OBTENTION DU GRADE DE DOCTEUR ÈS SCIENCES

PAR

Aurélien BORNET

acceptée sur proposition du jury:

Prof. S. Gerber, présidente du jury
Prof. G. Bodenhausen, Dr S. Jannin, directeurs de thèse
Prof. L. Emsley, rapporteur
Dr M. Lerche, rapporteuse
Dr J. Lohman, rapporteur

ÉCOLE POLYTECHNIQUE
FÉDÉRALE DE LAUSANNE

Suisse
2015

« Un modèle n'est rien d'autre qu'un récit, et à travers les erreurs des abstractions et modèles existants (qui fonctionnent bien par ailleurs), on trouve le chemin vers de nouveau récits. Le reliquat qui n'entre pas dans les équations des théories actuelles contient souvent la clé de nouveaux horizons. Les scientifiques ne devraient donc pas considérer leurs erreurs comme négligeables mais au contraire leur consacrer un maximum d'attention, car c'est probablement là que pourraient se trouver les rudiments d'un système axiomatique compétemment nouveau (et peut-être meilleur).Cela est pareillement vrai des existences personnelles. »

Tomas Sedlacek

L'économie du bien et du mal

Abstract

Nuclear Magnetic Resonance (NMR) has become an inescapable technique for spectroscopic identification. Its main advantage comes from the sensitivity of NMR active nuclei embedded in a molecule to their chemical environment. NMR is also used daily in medical imaging. Magnetic Resonance Imaging (MRI) is not only remarkably versatile, but has the precious advantage of being non-invasive; moreover, the range of radiofrequency used implies that MRI deposit a limited amount of energy in tissues under investigation.

Nevertheless, compared to other spectroscopic methods, NMR suffers from a relative lack of sensitivity. Indeed as the NMR transitions are low in energy, the difference of populations between the levels involved, known as polarization, is extremely low. The NMR signal, which is directly proportional to this polarization, is thus many orders of magnitude inferior to the theoretical maximum at full polarization.

Dynamic Nuclear Polarization (DNP) allows one to circumvent this disadvantage by transferring the high electron spin polarization to the nuclear spins. This transfer happens via microwave irradiation under optimized conditions. The method has been constantly developed since the 'fifties. A substantial breakthrough was achieved in 2003 by Golman, Ardenkjaer-Larsen and their collaborators. They proposed to dissolve a sample that has been hyperpolarized at low temperature (at about 1 K) in order to inject it into an animal, or, *in fine*, into a human patient, and to follow its bio-distribution and eventual metabolic conversion by MRI. This technique, called Dissolution-DNP (D-DNP), allows a signal increase on the order of 10'000, opening the way to many new experimental possibilities.

Research in Dissolution-DNP was largely oriented toward the optimization of ^{13}C polarization because of its long lifetimes. In the course of this Thesis, an alternative way that takes advantage of the proton (^{1}H) polarization will be explored. Protons have the advantage that they can be polarized to a higher level in a shorter time compared to ^{13}C. Unfortunately, once ejected from the polarizer, in solution and at room temperature, the high proton magnetization will be short-lived compared to ^{13}C. Along the chapters of this Thesis, different approaches will be proposed to maximize the advantages of ^{1}H polarization, while minimizing its inconveniences.

It is possible to use a standard NMR technique, known as Cross-Polarization (CP), to transfer the abundant magnetization of hyperpolarized protons to other nuclei like ^{13}C, using suitable radiofrequency pulse sequences. The advantages of the ^{1}H polarization are exploited inside the polarizer, while the interesting properties of ^{13}C are put to use after dissolution. Still, it is also possible to observe directly the proton signal after dissolution. This can be extremely interesting, especially in the context of drug screening for pharmaceutical research. Two examples of such methods will be described. Finally, the use of hyperpolarized ^{1}H signals after dissolution can be greatly improved if their relaxation rates could be attenuated. A first way of doing this, consisting in removing the paramagnetic species by filtration, will be explored. The use of Long-Lived States (LLS) will also be presented.

Key words: Nuclear Magnetic Resonance (NMR); Dynamic Nuclear Polarization (DNP); Dissolution-DNP (D-DNP); proton hyperpolarization; TEMPO free radical; Cross-Polarization (CP); Long-Lived States (LLS); drug screening.

Résumé

La Résonance Magnétique Nucléaire (RMN) est une technique d'identification spectroscopique quasiment incontournable. Son avantage déterminant repose sur la sensibilité de chaque noyau actif en RMN d'une molécule donnée pour son environnement chimique. Ainsi, le spectre RMN de chaque molécule est différent et permet sa caractérisation sans ambiguïté. La RMN est aussi employée tous les jours en milieu hospitalier, en imagerie médicale. L'Imagerie par Résonance Magnétique (IRM) est non seulement polyvalente mais offre aussi le précieux avantage d'être non-invasive; de plus, la gamme de fréquences utilisées ne dépose quasiment pas d'énergie sur les tissus inspectés.

Cependant, comparée à d'autres méthodes spectroscopiques, la RMN souffre de son relatif manque de sensibilité. En effet, vu la faible énergie des transitions RMN, la différence des populations entre les niveaux d'énergie impliqués, connue sous le terme de polarisation, est extrêmement faible. Le signal RMN, qui est directement proportionnel à cette polarisation, est ainsi inférieur de plusieurs ordres de grandeur au maximum théorique correspondant à une polarisation totale.

La Polarisation Dynamique Nucléaire (DNP en anglais) permet de dépasser ce désavantage en transférant la haute polarisation des électrons aux noyaux. Ce transfert se fait par le biais d'irradiations micro-ondes dans des conditions optimisées. La méthode a été constamment développée depuis les années 50. Elle a connu un fort regain d'intérêt en 2003 grâce à l'avancée technique proposée par Golman, Ardenkjaer-Larsen et leurs collaborateurs consistant à dissoudre un échantillon polarisé par DNP à basse température (à environ 1 K) pour l'injecter dans un animal ou, *in fine*, dans un patient et à suivre sa métabolisation par IRM. Cette technique, nommée Dissolution-DNP (D-DNP), peut permettre une augmentation du signal de l'ordre de 10'000 ouvrant la voie à de nouvelles possibilités expérimentales.

Vu son temps de vie long, les recherches en Dissolution-DNP ont été largement orientées vers l'optimisation de la polarisation du carbone-13. Dans le cadre de cette Thèse, une voie alternative consistant à tirer profit de la polarisation du proton (^{1}H) est explorée. Le proton à l'avantage de polariser par DNP mieux et plus rapidement que le carbone-13. Cependant, une fois en dehors du polariseur, en solution et à température ambiante, cette polarisation élevée relaxe aussi très rapidement. Au cours des chapitres de cette Thèse, différentes approches vont être proposées qui permettent de maximiser les avantages du proton hyperpolarisé tout en minimisant ses inconvénients.

Il est possible d'utiliser une technique standard en RMN, la polarisation croisée (CP en anglais), pour transférer à l'aide de séquences d'impulsions radiofréquences l'abondante magnétisation du proton hyperpolarisé vers d'autres noyaux, comme le carbone-13, à l'intérieur du polariseur. Ainsi, les avantages du proton sont exploités dans le polariseur tout en tirant parti des propriétés intéressantes du carbone-13 après dissolution.

Il est aussi possible d'observer directement le signal du proton après dissolution. Son utilisation peut être extrêmement intéressante, notamment pour l'identification de nouvelles molécules interagissant avec des protéines d'intérêt pharmaceutique. Deux méthodes allant dans ce sens seront proposées.

Enfin, le signal du proton hyperpolarisé observé après dissolution peut être grandement amélioré en maîtrisant sa relaxation. Une première voie consistant à filtrer les espèces paramagnétiques va être explorée. L'utilisation d'états de spin à long temps de vie va finalement être présentée.

Mots-clés : Résonance Magnétique Nucléaire (RMN) ; Polarisation Nucléaire Dynamique (DNP) ; Dissolution-DNP (D-DNP) ; hyperpolarisation du proton ; radical TEMPO ; polarisation croisée (CP) ; états aux temps de vie longs (LLS) ; Identification de ligands.

Contents

Part A

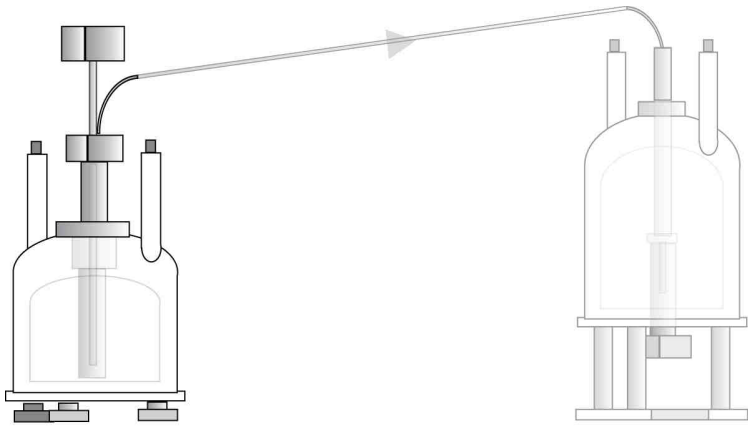

Chapter 1:

Introduction: NMR (in)sensitivity and Dissolution-DNP

1.1 Lack of sensitivity in NMR

1.1.1 Low polarization

"*It is well known that an assembly of magnetic moments μ embedded in a sample of bulk matter in thermal equilibrium at a temperature T will, when placed in a magnetic field H orient themselves preferentially in the direction of the field. This orientation is not perfect: there is competition between the magnetic energy μH, which tends to orient the moments parallel to the field and the thermal energy kT, which destroys the orientation. If N is the number of moments per unit volume, the magnetization M along the field will reach the value M = NμP, where P, a number smaller than unity, is called the polarization.*" (1)

This statement of Anatole Abragam in the *Proceeding of the International Conference of Polarized target and Ion Sources* of 1966 illustrates the central role of polarization in Nuclear Magnetic Resonance (NMR) (2-9). The intensity of the main observable in NMR, the macroscopic magnetization M, is proportional the nuclear polarization, but, as the ratio $\mu B/k_B T$ is usually a small number, far below unity, the nuclear polarization will be extremely modest. The subject of the present Thesis is the development of methods that allow one to increase the nuclear polarization as close as possible to unity.

The original motivation of NMR was the measurement of nuclear magnetic moments ($\boldsymbol{\mu}$). The majority of all nuclei have a non-vanishing spin angular momentum ($\boldsymbol{I}$) (see the tables in (8) for example), a vector quantity with a magnitude characterized by the nuclear spin quantum number (I): $|\boldsymbol{I}| = \hbar[I(I+1)]^{½}$, where $\hbar$ is the Plank constant divided by 2π. The orientation of the spin angular momentum in space is quantized. By definition the value of the z component of $\boldsymbol{I}$ is specified as $I_z = \hbar m$, with the magnetic quantum number $m = [-I, -I+1, \ldots, I]$. It can be shown (2) that the nuclear magnetic moment is collinear with the spin angular momentum, and therefore, $\boldsymbol{\mu} = \gamma \boldsymbol{I}$ and $\mu_z = \gamma I_z = \gamma \hbar m$. The proportionality constant specific for each nucleus, γ, is known as the gyromagnetic ratio. This moment gives rise to nuclear magnetism.

If a large assembly of nuclei with elementary spin moments is immersed in a magnetic field $\boldsymbol{B}$ with a magnetic field strength B_0, a net macroscopic magnetization $\boldsymbol{M}$ will appear. The energy of a magnetic moment interacting with a magnetic field is given by the scalar product $E = -\boldsymbol{\mu}\,\boldsymbol{B}$, which is $E = -\mu_z B_0$ in the presence of a strong magnetic field of amplitude B_0 determining the quantization axis z. By definition of μ_z, it results that the interaction between a magnetic moment and a magnetic field will result in $2I+1$

energy levels, known as Zeeman levels, that are equally spaced in the absence of spins-spins couplings and quadrupole interactions, with a spacing given by $E_m = -\gamma\hbar m B_0$. The relative populations of the energy levels, n_m, obey a statistical Boltzmann distribution:

$$n_m \propto \exp\left(\frac{-E_m}{k_B T}\right) = \exp\left(\frac{\gamma\hbar m B_0}{k_B T}\right) \tag{1.1}$$

where k_B is the Boltzmann constant and T the temperature. As the lowest energy levels will be (slightly) more populated, this will give rise to a bulk magnetic moment ***M***, the vector sum of the magnetic moments of all individual nuclei.

The strength of this magnetic moment, and therefore of the NMR signal intensity, will depend on the difference of populations of the energy levels. For spins with $I = ½$, which have only two energy levels, usually labelled α and β (shorthand for $m = \pm ½$), the polarization can be defined as:

$$P = \frac{n_\alpha - n_\beta}{n_\alpha + n_\beta} \tag{1.2}$$

Following Equation 1.1, the ratio of the population of the two levels is given by:

$$\frac{n_\beta}{n_\alpha} = \exp\left(\frac{-\Delta E}{k_B T}\right), \text{ with } \Delta E = E_\beta - E_\alpha = \gamma\hbar B_0, \text{ thus} \tag{1.3}$$

$$P = \frac{n_\alpha - n_\beta}{n_\alpha + n_\beta} = \frac{1 - n_\beta / n_\alpha}{1 + n_\beta / n_\alpha} = \frac{1 - \exp\left(-\Delta E / k_B T\right)}{1 + \exp\left(-\Delta E / k_B T\right)} \tag{1.4}$$

And with $\tanh(x) = \frac{e^x - e^{-x}}{e^x + e^{-x}} = \frac{1 - e^{-2x}}{1 + e^{-2x}}$ (1.5)

$$P = \tanh\left(\frac{\Delta E}{2k_B T}\right) = \tanh\left(\frac{\gamma\hbar B_0}{2k_B T}\right) \tag{1.7}$$

From Equation 1.7, one can easily see that the polarization between two energy levels, and thus the signal arising from the corresponding transition, will depend on their energy difference. As shown in Figure 1.1, compared to other spectroscopic techniques, NMR involves low energy transitions. Therefore the polarization between the levels involved will be extremely low. For example, the proton polarization in a typical field of 9.4 T (400 MHz) at room temperature will be only $P(^1\text{H}) \approx 0.003\%$ (other polarization values can be found in Table 1.1). It implies that, compared to other spectroscopies techniques, NMR suffers from low sensitivity.

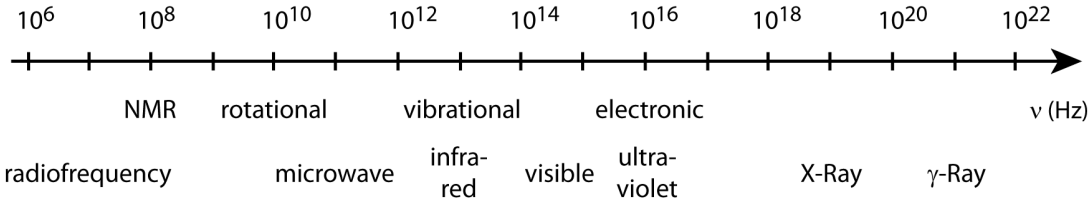

Figure 1.1: Typical transition energies in the electromagnetic spectrum (Adapted from PJ Hore (5))

In the limit where $\Delta E/k_B T$ is a small number, which is the case for standard NMR conditions, it is possible to make a linear expansion of Boltzmann's law (since exp(-x) ≈ 1 - x). For low polarization, one obtains from Equation 1.4:

$$P = \frac{\Delta E}{2k_B T} = \frac{\gamma \hbar B_0}{2k_B T} \tag{1.8}$$

Despite its low signal intensity, NMR was developed far beyond the simple measurement of nuclear moments. NMR may not be sensitive, but it makes a lot of sense. Even subtle changes in the environment of the nuclei can be clearly detected. Therefore NMR became a major and versatile tool in the study of finer properties of the analytes, such as chemical structures, reaction rates, chemical equilibria, bio-molecular 3D structures, internal motions, *etc*. It is difficult to find a chemical laboratory without an NMR spectrometer. Moreover, its drawback, the low energy of the transitions involved, means also that the energy deposition is low. Therefore, when combined with spatial imaging of living people, the low energy becomes a powerful advantage. Today, there is no hospital without MRI scanner.

Finally, this low NMR polarization is not the end of the story, and there must be a huge room for improvement. This will be the subject of the present Thesis, where methods to push nuclear polarization as close as possible to unity will be developed.

1.1.2 How to improve the NMR signal

Inspection of Equations 1.7 and 1.8 shows that it is possible to act on three variables to increase the nuclear polarization, and thus the NMR signal.

First, one can act on the magnetic field B_0. The signal intensity should increase linearly with the field at low polarization (Figure 1.2). Nevertheless, the sophistication of the required technology, and thus the price of the magnet, does by no means increase linearly with B_0. Moreover, the signal-to-noise ratio (SNR) does not vary linearly with B_0, but with $(B_0)^{3/2}$. The highest field commercially on offer for the moment is limited to 28.2 T (1.2 GHz for ^{1}H), which corresponds to a polarization $P(^1\text{H})$ = 0.0096%, still far below 1. Usually the rationale behind the purchase of a high field magnet is driven more by increases of resolution rather than increases of polarization.

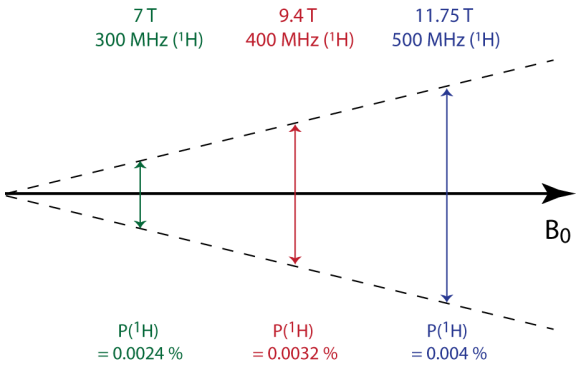

Figure 1.2: Proton polarization at different magnetic fields (B_0 = 7 T, 9.4 T and 11.75 T) calculated with Equation 1.8.

One can also act on the sample temperature *T*. According to Equations 1.7 and 1.8, the polarization will be higher at low temperatures. Table 1.1 shows some polarization values as a function of *T* calculated for ^{1}H and ^{13}C at B_0 = 3.35 T and 6.7 T with Equation 1.7. As the temperature decreases, molecular motions are slowed down (τ_c, the rotational correlation time, increases) and the transverse relaxation time constant T_2 drops (see Figure 1.3a). As the NMR line-width is inversely proportional to T_2 ($\Delta\nu_{½}$(NMR) = $(\pi T_2)^{-1}$), the peaks will become broader at lower temperatures (Figure 1.3b). Therefore, even if the signal intensity increases, the resolution and the SNR will decline at lower temperatures.

Moreover, as can be seen in Table 1.1, at (pumped) liquid helium temperatures, the nuclear polarization still remains below 1%. Only the use of dilution refrigerators going to millikelvin temperatures permits one to reach a substantial polarization, using the so called “brute force method” (10). Here the main drawback is the long spin lattice relaxation time constant T_1 (see Figure 1.3a).

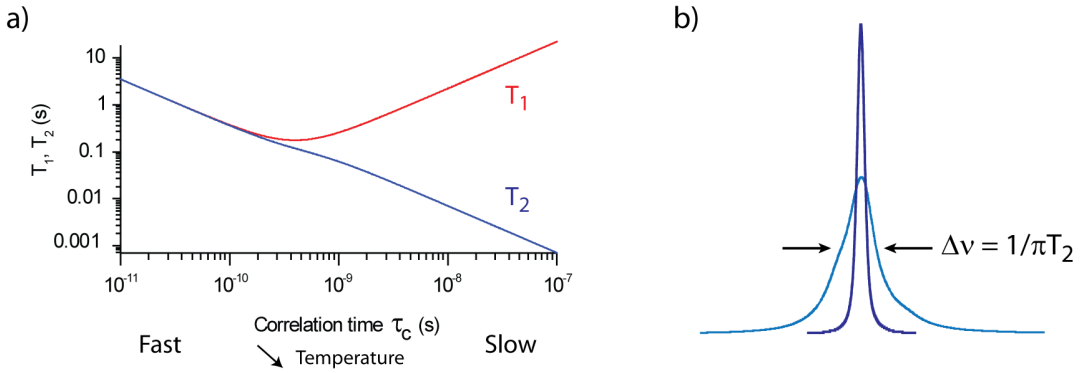

Figure 1.3: **a**) Dependence of T_1 and T_2 on the rotational correlation time, adapted from PJ Hore (5), calculated with $1/T_2 = ½\gamma^2\langle B^2\rangle J(\omega_0) + ½\gamma^2\langle B^2\rangle J(0)$ and $1/T_1 = \gamma^2\langle B^2\rangle J(\omega_0)$ (11), with $J(\omega) = 2\tau_c/(1+ \omega^2\tau_c)$, using $\gamma^2\langle B^2\rangle = 4.5\ 10^9\ s^{-2}$ and $\omega_0/2\pi$ = 400 MHz. **b**) Representation of the NMR linewidth Δν as a function of the transverse relaxation time constant T_2.

The last parameter that influences the nuclear polarization in Equations 1.7 and 1.8 is the gyromagnetic ratio. Obviously, the experimentalist cannot change the magnetic moment of the nuclei under investigation, but it is possible to transfer the polarization of a nuclear species with high gyromagnetic ratio, for example ^{1}H, to an insensitive one, like ^{13}C or ^{15}N (Figure 1.4a). Such polarization transfer can be done in liquid state NMR via INEPT (12) or NOE (13, 14), and in solids by Cross Polarization (15, 16) (see

Chapter 3). The maximal polarization enhancement will be primarily limited by the nucleus with the higher γ.

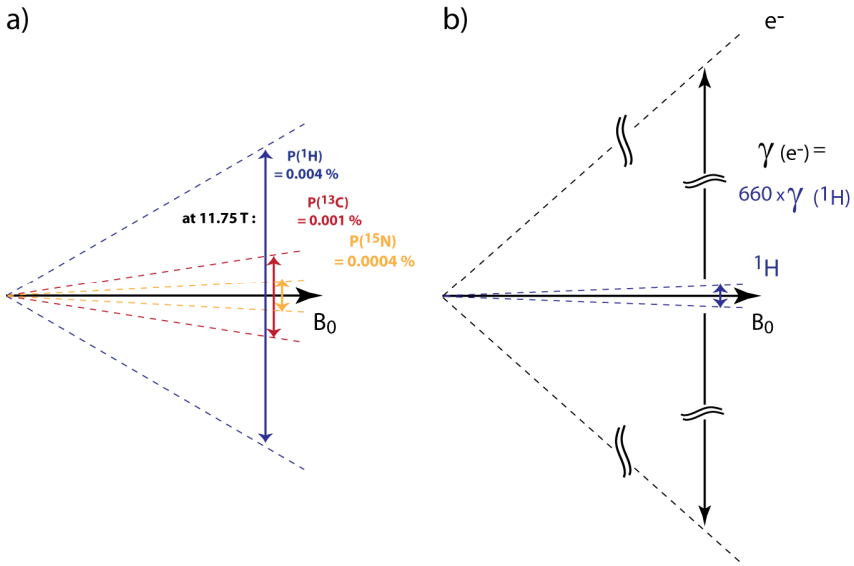

Figure 1.4. **a**) Polarization values of ^{1}H, ^{13}C and ^{15}N calculated with Equation 1.8 at 300 K and 11.75 T (500 MHz for ^{1}H). **b**) Schematic representation of the proton polarization compared to the electron polarization, both as a function of the magnetic field.

Other factors, like improvements of electronics, cryoprobes, dedicated probeheads, optimization of the sample volume and preparation, *etc.* will also influence the SNR. Nevertheless, combining all of these options, the maximal gain will be in the order of a factor ten to fifty. This is far from the theoretical maximum of 50 000 – 100 000 that could be expected if the nuclear polarization would have reached a value of 100%. As it will be shown in the next Section, Dynamic Nuclear Polarization techniques, which transfer the high polarization from electrons to nuclei, can provide such high enhancements, albeit at the cost of a few concessions.

1.2 DNP basic principles and basic experiments

Electrons have a gyromagnetic ratio that is almost three orders of magnitude larger than the one of nuclei. For example, γ(e) = 660γ(^{1}H) (Figure 1.4b). The polarization *P*(*e*) of electronic spins located on paramagnetic atoms or ions is large and may approach 100% at fields and temperatures that can be easily achieved. Table 1.1 reports *P*(*e*) at different temperatures in magnetic fields of 3.35 and 6.7 T (see also Figure 1.5).

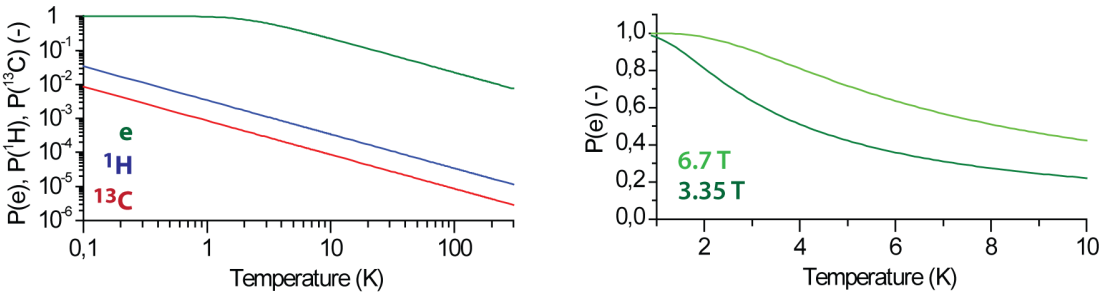

Figure 1.5: **a**) Electronic and nuclear (^{1}H, ^{13}C) polarization calculated as a function of the temperature at B_0 = 3.35 T with equation 1.7. **b**) Electronic polarization calculated between 1 and 10 K at B_0 = 3.35 and 6.7 T.

The idea of Dynamic Nuclear Polarization is to transfer the large Boltzmann polarization of the electrons to coupled nuclei via microwave irradiation (Figure 1.5a). This idea was first proposed by Overhauser (14) and validated by Carver and Slichter (17). The details of the mechanisms of transfer will be developed in the Chapter 2. As shown in Figure 1.5 and Table 1.1, the electronic polarization, and therefore the expected nuclear enhancement, becomes substantial only below 10 K. Therefore, DNP (among other reasons) is usually performed at low temperatures. But, as shown in Figure 1.3, at low temperatures the NMR line-widths become abominable. Because one must choose between the primary objectives of polarization or resolution, field of DNP has split in two different sub-techniques: Magic Angle Spinning-DNP (MAS-DNP) and the Dissolution-DNP (D-DNP).

	B_0 (T)	1.2 K	2.2 K	4.2 K	10 K	100 K	300 K
$P(e)$ (%)	3.35	95.42	77.15	49.02	22.15	2.27	0.75
	6.7	99.89	96.73	79.05	42.23	4.55	1.50
$P(^{1}H)$ (%)	3.35	0.28	0.15	0.081	0.034	0.0035	0.0011
	6.7	0.57	0.31	0.16	0.068	0.0069	0.0023
$P(^{13}C)$ (%)	3.35	0.072	0.039	0.020	0.0086	0.00087	0.00028
	6.7	0.14	0.078	0.041	0.017	0.0017	0.00057

Table 1.1: Electronic and nuclear (^{1}H, ^{13}C) polarizations in magnetic fields B_0 = 3.35 or 6.7 T calculated at different temperatures with equation 1.7.

1.2.1 Magic Angle Spinning-DNP

MAS-DNP was initially developed by Vriend *et al.* (18) in 1985, but only became popular after 1992 in the wake of the remarkable successes of Griffin and co-workers at MIT (19). Although the expression 'low temperature', which in this context typically refers to the range 90 < T < 110 K, is fully justified for magic angle spinning, it is a bit confusing when comparing with Dissolution-DNP which is usually carried out at T = 1.2 K. Indeed, with the MAS-DNP technique, the choice was made to sacrifice some electronic polarization compared to Dissolution-DNP, and thus some nuclear enhancement, by running the experiments at higher temperatures, where NMR line-widths are narrow enough to extract useful information *in situ*. Compared to Dissolution-DNP, the main advantage is that the transfer of polarization is done at the beginning of the experiment, and once this has been achieved, normal solid-state NMR sequences can be run, including acquisition of 2D spectra, multiple-scan accumulations, and phase cycling.

Under favourable conditions, the gain in sensitivity can exceed two orders of magnitude. More typically however, an enhancement factor ε_{DNP} = 20 is regarded as satisfactory, since it leads to a time-saving of $(\varepsilon_{DNP})^2$ = 400, thus allowing to achieve in 24 hours what would normally require more than a year. The overall DNP efficiency depends, among other factors, on the choice and concentration of the (bi)radicals, on the acceleration of the relaxation times that allows one to reduce the recovery delays, on a partial quenching of the signal intensity, on the temperature, and on the static magnetic field.

Performing solid-state DNP experiments at high magnetic fields requires several accessories in addition to a normal MAS setup. Currently, only gyrotrons can generate microwave fields that are sufficiently intense to saturate the EPR transitions, *i.e.,* about 5 W in continuous mode. For NMR spectrometers operating at proton frequencies of 400, 600 or 800 MHz (9.4, 14.1 or 18.8 T), the microwave frequencies must be 263.7, 395.6, and 527.5 GHz, respectively. A sophisticated 'corrugated' low-loss transmission line can guide the microwaves from the gyrotron to the sample that is spinning at rates on the order of $10 < \nu_{rot} < 15$ kHz in a specially designed MAS probe. A suitable set of heat exchangers generates three separately controlled jets of nitrogen to cool the sample, support the bearing, and drive the spinning of the rotor. Figure 1.6 shows a schematic layout and a picture of the MAS-DNP setup that has been running at EPFL since 2010. The main components and their characteristics have been described in detail by Rosay *et al.* (20).

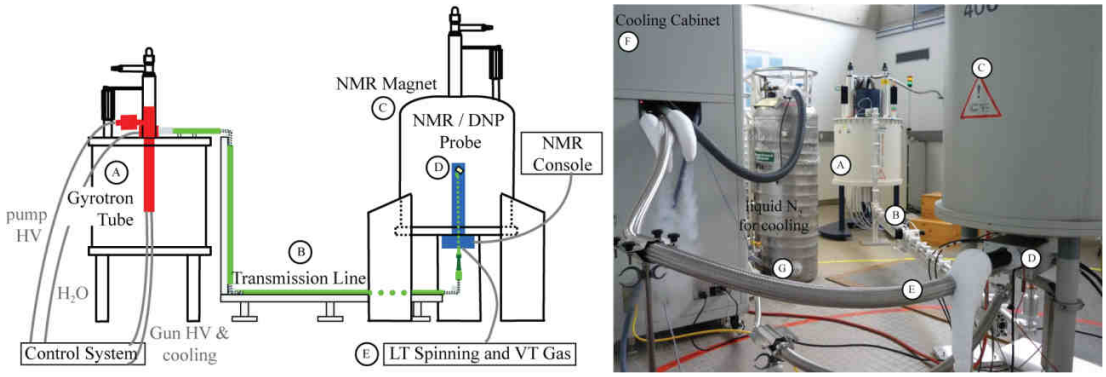

Figure 1.6: MAS-DNP set-up at EPFL. Microwaves with a wave-length of 1.14 mm (ca. 5 W at 263.7 GHz) are generated by a gyrotron tube inserted into a 9.4 T magnet (A) and transmitted via the transmission line (B) to the MAS probe (D) in the NMR magnet (C), in our case a wide-bore 9.4 T magnet with a field-sweep capability for proton NMR at 400 MHz that can be used in triple-channel mode (^{1}H, ^{13}C, ^{14}N or ^{1}H, ^{13}C, ^{15}N) or in double-channel mode (typically ^{1}H plus ^{13}C, ^{29}Si, or ^{27}Al). The zirconia or sapphire rotors with an outer diameter of 3.2 mm are spun up to ν_{rot} = 16 kHz at temperatures near T = 100 K using three nitrogen gas flows for cooling, bearing and spinning (E) that are regulated by a heat exchanger (F) driven with gaseous and liquid nitrogen (G). (Adapted from Veronika Vitzthum's EPFL thesis (21))

MAS-DNP has proven to have tremendous potential, for example for the characterisation of functionalized nanoporous materials (22-25), for the study of *E. coli* ^{13}C/^{15}N labelled protein without extraction, purification and reconstruction steps (26) as well as for the acquisition of 2D ^{13}C-^{13}C spectra of native membrane proteins (27).

1.2.2 Dissolution-DNP

Dissolution-DNP takes the option to separate the site where the polarization is transferred from the electrons to the nuclei, the polarizer, and the site where it is detected. The method was invented and developed since 2003 by Ardenkjaer-Larsen *et al.* (28). It is based on the non-trivial idea that the polarization that was built up in a static solid at low temperature will survive the phase change to room temperature and the transfer to a solution-state spectrometer. The separation between the polarizer and the detection apparatus lifts the need for making compromises between the electronic polarization and spectral resolution of the NMR spectra.

As there is no need for resolution, the polarizer can run at temperatures as low as 1 K, where the electronic polarization is close to unity. Three main pieces constitute a polarizer: a cryostat with pumped liquid helium, a magnet to go to optimal $P(e)$ conditions, and a microwave source irradiating at the corresponding electronic frequency (see Figure 1.7). Note that practically, the availability of µW sources determines the magnetic field of the polarizer.

At EPFL, Dissolution-DNP is performed with home-built polarizers (29-31). In our laboratory, we use a continuous-flow ^{4}He cryostat operating at T = 1.2 K which can be inserted into either of two wide-bore cryomagnets with B_0 = 3.35 or 6.7 T. For B_0 = 3.35 T, microwave irradiation at $\nu_{\mu w}$ = 93.75 – 94.25 GHz generated by an ELVA microwave source provides a maximum power $P_{\mu w}$ = 400 mW. The frequency can be doubled to 187.5 – 188.5 GHz with 100 mW for operation at B_0 = 6.7 T. The apparatus was developed in close collaboration with the Paul Scherrer Institute (with Dr. B. van den Brandt, Dr. P. Hautle and Dr. T. A Konter).

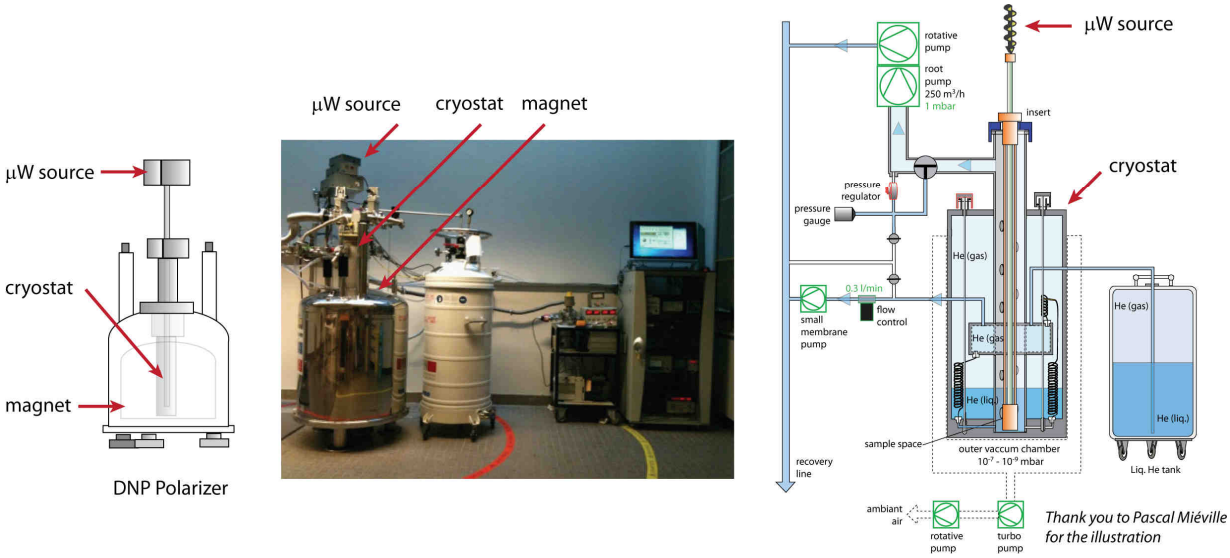

Figure 1.7: Picture and scheme of the Dissolution-DNP polarizer running at EPFL (Schemes shared by Dr. Pascal Miéville).

Once dissolved and transferred, Dissolution-DNP gives access to record enhancements of the nuclear polarization, with ε_{DNP} between 100 and 100 000 depending on the relaxation time of the observed nucleus and of the transfer time. There is however a price to pay. This high nuclear magnetization will be only available once per dissolution 'shot'. Therefore, in contrast to MAS-NMR, one cannot simply

apply standard NMR sequences to the hyperpolarized sample. The detection sequences always have to be adapted, if not reinvented, to conform to this single-shot requirement.

Dissolution-DNP was originally developed in view of *in vivo* MRI applications. It has been shown that the enzymatic conversion of pyruvate into lactate is significantly faster in cancer cells than in healthy tissue (32). This opens new perspectives for cancer diagnosis, in particular for prostate cancer. The most impressive result up to now is the accomplishment of real-time localized spectroscopy of tumors in human patients (33). This can be achieved with a DNP polarizer specially developed for clinical intent, where the entire set-up is kept under sterile conditions (34).

The target for dissolution DNP is usually pyruvate that is isotopically enriched with ^{13}C on the quaternary carbonyl site, because of its long T_1 relaxation time, and its chemical shift that is not hidden by background signals, so that the signal-to-noise ratio is maximized after injection into living animals or humans. Most peer-reviewed articles on D-DNP are concerned with metabolic imaging of tumors with 1-^{13}C pyruvate. Nevertheless, the technique can be used in combination with a variety of other NMR or MRI methods, using an extensive diversity of different molecules and enhanced nuclei. One can cite for example *in vitro*, as well as in-cell, enzyme metabolism studies (35, 36), drug screening (37) or the monitoring of chemical reactions, including the detection of intermediates (38). Further hyperpolarized NMR applications can be found in Reference (39). The coupling with ultrafast ^{1}H-^{13}C and ^{1}H-^{15}N HSQC (40) is also a nice response to the single-shot requirement of DNP.

1.3 Typical D-DNP experiments

A Dissolution-DNP experiment can be divided in five steps that happen in three different areas, as shown in Figure 1.8. The first one, which is often forgotten but of primary importance, is the sample preparation. To preform efficient DNP, the analyte of interest has to be put in contact with paramagnetic species, like free radicals. Trityl or TEMPO, and derivatives are usually chosen as polarizing agents. One first has to find a solvent to co-solubilize both the analyte and the most appropriate derivative of the radicals. Moreover, as the polarizing agent needs, in most cases, to be homogenously distributed, the sample should not crystalize upon freezing, but must stay glassy. Therefore, solvents, or mixtures of solvents that have such properties should be used, like for example, H_2O:glycerol (1:1), H_2O:ethanol (2:1), H_2O:DMSO (2:3), toluene:THF (9:1) or toluene:$CHCl_3$ (2:1). Finally, depending on the cases, the DNP process efficiency could depend on the sample protonation, therefore, the solvents cited above could be partially deuterated. Once prepared, a sample volume between 5 and 1000 µL (in our laboratory) is loaded in the polarizer in the sample space in Figure 1.7.

Once cooled down to liquid helium temperatures (4.2 K) or below at low pressures (T = 1.2 K at p(He) = 0.82 mbar), the second step, the DNP polarization, can be carried out. This is usually performed in a magnetic field of 3.35 T, but it can be done at higher field, like 6.7 T in the majority of the experiments presented in the course of this Thesis. The sample is irradiated with microwaves and the electron polarization is transferred to the nuclei via different possible mechanisms that will be described in Chapter 2. In our laboratory, one can possibly use Cross Polarization to transfer the high proton magnetization to heteronuclei, as will be developed in Chapter 3. The microwave irradiation frequency can optionally be modulated to decreases the required concentration of the polarizing agents (see Chapter 4). Depending on the nuclei and on the radicals used, the DNP build-up can last between minutes and hours. At the DNP steady state, the nuclear polarization values can vary between 10 and 100%.

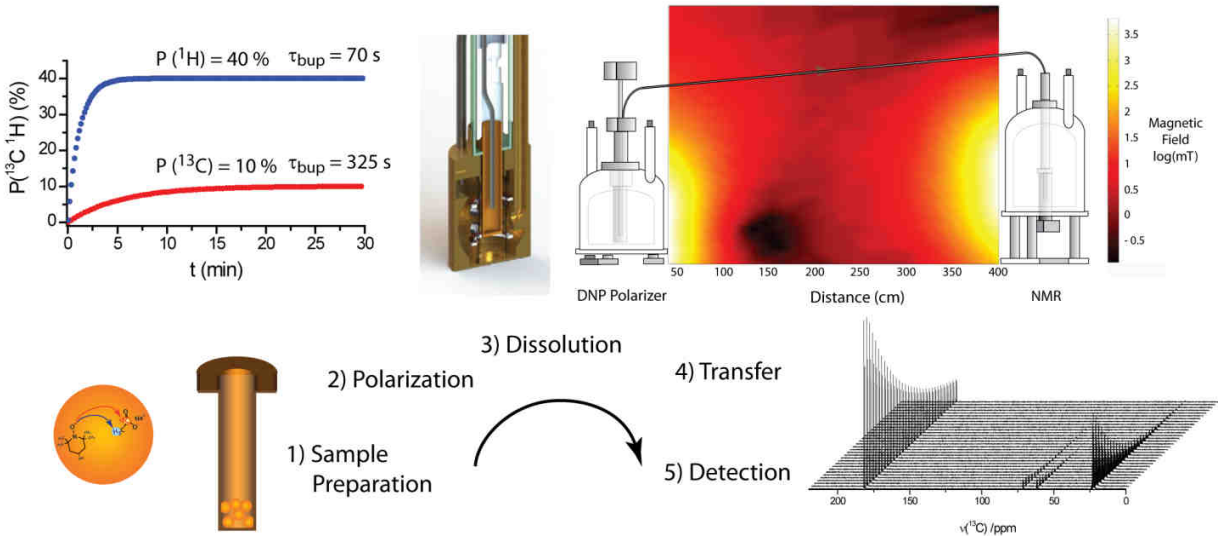

Figure 1.8: Schematic subdivisions of a Dissolution-DNP experiment.

Once the desired level of polarization is reached, the solid frozen sample need to be transferred to the detection apparatus at room temperature. The hyperpolarized sample is rapidly dissolved by a burst of hot water preheated to T = 400 K at a pressure of 1.0 MPa. It is then pushed toward the detection spectrometer. The life-time of the DNP-enhanced polarization is normally limited by the longitudinal (spin-lattice) relaxation time T_1, which tends to be short when the sample is travelling through the so-called 'death valley' on its voyage between the polarizer and the NMR or MRI magnet, through an area where the field can drop as low as the earth's field, *i.e.*, about 35 µT, or even below if it is cancelled by the stray field of the NMR magnets. This problem can be avoided in part by 'sandwiching' the PTFE tube that carries the solution (typically a 3 mm outer diameter tube) between rows of small permanent magnets. If one uses alloys of neodymium, iron and boron, one can maintain a field close to 1 T during the entire voyage (41). In addition, provided the sample contains pairs of spins, the polarization can be preserved by a temporary conversion into Long-Lived States. The use of such techniques will be developed in Chapter 8. At this point, the electrons needed to build up the high nuclear polarization are no longer desired, as they will destroy the magnetization through paramagnetic relaxation. Among other things, it is possible to reduce the resulting losses by using Vitamin C (42). A new approach, consisting in grafting the polarizing agent onto a nanoporous silica material that can be filtered during dissolution will be described in Chapter 7.

Note that in the case of a clinical injection of hyperpolarized material into human patients, a stringent quality control of the sample (pH, temperature, concentration, purity, …) has to be carried out. This additional step can take about a minute or so.

In the last step, the hyperpolarized material will have reached the NMR or MRI spectrometer. In the case of imaging, the analyte still needs to diffuse to its target through the body of the patient or animal. At this point, the DNP enhanced experiment can finally start. The range of possible measurements is only limited by the imagination of the experimentalist, and by his ability to adapt himself to the single-shot requirement. Two examples of experiments using hyperpolarized protons in the context of drug screening will be discussed in Chapters 5 and 6.

References

1. Abragam A (1966) Polarized Targets : How ? *International Conference on Polarized Target and Ion Sources*.
2. Abragam A (1961) *Principles of Nuclear Magnetism* (Oxford University Press).
3. Cavanagh J (2007) *Protein NMR spectroscopy : principles and practice* (Academic Press, Amsterdam ; Boston) 2nd Ed.
4. Ernst RR, Bodenhausen G, & Wokaun A (1987) *Principles of nuclear magnetic resonance in one and two dimensions* (Oxford University Press, Oxford; New York).
5. Hore PJ (1995) *Nuclear magnetic resonance* (Oxford University Press, Oxford ; New York).
6. Hore PJ, Jones JA, & Wimperis S (2000) *NMR, the toolkit* (Oxford University Press, Oxford ; New York).
7. Keeler J (2005) *Understanding NMR Spectroscopy* (Wiley, Chichester, England).
8. Levitt MH (2008) *Spin dynamics : basics of nuclear magnetic resonance* (Wiley, Chichester, England) 2nd Ed.
9. Duer MJ (2004) *Introduction to solid-state NMR spectroscopy* (Blackwell, Oxford, UK ; Malden, MA).
10. Roberts LD &Dabbs JWT (1961) Nuclear Orientation. *Ann Rev Nucl Sci* 11:175-212.
11. Slichter CP (1990) *Principles of magnetic resonance* (Springer-Verlag, Berlin ; New York) 3rd enl. and updated Ed.
12. Morris GA &Freeman R (1979) Enhancement of Nuclear Magnetic-Resonance Signals by Polarization Transfer. *J. Am. Chem. Soc.* 101(3):760-762.
13. Anderson WA &Freeman R (1962) Influence of a Second Radiofrequency Field on High-Resolution Nuclear Magnetic Resonance Spectra. *J. Chem. Phys.* 37(1):85.
14. Overhauser AW (1953) Polarization of Nuclei in Metals. *Phys. Rev.* 92(2):411-415.
15. Hartmann SR &Hahn EL (1962) Nuclear Double Resonance in Rotating Frame. *Phys. Rev.* 128(5):2042.
16. Pines A, Waugh JS, & Gibby MG (1972) Proton-Enhanced Nuclear Induction Spectroscopy - Method for High-Resolution NMR of Dilute Spins in Solids. *J. Chem. Phys.* 56(4):1776.
17. Carver TR &Slichter CP (1953) Polarization of Nuclear Spins in Metals. *Phys. Rev.* 92(1):212-213.
18. Wind RA, Duijvestijn MJ, Vanderlugt C, Manenschijn A, & Vriend J (1985) Applications of Dynamic Nuclear-Polarization in C-13 Nmr in Solids. *Prog. Nucl. Magn. Reson. Spectrosc.* 17:33-67.
19. Barnes AB, Corzilius B, Mak-Jurkauskas ML, Andreas LB, Bajaj VS, Matsuki Y, Belenky ML, Lugtenburg J, Sirigiri JR, Temkin RJ, Herzfeld J, & Griffin RG (2010) Resolution and polarization distribution in cryogenic DNP/MAS experiments. *Phys. Chem. Chem. Phys.* 12(22):5861-5867.
20. Rosay M, Tometich L, Pawsey S, Bader R, Schauwecker R, Blank M, Borchard PM, Cauffman SR, Felch KL, Weber RT, Temkin RJ, Griffin RG, & Maas WE (2010) Solid-state dynamic nuclear polarization at 263 GHz: spectrometer design and experimental results. *Phys. Chem. Chem. Phys.* 12(22):5850-5860.
21. Vitzthum V (2012) Improving Sensitivity in Solid State NMR: Surfaces, Quadrupolar Nuclei and Dynamic Nuclear Polarization. PhD Thesis (Ecole Polytechnique Fédérale de Lausanne, Lausanne).
22. Griffin RG (2010) Clear signals from surfaces. *Nature* 468(7322):381-382.
23. Lelli M, Gajan D, Lesage A, Caporini MA, Vitzthum V, Mieville P, Heroguel F, Rascon F, Roussey A, Thieuleux C, Boualleg M, Veyre L, Bodenhausen G, Coperet C, & Emsley L (2011) Fast Characterization of Functionalized Silica Materials by Silicon-29 Surface-Enhanced NMR Spectroscopy Using Dynamic Nuclear Polarization. *J. Am. Chem. Soc.* 133(7):2104-2107.

24. Lesage A, Lelli M, Gajan D, Caporini MA, Vitzthum V, Mieville P, Alauzun J, Roussey A, Thieuleux C, Mehdi A, Bodenhausen G, Coperet C, & Emsley L (2010) Surface Enhanced NMR Spectroscopy by Dynamic Nuclear Polarization. *J. Am. Chem. Soc.* 132(44):15459-15461.
25. Vitzthum V, Mieville P, Carnevale D, Caporini MA, Gajan D, Coperet C, Lelli M, Zagdoun A, Rossini AJ, Lesage A, Emsley L, & Bodenhausen G (2012) Dynamic nuclear polarization of quadrupolar nuclei using cross polarization from protons: surface-enhanced aluminium-27 NMR. *Chem. Commun.* 48(14):1988-1990.
26. Renault M, Pawsey S, Bos MP, Koers EJ, Nand D, Tommassen-van Boxtel R, Rosay M, Tommassen J, Maas WE, & Baldus M (2012) Solid-State NMR Spectroscopy on Cellular Preparations Enhanced by Dynamic Nuclear Polarization. *Angew. Chem. Int. Edit.* 51(12):2998-3001.
27. Linden AH, Lange S, Franks WT, Akbey U, Specker E, van Rossum BJ, & Oschkinat H (2011) Neurotoxin II Bound to Acetylcholine Receptors in Native Membranes Studied by Dynamic Nuclear Polarization NMR. *J. Am. Chem. Soc.* 133(48):19266-19269.
28. Ardenkjaer-Larsen JH, Fridlund B, Gram A, Hansson G, Hansson L, Lerche MH, Servin R, Thaning M, & Golman K (2003) Increase in signal-to-noise ratio of > 10,000 times in liquid-state NMR. *Proc. Natl. Acad. Sci. U.S.A.* 100(18):10158-10163.
29. Comment A, van den Brandt B, Uffmann K, Kurdzesau F, Jannin S, Konter JA, Hautle P, Wenckebach WTH, Gruetter R, & van der Klink JJ (2007) Design and performance of a DNP prepolarizer coupled to a rodent MRI scanner. *Concept. Magn. Reson. B* 31B(4):255-269.
30. Jannin S (2009) Dynamic Nuclear Polarization Techniques for Magnetic Resonance Imaging and Particles Targets Experiments. PhD Thesis (Ecole Polytechnique Fédérale de Lausanne, Lausanne).
31. Kurdzesau F (2009) Some Methods of Dynamic Nuclear Polarization for Use in Metabolic Imaging. PhD Thesis (Ecole Polytechnique Fédérale de Lausanne, Lausanne).
32. Kurhanewicz J, Vigneron DB, Brindle K, Chekmenev EY, Comment A, Cunningham CH, DeBerardinis RJ, Green GG, Leach MO, Rajan SS, Rizi RR, Ross BD, Warren WS, & Malloy CR (2011) Analysis of Cancer Metabolism by Imaging Hyperpolarized Nuclei: Prospects for Translation to Clinical Research. *Neoplasia* 13(2):81-97.
33. Nelson SJ, Kurhanewicz J, Vigneron DB, Larson PEZ, Harzstark AL, Ferrone M, van Criekinge M, Chang JW, Bok R, Park I, Reed G, Carvajal L, Small EJ, Munster P, Weinberg VK, Ardenkjaer-Larsen JH, Chen AP, Hurd RE, Odegardstuen LI, Robb FJ, Tropp J, & Murray JA (2013) Metabolic Imaging of Patients with Prostate Cancer Using Hyperpolarized [1-C-13]Pyruvate. *Sci. Transl. Med.* 5(198).
34. Ardenkjaer-Larsen JH, Leach AM, Clarke N, Urbahn J, Anderson D, & Skloss TW (2011) Dynamic Nuclear Polarization Polarizer for Sterile Use Intent. *NMR Biomed.* 24(8):927-932.
35. Cabella C, Karlsson M, Canape C, Catanzaro G, Serra SC, Miragoli L, Poggi L, Uggeri F, Venturi L, Jensen PR, Lerche MH, & Tedoldi F (2013) In vivo and in vitro liver cancer metabolism observed with hyperpolarized [5-C-13]glutamine. *J. Magn. Reson.* 232:45-52.
36. Meier S, Karlsson M, Jensen PR, Lerche MH, & Duus JO (2011) Metabolic pathway visualization in living yeast by DNP-NMR. *Mol Biosyst* 7(10):2834-2836.
37. Lee Y, Zeng HF, Ruedisser S, Gosser AD, & Hilty C (2012) Nuclear Magnetic Resonance of Hyperpolarized Fluorine for Characterization of Protein-Ligand Interactions. *J. Am. Chem. Soc.* 134(42):17448-17451.
38. Jensen PR, Meier S, Ardenkjaer-Larsen JH, Duus JO, Karlsson M, & Lerche MH (2009) Detection of low-populated reaction intermediates with hyperpolarized NMR. *Chem. Commun.* (34):5168-5170.
39. Meier S, Jensen PR, Karlsson M, & Lerche MH (2014) Hyperpolarized NMR Probes for Biological Assays. *Sensors* 14(1):1576-1597.

40. Frydman L &Blazina D (2007) Ultrafast two-dimensional nuclear magnetic resonance spectroscopy of hyperpolarized solutions. *Nat. Phys.* 3(6):415-419.
41. Milani J, Vuichoud B, Bornet A, Mieville P, Mottier R, Jannin S, & Bodenhausen G (2015) A Magnetic Tunnel to Shelter Hyperpolarized Fluids. *Rev. Sci. Instrum.*
42. Mieville P, Ahuja P, Sarkar R, Jannin S, Vasos PR, Gerber-Lemaire S, Mishkovsky M, Comment A, Gruetter R, Ouari O, Tordo P, & Bodenhausen G (2010) Scavenging Free Radicals To Preserve Enhancement and Extend Relaxation Times in NMR using Dynamic Nuclear Polarization. *Angew. Chem. Int. Edit.* 49(35):6182-6185.

Chapter 2:

A simple-minded pictorial representation of DNP mechanisms

2.1 Typical DNP samples and observables

2.1.1 DNP spectra, polarizations and build-up times

DNP mechanisms depend on many variables, like the electronic and nuclear concentration, the shape of the ESR spectrum, the nuclear gyromagnetic ratio, the electronic and nuclear relaxation rates (T_{1e}, T_{2e}, T_{1n} and T_{2n}), to cite only the main variables. Some of these parameters are field and/or temperature dependent and cannot be varied experimentally independently from each other, since most of them are interdependent. For a DNP experimentalist, there are two observables that can be used as a probe of the DNP mechanism under variable conditions: the maximal polarization $P^{max}(n)$ that can be reached for one or several nuclear spins n like ^{1}H or ^{13}C, and the time constant $\tau_{DNP}(n)$ that characterizes their DNP build-up behavior by fitting to a mono-exponential curve. These two observables can be probed for different microwave irradiation frequencies $\nu_{\mu W}$, leading to a so-called DNP spectrum. The analysis of the influence of different electronic or nuclear parameters on the shape of such spectra, especially on the difference in microwave frequencies between the positive and negative optima of the enhancement (referred to here as $\Delta_{DNP}{}^{max}(\nu)$) provides a way to understand and sort out different DNP mechanisms or to highlight the effect of each parameter. In Figure 2.1, examples of $P^{max}(n)$ and $\tau_{DNP}(n)$ DNP frequency spectra can be seen for $n = {}^{1}H$ and ^{13}C at $B_0 = 6.7$ T and $T = 4.2$ K.

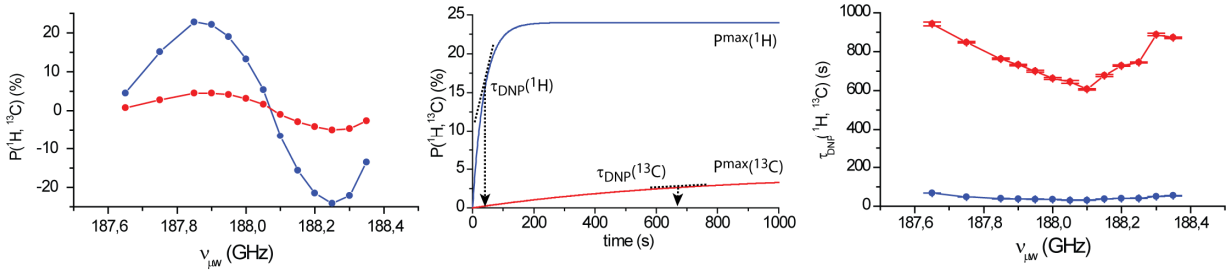

Figure 2.1: DNP frequency dependence of $P^{max}(n)$ (left) and $\tau_{DNP}(n)$ (right) for $n = {}^{1}H$ (blue) and $n = {}^{13}C$ (red) measured at $B_0 = 6.7$ T and $T = 4.2$ K in our polarizer. ^{1}H and ^{13}C DNP build-up curves (center) measured under the same conditions with a fixed microwave frequency $\nu_{\mu W} = 187.7$ GHz.

In this chapter I will first describe in section 2.2 the two main DNP mechanisms, the Solid Effect (SE) and the Cross Effect (CE), in a simple graphical way, using mainly the spin "flip-flop" model. I will also introduce the third DNP mechanism, known as Thermal Mixing (TM), that occurs especially under conditions where D-DNP is performed (3.35 T and 1.2 K). In Section 2.3, some ways to separate the three mechanisms experimentally will be proposed. Finally, in section 2.4, I will propose a simple rate

equation model that can simulate the influence on the final polarization $P^{max}(n)$ and on the DNP build-up time constant $\tau_{DNP}(n)$ of parameters such as the microwave field strength, the electronic polarization, the nuclear relaxation rate and the density of nuclear spins. This model is based on the work of Rosso *et al.* (1-3). For the discussions in section 2.3 and 2.4, I will corroborate simulations of the influence of various parameters by recording experimental data. The parameters used with the two models are chosen to simulate DNP experiments in a magnetic field B_0 = 6.7 T and a temperature between T = 4.2 K and 1.2 K, since the majority of the work done for this thesis was realized under these conditions.

2.1.2 DNP Sample

The first step in any DNP experiment, sometimes the most time-consuming, is the optimization of the sample preparation. The aim is to put the free electrons in contact with the nuclei to be polarized for various DNP mechanisms to occur most effectively.

Depending on the nucleus to be polarized, the choice of the radical is of crucial importance. More precisely its linewidth is a central parameter, as it will be shown in Sections 2.2 and 2.3. For example, radicals with narrow ESR lines, like Trityl (4-6), have shown to polarize low gamma nuclear spins *n* like ^{13}C very efficiently. On the other hand, radicals with broad lines, like TEMPO and its derivatives, are better to polarize protons, which represent an advantage or a drawback depending on the situation. Figure 2.2a shows the ESR spectrum of 50 mM TEMPOL in D_2O:Glycerol-d_8 (1:1) acquired in our polarizer at B_0 = 6.7 T and T = 1.2 K by longitudinally detected ESR (LODESR) with a home built apparatus (7) inspired by the work of Granwehr *et al.* (8). The width at half height $\Delta\nu_{½}$(ESR) = 300 MHz and the total width $\Delta\nu_{10\%}$(ESR) = 680 MHz. This spectrum, or approximations that can be used fitting it, will be used in the simulations of Section 2.3.

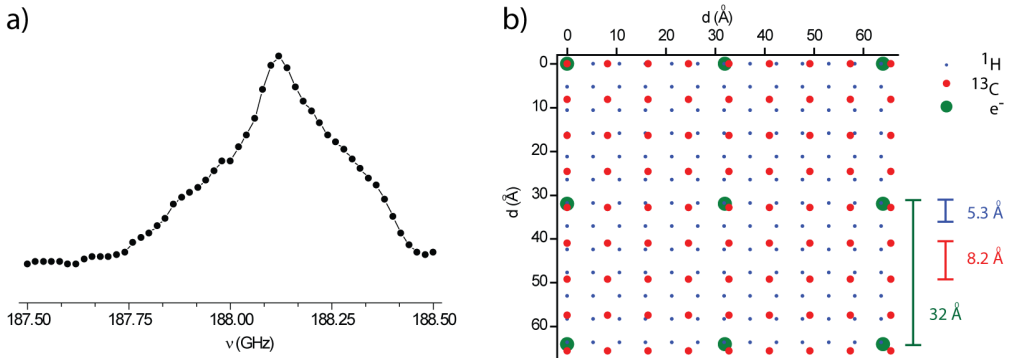

Figure 2.2 **a)** ESR spectrum of 50 mM TEMPOL acquired in our DNP polarizer at B_0 = 6.7 T and T = 1.2 K. **b)** Schematic distributions of the free radicals (green dots), ^{1}H nuclei (blue dots) and ^{13}C nuclei (red dots) in a standard sample of 3 M enriched 1-^{13}C acetate with 50 mM TEMPOL in H_2O:D_2O:Glycerol-d_8 (1:4:5).

A second optimization that must be done during sample preparation concerns the concentrations of the free radicals and of the molecules to be polarized. This will influence the inter-electronic and electron-nuclear distances and have an impact on many important parameters that play a crucial role for the DNP mechanisms. The electron concentration will influence the nuclear and electronic relaxation time constants (T_{1n}, T_{2n}, T_{1e} and T_{2e}), but also the electron-electron dipole-dipole couplings (9) and the hyperfine electron-nuclei interactions (10) that depend on r_{ee}^{-3} and r_{en}^{-3}, the inter-electron and electron-nuclear distances, respectively. Dipolar and hyperfine interactions play a central role in DNP polarization transfer. It is also possible to modulate the density of the spins to be polarized, more precisely the

number of spins around each paramagnetic centre, by changing the degree of deuteration of the proton sites or the concentration of isotopes labels ^{13}C, ^{15}N, ^{6}Li, ^{29}Si, ^{129}Xe, *etc.* The inter-spin distances of a sample containing 50 mM TEMPOL, the standard concentration used at 6.7 T and 1.2 K, 3 M 1-^{13}C acetate and various degrees of deuteration are reported in Table 2.1 and schematized in Figure 2.2b. The number of nuclei in a sphere of 1 nm radius and the number of electrons in a sphere of 4.7 nm radius around an electronic centre are also reported. This radius of 4.7 nm corresponds to an electron-electron interaction of 0.5 MHz (11). These numbers will be used in the simulations in the Section 2.4.

	Spin density [spins/cm^3]	Inter-spin distance (<d>) [Å]	Number of spins in a sphere with a radius of	
			4.7 nm	1 nm
50 mM TEMPOL	3.0 10^{19}	32	13	
3 M 1-^{13}C acetate	1.8 10^{21}	8.2		7
10% H_2O	6.6 10^{21}	5.3		27
100% H_2O	6.6 10^{22}	2.4		277

Table 2.1: Spin density and inter-spin distances for a standard sample of 3 M 1-^{13}C acetate with 50 mM TEMPOL with 0, 10 and 100 % ^{1}H. The numbers of electrons in a sphere of 4.7 nm radius around an electronic center, and the number of ^{13}C and ^{1}H nuclei in a sphere of 1 nm radius around an electronic center under the same conditions.

A homogeneous distribution of free radicals across the sample is usually believed to be necessary to ensure efficient DNP polarization. Indeed, we experimentally observe that it is crucial to prevent the crystallization of the sample upon cooling to low temperatures, as this will result in the expulsion of radicals to the interfaces between crystallites. The DNP sample is thus usually prepared in a glass-forming solvent, like pure pyruvic acid, H_2O:Glycerol (1:1), H_2O:Ethanol (2:1) H_2O:DMSO (2:3) or Toluene:THF (9:1).

2.1.3 ESR of TEMPO

The free radical TEMPO (2,2,6,6-Tetramethylpiperidine 1-oxyl) or its derivatives will be used as a source of unpaired electrons in almost all experiments presented in this Thesis. Different kinds of interactions will contribute to the shape of the ESR spectrum of TEMPO.

Due to the delocalization of the unpaired electron on the N-O bond, the electron will be influenced by the proximity of the ^{14}N nuclear spin (I = 1). This resulting hyperfine coupling will split the electron Zeeman energy levels in three sub-levels corresponding to the three nuclear states of ^{14}N. The amplitude of this splitting is described by the hyperfine tensor $A(\theta,\phi)$, which is orientation dependent, θ and ϕ being the polar and azimuthal angles that describe the orientation of the magnetic field with respect to the principal axes of the hyperfine tensor.

In standard DNP samples, the free radicals are homogeneously distributed and randomly oriented. Therefore, each electron may experience a slightly different local magnetic field, which gives rise to an anisotropic ESR spectrum. This source of broadening is called the *g*-anisotropy. The electron Landé factor can be described by a tensor $g(\theta,\phi)$. The contributions of the *g*-anisotropy and of the hyperfine coupling *A* give rise to *inhomogeneous* broadening. Note that the *g*-anisotropy depends linearly on B_0, whereas the hyperfine coupling is field-independent.

As the free radical concentration is high, the distance between the unpaired electrons will be short enough to observe an additional source of broadening due to the mutual perturbation of neighboring spins through dipolar *e-e* interactions. Under our DNP conditions, especially at high field, this broadening, called *homogeneous* broadening is generally smaller than the inhomogeneous one. Note that it is also field-independent. More detailed information on the ESR spectrum of TEMPO under DNP conditions as well as simulations of its ESR lineshape can be found in the theses of S. Jannin (12), p. 5-15, and of P. Miéville (13), p. 15-24.

The relative magnitudes of the contributions of homogeneous broadening of the EPR linewidth, δ, with respect to the inhomogeneous spectral breadth, Δ, has implications on the theoretical model chosen to describe the DNP mechanism (Cross Effect vs. Thermal Mixing). Indeed, at high radical concentration (high homogeneous broadening), the spectrum is quasi-continuous and the energy levels cannot be known in detail, so that a full quantum mechanical approach becomes difficult. Figure 2.3 shows, in an exaggerated way, the difference between inhomogeneously and homogeneously broadened ESR spectra, as well as the representation of the homogeneous linewidth, δ, and the inhomogeneous spectral breadth Δ.

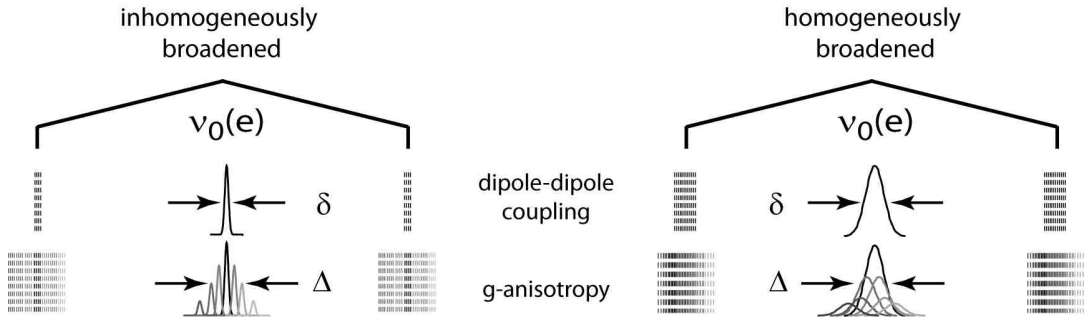

Figure 2.3: Schematic representations of inhomogeneously and homogeneously broadened ESR spectra.

2.2 Solid Effect, Cross Effect and Thermal Mixing mechanisms

The idea of transferring the large Boltzmann polarization of unpaired electrons to coupled nuclei was first proposed by Overhauser in 1952 at an APS meeting and published in 1953 (14). At the same time, Carver and Slichter brought the experimental proof of the validity of this suggestion for ^{7}Li (15) and in 1956 also for ^{1}H (16). This mechanism is now known as the Overhauser effect (OE). Following these experiments, additional pioneering DNP works were conducted. In 1957, the transfer of electron polarization to nuclei via the irradiation of a forbidden transition was proposed by Jeffries (17). The theory and experimental demonstrations of this mechanism, known today as Solid Effect (SE), were then further developed (18-21). SE requires the electrons to have EPR spectra with homogeneous linewidths (δ) and inhomogeneous spectral breadths (Δ) that must be smaller than the nuclear Larmor frequency (δ, $\Delta < \nu_0(n)$) (18, 22). A signature of polarization through SE is that the maximum positive and negative enhancements are separated by $2\nu_0(n)$. In 1967, Hwang and Hill (23, 24), following theoretical work by Kessernikh *et al.* (25, 26), showed that at high concentrations of free electrons an additional polarization mechanism appears, shifting the maximal enhancement peaks towards each other. This new mechanism, called Cross Effect (CE), becomes dominant if $\Delta > \nu_0(n) > \delta$. Finally, if electron-electron interactions are strong, the homogeneous EPR linewidth can become larger than the nuclear Larmor frequency ($\delta > \nu_0(n)$). In this case, if the electronic spin diffusion is more efficient than spin lattice relaxation, all

electrons that contribute to the ESR line are connected together. The description of DNP mechanisms requires the inclusion of this collective interaction between the electrons and the nuclei. Therefore, to describe this collective mechanism, a many-particle theory based on quantum statistics and spin thermodynamics instead of discrete transitions of single spins is needed. This theory, referred to as Thermal Mixing (TM), is based on the description by Provotorov (27, 28) in 1962 of the electron-nuclei system under microwave saturation in terms of reservoirs that are in thermal contact, using the spin temperature (29-31) concept. In the course of the years, the theory was improved by numerous contributions (32-37). New insights recently came from the development of Dissolution-DNP (5, 12, 38, 39).

2.2.1 Solid Effect

The Solid Effect (SE) (40, 41) is a two-spin process involving a single electron (*e*) coupled by magnetic dipole-dipole interactions to a single nuclear spin (*n*). The energy levels of such an *e-n* spin system, as well as the excess or deficit of their populations with respect to the saturated state, are represented in Figure 2.4. For simplicity, the Boltzmann electron and nuclear polarizations are defined as $P(e)$ = 100% and $P(n)$ = 0%. The transfer of the electron spin polarization to the nucleus can be induced by an off-resonance microwave irradiation at frequency $\nu_{\mu W} = \nu_0(e) - \nu_0(n)$ or $\nu_{\mu W} = \nu_0(e) + \nu_0(n)$ (where $\nu_0(e)$, $\nu_0(n)$ are the electronic, respectively nuclear, Larmor frequencies). Irradiating downfield at $\nu_{\mu W} = \nu_0(e) - \nu_0(n)$, one will hit the double-quantum (DQ) transition (flip-flip) of the *e-n* two-spin system.

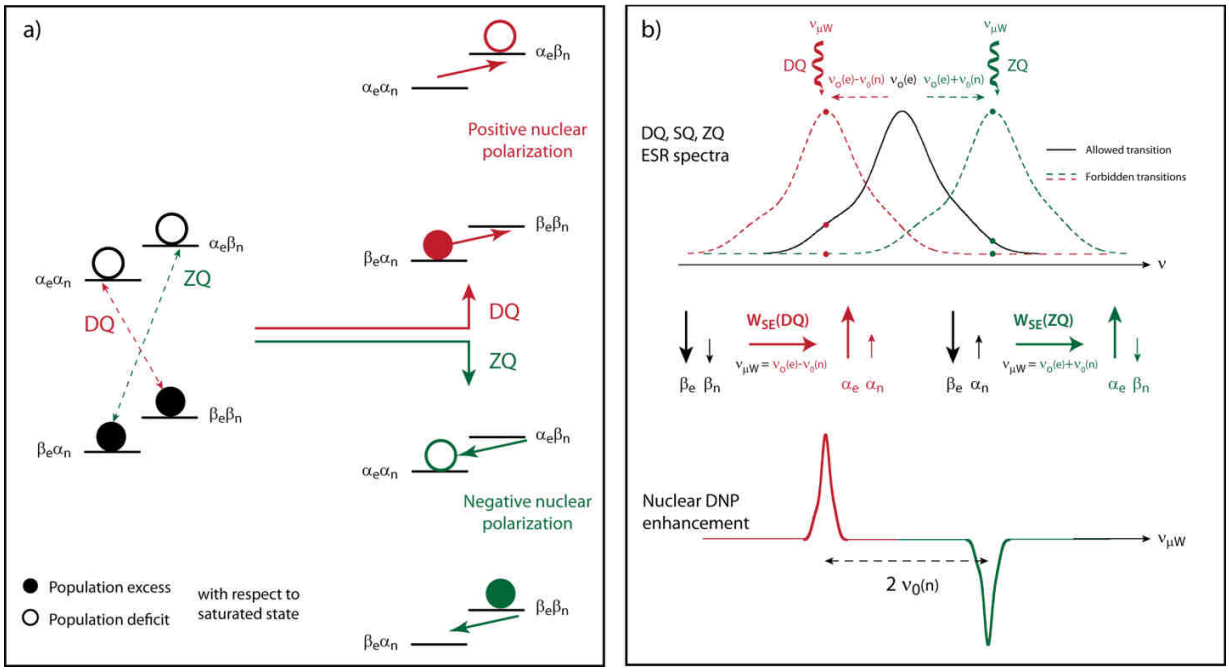

Figure 2.4: **a)** Energy level diagram to illustrate the Solid Effect mechanism and deviations of the populations from a saturated state: at Boltzmann equilibrium (black); after saturation of the double-quantum (DQ) *e-n* transition (red); or after saturation of the zero-quantum (ZQ) *e-n* transition (green). **b)** Schematic representation of the DQ (red), SQ (black) and ZQ (green) ESR spectra. The dotted lines DQ and ZQ underline the fact that the transition is forbidden and thus has lower probability. Schematic ''flip-flop'' representation of the Solid Effect mechanism via irradiation at the DQ (red) or ZQ (green) *e-n* transition. Schematic NMR spectrum enhanced by SE mechanism.

Similarly, upfield irradiation at $\nu_{\mu W} = \nu_0(e) + \nu_0(n)$ correspond to a zero-quantum (ZQ) transition (flip-flop) (See Figure 2.4). Such transitions, often called ''forbidden transitions'' are in reality second-order transitions that are partially allowed because of non-secular components of the hyperfine coupling (17, 18).

The saturation of the DQ transition will lead to a positive nuclear polarization, whereas the saturation of the ZQ *e-n* transition leads to a negative enhancement (Figure 2.4a). The overall nuclear DNP enhancement at a given microwave frequency will be given by the superposition of the DQ and SQ contributions. If the width of the ESR spectrum becomes larger than the nuclear Larmor frequency, this superposition could become destructive. In this case, the mechanism is referred to as "Differential Solid Effect" (42). As can be seen in Figure 2.4b, the maxima of the positive and negative enhancements are separated by twice the nuclear Larmor frequency.

As it involves a second order transition, SE requires intense microwaves irradiation. The probability of such ''forbidden'' transitions is low compared to single-quantum ESR transitions. It is possible to model quantum mechanically the Solid Effect to calculate these probabilities and simulate the polarization enhancement in such model system. Excellent QM treatments of the DNP mechanism at high field and low temperature are proposed by Griffin *et al.* (41), by Kockenberger *et al.* (43) and by Vega *et al.* (44).

2.2.2 Cross Effect

Unlike SE which relies on ''forbidden'' second-order transitions, the Cross Effect (CE) (41, 45) mechanism is based on allowed transitions.

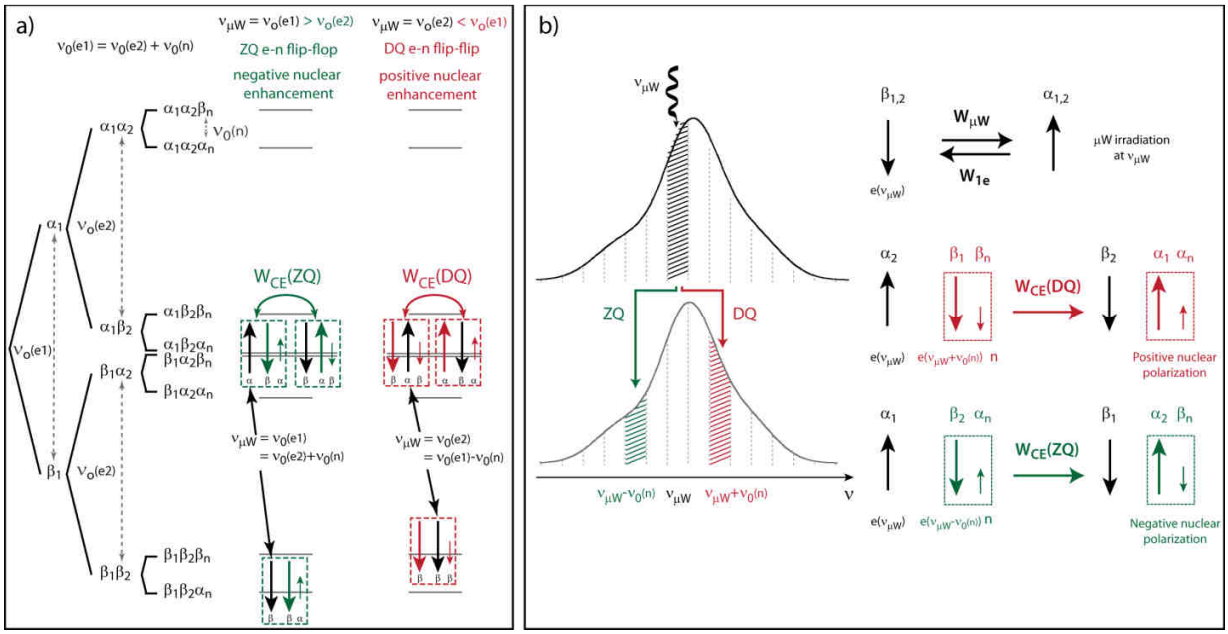

Figure 2.5: **a)** Energy level diagram for a three-spin system e_1-e_2-n meeting the condition for the cross effect (CE) ($\nu_0(e_1) = \nu_0(e_2) - \nu_0(n)$). Transition pathway for CE (ZQ) (green), $\nu_{\mu W} = \nu_0(e_1) > \nu_0(e_2)$ and CE (DQ) (red), $\nu_{\mu W} = \nu_0(e_2) < \nu_0(e_1)$. **b)** Schematic representation of the coupling pair of electrons involved in the CE (ZQ) and CE (DQ) mechanism. Schematic ''flip-flop'' representation of the Cross Effect mechanism.

The CE mechanism can be described by a three-spin process involving one nucleus *n* and two dipolar coupled electrons (e_1, e_2) with EPR frequencies that satisfies the relation $\nu_0(e_1) = \nu_0(e_2) - \nu_0(n)$. This can be the case if e_1 and e_2 have two different molecular orientations resulting in two different effective ESR resonance frequencies. The energy levels of such a 3-spin system are shown in Figure 2.5a. If the two dipolar-coupled electrons are separated in frequency by the Larmor frequency of the nucleus, $\nu_0(n)$, *i.e.,* if the CE condition mentioned above is fulfilled, the energy levels $\alpha_{e1}\beta_{e2}\alpha_n$ and $\beta_{e1}\alpha_{e2}\beta_n$ are degenerate.

The effect of an irradiation at $\nu_{\mu W} = \nu_0(e_1) > \nu_0(e_2)$ can be separated into two steps (treating only the useful transitions to describe the CE effect): (1) The population of the energy level $\beta_{e1}\beta_{e2}\alpha_n$ (half of the total population if $P(e) = 100\%$ and $P(n) = 0\%$) will be excited to $\alpha_{e1}\beta_{e2}\alpha_n$ via a spin flip of e_1 at $\nu_0(e_1)$. (2) Since the two levels are degenerate, the CE enhancement can occur later on via an energy-conserving flop-flip-flop between $\alpha_{e1}\beta_{e2}\alpha_n$ and $\beta_{e1}\alpha_{e2}\beta_n$ ($\uparrow\downarrow\uparrow$, $\downarrow\uparrow\downarrow$) resulting in an increase of the β_n population, and thus in a negative nuclear enhancement (See Figure 2.5). In my notation, this CE process involving a coupled electron e_2 that is lower in energy than the irradiated one is referred as CE (ZQ) as it involves a flip-flop between e_2 and *n*.

Similarly, the irradiation at $\nu_{\mu W} = \nu_0(e_2) < \nu_0(e_1)$ can be described in two steps. Note that here, in Figure 2.5a, the µW-excited electron is the central one (e_2) and e_1-*n* are coupled. Irradiation at $\nu_0(e_2)$ will transfer the population of the energy level $\beta_{e1}\beta_{e2}\beta_n$ to $\beta_{e1}\alpha_{e2}\beta_n$. Since they are degenerate, a flip-flop-flip can occur between $\beta_{e1}\alpha_{e2}\beta_n$ and $\alpha_{e1}\beta_{e2}\alpha_n$ leading to positive nuclear CE enhancement (See Figure 2.5). Again, I refer to this mechanism as CE (DQ), because of the flip-flip of e_1 and *n* involved in the DNP enhancement.

In these two descriptions, the fate of half of the total population that resides in the $\beta_{e1}\beta_{e2}\beta_n$ state for CE (ZQ) and in $\beta_{e1}\beta_{e2}\alpha_n$ for CE (DQ) is not treated. Indeed, it will also be excited by µW irradiation (at $\nu_0(e_1)$ or $\nu_0(e_2)$ respectively), but will relax back via T_{1e} as their excited states are not degenerate. Moreover, the overall CE process (µW excitation and energy-conserving CE transition) is in competition with the electronic and nuclear relaxation T_{1e} and T_{1n}, as well as with the CE back-transition that is allowed and equally probable. This will be treated in more detail in the Section 2.4.

As for the previous description of SE, this model does not say anything about the probability of W_{CE} transitions. To access this information, a quantum-mechanical treatment of this 3-spin system should be done under µW irradiation (41, 45, 46), but this is beyond the scope of this thesis.

2.2.3 Thermal Mixing

The two models presented above neglect the effect of dipole-dipole interactions among the electrons. Under such interactions, if the electronic spin diffusion is more efficient than the spin lattice relaxation, the electron spin system will respond as a whole to microwave irradiation. The description of the DNP process should include such collective effects. A new approach using a many-particle thermodynamic description rather than a quantum description of single-particle discrete transitions was developed. This mechanism is referred to as Thermal Mixing (TM). The description below is based on reviews by Atsarkin (35, 47, 48) and Goertz (49).

The central quantity of the process is the spin temperature (29-31). As shown in Chapter 1, for any system with energy levels E_1 and E_2, with an energy difference $\Delta E_{1,2}$, the ratio n_1/n_2 of the populations of the two energy levels will be given by Boltzmann's law :

$$\frac{n_1}{n_2} = \exp\left(\frac{-\Delta E_{1,2}}{k_B T_{1,2}}\right) \tag{2.1}$$

It is therefore possible to express a population difference between the two levels E_1 and E_2 in terms of a spin temperature:

$$T_{1,2} = -\frac{\Delta E_{1,2}}{k_B\left(\ln(n_1) - \ln(n_2)\right)} \tag{2.2}$$

The same rearrangement can be done for the expression of the polarization described in Equation 1.7 in Chapter 1.

In the simplest case of thermal equilibrium, $T_{1,2}$ is given by the temperature of the heat bath surrounding the system, *i.e.,* the temperature T_L of the lattice. As soon as the system is moved out of equilibrium, $T_{1,2}$ will diverge from T_L. For example, saturation will heat $T_{1,2}$ and hyperpolarization will cool it down. The parameter $T_{1,2}$ thus reflects the ordering of the system, no matter by which mechanism it may have attained this order.

The spin temperature concept was used by Redfield (31) to describe the evolution of a spin system under strong irradiation. Such a system is most simply described in a rotating reference frame (noted here by an asterisk *) given by the irradiation frequency $\nu_{\mu W}$ (in the case of the electronic spin system). In such a frame, the quantization axis is given by the direction of the effective field B_{eff}, the vector sum of the μW field B_1^* and of the longitudinal field $B_0^* = \Delta\nu/\gamma$ (where $\Delta\nu = \nu_{\mu W} - \nu_0(e)$ is the offset of the microwave frequency and γ is in frequency units). Therefore, when a microwave irradiation is applied with a frequency $\nu_{\mu W}$ close to the electron frequency $\nu_0(e)$, the spin temperature (T_{Ze}*) of the electron Zeeman system is reduced by a factor - $\Delta\nu/\nu_0(e)$. As a result, the corresponding equilibrium temperature in the rotating frame is as low as $T_{Ze}^* = -T_L\,\Delta\nu/\nu_0(e)$.

Provotorov (27, 28) described the resonant saturation of an electronic system experiencing efficient spin-spin diffusion under a weak transverse field in the high temperature approximation. The system is described by two reservoirs; the electron Zeeman reservoir Z(*e*) and the spin-spin subsystem SS(*e*) corresponding to the splitting of the electron spin Hamiltonian in two commuting parts, the Zeeman and the truncated dipolar Hamiltonians. Each of these reservoirs possesses its own spin temperature T_{Ze}, respectively T_{SSe}. Provotorov described the evolution of the two inverse spin temperatures $\beta_{Ze} = (k_B T_{Ze})^{-1}$ and $\beta_{SSe} = (k_B T_{SSe})^{-1}$ with two simple rate equations under conditions of arbitrary saturation. If such a two-temperature model is applicable to the system, the Provotorov equations predict that under microwave irradiation at frequency $\nu_{\mu W} = \nu_0(e) + \Delta\nu$, the values of β_{Ze} and β_{SSe} become different. Microwave irradiation with a frequency that is slightly off-resonance from $\nu_0(e)$ will push T_{Ze} and T_{SSe} away from the thermal equilibrium situation where they are equal to the lattice temperature T_L. Part of the energy quanta $h\nu_{\mu W}$ provided by the μW irradiation will be absorbed by the Zeeman system, and the remaining part will be either absorbed or emitted by the electronic dipolar system. It is thus possible to cool down the electron dipolar bath by irradiation at a frequency slightly different from the electron Larmor frequency. Figure 2.6a shows the distribution of the populations across the energy levels if $T_{Ze} = T_{SSe} = T_L$, or if $T_{SSe} \neq T_{Ze}$, where T_{SSe} can be positive or negative.

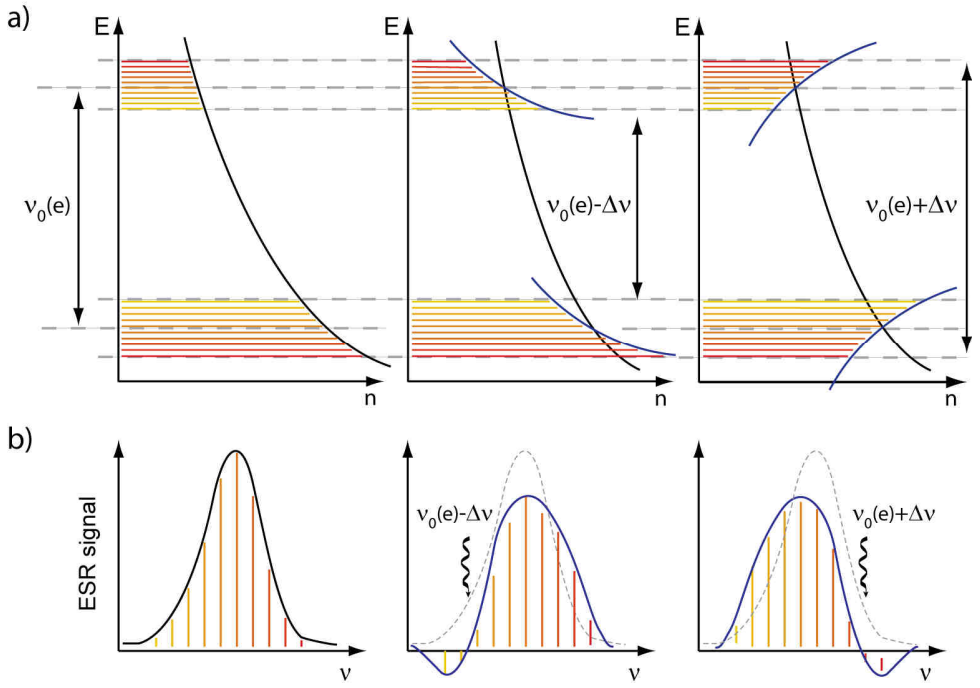

Figure 2.6: **a**) Dynamic cooling of the electronic dipole-dipole reservoir induced through microwave irradiation with a frequency shift $\Delta\nu = \nu_{\mu W} - \nu_0(e)$. The abscissae give the relative populations in the energy levels and the vertical axis represents the energy. **b**) Schematic representation of the ESR line-shape under the conditions described in **a**. Adapted from (35) and (13).

The Provotorov equations predict a characteristic distortion of the EPR absorption line-shape under conditions of saturation with $\Delta\nu \neq 0$. Following the population distribution described in Figure 2.6a, if spin diffusion is faster than spin-lattice relaxation, the µW irradiation with a slight offset $\Delta\nu$ should give rise to a region of emission and of increased absorption in the ESR spectrum (Figure 2.6b). Such shapes, which are diagnostic of two distinct spin temperatures, were indeed observed experimentally (See Reference (35)).

The nuclear spin system can then be included. If the NMR Larmor frequency $\nu_0(n)$ falls in the range of the characteristic electron dipolar linewidth (*i.e.* if $\nu_0(n) < \Delta$), energy exchanges between the electron dipolar subsystem and the nuclear Zeeman bath are possible. Such exchanges will happen via electron-nucleus dipole-dipole interactions and electron-electron flip-flops, *i.e.*, via the same kind of contributions as in the CE mechanism. This is why "*one can consider the Thermal Mixing process as a generalization of the 3-spin CE to real many-particle spin-spin interactions*" (Atsarkin in (47, 48)). The spin temperature T_{SSe} of the electron dipolar bath will tend to become equal to the nuclear Zeeman spin temperature T_{Zn}. A decrease of T_{Zn} corresponds to an increase of the nuclear polarization as $P(n) = \tanh(\hbar\nu_0(n)/k_B T_{Zn})$.

A complete description of the DNP process in thermodynamical language, with the concepts of spin temperature, thermal balance, and contacts between heat reservoirs, is thus possible. A schematic picture is shown in Figure 2.7. Under microwave irradiation, there are two lattice reservoirs. The first one is in the rotating frame, strongly cooled to $T_L^* = -T_L\, \Delta\nu/\nu_0(e)$, which acts as a refrigerator for the electronic Zeeman subsystem with relaxation rate $W_1(e)$. As they are not resonant with the µW irradiation, the electron dipolar bath SS(*e*) and the nuclear Zeeman bath Z(*n*) are connected to the lattice

with a "normal" temperature T_L with relaxation rates W_1(SS) and $W_1(n)$. The cold electron Zeeman bath $Z^*(e)$ is coupled to the electron dipolar bath via microwave pumping with a rate $W_{\mu W}$.

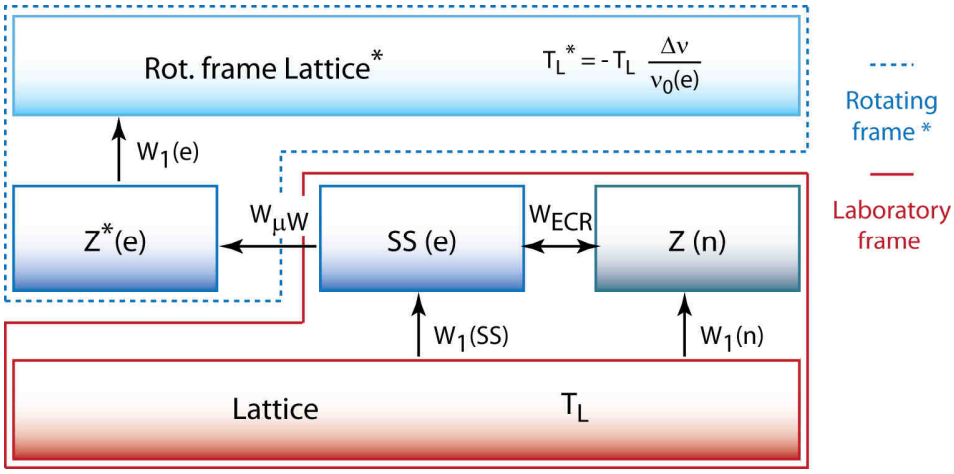

Figure 2.7: Heat flow diagram to illustrate Thermal Mixing (TM). The arrows show the channels of thermal exchange. The corresponding rates are the transition probabilities W.

The reservoirs SS(*e*) and Z(*n*) are connected via Thermal Mixing. Using this thermal balance diagram, it is in theory possible to calculate the steady-state enhancement of the nuclear polarization. Nevertheless, to be able to obtain qualitative predictions, some of the approximations have to be lifted. The model was first extended to the case of inhomogeneous EPR broadening with fast spectral diffusion, using the concept of spin packets (35). The model was also verified in the low-temperature limit by Borghini (37) and a nuclear leakage factor was added by de Boer (36). More recently, a model for partial saturation at low temperature was also proposed (12, 38).

The conditions where hyperpolarization of nuclei via Thermal Mixing can happen are actually quite strict. The width of the ESR line should be larger than the Larmor frequency of the nucleus to be polarized. Furthermore, the electronic spectral diffusion within the EPR spectrum should be faster than the electron spin lattice relaxation. These conditions are favoured at low field, at low temperature (longer T_{1e}) or at high electron concentration (faster spin diffusion). Interestingly, these requirements are fulfilled in standard Dissolution-DNP conditions (3.35 T, 1.2 K, 15-30 mM radicals). A great deal of evidence shows that TM is indeed the dominant mechanism under such conditions. Nevertheless, at higher fields, *e.g.*, at 6.7 T as in the experiments presented in this thesis, the situation is more complicated and a competition between SE, CE and TM happened. This subject will be developed in more detail in the Section 2.3.

2.3 Distinguishing between DNP mechanisms

2.3.1 Exclusion of mechanisms

In some cases, the conditions are such that some DNP mechanisms can be readily excluded. If the ESR linewidth of radical is smaller than the Larmor frequency of the nuclei to be polarized, neither Cross Effect nor Thermal Mixing will be possible and the polarization will happen only through the Solid Effect (See Figure 2.9a for an example). Note that the contrary is not true: if $\Delta\nu_{½}$(ESR) > $\nu_0(n)$, polarization via

SE is possible, as shown below. Moreover, as SE happens through a forbidden transition, it is most likely that this mechanism will not be favoured if the microwave irradiation field strength is low. For example, in our D-DNP polarizer, there is no resonant cavity for µW, so that $\nu_{1\mu W}$ is very low, between 1 and 10 kHz. Under these conditions, polarization will most likely build up via CE or TM mechanisms, which involve allowed single-quantum electronic transitions.

It is also important to remember that Thermal Mixing can occur only if the electronic spectral diffusion is fast compared to T_{1e}, especially in the case of inhomogeneously broadened ESR spectra, where the electronic magnetization has to diffuse from spin packet to spin packet. In the case of a system of non-interacting spin packets, only a fraction of the ESR spectrum will be saturated and holes will be burned in the ESR line shape. The nuclear polarization will eventually build up via the Cross Effect but not via TM. In this context, the usual conditions at 3.35 T and 1.2 K are favourable to the establishment of electronic Thermal Mixing. T_{1e} is on the order of 1 s and spin diffusion is fast at high electron concentration (15 - 30 mM). Nevertheless, T_{1e} decreases extremely fast at higher temperatures, thus excluding TM. Moreover, as the *g* anisotropy is field-dependent, whereas the homogeneous broadening is not, increasing the field will slow down spin diffusion (see Figure 2.3 for an illustration). The homogeneous broadening can be augmented by increasing the radical concentration, but this will also affect the electronic spin-lattice relaxation time. Therefore, at higher fields, like under our conditions at B_0 = 6.7 T, Thermal Mixing is less favoured, and we should be in a transition regime between TM and CE. Some evidence for this regime will be shown in the next Sections.

2.3.1 Simulations of DNP frequency spectra

As shown in Section 2.1, a diagnostic tool to distinguish between SE and CE contribution is the inspection of the difference Δ_{max}^{DNP} of µW frequencies between the positive and negative DNP maxima. Indeed, with the 2-spin *e*-*n* and 3-spin e_1-e_2-*n* models used in section 2.2 Δ_{max}^{DNP}(SE) should be twice as large as the nuclear Larmor frequency, and Δ_{max}^{DNP}(CE) should be equal to $\nu_0(n)$. Nevertheless, the ESR linewidth of the radicals also plays an important role in determining the shape of the DNP frequency spectra. As $\Delta\nu_{½}$(ESR) becomes larger than $\nu_0(n)$, the situation becomes less clear-cut, and Δ_{max}^{DNP}(SE or CE) deviate from $2\nu_0(n)$ respectively from $\nu_0(n)$.

The EPR lineshape of the free radicals can be used to calculate qualitatively the contributions of the Solid Effect and the Cross Effect to the DNP frequency spectra. This approach shown below is inspired by the one developed by Vega *et al.* (11, 44, 50, 51). Even if it is used here in a more simplistic way, it allows one to see qualitatively the influence of the ESR linewidth. Following the description in 2.2.1 and 2.2.2, the contributions of SE to the shape of the DNP frequency spectra can be estimated, taking the fraction of electrons at each irradiation frequency $\nu_{\mu W}$ that contribute to a net nuclear enhancement (negative + positive contributions). Similarly, at each irradiation frequency $\nu_{\mu W}$, the electrons contributing to a net nuclear enhancement (negative + positive contributions) by the CE mechanism can be estimated considering the product of the electrons irradiated and their coupling partners that match the CE (ZQ) or CE (DQ) conditions:

$$SE\left(\nu_{\mu W}\right) = a_{SE}\left[I_{ESR}\left(\nu_{\mu W}+\nu_0(n)\right) - I_{ESR}\left(\nu_{\mu W}-\nu_0(n)\right)\right]; \tag{2.3}$$

$$CE\left(\nu_{\mu W}\right) = a_{CE} I_{ESR}\left(\nu_{\mu W}\right)\left[I_{ESR}\left(\nu_{\mu W}+\nu_0(n)\right) - I_{ESR}\left(\nu_{\mu W}-\nu_0(n)\right)\right]. \tag{2.4}$$

where $I_{ESR}(\nu_{\mu W})$ is the ESR intensity at frequency $\nu_{\mu W}$, and a_{SE} , a_{CE} are the contributions of the SE and CE mechanisms.

Different DNP frequency spectra for ^{1}H were calculated using equations 2.3 and 2.4 for the SE and CE mechanisms described above. A single Gaussian with a central frequency ν_0(ESR) = 188.1 GHz (TEMPO at 6.7 T) and a variable ESR linewidth ($\Delta\nu_{½}$(ESR)) was used and the proton frequency was set to $\nu_0(^{1}H)$ = 285 MHz (^{1}H frequency at 6.7 T). As can be seen in Figure 2.8a,b, radicals with ESR lines narrower than the Larmor frequency of the nucleus will polarize exclusively through SE mechanism. Under these conditions, there is no chance of finding a pair of coupled electrons that can contribute to DNP through the CE mechanism.

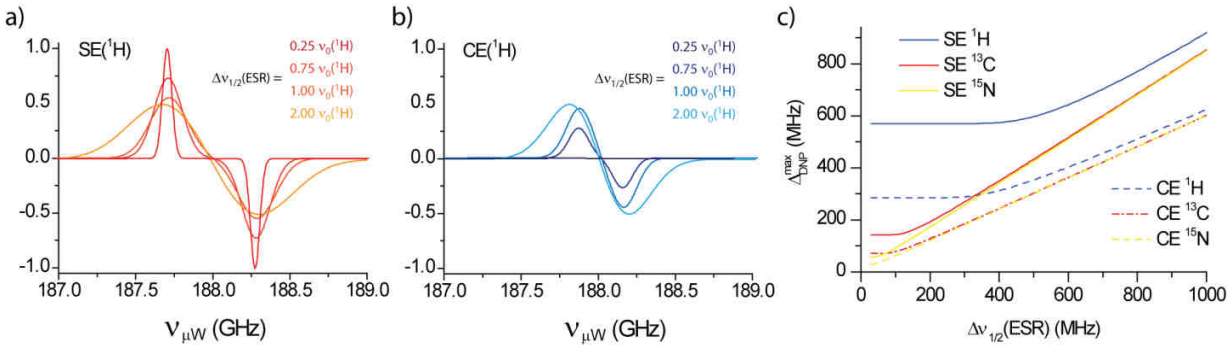

Figure 2.8: **a**) Contributions due to the solid effect (SE) calculated with Equation 2.3 using a single Gaussian centered at ν_0(ESR) = 188.1 GHz with a variable width at half-height $\Delta\nu_{½}$(ESR). $\nu_0(^{1}H)$ = 285 MHz (proton Larmor frequency at 6.7 T). **b**) CE contributions calculated with Equation 2.4 under the same conditions as in (**a**). **c**) Difference between the positive and negative extrema of the SE and CE contributions in the DNP frequency spectra Δ_{max}^{DNP}(SE,CE) as a function of the width at half-height $\Delta\nu_{½}$(ESR) for three nuclear Larmor frequencies $\nu_0(n = {}^{1}H)$ = 285 MHz, $\nu_0(n = {}^{13}C)$ = 71.25 MHz and $\nu_0(n = {}^{15}N)$ = 28.5 MHz, calculated with Equations 2.3 and 2.4 as in (**a**) and (**b**).

With the model used here, the electron contributions are summed over the ESR lineshape, so that Δ_{max}^{DNP}(SE, CE) changes. To show this, Δ_{max}^{DNP} is calculated as function of the width of the ESR line as reported in Figure 2.8c for three different Larmor frequencies, $\nu_0(n)$ = 285, 71.25 and 28.5 MHz representing ^{1}H, ^{13}C and ^{15}N at B_0 = 6.7 T. As the ESR linewidth increases, the frequency difference between the negative and positive DNP maxima increases. For the SE contribution, Δ_{max}^{DNP}(SE) starts at $2\nu_0(n)$ and increases when $\Delta\nu_{½}(ESR)/\nu_0(n) > 1$, *i.e.*, when the electron linewidth becomes larger than the nuclear Larmor frequency. For the CE contribution, Δ_{max}^{DNP}(CE) starts at ν_0(n) and increases when $\Delta\nu_{½}(ESR)/\nu_0(n) > 1$. Moreover, for very large ESR linewidths compared to the nuclear Larmor frequency, Δ_{max}^{DNP}(SE) respectively Δ_{max}^{DNP}(CE) tends to a common value regardless of the nucleus *n*.

To illustrate the influence of the ESR linewidth of the free radical on the dominant DNP mechanism, two experimental DNP frequency spectra are shown in Figure 2.9. In the first example the protons of polystyrene (d_8:d_5 95:5) are polarized by 40 mM BDPA, a narrow linewidth radical ($\Delta\nu_{½}(ESR) < \nu_0(^{1}H)$), at B_0 = 6.7 T and T = 4.2 K. As $\Delta\nu_{½}$(ESR) is smaller than the ^{1}H Larmor frequency, it is mainly the Solid Effect that contributes to the DNP enhancement. As expected, the difference between the frequencies of maximal positive and negative enhancements Δ_{max}^{DNP} is $2\nu_0(^{1}H)$. Note also the presence of an enhancement at $\nu_{\mu W} = \nu_0$(ESR) via the Overhauser mechanism (data kindly shared by Xiao Ji). This mechanism will not be analysed here. In the second example, 3 M sodium acetate-1^{13}C in H_2O:D_2O:Gly-d_8 (1:4:5) was polarized under the same conditions by 50 mM TEMPOL, which has a broad ESR linewidth

($\Delta\nu_{½}$(ESR) = 300 ± 5 MHz). The ^{1}H and ^{13}C intensities are normalized. As shown above, since $\Delta\nu_{½}$(ESR) is larger than the ^{13}C Larmor frequency, the µW frequency difference between maximal positive and negative DNP enhancements tends to shift to a common value with the one of ^{1}H. Δ_{max}^{DNP} in both ^{1}H and ^{13}C DNP spectra is larger than $\nu_0(^{1}H)$ and $\nu_0(^{13}C)$, respectively.

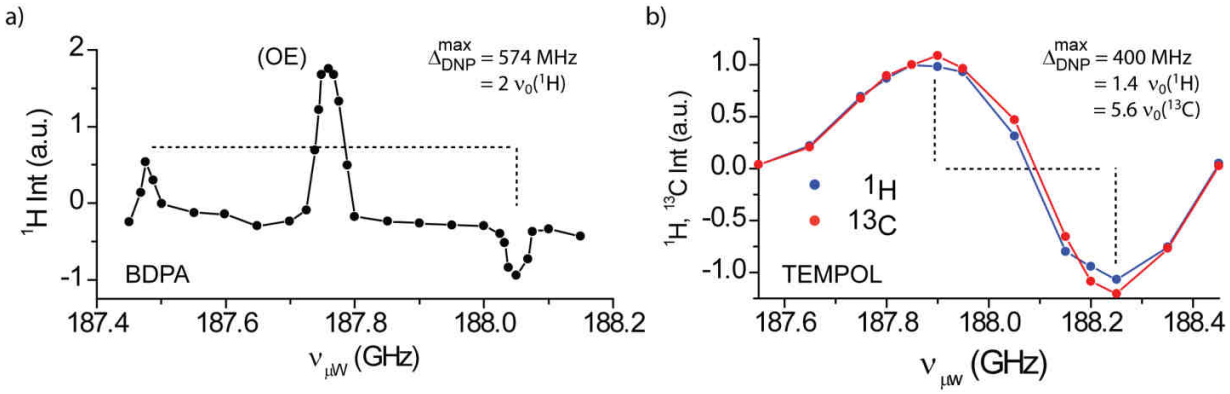

Figure 2.9: **a**) Normalized experimental ^{1}H DNP spectrum of polystyrene (d_8:d_5 95:5) polarized by 40 mM BDPA at B_0 = 6.7 T and T = 4.2 K. **b**) Normalized experimental ^{1}H and ^{13}C DNP spectra of 3 M 1-^{13}C acetate in H_2O:D_2O:Gly-d_8 (1:4:5) polarized by 50 mM TEMPOL at B_0 = 6.7 T and T = 4.2 K.

To be informative, the analysis of the DNP spectrum should not only include the ESR linewidth, but also the influence of other parameters, such as the microwave saturation of the EPR line, the electronic and nuclear relaxation rates and the electronic and nuclear spectral diffusion rates. In recent years, many authors have developed advanced models of the DNP mechanism, notably via a full quantum mechanical treatment of the Solid Effect and of the Cross Effect, as proposed by Griffin *et al*. (41) by Kockenberger *et al*. (43, 46) and Vega *et al*. (40, 45, 52, 53). It is therefore possible to predict "*ab initio*" the shape of the DNP frequency spectra for different conditions and to compare it to experimental data in order to study the contributions of the different mechanisms. This approach was mainly developed in the group of Vega (11, 40, 44, 45, 50, 51, 54, 55). They computed the spin Hamiltonian of interacting 2-spin systems *e-n* for SE or 3-spin system e_1-e_2-*n* for CE, diagonalized its matrix representation in the rotating frame of the electrons in order to introduce different relaxation rates. Then, solving the Liouville - von Neuman equation in the presence of the µW field, the evolution of the system is obtained. Enhancements as a function of the microwave irradiation frequency (DNP spectra) can be obtained for both SE and CE effects. The fit of experimental data with these two "basis" spectra allows one to determine the relative contributions of SE and CE under different conditions (temperature, type of radical, radical concentration, µW field strength, etc.)

In their analysis, with a microwave power of 600 kHz, they showed that at temperatures between 20 and 4 K, the SE contribution to the DNP enhancement becomes dominant with respect to CE. In a recent study (54), these authors analysed the influence of the microwave power on the DNP spectra. They showed that a reduction of the µW power to $\nu_{1\mu W}$ = 60 kHz almost suppresses the SE contribution and increases the CE effect at low temperatures. This trend, also reported by Han *et al.* (55) agrees with our observations at 6.7 T and 1.2 K. This makes sense: since the microwave field strength in our polarizer is as low as $\nu_{1\mu W}$ = 1 - 10 kHz, we are far from ESR saturation.

It is possible to fit the DNP spectra shown in Figure 2.9b with an admixture of SE and CE "basis spectra" calculated with Equations 2.3 and 2.4, but including the influence of the µW saturation and of electronic

spectral diffusion. The Matlab notebook used for the calculations is given in the Appendix of this Chapter. A nearly pure (95 %) CE basis shape gives the best fit of the experimental ^{1}H and ^{13}C DNP spectra. Moreover, admixtures of CE and SE "basis spectra" are not sufficient to perfectly match the experimental data, indicating that under our DNP conditions, Thermal Mixing should still be active.

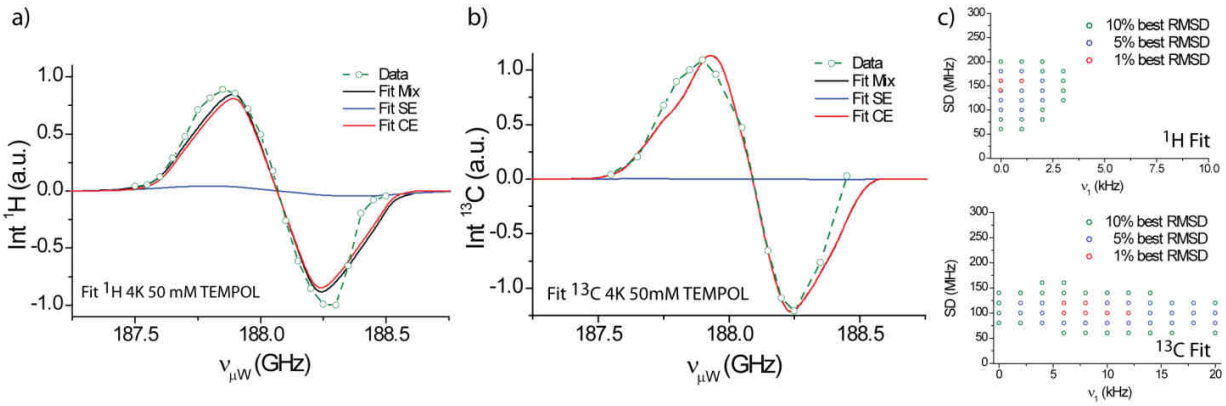

Figure 2.10: Fit of the DNP spectra of ^{1}H (**a**) and ^{13}C (**b**) DNP of 3 M 1-^{13}C acetate in H_2O:D_2O:Gly-d_8 (1:4:5) polarized by 50 mM TEMPOL at B_0 = 6.7 T and T = 4.2 K with ''basic'' SE and CE contributions calculated using Equations shown in the Appendix to this Chapter. The microwave field strength and the bandwidth $\Delta\nu_{\mu W}$(SD) simulating electronic spin diffusion are varied to obtain ''basic'' SE($\nu_{\mu W}$) and CE ($\nu_{\mu W}$) responses. For each combination $\nu_{1\mu W}$ and $\Delta\nu_{\mu W}$(SD), the best RMSD are reported in **c** (10% (green), 5% (blue) 1% (red).

2.3.2 Common nuclear spin temperature

A key difference between the SE/CE and TM mechanisms resides in the fact that in the first case the transferred quantity is the electronic polarization, whereas in the second it is the spin temperature. In the case of Thermal Mixing, all polarized nuclei should have a common spin temperature, whatever the irradiation frequency. Therefore, their steady-state DNP polarizations should be proportional to their gyromagnetic ratios γ and their normalized DNP spectra should have the same shape for all nuclei. On the contrary, for CE and SE, at least in the limit where the ESR linewidth is not much larger than $\nu_0(n)$, the DNP spectra of each nucleus should be different, with a difference Δ_{max}^{DNP} between the optima of $2\nu_0(n)$ for SE or $\nu_0(n)$ for CE, but the intensity of each DNP spectrum should be the same.

For many isotopes at 3.35 T and 1.2 K, it was shown that different nuclei polarized in the same sample shared the same Zeeman spin temperature (39). This is clear evidence that the major contribution stems from Thermal Mixing under these conditions. An example of DNP spectra of ^{1}H and ^{13}C of 1-^{13}C sodium acetate polarized by 33 mM TEMPO at 3.35 T and 1.2 K is shown in Figure 2.11 (56).

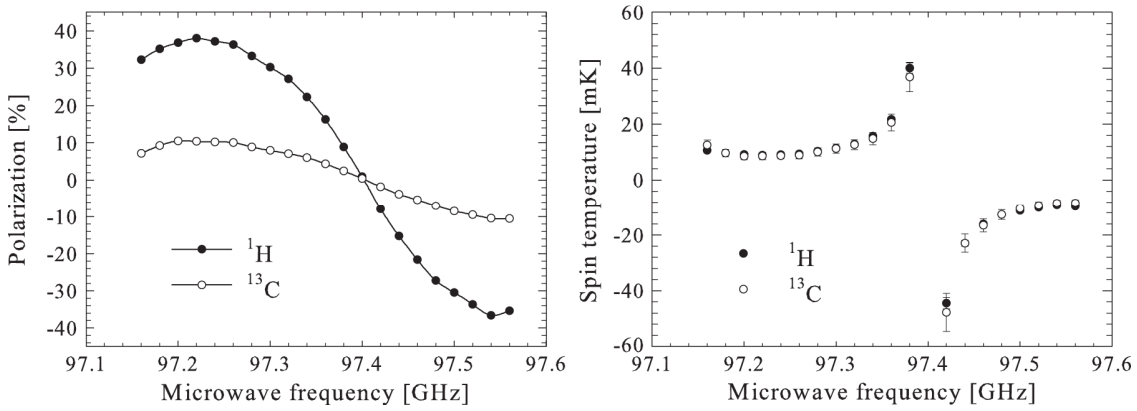

Figure 2.11: Microwave DNP spectra measured in a frozen 3 M sodium acetate solution in 67/33 vol% deuterated water/ethanol doped with 33 mM TEMPO. Absolute polarizations (left) and corresponding spin temperatures (right) (Adapted from (56)).

Measurements of steady-state DNP polarizations of 3 M 1-^{13}C acetate in the presence of 30 mM TEMPOL at 3.35 T at different temperatures show the same trends (57) (see Table 2.2 in Section 2.5.1). Nevertheless, if the field is increased to 6.7 T, the Zeeman spin temperatures of ^{1}H and ^{13}C in the DNP steady state are no longer the same (58) (see Table 2.3 in Section 2.5.2). This indicates that, under our conditions, TM becomes less efficient at higher fields and competes with CE.

It can be seen in Figure 2.9b that, even if they no longer share a common spin temperature, ^{1}H and ^{13}C have a DNP spectrum with similar normalized shapes at 6.7 T with an optimized TEMPOL concentration (50 mM). Nevertheless, if the free radical concentration is decreased, *i.e.,* if the homogeneous broadening is decreased, the positive and negative ^{13}C DNP maxima tend to shift away from the one of ^{1}H, and $\Delta_{max}^{DNP}(^{13}C)$ shrinks. This can be seen in Figure 2.12 where ^{1}H and ^{13}C DNP spectra of 1-^{13}C acetate 3 M were recorded for different TEMPOL concentrations at 4.2 K.

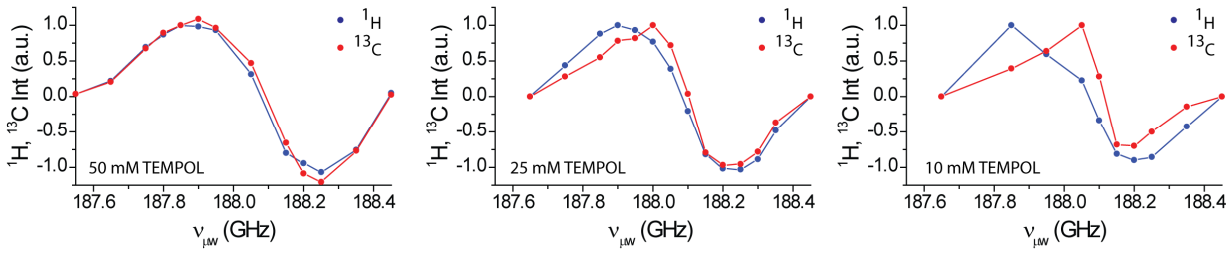

Figure 2.12: Comparison between the normalized ^{1}H and ^{13}C DNP spectra of 3 M 1-^{13}C acetate in H_2O:D_2O:Gly-d_8 (1:4:5) polarized by 50, 25 and 10 mM TEMPOL at B_0 = 6.7 T and T = 4.2 K.

2.3.3 Inspection of the saturated ESR spectrum

Another way to identify the dominant DNP mechanism could be to observe the ESR spectrum of a DNP sample under microwave irradiation. As shown in Figure 2.6 in Chapter 2.2.3, if Thermal Mixing occurs, *i.e.,* if electronic spin diffusion is fast enough, a µW irradiation with a slight offset Δν should give rise to region of emission and of increased absorption in the ESR spectrum. On the other hand, when spectral diffusion within the EPR spectrum is less effective, the microwave pumping should produce a "hole-burning" effect in the ESR shape.

2.4 Simulations of DNP dynamics with rate equations

In this section we discuss an approach, based on the work by Rosso *et al.* (1-3) using rate equations, to see the effect on the CE efficiency of electronic parameters (the μW saturation and the electronic polarization) and of nuclear parameters (T_{1n} and the number of protons to be polarized) on the final polarization and on DNP build-up rates.

2.4.1 Cross Effect Model 1 (without spin diffusion)

This model of rate equations will only be applied here for the Cross Effect mechanism. It can be easily adapted to SE. In this first model, the electronic spin diffusion will be approximated by the digitization of the ESR spectrum and no nuclear spin diffusion will be considered. The later can be added in a more advanced model (section 2.4.2). Only three species will be considered: the fraction of the electrons irradiated at the microwave frequency $\nu_{\mu W}$ ($e(\nu_{\mu W})$), in black in Figure 2.13 and 2.14; the fraction of the electrons that are coupled to ($e(\nu_{\mu W})$ and satisfy the CE (DQ) condition, resonating upfield at $\nu_{\mu W} + \nu_0(n)$ (in red), or the electrons coupled to ($e(\nu_{\mu W})$ and satisfying the CE (ZQ) condition, resonating downfield at $\nu_{\mu W} - \nu_0(n)$ (in green); and the nuclei coupled to $e(\nu_{\mu W} + \nu_0(n))$ or $e(\nu_{\mu W} - \nu_0(n))$. Each of them can be either in the α or β state.

The entire pathway for positive nuclear polarization (CE (DQ)) is drawn in Figure 2.13a. This one can be considered in parallel to Figure 2.4.

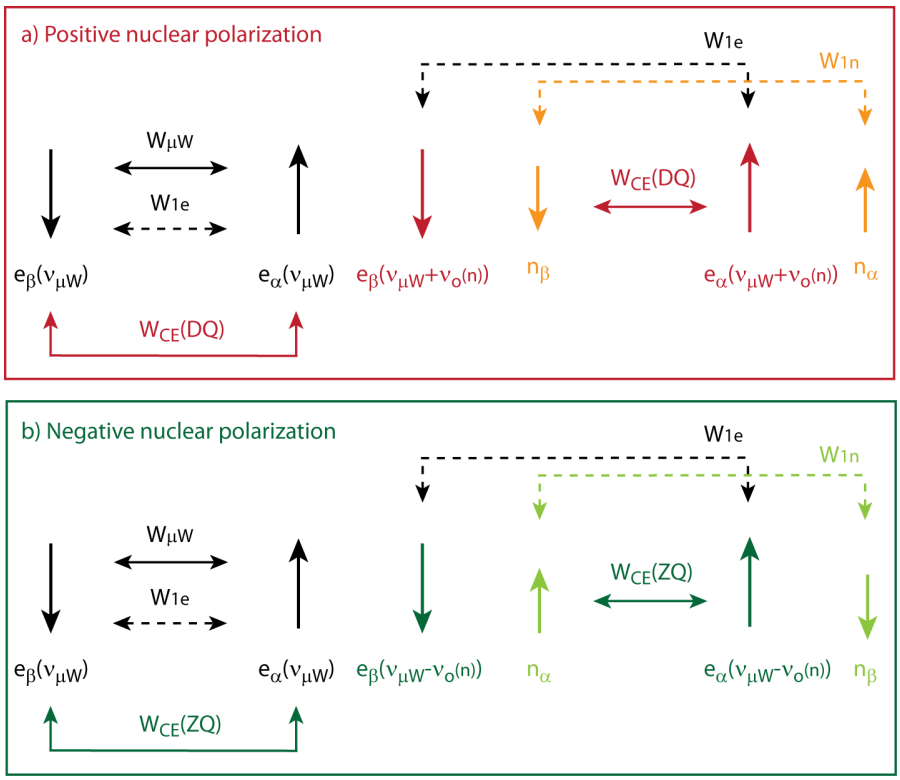

Figure 2.13: Pathways of the CE (DQ, ZQ) mechanisms described by a model without electronic or nuclear spin diffusion. $e(\nu_{\mu W})$ (black) is the irradiated electronic spin, $e(\nu_{\mu W} + \nu_0(n))$ (red) and $e(\nu_{\mu W} - \nu_0(n))$ (green) are coupled to $e(\nu_{\mu W})$ and polarize their coupled nuclei, *n*, via CE (DQ) (**a**) or CE (ZQ) (**b**).

Starting with $e_\beta(\nu_{\mu W})$ in the β state, this electron will be excited by microwave irradiation to the α state $e_\alpha(\nu_{\mu W})$ with a certain rate $W_{\mu W}$ in competition with the electronic spin lattice relaxation that drives the $e_\beta(\nu_{\mu W})$ and $e_\alpha(\nu_{\mu W})$ populations back to Boltzmann equilibrium with a rate W_{1e}. An excited electron $e_\alpha(\nu_{\mu W})$ can also make an energy-conserving "flop-flip-flip" if it is coupled to an electron resonating at $\nu_{\mu W} + \nu_0(n)$ in the β state, itself coupled to a nucleus in the β state. This transition occurs with a certain rate W_{CE}(DQ). The "flip-flop-flop" back-transition has an equal probability, and thus the same rate. Once out of equilibrium, the β and α populations of $e(\nu_{\mu W} + \nu_0(n))$ will return to Boltzmann equilibrium with the electron spin lattice relaxation rate W_{1e}, like the n_α and n_β populations, but through nuclear spin lattice relaxation rate W_{1n}, which is much slower.

The pathway for negative nuclear polarization (CE (ZQ)) is the same except that the nuclear population is pushed out of Boltzmann equilibrium through the coupling of $e_\alpha(\nu_{\mu W})$ with $e_\beta(\nu_{\mu W} - \nu_0(n))$ and n_α populations.

The rates equations corresponding to the pathway of Figure 2.13 (positive polarization) for the six populations are shown in Equation 2.9. For the sake of clarity, $e_\beta(\nu_{\mu W})$ and $e_\alpha(\nu_{\mu W})$ of Figure 2.13a are replaced by $e_{1,\beta}$ and $e_{1,\alpha}$, while $e_\beta(\nu_{\mu W} + \nu_0(n))$ and $e_\alpha(\nu_{\mu W} + \nu_0(n))$ are replaced by $e_{2,\beta}$ and $e_{2,\alpha}$.

$$
\begin{aligned}
\frac{de_{1\beta}(t)}{dt} &= -W_{\mu W}e_{1\beta}(t) + W_{\mu W}e_{1\alpha}(t) - W_{1e}(1-P_e)e_{1\beta}(t) + W_{1e}(1+P_e)e_{1\alpha}(t) \\
&\quad + W_{CE}(DQ)e_{1\alpha}(t)e_{2\beta}(t)n_\beta(t) - W_{CE}(DQ)e_{1\beta}(t)e_{2\alpha}(t)n_\alpha(t) \\
\frac{de_{1\alpha}(t)}{dt} &= -\frac{de_{1\beta}(t)}{dt} \\
\frac{de_{2\beta}(t)}{dt} &= -W_{1e}(1-P_e)e_{2\beta}(t) + W_{1e}(1+P_e)e_{2\alpha}(t) - W_{CE}(DQ)e_{1\alpha}(t)e_{2\beta}(t)n_\beta(t) + W_{CE}(DQ)e_{1\beta}(t)e_{2\alpha}(t)n_\alpha(t) \\
\frac{de_{2\alpha}(t)}{dt} &= -\frac{de_{2\beta}(t)}{dt} \\
\frac{dn_\beta(t)}{dt} &= -W_{1n}(1+P_n)n_\beta(t) + W_{1n}(1-P_n)n_\alpha(t) - W_{CE}(DQ)e_{1\alpha}(t)e_{2\beta}(t)n_\beta(t) + W_{CE}(DQ)e_{1\beta}(t)e_{2\alpha}(t)n_\alpha(t) \\
\frac{dn_\alpha(t)}{dt} &= -\frac{dn_\beta(t)}{dt}
\end{aligned}
\tag{2.3}
$$

The next step consists in setting realistic starting conditions for the 6 populations that will evolve with rate equations 2.3. To do so, the ESR spectrum of 50 mM TEMPOL at 6.7 T and 4.2 K is digitized in steps of 71.25 MHz. Note that this digitizing step mimics the electronic spin diffusion. For simplicity, it is assumed that at $\nu_{\mu W}$, the DNP enhancement occurs only through CE (DQ). Indeed, as can be seen in the example described in Figure 2.14, no electrons resonate at $\nu_{\mu W} - \nu_0(n)$, and thus no negative DNP enhancement can occur via CE (ZQ).

In our example, we assume that on average the irradiated electrons will have a chance to undergo an energy-conserving $e_{1\alpha}e_{2\beta}n_\beta \leftrightarrow e_{1\beta}e_{2\alpha}n_\alpha$ transition with a coupled electron resonating at $\nu_{\mu W} + \nu_0(n)$ sitting in a sphere of 6 nm around $e(\nu_{\mu W})$. Admittedly, this is a rough approximation. In fact, the rate W_{CE}(DQ) will depend on the electron-electron dipole-dipole coupling, and thus on the *e-e* distance. Nevertheless to obtain a mere qualitative picture of the effect of electronic and nuclear parameters on the DNP process, this approximation is sufficient. In a sample of 50 mM TEMPO, each electron is surrounded by 25 other neighbouring electrons in a sphere of 6 nm.

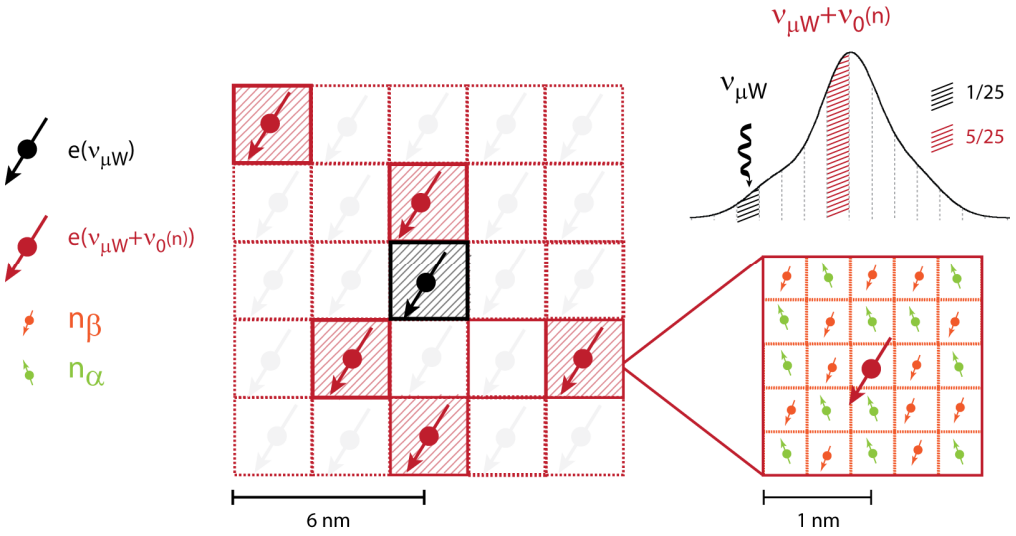

Figure 2.14: Schematic representations of the irradiated electron $e(\nu_{\mu W})$ (in black), its coupled electrons fulfilling the CE (DQ) condition $e(\nu_{\mu W} + \nu_0(n))$ (in red) and the nuclei (in orange and green) involved in the DNP polarization via CE (DQ) mechanism described in our rate equation model.

In the scheme of Figure 2.14, these 25 electrons that are sufficiently strongly coupled to $e(\nu_{\mu W})$ are projected onto a plane for the sake of readability. Normalizing the ESR spectrum so that $e(\nu_{\mu W})$ represents 1/25 of the total number of electrons N_e, $e(\nu_{\mu W} + \nu_0(n))$ will represent 5/25 of N_e in our example. So on average, each electron irradiated at $\nu_{\mu W}$ will have 5 surrounding electrons that are capable of polarizing the nuclei via CE (DQ), *i.e.,* that resonate at $\nu_{\mu W} + \nu_0(n)$, and that are sufficiently strongly coupled.

We assume that nuclei sitting in a sphere of 1 nm radius around an electron can be polarized via CE. Again, this is a rough approximation because (1) the rate W_{CE} depends on the *e-n* distance, (2) we only consider the core nuclei (a model considering the bulk nuclei polarized via nuclear spin diffusion will be described in section 2.4.2). But again, this model is sufficient for our purpose and has the advantage of being simple enough to be solved numerically. In the case of our standard DNP sample presented in 2.1.2 with 10% ^{1}H, 25 proton spins lie within a sphere of 1 nm around $e(\nu_{\mu W} + \nu_0(n))$. Like for the electron, the nuclei presented in the scheme of Figure 2.13 are projected onto a plane for the sake of readability.

The evolution of the 6 populations described by the system of rate equations 2.3 and Figure 2.13 can be easily solved numerically with Mathematica (the notebook used to solved this system is given in the Appendix of this Chapter). The initial conditions of the populations are given by the definitions of the electronic and nuclear polarizations $P(e)$ and $P(n)$:

$$\begin{aligned} e_{1,\beta}(t=0) &= N_{e,0}\left(1+P(e)\right)/2, \quad & e_{1,\alpha}(t=0) &= N_{e,0}\left(1-P(e)\right)/2 \\ e_{2,\beta}(t=0) &= N_{e,D}\left(1+P(e)\right)/2, \quad & e_{2,\alpha}(t=0) &= N_{e,D}\left(1-P(e)\right)/2 \\ n_{\alpha}(t=0) &= N_{n}\left(1+P(n)\right)/2, \quad & n_{\beta}(t=0) &= N_{n}\left(1-P(n)\right)/2 \end{aligned} \tag{2.4}$$

Like before, $e_\beta(\nu_{\mu W})$ and $e_\alpha(\nu_{\mu W})$ are replaced by $e_{1,\beta}$ and $e_{1,\alpha}$, while $e_\beta(\nu_{\mu W} + \nu_0(n))$ and $e_\alpha(\nu_{\mu W} + \nu_0(n))$ are replaced by $e_{2,\beta}$ and $e_{2,\alpha}$, for the sake of readability. $N_{e,0}$, $N_{e,D}$ and N_n represent the relative fractions of

irradiated electrons $e(\nu_{\mu W})$, of electrons coupled to $e(\nu_{\mu W})$ resonating at $\nu_{\mu W} + \nu_0(n)$, and of nuclei coupled to $e(\nu_{\mu W} + \nu_0(n))$.

Within the limits of the approximations outlined above, it is possible to vary µW, electronic and nuclear parameters, to solve numerically the equations 2.3 and to access to the population of the states $e_{\beta,\alpha}(\nu_{\mu W})$, $e_{\beta,\alpha}$ $(\nu_{\mu W} + \nu_0(n))$ and $n_{\alpha,\beta}$ for different irradiation times t. The nuclear polarization $P(n)(t)$ is calculated as $(n_\alpha(t)-n_\beta(t))/(n_\alpha(t)+n_\beta(t))$. The fit of $P(n)(t)$ to a mono-exponential function permits one to extract the simulated DNP build-up time constant $\tau_{DNP}(n)$ for different parameters. In the next sections, unless specified, these parameters are set by default to: $N_{e,0} = 1$, $N_{e,D} = 5\ N_{e,0}$, $N_n = 25\ N_{e,D}$; $P(e) = 0.98$, $P(n) = 0.006$; $T_{1e} = 1/W_{1e} = 1$ s, $T_{1n} = 1/W_{1n} = 1000$ s; $T_{CE} = 1/W_{CE} = 1$ s; $W_{\mu W} = 1/5\ s^{-1}$.

Influence of the CE efficiency, the µW field strength and the electronic polarization:

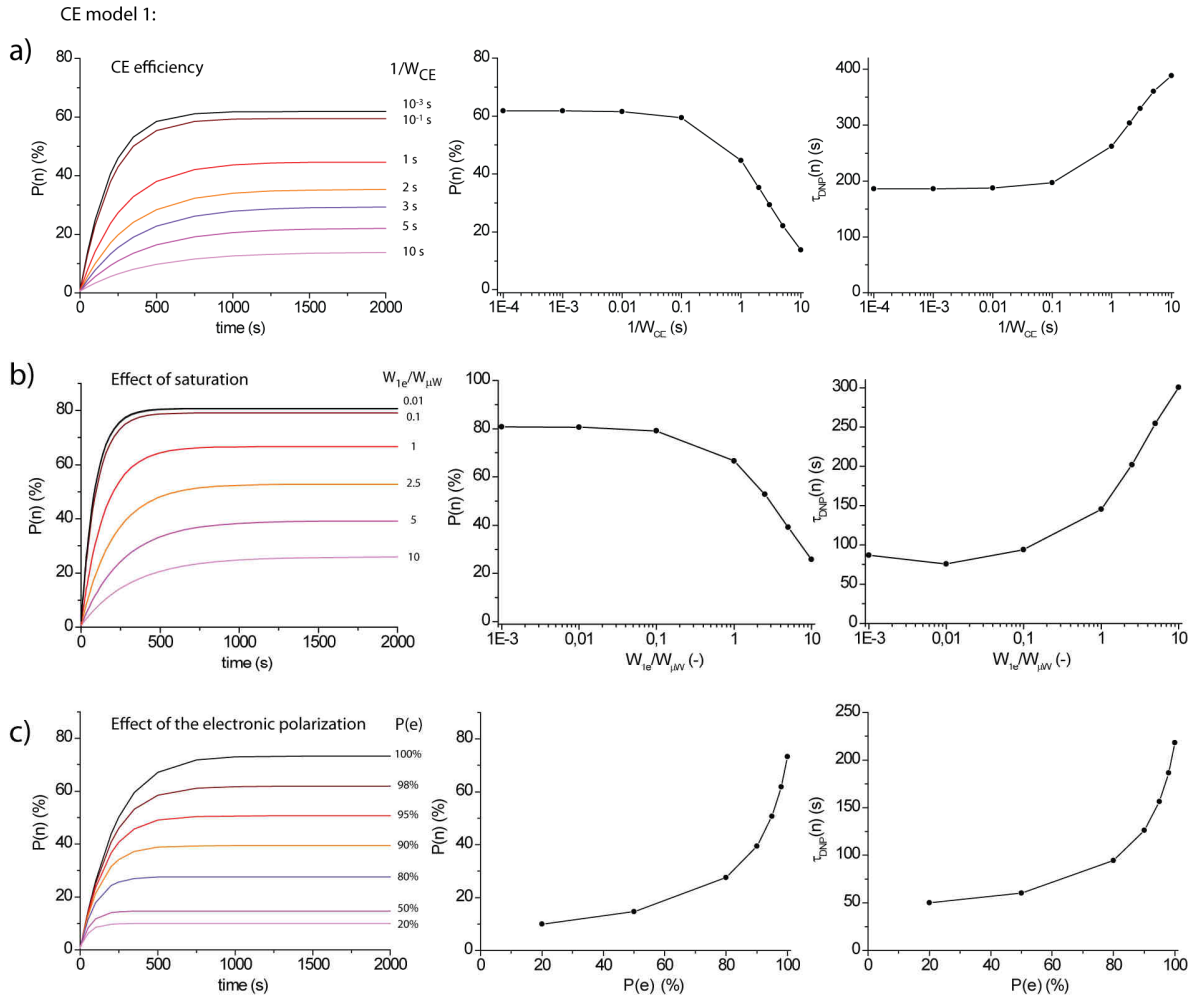

Figure 2.15: Calculations of $P(n)$ (t) obtained by numerically solving the system of rate equations 2.3, which describes the CE model 1 (without nuclear or electronic spin diffusion), varying **a)** the CE efficiency, **b)** the microwave field strength, **c)** the electronic polarization. Unless they are varied, the parameters are set to $N_{e,0}$ =1, $N_{e,D} = 5\ N_{e,0}$, $N_n = 25\ N_{e,D}$; $P(e) = 0.98$, $P(n) = 0.006$; $T_{1e} = 1/W_{1e} = 1$ s, $T_{1n} = 1/W_{1n} = 1000$ s; $T_{CE} = 1/W_{CE} = 1$ s; $W_{\mu W} = 1/5\ s^{-1}$. The maximal nuclear polarization and the DNP build-up time constant extracted by a mono-exponential fit of $P(n)$ (t) are reported.

In Figure 2.15, some of the electronic parameters are varied. For each case, $P(n)(t)$ is shown, as well as $P(n)^{max}$ and $\tau_{DNP}(n)$. The rate W_{CE} at which the CE transition occurs is the central parameter of the process. It can be seen as a measure of the efficiency of the contact between the electrons and the nuclei. W_{CE} competes with the electronic spin lattice relaxation. If $1/W_{CE}$ is fast compared to T_{1e} (T_{1e} = 1 s in our simulations), the maximal polarization reaches a plateau and the DNP build-up is fast (Figure 2.15a). If $1/W_{CE} = T_{1e}$, the CE transition becomes the rate-limiting process, and both $P(n)^{max}$ and $\tau_{DNP}(n)$ become highly dependent on W_{CE}. In fact, introducing an inefficient *e-n* contact in the model can mimic slow electron spin diffusion (2).

Figure 2.15b shows the importance of the microwave field strength. The rate $W_{\mu W}$ at which the electrons are excited competes with $1/T_{1e}$. Below the saturation limit, the more intense $\nu_{1\mu W}$, the more electronic spins $e_\alpha(\nu_{\mu W})$ are available to polarize the nuclei via the CE process. Increasing $\nu_{1\mu W}$ increases the nuclear polarization and shortens the DNP build-up time constants. Once the electrons under irradiation are saturated, both $P(n)^{max}$ and $\tau_{DNP}(n)$ reach a plateau.

Finally, it can be seen in Figure 2.15c that, due to leakage rates, the maximal nuclear polarization is not linearly proportional to the electronic polarization $P(e)$. At high polarization levels, $P(n)^{max}$ is extremely sensitive to $P(e)$. For example, between $P(e) = 100\%$ and $P(e) = 95\%$, with our model, we calculated that $P(n)^{max}$ is reduced by 37.5% from 80% to 50%. Similarly, as $P(e)$ increases, the DNP build-up slows down. This can be one of the multiple causes of the changes in experimental DNP behaviour observed when the field was doubled form 3.35 T to 6.7 T (see Section 2.5).

Effect of the nuclear relaxation time T_{1n}

In the discussion proposed in Section 2.3 based on the analysis of DNP spectra, it was not possible to get information about the influence of nuclear parameters on the DNP process. Indeed, unlike free electrons, the nuclei only have a minor impact on the shape of the DNP spectrum. With the present model based on rate equations, it is possible to describe and predict the influence of some nuclear parameters on the final polarization and build-up rates. As it can be seen in Figure 2.13, the nuclear relaxation rate $1/T_{1n}$ will be opposed to the DNP process, driving the hyperpolarized populations back to Boltzmann equilibrium. In the same manner as in the theory of Thermal Mixing, this can be referred to as a leakage factor (36). If $1/T_{1n}$ is fast compared to the DNP process, the nuclear populations will never reach the same polarizations as the electrons, but will stabilize at a much lower steady-state polarization because of the leakage (Figure 2.16a).

It is difficult to correlate information extracted from the analysis of our model with experimental data. Indeed, as they are interconnected, it is almost impossible to vary experimentally only one parameter at a time. Nevertheless, in the case of T_{1n}, a DNP sample fulfills this mission quite well. A mixture of Toluene-d_8:THF 9:1 with 50 mM TEMPO at 6.7 T shows drastic changes of proton T_{1n} between T = 4.2 and 1.2 K. In Figure 2.16b, T_{1n} (^{1}H) varies from 10 s to 1000 s in this small temperature range. Bearing in mind that other parameters like $P(e)$, T_{1e}, T_{2n}, etc. are also temperature-dependent, we conclude that in this sample $P_{max}(^1H)$ and $\tau_{DNP}(^1H)$ depend mainly on T_{1n}. As shown in figure 2.16b, the maximal ^{1}H polarization and the build-up time constant measured experimentally as a function of T_{1n} follow the same trend as the one predicted with our simple model of rate equations.

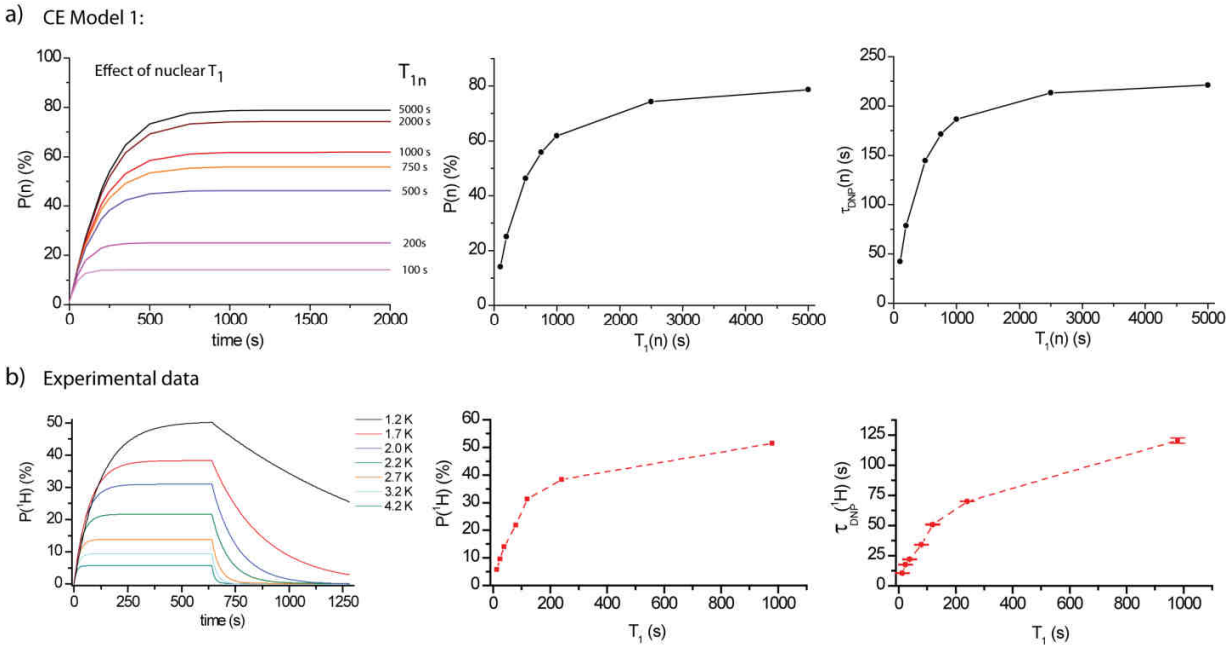

Figure 2.16: **a)** Calculation of $P(n)(t)$ obtained by numerically solving the system of rate equations 2.3, varying the nuclear relaxation time constant T_{1n}. The other parameters are set to $N_{e,0}$ =1, $N_{e,D}$ = 5 $N_{e,0}$, N_n = 25 $N_{e,D}$; $P(e)$ = 0.98, $P(n)$ = 0.006; T_{1e} = 1/W_{1e} = 1 s; T_{CE} = 1/W_{CE} = 1 s; $W_{\mu W}$ = 1/5 s^{-1}. The maximal nuclear polarization, as well as the DNP build-up time constant are extracted by mono-exponential fit of $P(n)$ (t). **b)** DNP build-up of Toluene-d_8:THF 9:1with 50 mM TEMPO at B_0 = 6.7 T, under µW irradiation ($\nu_{\mu W}$ = 188.3 GHz, $P_{\mu W}$ = 100 mW) and T_{1n} decay as function of the temperature, T = 1.2 – 4.2 K. The maximal ^{1}H polarization and the build-up time constant are also reported as function of T_{1n}.

Effect of the density of nuclear spins to be polarized:

A second important nuclear parameter is the density of the nuclei to be polarized, or the number of nuclear spins coupled to the electrons involved in the DNP mechanism. In terms of Thermal Mixing theory, this can be seen as a "heat load". Because of T_{1n} relaxation or leakage, the higher the number of spins to be polarized by each electron, the lower the final steady-state nuclear polarization. In the same manner, the larger the number of nuclei that must be polarized, the longer the build-up time constant (Figure 2.17a).

It is quite straightforward to vary the density of the protons spins to be polarized by controlling the degree of deuteration of the DNP sample. In Figure 2.17b, the maximal ^{1}H polarizations as well as the DNP build-up time constants are shown as a function of the µW irradiation frequency for samples of 1-^{13}C acetate in glycerol:water (1:1) with 5, 10 or 100% of protons, at B_0 = 6.7 T and T = 4.2 K. Even if some other parameters, especially T_{2n}, may be perturbed, the proton density is the main variable in these experiments. The experimental $P_{max}(^1H)$ and $\tau_{DNP}(^1H)$ as function of the number of nuclear spins follows the same trend as predicted by the simple rate equation model (Figure 2.17). One can also see that the proton density has no influence on the shape of the DNP spectrum.

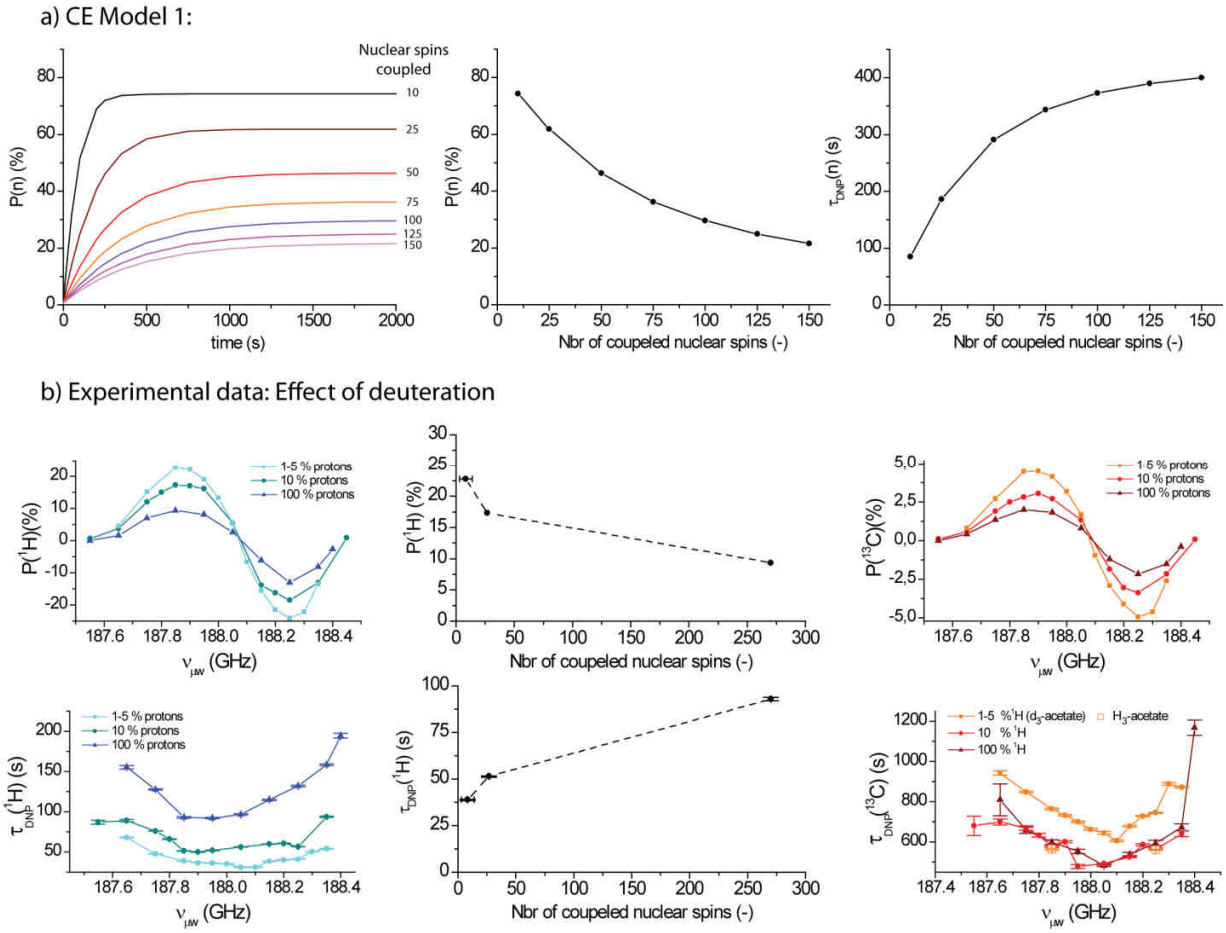

Figure 2.17: **a)** Calculation of $P(n)$ (t) obtained by numerically solving the system of rate equations 2.3, varying the number of nuclear spins N_n coupled to each electron. The other parameters are set to $N_{e,0}$ =1, $N_{e,D}$ = 5 $N_{e,0}$; $P(e)$ = 0.98, $P(n)$ = 0.006; T_{1e} = 1/W_{1e} = 1 s, T_{1n} =1/W_{1n} = 1000 s; T_{CE} = 1/W_{CE} = 1 s; $W_{\mu W}$ = 1/5 s^{-1}. The maximal nuclear polarization and the DNP build-up time constant are extracted by mono-exponential fits of $P(n)$(t). **b)** ^{1}H and ^{13}C DNP spectra of 3 M 1-^{13}C acetate in water:glycerol (1:1) protonated to 5, 10, 100% at B_0 = 6.7 T and T = 4.2 K, under µW irradiation ($\nu_{\mu W}$ = 188.3 GHz, $P_{\mu W}$ = 100 mW). The maximal ^{1}H polarizations and build-up time constants are also shown as a function of N_n.

Interestingly, the maximal ^{13}C polarization is also influenced by the proton density, but not the ^{13}C build-up time constant (Figure 2.17b). An electron $e_\alpha(\nu_{\mu W})$ excited by µW can polarize both ^{1}H and ^{13}C spins. If the proton concentration increases, there will be less chance for ^{13}C to be involved in DNP mechanism with a given excited electron. This explains why free electrons that have bandwidths narrower than $\nu_0(^1H)$, like those of Trityl (4-6), polarize low-γ nuclei like ^{13}C more efficiently. Some experimental results will be given in Section 2.5.

2.4.2 Cross Effect Model 2 (with nuclear spin diffusion)

Model 1 proposed in Section 2.4.1 describes all nuclei as a single species. Nevertheless, due to the distribution of *e-n* distances, they should be divided at least in two sub-categories: the core nuclei, which are close to the electrons, can be polarized, but have short T_{1n}; and the nuclei of the bulk, which are far away from the electrons, cannot be polarized directly, but have long T_{1n}. The two populations

communicate with each other via nuclear spin diffusion process. This first approximation only simulates a contact between the two baths of nuclear species. A real spin diffusion model is beyond the scope of this Thesis.

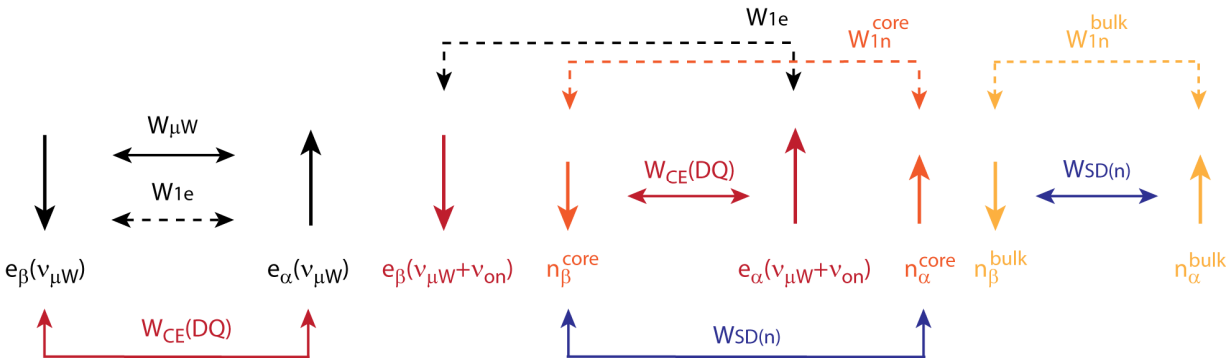

Figure 2.18: Pathways of the CE (DQ) mechanisms described by a model with nuclear spin diffusion. $e(\nu_{\mu W})$ (black) is the irradiated electronic spin, $e(\nu_{\mu W} + \nu_0(n))$ (red) is coupled to $e(\nu_{\mu W})$ and polarize their coupled nuclei, n^{core} (orange), via CE (DQ). The nuclei of the bulk, n^{bulk} (yellow) are in contact with nuclei of the core via nuclear spin diffusion.

Model 1 can be modified to take nuclear spin diffusion into account. Figure 2.18 shows the schematic DNP pathway for positive polarization through CE (DQ) including two nuclear sub-species, the core and bulk nuclei, n^{core} and n^{bulk}. The scheme is the same as in Figure 2.13, except that the polarization of the core population is transmitted to the bulk via energy-conserving flop-flip processes with a rate $W_{SD} = 1/T_{SD}$. Each nuclear population is brought back to Boltzmann equilibrium with its own relaxation rate $W_{1n} = 1/T_{1n}$.

The system of rate Equations 2.3 has to be slightly modified to take into account the distinction between core and bulk nuclei and the nuclear spin diffusion:

$$\frac{de_{1\beta}(t)}{dt}, \frac{de_{1\alpha}(t)}{dt}, \frac{de_{2\beta}(t)}{dt}, \frac{de_{2\alpha}(t)}{dt} \text{ like Equation 2.3}$$

$$\begin{aligned}
\frac{dn_{\beta}^{core}(t)}{dt} &= -W_{1n}(1+P_n)n_{\beta}^{core}(t) + W_{1n}(1-P_n)n_{\alpha}^{core}(t) - W_{CE}(DQ)e_{1\alpha}(t)e_{2\beta}(t)n_{\beta}^{core}(t) \\
&\quad + W_{CE}(DQ)e_{1\beta}(t)e_{2\alpha}(t)n_{\alpha}^{core}(t) + W_{SD}(n)n_{\alpha}^{core}(t)n_{\beta}^{bulk}(t) - W_{SD}(n)n_{\beta}^{core}(t)n_{\alpha}^{bulk}(t) \qquad (2.5) \\
\frac{dn_{\alpha}^{core}(t)}{dt} &= -\frac{dn_{\beta}^{core}(t)}{dt} \\
\frac{dn_{\beta}^{bulk}(t)}{dt} &= -W_{1n}(1+P_n)n_{\beta}^{bulk}(t) + W_{1n}(1-P_n)n_{\alpha}^{bulk}(t) - W_{SD}(n)n_{\alpha}^{core}(t)n_{\beta}^{bulk}(t) + W_{SD}(n)n_{\beta}^{core}(t)n_{\alpha}^{bulk}(t) \\
\frac{dn_{\alpha}^{bulk}(t)}{dt} &= -\frac{dn_{\beta}^{bulk}(t)}{dt}
\end{aligned}$$

The Mathematica code used to solve this system of equations numerically is given in the Appendix of this chapter.

The relaxation time T_{1n} of the n^{core} nuclei close to the electrons can be set to a more realistic short value (T_{1n}^{core} = 25 s was used in the simulations presented above). This results in a lower maximal polarization

of the core nuclei. The CE efficiency and the microwave transition rate have to be adapted to simulate a realistic polarization. As underlined by Rosso *et al.* (2), the use of underestimated $W_{1\mu W}$ and W_{CE} permits one to mimic slow spin diffusion, like for Model 1 in Section 2.4.1.

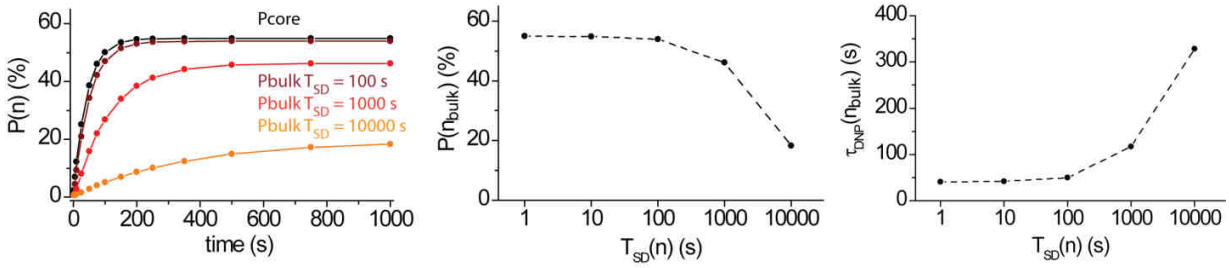

Figure 2.19: Calculation of $P(n_{core})$ (t) (black) and $P(n_{bulk})$ (t) (red-yellow) solving numerically the system of rates equations 2.5, varying the nuclear spin diffusion time constant (T_{SD}). The other parameters are set to $N_{e,0}$ =1, $N_{e,D}$ = 5 $N_{e,0}$, N_n^{core} = 25 $N_{e,D}$, N_n^{bulk} = 125 $N_{e,D}$; $P(e)$ = 0.98, $P(n)$ = 0.006; T_{1e} = 1/W_{1e} = 1 s, T_{1n}^{core} =1/W_{1n}^{core} = 25 s, T_{1n}^{bulk} =1/W_{1n}^{bulk} = 1000 s; T_{CE} = 1/W_{CE} = 0.01 s; $W_{\mu W}$ = 1/0.1 s^{-1}. The maximal bulk nuclear polarization, as well as the DNP build-up time constant are extracted by mono-exponential fit of $P(n_{bulk})$ (t).

For diffusion constants that are fast compared to $1/T_{1n}^{bulk}$, the polarization of the bulk will converge towards the polarization of the core nuclei. The bulk polarization will diverge from the core polarization only if $1/T_{SD}$ becomes slow with respect to $1/T_{1n}^{bulk}$. In this case, $P_{max}^{bulk}(n)$ will decreases due to T_{1n} leakage. This happens only for extremely slow T_{SD}, as can be seen in Figure 2.19. Thus, except for extremely low electron and nuclear concentrations, Model 1 with adapted W_{CE} and $W_{1\mu W}$ is sufficient to describe qualitatively the influence of electronic and nuclear parameter on the DNP process.

2.4.3 How to polarize nucleus 1 through nucleus 2 without microwave?

As shown in Section 4.2.1, nuclei with different gyromagnetic ratios influence each other in the DNP process. In the experiments described below, it is shown that it is possible to transfer polarization of one nucleus to another via electrons, without applying any microwaves. This experiment was proposed by Goldman *et al.* in 1973 (59) and is considered as a proof that the Thermal Mixing mechanism is effective. In TM language, the contact between two nuclear reservoirs which brings them to a common spin temperature is achieved through their contacts with the electronic spin-spin reservoir. In the next Section, it will be shown that it is also possible to explain this experiment with the CE rate equations.

For this experiment, we used a sample of 3 M 1-^{13}C acetate in D_2O:Glycerol-d_8 (1:1) with 30 mM TEMPOL at 3.35 T and 1.2 K. As we shall see below, the field is important. The experiment is described in Figure 2.20a. First, the ^{1}H spins are polarized by microwave irradiation to $P(^1H)$ = 40% . Then the microwave irradiation is switched off, and the ^{13}C magnetization is destroyed by a train of 90° pulses. The evolution of the ^{13}C magnetization is the monitored with small angle (5°) pulses.

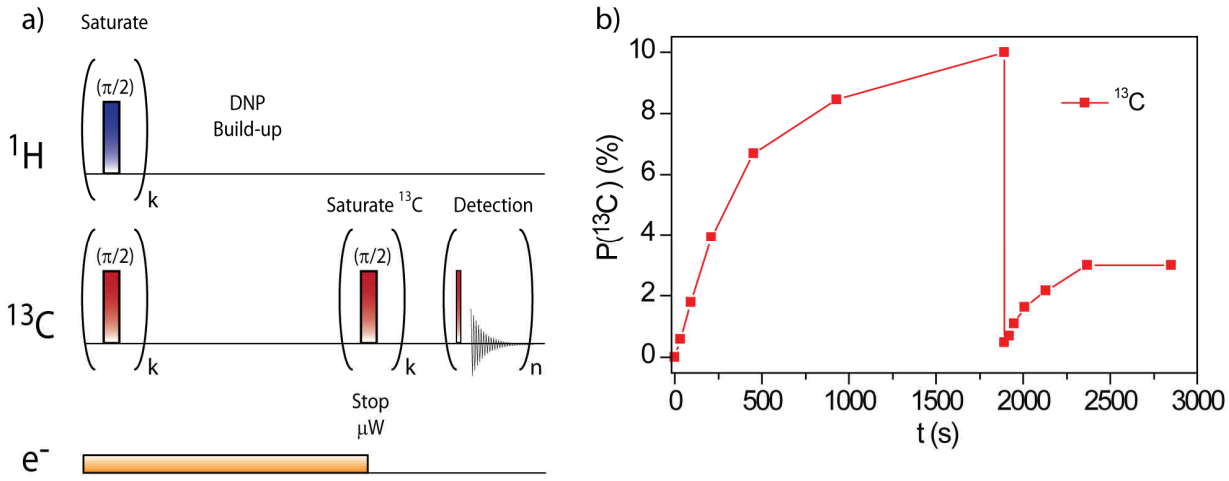

Figure 2.20: **a)** Pulse sequence to monitor the spontaneous transfer of polarization from ^{1}H polarized by DNP to ^{13}C. **b)** ^{13}C DNP build-up, destruction of the ^{13}C magnetization followed by the transfer of ^{1}H polarization to ^{13}C. The data are acquired on a sample of 3 M 1-^{13}C acetate in D_2O:Glycerol-d_8 (1:1) with 30 mM TEMPOL at B_0 = 3.35 T, T = 1.2 K.

As can be seen in Figure 2.20b, after its destruction, the ^{13}C polarization comes back to $P(^{13}C) \approx 3\%$, which is well above the Boltzmann polarization $P(^{13}C) = 0.0086\%$ (at this field and this temperature) with a fast build-up rate. Clearly, the enhanced ^{1}H polarization is transferred to the ^{13}C nuclei. In terms of Thermal Mixing theory, one speaks of a contact between the cold ^{1}H spin bath and the hot ^{13}C spin bath.

It is also possible to explain this effect using the "flip-flop" model developed in 4.2.1, as illustrated in Figure 2.21. At the starting point ① in Figure 2.21, the polarization of nucleus n_1 (^{1}H in our case) is high, $n_{1\alpha} >> n_{1\beta}$, and the polarization of n_2 (^{13}C in this example) vanishes since $n_{2\alpha} = n_{2\beta}$. The electrons, although they must be highly polarized, should *not* be fully polarized. This is extremely important, as will be seen later. If $P_e \neq 1$, it is possible for $n_{1\alpha}$ that is not in Boltzmann equilibrium to be coupled to an electron in the higher Zeeman energy state, $e_\alpha(\nu + \nu_{0n1})$, itself coupled to an electron in its β state fulfilling the CE (DQ) condition, $e_\beta(\nu)$. An energy-conserving flip-flop-flop can occur, promoting $e_\beta(\nu)$ to $e_\alpha(\nu)$, as shown at time ② in Figure 2.21. This is the central step of the transfer of polarization of n_1 to n_2. The promoted electron $e_\alpha(\nu)$ can also be coupled to an electron fulfilling the CE (DQ) condition with n_2 ($e_\beta(\nu + \nu_{0n2})$ (③ in Figure 2.21). Thus n_2 can be polarized via this CE (DQ) mechanism (④ in Figure 2.21). According to this model, the highly polarized nucleus n_1 transfers its magnetization to n_2 via the electron. One has to be aware that the model presented in Figure 2.21 is simplified. Indeed, from ① to ②, the couple $e_\alpha(\nu + \nu_{0n1})$ - $n_{1\alpha}$ could also excite an electron on the other side of the spectrum via CE (ZQ). Similarly, n_2 could also be polarized negatively via CE (ZQ) with an electron $e_\beta(\nu - \nu_{0n2})$ between③ and ④. Moreover, the electrons involved in the mechanism do not all belong to a single "spin packet" as in Figure 2.21, normally the contribution of all the electrons of the ESR spectrum should be summed. The final polarization will thus be given by a superposition of contributions from all possible pathways, which could be constructive or destructive.

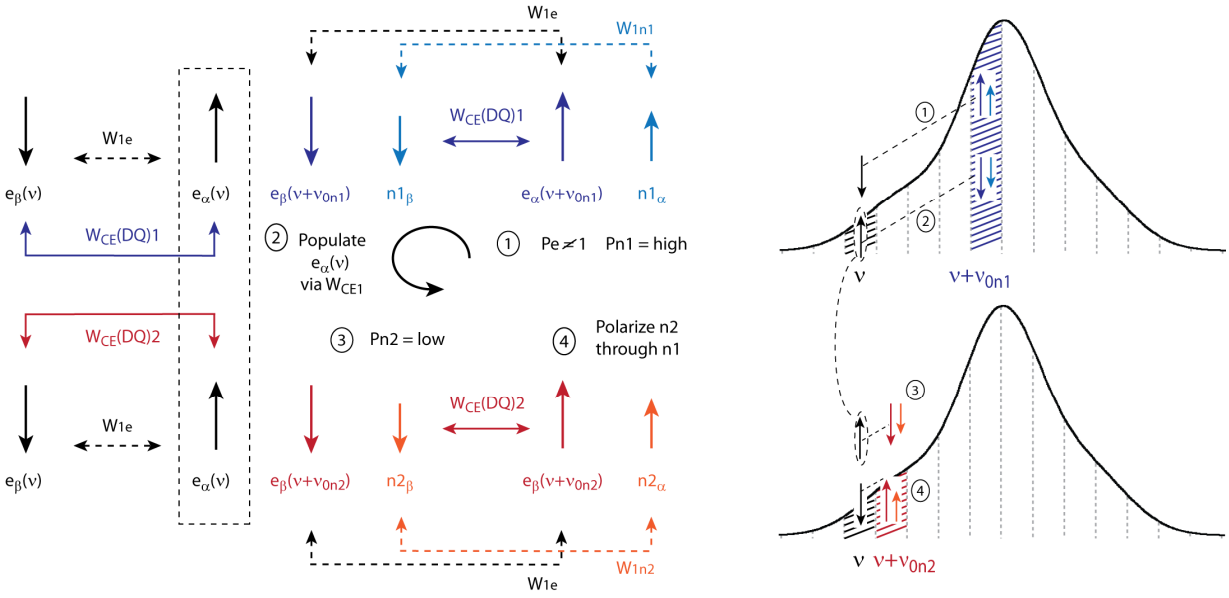

Figure 2.21: Pathway of the transfer of the polarization n_1 to n_2. The contributions of the electrons of a single "spin packet" are assumed to occur exclusively via the CE (DQ) mechanism. The polarization of the nucleus is high, $n_{1\alpha} >> n_{1\beta}$, and the polarization of n_2 (^{13}C) is zero ($n_{2\alpha} = n_{2\beta}$). The electrons, even if highly polarized, are not fully polarized $P(e) \neq 1$.

Keeping this approximation in mind, one can nevertheless write the rate equations of the eight populations involved in this specific pathway:

$$
\begin{aligned}
\frac{de_{1\beta}(t)}{dt} &= -W_{1e}(1-P_e)e_{1\beta}(t) + W_{1e}(1+P_e)e_{1\alpha}(t) + W_{CE1}(DQ)e_{1\alpha}(t)e_{2\beta}(t)n_{1\beta}(t) - W_{CE1}(DQ)e_{1\beta}(t)e_{2\alpha}(t)n_{1\alpha}(t) \\
&\quad + W_{CE1}(DQ)e_{1\alpha}(t)e_{3\beta}(t)n_{2\beta}(t) - W_{CE1}(DQ)e_{1\beta}(t)e_{3\alpha}(t)n_{2\alpha}(t) \\
\frac{de_{1\alpha}(t)}{dt} &= -\frac{de_{1\beta}(t)}{dt} \\
\frac{de_{2\beta}(t)}{dt} &= -W_{1e}(1+P_e)e_{2\beta}(t) + W_{1e}(1-P_e)e_{2\alpha}(t) - W_{CE1}(DQ)e_{1\alpha}(t)e_{2\beta}(t)n_{1\beta}(t) + W_{CE1}(DQ)e_{1\beta}(t)e_{2\alpha}(t)n_{1\alpha}(t) \\
&\quad - W_{CE1}(DQ)e_{1\alpha}(t)e_{3\beta}(t)n_{2\beta}(t) + W_{CE1}(DQ)e_{1\beta}(t)e_{3\alpha}(t)n_{2\alpha}(t) \\
\frac{de_{2\alpha}(t)}{dt} &= -\frac{de_{2\beta}(t)}{dt} \\
\frac{dn_{1\beta}(t)}{dt} &= -W_{1n1}(1+P_{n1})n_{1\beta}(t) + W_{1n1}(1-P_{n1})n_{2\alpha}(t) - W_{CE1}(DQ)e_{1\alpha}(t)e_{2\beta}(t)n_{1\beta}(t) + W_{CE1}(DQ)e_{1\beta}(t)e_{2\alpha}(t)n_{1\alpha}(t) \\
\frac{dn_{1\alpha}(t)}{dt} &= -\frac{dn_{1\beta}(t)}{dt} \\
\frac{dn_{2\beta}(t)}{dt} &= -W_{1n2}(1+P_{n2})n_{2\beta}(t) + W_{1n2}(1-P_{n2})n_{2\alpha}(t) - W_{CE2}(DQ)e_{1\alpha}(t)e_{3\beta}(t)n_{2\beta}(t) + W_{CE2}(DQ)e_{1\beta}(t)e_{3\alpha}(t)n_{2\alpha}(t) \\
\frac{dn_{2\alpha}(t)}{dt} &= -\frac{dn_{2\beta}(t)}{dt}
\end{aligned}
\tag{2.6}
$$

For the sake of readability, $e_\beta(\nu_{\mu W})$ and $e_\alpha(\nu_{\mu W})$ are replaced by $e_{1,\beta}$ and $e_{1,\alpha}$, while $e_\beta(\nu_{\mu W} + \nu_0(n))$ and $e_\alpha(\nu_{\mu W} + \nu_0(n))$ are replaced by $e_{2,\beta}$ and $e_{2,\alpha}$. The Mathematica code used to solve this system of equations numerically is given in the Appendix of this Chapter.

According to our model, it is important for the transfer of polarization between the two nuclei n_1 and n_2 to occur to have some electrons available in the high-energy α Zeeman state. Therefore, the transfer from n_1 to n_2 is disadvantaged if the electron polarization is too high. In Figure 2.22, the evolution of the polarization transferred from n_1 to n_2 is calculated using Equations 2.6, starting with $P(n_1)$ = 100%, $P(n_2)$ = 0% and varying $P(e)$, keeping T_{1n} and T_{1e} constant.

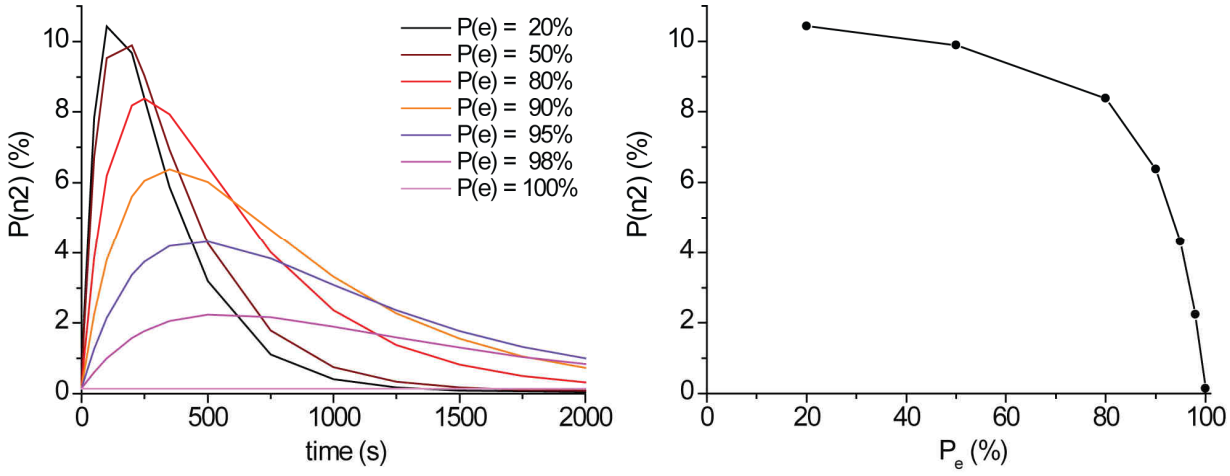

Figure 2.22: Calculation of the transferred polarization $P(n_2)$ (t) by numerically solving the system of rate equations 2.6, varying the electron polarization $P(e)$. The other parameters are set to $N_{e,0}$ =1, $N_{e,D}$ = 5 $N_{e,0}$, N_{n1} = 25 $N_{e,D}$, N_{n2} = 7 $N_{e,D}$; $P(n_1)$ (t=0) = 100%, $P(n_2)$ (t=0) = 0%, $P(n_1)$ = 0.006, $P(n_2)$ = $P(n_1)/4$; T_{1e} = 1/W_{1e} = 1 s, T_{1n1} =1/W_{1n1} = 1000 s, T_{1n2} =1/W_{1n2} = 2000 s; T_{CE1} = 1/W_{CE1} = 1 s, T_{CE2} = 1/W_{CE2} = 4*T_{CE1}.

If P(e) = 100%, the transfer does not take place at all. By decreasing P(e), *i.e.*, by increasing the population of e_α, the transfer becomes more and more efficient.

This last result can explain some unexpected observations. Indeed, the transfer of polarization is more efficient at B_0 = 3.35 T than at 6.7 T. This is counterintuitive because at higher field $P(^1H)$ is higher and both $T_1(^1H)$ and $T_1(^{13}C)$ are longer, which should favour the final polarization transferred to ^{13}C. But the electron polarization reaches $P(e)$ = 99.9 % at 6.7 T and 1.2 K, whereas $P(e)$ is only 95.5 % at 3.35 T and 1.2 K. The fact that the electronic polarization is too close to 100 % can thus be one explanation of the loss of efficiency of the transfer of nuclear polarization at higher fields.

To confirm the influence of the electronic polarization predicted by our model, we tried the following experiments. A sample of 3 M 1-^{13}C acetate in H_2O:D_2O:Glycerol-d_8 (1:4:5) with 40 mM TEMPOL was polarized to $P(^1H)$ ≈ 60 % at 6.7 T and 2.2 K. Then, as in Figure 2.20a, the microwave irradiation was interrupted and the ^{13}C magnetization was destroyed by saturation. The transfer of polarization was then observed with small angle pulses at different P(e) corresponding to different sample temperatures.

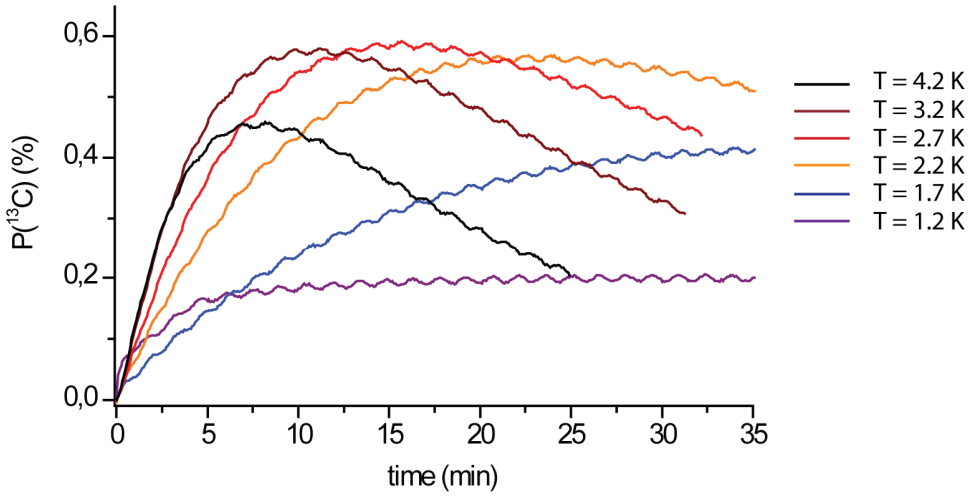

Figure 2.23: Polarization transferred from ^{1}H to ^{13}C in a sample of 3 M 1-^{13}C acetate in H_2O:D_2O:Glycerol-d_8 (1:4:5) with 40 mM TEMPOL at 6.7 T at variable temperatures between 4.2 and 1.2 K. ^{1}H is always polarized at 2.2 K with $f_{\mu W}$ = 188.3 GHz, $P_{\mu W}$ = 87.5 mW to keep the starting polarization constant to $P(^{1}H) \approx 60\%$.

As can be seen in Figure 2.23, the transfer is extremely inefficient at T = 1.2 K. As the sample temperature increases, the maximal polarization transferred to ^{13}C increases until an optimum at T = 3.2 K. At high temperatures it decreases again, since $T_1(^{1}H)$ and $T_1(^{13}C)$ become too short (because ^{1}H is always polarized at 2.2 K, the starting ^{1}H polarization does not vary). Note that the relaxation rates were not changed in the simulations in Figure 2.22. Thus this experiment confirms the role of P(e) predicted by our simple "flip-flop" model.

2.5 Real Data

In the end, the only parameters that are relevant for the DNP experimentalist is the maximal polarization $P^{max}(n)$ that can be achieved for the nuclei n to be investigated, and the time $5\tau_{DNP}(n)$ needed to reach this polarization. As shown in the course of this Chapter, these two parameters depend on many different and interdependent parameters. Up to now no single model, even the most ambitious, is able to predict these two parameters *ab initio*. In this last section, we show experimental DNP build-up curves recorded under different conditions, for different types of radicals and fields.

2.5.1 DNP at 3.35 T

This field was chosen because, due to radar research, solid-state microwave sources operating at $\nu_{\mu W} \approx$ 94 GHz are commercially available. This frequency corresponds to the electron Larmor frequency at B_0 = 3.35 T. Originally, Dissolution-DNP was developed to enhance magnetic resonance imaging. ^{13}C was chosen as a target nucleus because 1) carbon is present in many molecules that play a role in biology, 2) labelling techniques for such molecules are available, 3) there is no *in vivo* background in contrast to ^{1}H, 4) quaternary carbons have long T_1's in liquid phase at room temperature, therefore the DNP magnetization created in the polarizer will be able to survive after dissolution. Trityl, a radical with narrow lines, was specially developed to polarize ^{13}C (4-6). Indeed, as it does not polarize protons, leakage through $T_1(^{1}H)$ will not harm the polarization. At T = 1.2 K and B_0 = 3.35 T, Trityl can polarize carbon-13 up to $P(^{13}C)$ = 36 % with a long build-up time constant of 2300 s (60) (Figure 2.24a). With such

$\tau_{DNP}(^{13}C)$, one has to wait between 2 and 4h to reach a maximal polarization. This is long but still acceptable. Apart from its price, Trityl has the drawback that it is hard to solubilize in aqueous solution. An alternative consists in using nitroxyl radicals such as TEMPO with broad ESR lines. Nitroxyl radicals can polarize protons efficiently ($P(^1H)$ = 40%, $\tau_{DNP}(^1H)$ = 70 s at 1.2 K), which is an obvious advantage if one wants to work with this nucleus, but nitroxyl radicals are a drawback for ^{13}C DNP since the maximal direct polarization is low, i.e., $P(^{13}C)$ = 10%, $\tau_{DNP}(^{13}C)$ = 325 s at 1.2 K. Nevertheless, with nitroxyl radicals, one can benefit of reasonably fast ^{13}C build-up rates and extremely short $\tau_{DNP}(^1H)$ (57, 61) (Figure 2.24b).

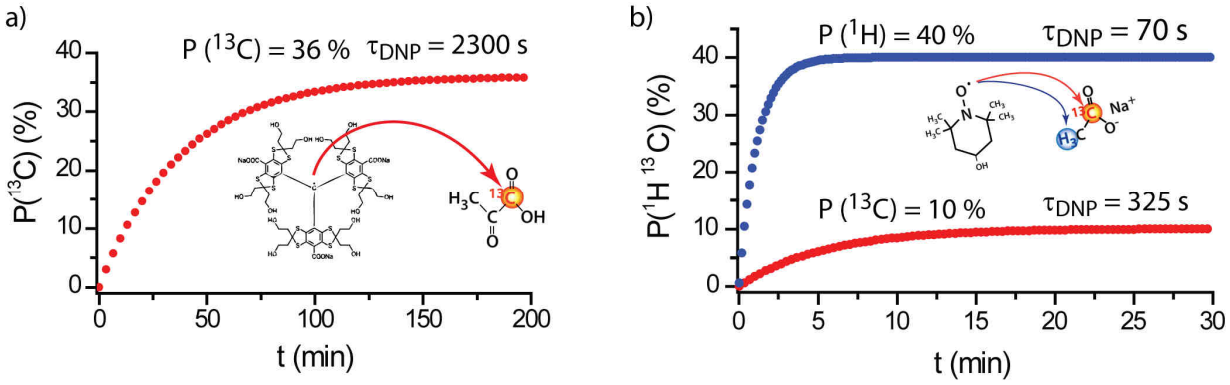

Figure 2.24: **a)** Typical DNP build-up of 1-^{13}C pyruvic acid with 15 mM Trityl at 1.2 K and 3.35 T (60) **b)** Typical ^1H (blue) and ^{13}C (red) DNP build-up curves of 3 M 1-^{13}C acetate with 30 mM TEMPOL in D_2O:Glycerol-d_8 (1:1) at 1.2 K and 3.35 T (57, 61).

The DNP build-up time constants and the maximal polarization for ^1H and ^{13}C measured at 3.35 T at different temperatures are reported in Table 2.2.

T (K)	$P(^1H)$ (%)	$\tau_{DNP}(^1H)$ (s)	$P(^{13}C)$ (%)	$\tau_{DNP}(^{13}C)$ (s)	$\varepsilon_{DNP}(^1H/^{13}C)$
1.2	40	70	10	324	4
2.2	24	57	6	267	4
3	12	32	3	222	4
4.2	8	22	2	158	4

Table 2.2: ^1H and ^{13}C polarizations and corresponding build-up time constants of 3 M 1-^{13}C labelled acetate with 30 mM TEMPOL in 100% deuterated water:ethanol (2:1) at B_0 = 3.35 T for variable temperatures.

2.5.2 DNP at higher fields

As shown in Section 2.4, at high polarization, even small increases in P(e) can have drastic effects on the final nuclear polarization. The elongation of the nuclear T_1(n) is also beneficial for P^{max}(n). Therefore, increasing the field could be useful for DNP. Studies at 4.5 T with Trityl (62) and at 5 T with TEMPO (63) report increases in nuclear polarization, albeit at the price of longer build-up time constants, which become prohibitive for Trityl. A second difficulty is to find sources that can irradiate at higher microwave frequencies. In our laboratory, the DNP polarizer used at 3.35 T was adapted by doubling both the microwave frequency and the field. The superconducting magnet designed for 7.05 T (Oxford Instruments) was run at B_0 = 6.7 T. The microwave source (ELVA) initially operating at 94 GHz was coupled to a frequency doubler (VDI/D200) to yield $\nu_{\mu W}$ = 188 GHz at the price of a reduction in maximal power with $P^{max}{}_{\mu W}$ (188 GHz) = 120 mW and $P^{max}{}_{\mu W}$ (94 GHz) = 400 mW. At T = 1.2 K, using a frozen glassy solution containing 50 mM TEMPO as polarizing agent, a polarization $P(^{13}C)$ = 36% can be obtained

directly with a long build-up time constant $\tau_{DNP}(^{13}C)$ = 2000 s. The proton polarization builds up to $P(^{1}H)$ = 91% in a much shorter time $\tau_{DNP}(^{1}H)$ = 150 s (Figure 2.25)(58).

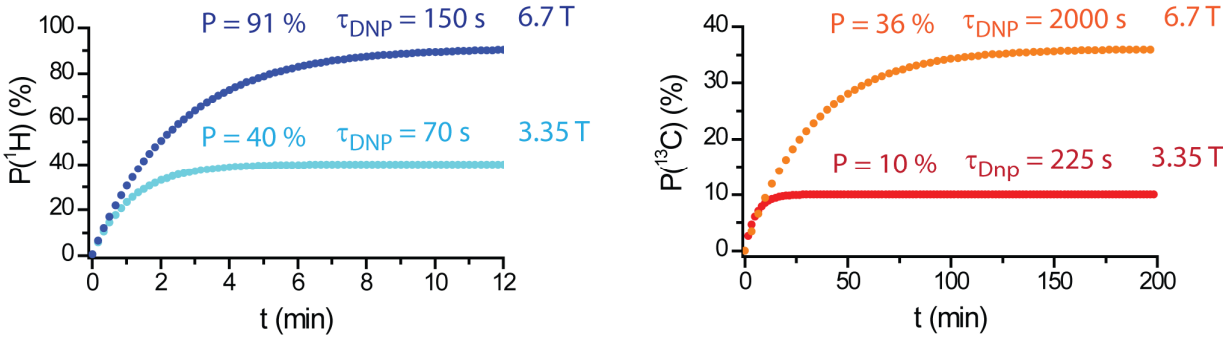

Figure 2.25: Comparison between ^{1}H (blue) and ^{13}C (red) DNP build-up curves of 3 M 1-^{13}C acetate in D_2O:Glycerol-d_8 (1:1) at 1.2 K and 3.35 T (30 mM TEMPOL) (57, 61) and 6.7 T (50 mM TEMPOL) (58).

The DNP build-up rates and maximal polarization for ^{1}H and ^{13}C at different temperatures measured at 6.7 T are also reported in Table 2.3.

T (K)	$P(^{1}H)$ (%)	$\tau_{DNP}(^{1}H)$ (s)	$P(^{13}C)$ (%)	$\tau_{DNP}(^{13}C)$ (s)	$\varepsilon_{DNP}(^{1}H/^{13}C)$
1.2	91	150	36	1980	2.5
2.2	60	52	22.5	1010	2.6
4.2	25	25	5.5	359	4.5

Table 2.3: ^{1}H and ^{13}C polarizations and corresponding build-up time constants of 3 M 1-13C labelled acetate with 50 mM TEMPOL in 100% deuterated water:ethanol (2:1) at B_0 = 6.7 T for variable temperatures.

In the next Chapters, I will show how it is possible to take advantage of this high ^{1}H polarization that can rapidly be made available. The proton polarization can be transferred to other low-gamma nuclei via Cross Polarization (Chapter 3). Highly polarized protons can be used to populate so called Long-Lived States (Chapters 5 and 8). Hyperpolarized water is a good target for so-called LOGSY experiments that can be useful for drug screening (Chapter 6).

References

1. Serra SC, Filibian M, Carretta P, Rosso A, & Tedoldi F (2014) Relevance of electron spin dissipative processes to dynamic nuclear polarization via thermal mixing. *Phys. Chem. Chem. Phys.* 16(2):753-764.
2. Serra SC, Rosso A, & Tedoldi F (2012) Electron and nuclear spin dynamics in the thermal mixing model of dynamic nuclear polarization. *Phys. Chem. Chem. Phys.* 14(38):13299-13308.
3. Serra SC, Rosso A, & Tedoldi F (2013) On the role of electron-nucleus contact and microwave saturation in thermal mixing DNP. *Phys. Chem. Chem. Phys.* 15(21):8416-8428.
4. Ardenkjaer-Larsen JH, Fridlund B, Gram A, Hansson G, Hansson L, Lerche MH, Servin R, Thaning M, & Golman K (2003) Increase in signal-to-noise ratio of > 10,000 times in liquid-state NMR. *Proc. Natl. Acad. Sci. U.S.A.* 100(18):10158-10163.
5. Ardenkjaer-Larsen JH, Macholl S, & Johannesson H (2008) Dynamic nuclear polarization with trityls at 1.2 K. *Appl. Magn. Reson.* 34(3-4):509-522.

6. Wolber J, Ellner F, Fridlund B, Gram A, Johannesson H, Hansson G, Hansson LH, Lerche MH, Mansson S, Servin R, Thaning M, Golman K, & Ardenkjaer-Larsen JH (2004) Generating highly polarized nuclear spins in solution using dynamic nuclear polarization. *Nucl. Instrum. Meth. A* 526(1-2):173-181.
7. Bornet A, Milani J, Vuichoud B, Linde AJP, Bodenhausen G, & Jannin S (2014) Microwave frequency modulation to enhance Dissolution Dynamic Nuclear Polarization. *Chem. Phys. Lett.* 602:63-67.
8. Granwehr J, Leggett J, & Kockenberger W (2007) A low-cost implementation of EPR detection in a dissolution DNP setup. *J. Magn. Reson.* 187(2):266-276.
9. Duer MJ (2002) *Solid-State NMR Spectroscopy: Principles and Applications* (Blackwell Science, UK).
10. Schweiger A &Jeschke G (2001) *Principles of Pulse Electron Paramagnetic Resonance* (Oxford University Press, Oxford).
11. Shimon D, Hovav Y, Feintuch A, Goldfarb D, & Vega S (2012) Dynamic nuclear polarization in the solid state: a transition between the cross effect and the solid effect. *Phys. Chem. Chem. Phys.* 14(16):5729-5743.
12. Jannin S (2009) Dynamic Nuclear Polarization Techniques for Magnetic Resonance Imaging and Particles Targets Experiments. PhD Thesis (Ecole Polytechnique Fédérale de Lausanne, Lausanne).
13. Mieville P (2011) Chemical Developments in DNP-NMR. (Ecole Polytechnique Fédérale de Lausanne, Lausanne).
14. Overhauser AW (1953) Polarization of Nuclei in Metals. *Phys. Rev.* 92(2):411-415.
15. Carver TR &Slichter CP (1953) Polarization of Nuclear Spins in Metals. *Phys. Rev.* 92(1):212-213.
16. Carver TR &Slichter CP (1956) Experimental Verification of the Overhauser Nuclear Polarization Effect. *Phys. Rev.* 102(4):975-980.
17. Jeffries CD (1957) Polarization of Nuclei by Resonance Saturation in Paramagnetic Crystals. *Phys. Rev.* 106(1):164-165.
18. Abragam A &Proctor WG (1958) Une Nouvelle Methode De Polarisation Dynamique Des Noyaux Atomiques Dans Les Solides. *Cr. Hebd. Acad. Sci.* 246(15):2253-2256.
19. Borghini M &Abragam A (1959) Polarisation Dynamique Des Protons a Basse Temperature. *Cr. Hebd. Acad. Sci.* 248(12):1803-1805.
20. Leifson OS &Jeffries CD (1961) Dynamic Polarization of Nuclei by Electron-Nuclear Dipolar Coupling in Crystals. *Phys. Rev.* 122(6):1781-&.
21. Schmugge TJ &Jeffries CD (1965) High Dynamic Polarization of Protons. *Phys. Rev.* 138(6A):1785-&.
22. Erb E, Motchane JL, & Uebersfeld J (1958) Effet De Polarisation Nucleaire Dans Les Liquides Et Les Gaz Adsorbes Sur Les Charbons. *Cr. Hebd. Acad. Sci.* 246(14):2121-2123.
23. Hwang CF &Hill DA (1967) Phenomenological Model for New Effect in Dynamic Polarization. *Phys. Rev. Lett.* 19(18):1011-&.
24. Hwang CF &Hill DA (1967) New Effect in Dynamic Polarization. *Phys. Rev. Lett.* 18(4):110-&.
25. Kessenikh AV, Lushchikov VI, Manenkov AA, & Taran YV (1963) Proton Polarization in Irradiated Polyethylenes. *Sov. Phys-Sol. State* 5(2):321-329.
26. Kessenikh AV, Manenkov AA, & Pyatnitskii GI (1964) On Explanation of Experimental Data on Dynamic Polarization of Protons in Irradiated Polyethylenes. *Sov. Phys-Sol. State* 6(3):641-643.
27. Provotorov BN (1962) A Quantum-Statistical Theory of Cross Relaxation. *Sov. Phys. Jetp-USSR* 15(3):611-614.
28. Provotorov BN (1962) Magnetic Resonance Saturation in Crystals. *Sov. Phys. Jetp-USSR* 14(5):1126-1131.

29. Abragam A &Proctor WG (1958) Spin Temperature. *Phys. Rev.* 109(5):1441-1458.
30. Goldman M (1970) *Spin Temperature and Nuclear Magnetic Resonance in Solids* (Oxford University Press, Oxford).
31. Redfield AG (1955) Nuclear Magnetic Resonance Saturation and Rotary Saturation in Solids. *Phys. Rev.* 98(6):1787-1809.
32. Abragam A &Goldman M (1978) Principles of Dynamic Nuclear-Polarization. *Rep. Prog. Phys.* 41(3):395-467.
33. Abragam A &Goldman M (1982) *Nuclear magnetism: order and disorder* (Int. Ser. Monographs. Phys. (Clarendon Press, Oxford)).
34. Atsarkin VA (1978) Dynamic Nuclear-Polarization in Dielectric Solids. *Usp. Fiz. Nauk.* 126(1):3-39.
35. Atsarkin VA &Rodak MI (1972) Temperature of Spin-Spin Interactions in Electron-Paramagnetic Resonance. *Usp. Fiz. Nauk.* 107(1):3-&.
36. Boer WD (1976) Dynamic Orientation of Nuclei at Low-Temperatures. *J. Low Temp. Phys.* 22(1-2):185-212.
37. Borghini M (1968) Spin-Temperature Model of Nuclear Dynamic Polarization Using Free Radicals. *Phys. Rev. Lett.* 20(9):419-&.
38. Jannin S, Comment A, & van der Klink JJ (2012) Dynamic Nuclear Polarization by Thermal Mixing Under Partial Saturation. *Appl. Magn. Reson.* 43(1-2):59-68.
39. Kurdzesau F (2009) Some Methods of Dynamic Nuclear Polarization for Use in Metabolic Imaging. PhD Thesis (Ecole Polytechnique Fédérale de Lausanne, Lausanne).
40. Hovav Y, Feintuch A, & Vega S (2010) Theoretical aspects of dynamic nuclear polarization in the solid state - The solid effect. *J. Magn. Reson.* 207(2):176-189.
41. Hu KN, Debelouchina GT, Smith AA, & Griffin RG (2011) Quantum mechanical theory of dynamic nuclear polarization in solid dielectrics. *J. Chem. Phys.* 134(12).
42. Wenckebach WT (2008) The solid effect. *Appl. Magn. Reson.* 34(3-4):227-235.
43. Karabanov A, van der Drift A, Edwards LJ, Kuprov I, & Kockenberger W (2012) Quantum mechanical simulation of solid effect dynamic nuclear polarisation using Krylov-Bogolyubov time averaging and a restricted state-space. *Phys. Chem. Chem. Phys.* 14(8):2658-2668.
44. Hovav Y, Levinkron O, Feintuch A, & Vega S (2012) Theoretical Aspects of Dynamic Nuclear Polarization in the Solid State: The Influence of High Radical Concentrations on the Solid Effect and Cross Effect Mechanisms. *Appl. Magn. Reson.* 43(1-2):21-41.
45. Hovav Y, Feintuch A, & Vega S (2012) Theoretical aspects of dynamic nuclear polarization in the solid state - The cross effect. *J. Magn. Reson.* 214:29-41.
46. Karabanov A, Kwiatkowski G, & Kockenberger W (2012) Quantum Mechanical Simulation of Cross Effect DNP Using Krylov-Bogolyubov Averaging *Appl. Magn. Reson.* 43(3):461-461.
47. Atsarkin VA (2011) Dynamic nuclear polarization: Yesterday, today, and tomorrow. *J. Phys. Conf. Ser.* 324.
48. Atsarkin VA &Kessenikh AV (2012) Dynamic Nuclear Polarization in Solids: The Birth and Development of the Many-Particle Concept. *Appl. Magn. Reson.* 43(1-2):7-19.
49. Goertz ST (2004) The dynamic nuclear polarization process. *Nucl. Instrum. Meth. A* 526(1-2):28-42.
50. Banerjee D, Shimon D, Feintuch A, Vega S, & Goldfarb D (2013) The interplay between the solid effect and the cross effect mechanisms in solid state C-13 DNP at 95 GHz using trityl radicals. *J. Magn. Reson.* 230:212-219.
51. Shimon D, Feintuch A, Goldfarb D, & Vega S (2014) Static H-1 dynamic nuclear polarization with the biradical TOTAPOL: a transition between the solid effect and the cross effect. *Phys. Chem. Chem. Phys.* 16(14):6687-6699.

52. Hovav Y, Feintuch A, & Vega S (2011) Dynamic nuclear polarization assisted spin diffusion for the solid effect case. *J. Chem. Phys.* 134(7).
53. Hovav Y, Feintuch A, & Vega S (2013) Theoretical aspects of dynamic nuclear polarization in the solid state - spin temperature and thermal mixing. *Phys. Chem. Chem. Phys.* 15(1):188-203.
54. Vigier FM, Shimon D, Mugnaini V, Veciana J, Feintuch A, Pons M, Vega S, & Goldfarb D (2014) The C-13 solid DNP mechanisms with perchloro-triphenylmethyl radicals - the role of Cl-35,Cl-37. *Phys. Chem. Chem. Phys.* 16(36):19218-19228.
55. Walker SA, Edwards DT, Siaw TA, Armstrong BD, & Han S (2013) Temperature dependence of high field C-13 dynamic nuclear polarization processes with trityl radicals below 35 Kelvin. *Phys. Chem. Chem. Phys.* 15(36):15106-15120.
56. Kurdzesau F, van den Brandt B, Comment A, Hautle P, Jannin S, van der Klink JJ, & Konter JA (2008) Dynamic nuclear polarization of small labelled molecules in frozen water-alcohol solutions. *J. Phys. D Appl. Phys.* 41(15).
57. Bornet A, Melzi R, Jannin S, & Bodenhausen G (2012) Cross Polarization for Dissolution Dynamic Nuclear Polarization Experiments at Readily Accessible Temperatures 1.2 < T < 4.2 K. *Appl. Magn. Reson.* 43(1-2):107-117.
58. Jannin S, Bornet A, Melzi R, & Bodenhausen G (2012) High field dynamic nuclear polarization at 6.7 T: Carbon-13 polarization above 70% within 20 min. *Chem. Phys. Lett.* 549:99-102.
59. Cox SFJ, Bouffard V, & Goldman M (1973) Coupling of 2 Nuclear Zeeman Reservoirs by Electronic Spin-Spin Reservoir. *J Phys C Solid State* 6(5):L100-L103.
60. Ardenkjaer-Larsen JH, Leach AM, Clarke N, Urbahn J, Anderson D, & Skloss TW (2011) Dynamic Nuclear Polarization Polarizer for Sterile Use Intent. *NMR Biomed.* 24(8):927-932.
61. Jannin S, Bornet A, Colombo S, & Bodenhausen G (2011) Low-temperature cross polarization in view of enhancing dissolution Dynamic Nuclear Polarization in NMR. *Chem. Phys. Lett.* 517(4-6):234-236.
62. Johanneson H, Macholl S, & Ardenkjaer-Larsen JH (2009) Dynamic Nuclear Polarization of [1-C-13]pyruvic acid at 4.6 tesla. *J. Magn. Reson.* 197(2):167-175.
63. Jannin S, Comment A, Kurdzesau F, Konter JA, Hautle P, van den Brandt B, & van der Klink JJ (2008) A 140 GHz prepolarizer for dissolution dynamic nuclear polarization. *J. Chem. Phys.* 128(24).

Chapter 3:

Cross Polarization to transfer hyperpolarized magnetization from ^{1}H to ^{13}C

A substantial improvement of D-DNP can be achieved by the indirect use of the high and rapidly available ^{1}H polarization. Indeed, it is possible to transfer the proton magnetization to heteronuclei by means of Cross Polarization (CP) at 1.2 K prior to dissolution. In order to do so, a new device has to be added to the DNP polarizer, a doubly resonant NMR coil. In this Chapter, I will show how the CP technique was implemented for DNP at 3.35 T (1, 2) and 6.7 T (3-5). This work, inspired by preliminary research by A.J. Perez-Linde *et al.* (6), was carried out in collaboration with Bruker, especially with the help of Roberto Melzi.

3.1 Cross Polarization benefits for D-DNP

3.1.1 Abundant/high-γ and rare/low-γ nuclear spins in DNP

Dissolution Dynamic Nuclear Polarization was optimized to polarize efficiently low-gamma nuclear spins, mainly ^{13}C, but also ^{15}N (7), ^{129}Xe (8), ^{89}Y (9), *etc*. These nuclei have the advantage of having long relaxation time constants at room temperature. This implies that once highly polarized, they will retain most of their magnetization during dissolution and transfer. As shown in Chapter 2, Trityl radicals can be very efficient as direct polarizing agents for ^{13}C. These carbon-centered radicals display ESR lines with narrow widths, facilitating the direct build-up of ^{13}C polarization by Thermal Mixing while leaving the ^{1}H spins close to their thermal equilibrium. The highest ^{13}C polarization reported so far exceeds $P(^{13}C) = 35\%$ with a build-up time constant $\tau_{DNP}(^{13}C) = 2300$ s in a field $B_0 = 3.35$ T at $T = 1.2$ K (10). Although such high polarization levels can provide intense NMR signals after dissolution, the long DNP build-up times $\tau_{DNP}(^{13}C)$ at 1.2 K do not allow one to perform several dissolution processes in rapid succession, as required for many *in-vivo* experiments with high throughput.

On the other hand, for those who chose to avoid Trityl for ^{13}C DNP (or were forced to do so for economic reasons), the widely available and inexpensive TEMPO radical turned out to be a good option. TEMPO has a broad inhomogeneous ESR line, exceeding the ^{1}H Larmor frequency, resulting in an enhanced polarization not only for $P(^{13}C)$ but also for $P(^{1}H)$. Because of the ESR width, the ^{13}C polarization levels that have been reported are modest compared to those achieved with Trityl, typically $P(^{13}C) = 10\%$ in a field $B_0 = 3.35$ T at $T = 1.2$ K (1, 11, 12) (see also Table 2.2 in Chapter 2). TEMPO has the advantage of polarizing ^{13}C directly in a shorter build-up time than Trityl, with $\tau_{DNP}(^{13}C)$ reported under the same conditions as mentioned above varying between 400 and 600 s.

Free electrons with broad ESR lines polarize nuclear spins with high gyromagnetic ratios such as ^{1}H and ^{19}F very efficiently with short build-up times. As shown in Chapter 2, $P(^{1}H)$ = 40% and $\tau_{DNP}(^{1}H)$ = 70 s at 1.2 K and 3.35 T (1). Nevertheless, such high-γ spins were not used extensively in Dissolution-DNP. Their main drawback is that they tend to return rapidly to thermal equilibrium, so that, by the time the samples have arrived in the solution-state NMR or MRI system, the enhancements are usually modest. As a result, it is often not feasible to follow a chemical reaction or a metabolic process on the time scale of the lifetime of the hyperpolarization, which is limited by the spin-lattice relaxation time T_1.

As it will be developed in the course of this Chapter, the use of Cross Polarization (CP) (13-15) at low temperature in the DNP polarizer makes it possible to keep all the advantages of both the high-γ and low-γ nuclei while avoiding their drawbacks. This idea was already predicted in 1978 by Abragam and Goldman in their review paper (16): "*The production of large polarization is more difficult for small nuclear moments. (…) Rare isotopes are also difficult to polarize; when the nuclear concentration is low, spin diffusion is slow which reduces considerably the rate of DNP and the limit that leakage relaxation sets for its maximum value. The situation is evidently even worse when nuclear moments are both rare and small. There are situations, however, when this drawback becomes an asset. This is when besides the rare isotope S, there exist in the sample an abundant nuclear species I, with a large γ, easily polarized by DNP. It is then possible, having first polarized the spin I by conventional DNP to transfer a part of the order they have acquired to the spin S: in thermodynamic language, transfer some entropy from the spin S to the spin I.*"

3.1.2 Cross Polarization and Dissolution DNP

Such a transfer of polarization is indeed possible with a well-known NMR method: the Cross Polarization technique.

Cross Polarization, along with Magic Angle Spinning (MAS), is the most widely used technique in solid state NMR. The original idea of Hartmann and Hahn of nuclear double resonance in the rotating frame (13) was adapted by Pines, Gibby and Waugh (14, 15) in view of enhancing the NMR signal of dilute nuclear spins in solids. In such experiments, the large magnetization of a high-γ, abundant nucleus (here ^{1}H) is transferred to low-γ, rare spins (here called X). CP transfer of polarization can be understood as a thermodynamic equilibration between the thermal reservoirs of the two spin species (17). The general CP procedure is the following. The ^{1}H spins are polarized in high B_0 field by allowing the Boltzmann equilibrium to be established. A 90° excitation pulse followed by a spin lock pulse with an *rf* intensity $B_1(^{1}H)$ are then applied. In the rotating frame, precessing on resonance around B_0 at the ^{1}H *rf* irradiation frequency, B_0 vanishes and $B_1(^{1}H)$ determines the quantization axis. The ^{1}H spins are thus cooled down to a low spin temperature in this rotating frame. The next step consists in establishing a contact between the ^{1}H and X spins. To do so, a spin lock field of intensity $B_1(X)$ is applied. Again, $B_1(X)$ becomes the quantization axis for the X spins in the rotating frame precessing around B_0 at the X spin *rf* irradiation frequency. The contact between the two nuclear species is established if the so-called Hartmann-Hahn condition is fulfilled:

$$\gamma_{^{1}H} B_1(^{1}H) = \gamma_X B_1(X) \qquad (3.1)$$

Under such conditions, their respective energy differences in the rotating frames are equalized. If the Hartmann-Hahn condition is fulfilled, redistribution of energy between ^{1}H and X spins via energy-conserving transitions through the dipolar couplings will be allowed. The reduction of the high ^{1}H

magnetization in the rotating frame (which has a low spin temperature) will be compensated by energy-conserving reverse transitions of the X spins, leading ultimately to a high X magnetization along the direction of B_1(X) in the rotating frame.

A proper explanation of Cross Polarization requires the use of average Hamiltonian theory. Excellent reviews of such treatments can be found in the articles of Rovnyak (18) and Vega *et al.* (19).

3.2 Probe Compatible with Dissolution-DNP

3.2.1 Hardware

A new element has to be added to perform CP in the DNP polarizer: a doubly resonant NMR coil. Suitable hardware was developed by Dr Roberto Melzi in a joint project between our laboratory and Bruker (Dr Tonio Gianotti, Dr Joost Lohman, Dr Frank Engelke). Jonas Milani is currently developing CP coils for DNP in our group. The technical description of the design and building of these dedicated NMR coils for CP-DNP will be given elsewhere. In the present Chapter, only a few general elements will be presented.

The first version was a solenoid coil doubly tuned for ^{1}H and ^{13}C ($\nu(^{1}H)$ = 142.57 MHz and $\nu(^{13}C)$ = 35.85 MHz at B_0 = 3.35 T) (1, 2). Pictures and drawings of this CP-DNP probe are shown in Figure 3.1a. For an optimal quality factor, the capacitors have to be placed as close as possible to the coil. A constraint imposed by our system is the fact that the coil has to be at liquid helium temperatures in the cryostat of the polarizer. It is therefore impractical to adjust capacitors that are close to the coil. Nevertheless, fine tuning and matching of the circuit is necessary to insure efficient CP transfer. Moreover, the resonant frequency response of the coil is extremely sensitive to the temperature. Changes of the resonant frequency in the MHz range occur between liquid nitrogen and liquid helium temperatures. Therefore, a fine-tuning and matching box for each channel is added on top of the DNP probe, outside of the polarizer. The tuning and matching box is connected to the coil via coaxial cables (see Figure 3.1a). A standard solid-state NMR console is then connected to the coil in order to generate and amplify pulses and to acquire NMR signals. With our solenoidal coil, the two transmitters can generate *rf* field amplitudes of 65 kHz each with only about 14 and 22 W for the ^{1}H and ^{13}C channels respectively. Both Q factors are equal to 130. The *rf* circuitry display a rejection between the two channels higher than 30 dB for both ^{1}H and ^{13}C sides (1, 2). The same coil design was also adapted for DNP at 6.7 T (4) (see Section 3.3.2)

Another requirement of our system is that the sample volume within the coil should be easily and rapidly accessible in view of dissolving the sample after DNP-CP build-ups. It is technically possible to load solid beads into a horizontal solenoid coil and extract them, with a pneumatic system in the manner of a rotor in MAS-NMR, driven (in our case) by gaseous helium. This way of doing is nevertheless impractical and technically challenging. The horizontal solenoid coil design was thus replaced by a vertical saddle coil (3). It can be seen in Figure 3.1b that with such a design, a sample holder containing the DNP sample (up to 500 µL in our case) can be easily inserted into the active volume of the coil. The sample can be easily dissolved by coupling a dissolution stick on the top of the sample holder (see Figure 3.1b). For efficient CP, special attention was given to design a reliable *rf* coil that can induce homogeneous B_1 fields over the entire sample volume. However, because of arcing in superfluid helium at T = 1.2 K, the *rf* fields used for CP were limited to 15 kHz on the proton and carbon channels, using 15 and 25 W respectively.

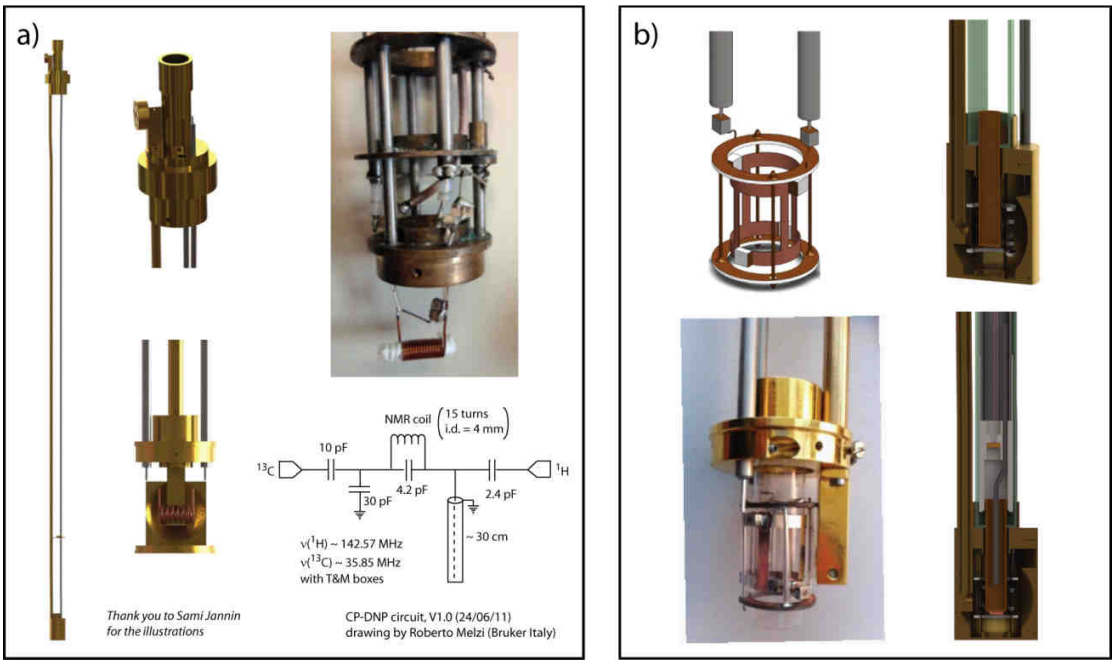

Figure 3.1: **a**). Illustration of the insert with a picture of the coil, and basic circuit of the CP-DNP system using a horizontal solenoid design that is not suitable for rapid dissolution. The circuit was drawn by Roberto Melzi (Bruker Italy.) **b**) Drawing and photo of the saddle coil design for rapid dissolution. In the two illustrations on the right, one can see how the sample holder can be inserted from the top into the active volume of the coil and how it is accessible for dissolution.

3.2.2 Pulse sequences

The standard Cross Polarization (CP) pulse sequence also has to be adapted to the Dissolution-DNP requirements (Figure 3.2). Unlike normal CP experiment, the goal here is not to observe enhanced ^{13}C signals in the polarizer, but to dissolve and transfer the sample prior to observation. Therefore, the ^{13}C magnetization should be aligned along the B_0 quantization axis at the end of the sequence, and not in the transverse plane. A 90° flip-back pulse (20) therefore has to be added at the end of the sequence for this purpose. Moreover, as will be shown at the end of this Section, usually multiple CP contacts are used to build up the enhanced ^{13}C magnetization. The ^{1}H magnetization that remains after each CP step should thus also be brought back along the z axis with a 90° flip-back pulse. Moreover, in order to exploit the longitudinal ^{13}C polarization that has been built up during the previous CP contacts, this longitudinal magnetization should be brought to the transverse plane before the CP contact, which explains the initial 90° pulse on the ^{13}C channel in Figure 3.2. Finally, a small-angle pulse can be added at the end of the sequence to monitor the build-up of the ^{13}C magnetization.

Two parameters then have to be optimized. First, the ^{1}H and ^{13}C *rf* field strengths during the contact pulses have to match the Hartmann Hahn condition. Usually this is done by varying the *rf* field strength on one channel, keeping the other constant. Both ^{1}H and ^{13}C polarizations are saturated prior to each multiple-contact sequence. The delay between saturation and the first CP contact can be shorter than the time needed for the proton magnetization to reach the DNP steady state, so as to minimize the time needed to perform each B_1 optimization.

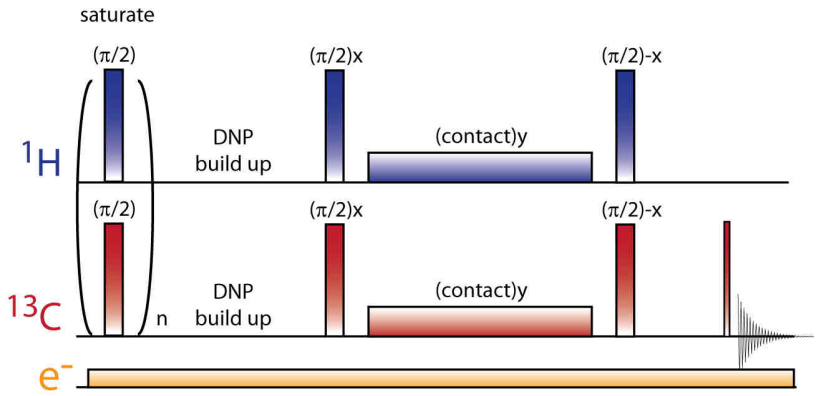

Figure 3.2: Adaptation of the standard CP sequence for Dissolution-DNP. One excitation pulse is added on the ^{13}C channel, as well as two flip-back pulses on both ^{1}H and ^{13}C channels. The CP build-up can be monitored by applying a small angle pulse after each CP contact.

In Figure 3.3a, the sequence described in Figure 3.2 is used, varying the B_1 field strength on the ^{13}C channel while keeping $B_1(^1H)$ = 55 kHz. Monitoring the signal permits one to find the optimum $B_1(^{13}C)$ that matches the Hartmann Hahn conditions. The second parameter that requires optimization is the duration of the CP contact time. An optimum should be found between the efficiency of the transfer of ^{1}H magnetization to ^{13}C and the destruction of ^{1}H magnetization by losses of coherence in the B_1 field that can be described by $T_{1\rho}$. Under DNP conditions (static solid at 1.2 K in the presence of paramagnetic species), $T_{1\rho}$ is extremely short, on the order of a few milliseconds. In Figure 3.3b, the sequence described in Figure 3.2, with an optimal *rf* field strength, is repeated while incrementing the contact time from 0.1 to 4 ms. It can be seen that a contact time of 1.8 ms is optimal. Finally, both *rf* field strength and contact time are limited by the possibility of arcing of the circuit, especially at low temperatures when liquid helium is pumped down to 0.8 mbar.

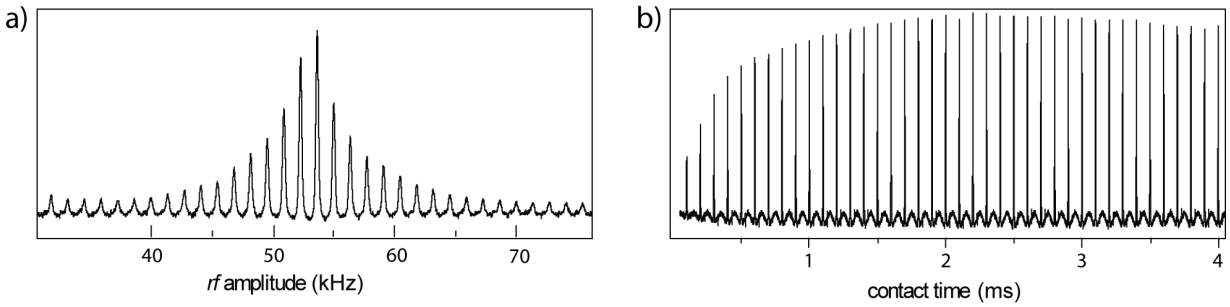

Figure 3.3: **a**) Example of optimization of the *rf* amplitude applied to the ^{13}C channel during a CP contact. A set of ^{13}C spectra are recorded for different $B_1(^{13}C)$ while keeping the *rf* amplitude $B_1(^1H)$ fixed (here 55 kHz). The Hartmann-Hahn condition is fulfilled when the ^{13}C intensity is maximized. **b**) Optimization of the CP contact time. The contact time length is incremented from 0.1 to 4 ms, with $B_1(^1H)$ and $B_1(^{13}C)$ matching the Hartmann-Hahn condition.

One problem of conventional CP under our conditions arises from the fact that the *rf* phase and amplitude have to be switched between the 90° excitation pulses and the CW contact pulses. The same switch occurs at the end of the contact pulses, before flipping the magnetization vectors back to the z axis. The NMR console used for our experiments needs at least 4 µs to switch the phase and amplitude. Under our DNP conditions at 1.2 K this delay is already long enough to lose an appreciable part of the

transverse magnetization by decoherence. To show this, the delay between the 90° pulses and the contact pulses, as well as the delay between the contact pulses and the 90° flip-back pulses in sequence described in Figure 3.2 were incremented from 1 to 17 µs. The ^{13}C signals observed after CP are shown in Figure 3.6a. If the switching delay could be made shorter, a substantial improvement in the magnetization transferred to ^{13}C could be achieved. Moreover, during this 4 µs delay, ^{1}H magnetization will also be lost, which is damageable in view of performing multiple CP contacts, as will be shown below. The 90° excitation and flip-back pulses are also critical in the standard CP sequence of Figure 3.2. The breadth of the ^{1}H spectrum is on the order of 50 kHz under standard DNP conditions at 3.35 T and 1.2 K (for ^{13}C, it is on the order of 6 kHz). It is therefore difficult to have a clean and controllable excitation over the entire width of the lines. Finally, the NMR linewidth is also a limiting parameter during the CP contact, as $B_1(^{1}H, ^{13}C)$ of our coil is relatively low.

The standard CP sequence shown in Figure 3.2 was modified to answer to these limitations. The pulse train 90^{o}_{x}-contact$_{y}$-90^{o}_{-x} was changed for Cross Polarization scheme inspired by preliminary work of Perez-Linde and Kockenberger (6) that uses an adiabatic half passage or an adiabatic inversion.

Adiabatic frequency-swept pulses can be used to transfer magnetization to the transverse plane or to perform an inversion (21). The carrier of the *rf* irradiation frequency is varied during the course of the pulse. In a classical description of the pulse (22, 23), the different magnetic field components and the spin magnetization vector can be followed in the so-called frequency- modulated frame (noted here with a prime '), which rotates at the variable frequency $\nu_{rf}(t)$ (Figure 3.4a). In this frame, the vector $B_1'(t)$ remains fixed during the pulse. If the carrier frequency of the pulse $\nu_{rf}(t)$ is initially applied far off-resonance from the Larmor frequency ν_0 of the spins of interest, the magnetic field amplitude in the frequency-modulated frame will be $B_0'(t) = (\nu_0 - \nu_{rf}(t))/\gamma$, with γ in frequency units. Therefore, the effective field $B_{eff}'(t)$ in this frame, given by the vector sum of $B_1'(t)$ and $B_0'(t)$, will change its orientation when $\nu_{rf}(t)$ varies. At the beginning of the pulse, when $\nu_{rf}(t) << \nu_0$, $B_{eff}'(t)$ is approximately collinear with z'. As $\nu_{rf}(t)$ approaches ν_0, the effective field rotates toward the transverse plane. If $\nu_{rf}(t)$ becomes larger than ν_0, the effective field vector will continues to rotate to -z' (see Figure 3.4a).

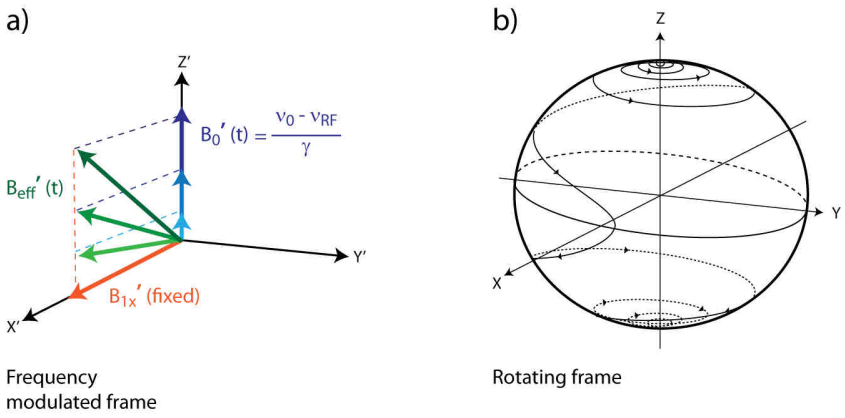

Figure 3.4: **a**) Illustration of the magnetic field components $B_{eff}'(t)$, $B_1'(t)$ and $B_0'(t)$ in a frequency-modulated frame which rotates at the variable frequency $\nu_{rf}(t)$. The magnetization vector follows $B_{eff}'(t)$. **b**) Trajectory of the effective field and of the magnetization during an inversion by adiabatic full-passage in a rotating frame which rotates at a fixed frequency. Reproduced from Pines *et al.* (21).

During adiabatic passage, the magnetization vector will be "locked" by the effective field, and will follow its change in orientation. If the pulse is stopped when the magnetization is in the transverse plane, one

speaks of an adiabatic half passage, whereas if the magnetization is inverted, one speaks of an adiabatic full-passage. The trajectories of $B_{eff}(t)$ in the frequency-modulated frame and in the rotating frame are shown in Figure 3.4.

In practice, the amplitude and phase of the pulse are continuously modulated, rather than its frequency, but the result is the same.

The most widely used version of frequency swept pulses is the hyperbolic secant (21). A more broadband version known as WURST (for uniform rate and smooth truncation) was developed by Freeman (24). We used this last one for our DNP Cross Polarization experiments.

Such swept pulses offer a perfect response to the problem posed by the standard CP sequence under DNP conditions. First, they invert or excite a wide frequency band. They are also insensitive to field inhomogeneities. Such pulses require less power to be efficient. Finally, as the magnetization follows the effective field, no phase switch prior to the contact pulse is necessary once the magnetization has reached the transverse plane. Such a CP sequence is shown in Figure 3.5a. An adiabatic half-passage is performed on both ^{1}H and ^{13}C channels to bring the proton and carbon magnetization in the transverse plane. The contact pulse can start immediately after, without any switching of the *rf* phase or amplitude. In Figure 3.5a, a version is shown where an amplitude ramp is applied on the ^{13}C channel so that CP is less sensitive to field inhomogeneities (25). At the end of the contact, the magnetization is brought back to the z axis with two frequency-swept adiabatic half passage pulses from $\nu_{rf}(t) = \nu_0(n)$ to $\nu_{rf}(t) << \nu_0(n)$.

It is also possible to remove the contact pulses and to use only adiabatic full-passage (AFP) pulses to perform Cross Polarization. To do so, the *rf* field intensities on both channels have to be set so that the two nuclei become in contact in the frequency-modulated frame during the (AFP) pulse. As each pulse will invert the magnetization, a second CP contact has to be performed to store the magnetization back along the +z axis between CP contacts (Figure 3.5b). Indeed, if only one CP contact was performed, the magnetization would be along the -z axis, and the DNP microwave irradiation would destroy the nuclear polarization, bringing the magnetization to a DNP steady-state with opposite sign. This method known as DOIN-CP (for double-inversion CP) was developed by A.J. Perez-Linde (6). This double adiabatic inversion is extremely convenient and robust to use. It was chosen in most experiments shown in this Thesis.

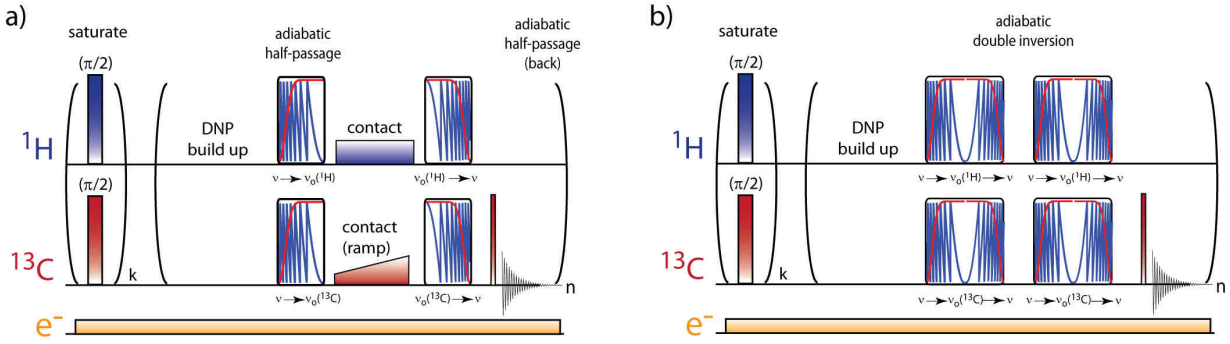

Figure 3.5: **a**) Multiple contact CP sequence using adiabatic half-passage sweeps on both channels to excite and flip-back the ^{1}H and ^{13}C magnetization, combined with CW contact pulses, the amplitude of which may be ramped. **b**) Multiple contact CP sequence where the magnetization is transferred during adiabatic inversion. The contact is established twice during each CP step, in the manner of the DOIN-CP sequence developed by A.J. Perez-Linde (6).

The comparison between standard CP presented in Figure 3.2 and double inversion CP described in Figure 3.5b is shown in Figure 3.6b for different *rf* field strengths. The CP efficiency is superior, especially at low power, when using adiabatic inversion.

Finally, it is important to note that the transfer of magnetization by adiabatic half- or full-passage pulses is different from Cross Polarization via adiabatic demagnetization in the rotating frame (ADRF) followed by adiabatic remagnetization in the rotating frame (ARRF) (14, 26). In thermodynamic terms, in the first case, the two Zeeman spin baths are put in contact, whereas in the second case the proton Zeeman order is transferred to dipolar order, which is then transferred to carbon-13 Zeeman order. This difference is clearly explained by Redfield (see Reference (27) p. 1020). In the context of DNP, Cross Polarization by ADRF is also possible. It was recently shown by Batel *et al*. (28) that the method is less efficient than adiabatic half-passage.

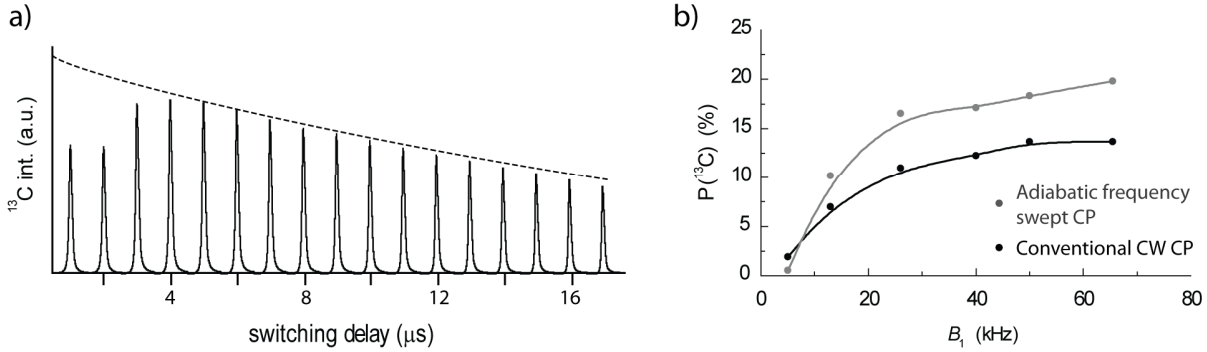

Figure 3.6: **a**) ^{13}C CP signals recorded with the sequence described in Figure 3.2, while incrementing the delay between the initial 90°x excitation and the contact pulses. **b**) ^{13}C CP polarization as a function of the *rf* field strength if Cross Polarization is performed either with conventional CW fields (as in Figure 3.2) or with adiabatic frequency-swept fields (as in Figure 3.5b).

A last optimization of the CP sequence for DNP conditions can be carried out. As the carbon magnetization relaxes slowly to its DNP steady state, and as the proton DNP build-up is fast, multiple-contact CP transfers can be accumulated (see Figure 3.7). This bypasses the problem of low CP efficiency, due to the fact that B_1 is weak compared to the nuclear linewidths.

It is possible to calculate the behaviour of the ^{1}H and ^{13}C magnetization during a multiple-contact CP sequence. One needs to know the maximal ^{1}H and ^{13}C polarizations $P(^1\text{H}, ^{13}\text{C})^{max}$ (without CP), the DNP build-up time constants, $\tau_{DNP}(^1\text{H}, ^{13}\text{C})$ and the time constant $\tau_{relax}(^{13}\text{C})$ of the relaxation towards the DNP steady state (*i.e.* to $P(^{13}\text{C})^{max}$). These five parameters will determine the build-up and decay of the ^{1}H and ^{13}C magnetization. The role of multiple CP contacts can then be considered after n = 1, 2, …, N contacts spaced by intervals Δ_{CP}. The ^{1}H polarization is recalculated at after each contact n according to the fraction of the ^{1}H magnetization preserved by the pulses $Ef_{CP}(^1\text{H})$):

$$P(^1H)\left(t' = n\Delta_{CP}\right) = Ef_{CP}(^1H)\; P(^1H)\left(t = n\Delta_{CP}\right) \tag{3.2}$$

where the prime stands for "after the CP contact", and n is the counter of the number of CP contacts. The same can be done with $Ef_{CP}(^{13}\text{C})$, the CP efficiency given by the fraction of the ^{1}H magnetization transferred to ^{13}C, when starting with $P(^{13}\text{C})$ = 0%. The fact that as the ^{13}C polarization increases, the transfer becomes less efficient has also to be taken into account. Therefore, one has:

$$P(^{13}C)(t'=n\Delta_{CP}) = P(^{13}C)(t=n\Delta_{CP}) + Ef_{CP}(^{13}C)\ \left(P(^{1}H)(t=n\Delta_{CP}) - P(^{13}C)(t=n\Delta_{CP})\right) \quad (3.3)$$

All these parameters affect the build-up curves calculated for multiple-contact CP from ^{1}H to ^{13}C shown in Figure 3.7. Such simulations allow one to determine the enhancement due to CP, ε_{CP} = $P(^{13}C)^{CP,max}/P(^{13}C)^{max}$.

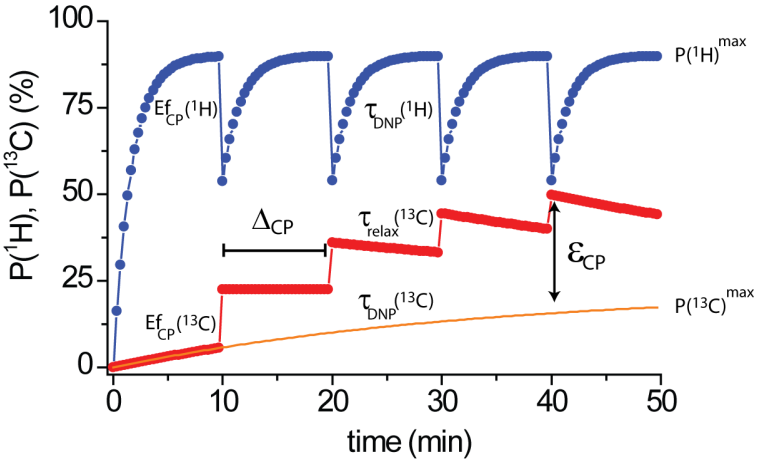

Figure 3.7: Build-up curves of the ^{1}H and ^{13}C polarizations during multiple-contact CP calculated with Equations 3.2 and 3.3, with $P(^{1}H)^{max}$ = 90%, $P(^{13}C)^{max}$ = 22.5%, $\tau_{DNP}(^{1}H)$ = 100 s, $\tau_{DNP}(^{13}C)$ = $\tau_{relax}(^{13}C)$ = 2000 s, $Ef_{CP}(^{1}H)$ = 50%, $Ef_{CP}(^{13}C)$ = 20% and Δ_{CP} = 10 min.

The only variable that can be adjusted experimentally is the inter-contact delay Δ_{CP}. All other variables are fixed for a given probe and sample.

In Figure 3.8a, the maximal CP enhancements as function of the delay Δ_{CP} between CP contacts are reported for different amounts of ^{1}H polarization that are preserved upon contact, keeping the ^{13}C CP efficiency fixed at a low value of 10%. Realistic polarizations, build-up curves and relaxation values for a standard DNP sample at 6.7 T and 1.2 K are considered (see Table 2.3). Note that the maximal possible enhancement is 2.5. The build-up time constant to reach such a CP steady state is also reported in the insert. Similar calculations are shown in Figure 3.8b, but with a better CP efficiency, $Ef_{CP}(^{13}C)$ = 50%. One can see that if the inter-contact delay is too long, the maximal enhancement will tend to a common value, regardless of $Ef_{CP}(^{1}H)$. This value is determined by the CP efficiency $Ef_{CP}(^{13}C)$. A better CP transfer efficiency will drastically accelerate the CP build-up. Finally, it can be seen that it is also important to preserve the ^{1}H magnetization during the CP contact to have a faster build-up to higher polarization values.

The ^{13}C polarization enhanced by CP from hyperpolarized ^{1}H tends to go back to its steady-state DNP equilibrium between the CP steps. If this relaxation could be controlled, even inefficient CP contacts would bring the ^{13}C enhancement to its theoretical maximum. This is shown in Figure 3.8c,d where CP build-up curves are calculated under the same conditions as in Figure 3.8a,b, but without ^{13}C relaxation. Possibly at a cost of slow build-up rates, the ^{13}C polarization tends to $P(^{1}H)^{max}$, even under the worst CP conditions.

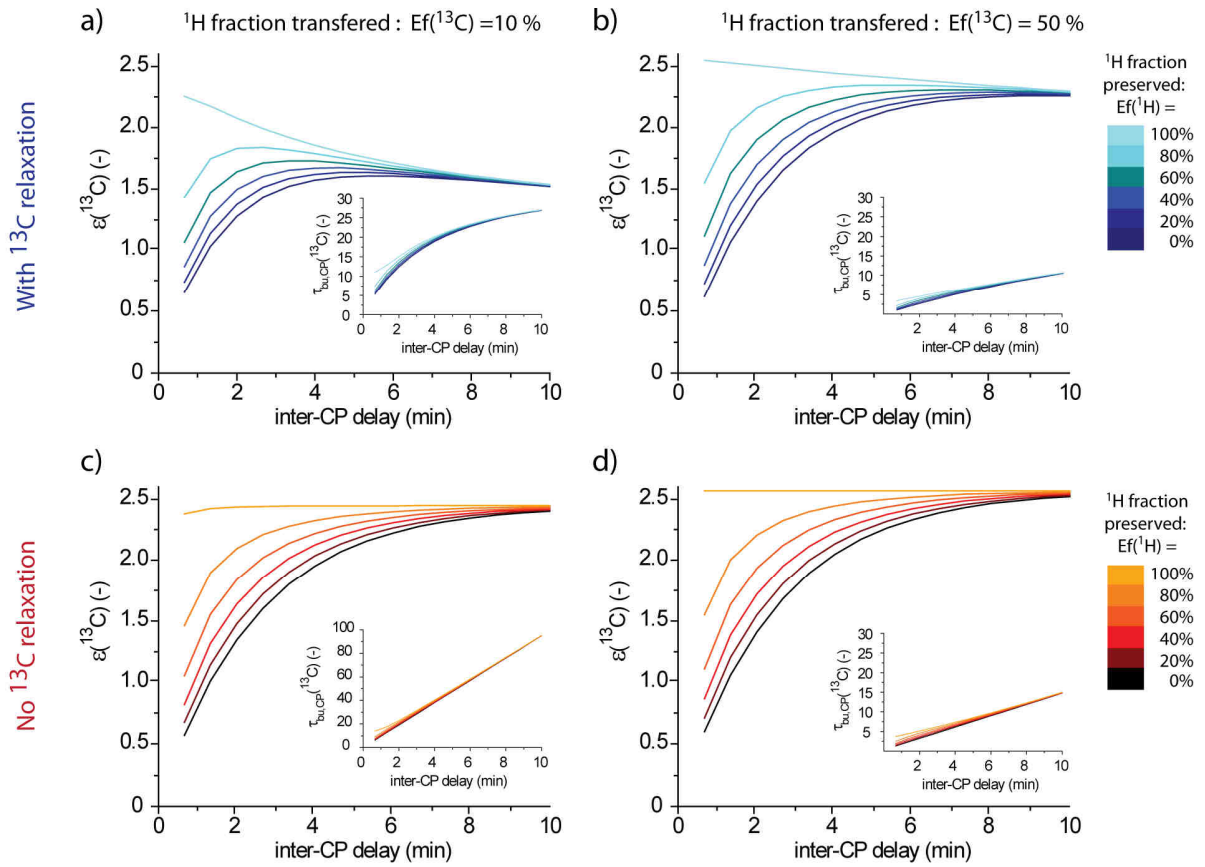

Figure 3.8: **a**) Maximal CP enhancements as well as CP build-up time constants (insert) as a function of the inter-CP delay Δ_{CP}, calculated with Equations 3.2 and 3.3 for different $Ef_{CP}(^{1}H)$, keeping $Ef_{CP}(^{13}C)$ constant to 10%. The DNP sample parameters are set to realistic values at 6.7 T and 1.2 K: $P(^{1}H)^{max}$ = 91%, $P(^{13}C)^{max}$ = 36%, $\tau_{DNP}(^{1}H)$ = 150 s, $\tau_{DNP}(^{13}C)$ = 1980s, $\tau_{relax}(^{13}C)$ = 2500 s. **b**) Same calculations as in (**a**), but with $Ef_{CP}(^{13}C)$ = 50%. **c, d**) Same calculations as in (**a**) and (**b**), but neglecting ^{13}C relaxation ($\tau_{relax}(^{13}C) = 10^{5}$ s).

3.3 Results

3.3.1 Cross-polarization at 3.35 T

The use of CP has the potential to increase the polarization from $P^{DNP}(^{13}C)$ to $P^{CP\text{-}DNP}(^{13}C) \approx P^{DNP}(^{1}H)$, theoretically by a factor up to $\varepsilon_{CP} \approx 4$, to a maximum absolute polarization $P^{CP\text{-}DNP}(^{13}C)$ = 40% at 1.2 K and 3.35 T. Moreover, the use of CP should theoretically allow one to obtain similar performances at $T > 2.2$ K than direct DNP at 1.2 K, thus allowing the cryogenic equipment to be greatly simplified. Figure 3.9 shows the DNP build-up curves of the ^{13}C polarization in 1-^{13}C labelled acetate with and without CP (2). The latter experiment used 5° pulses repeated every two minutes, while CP was performed as described in Fig. 3.5b with *rf* field amplitudes $\nu_1(^{1}H) = \nu_1(^{13}C)$ = 55 kHz and a contact time of 1 ms. When using CP, a maximum ^{13}C spin polarization of $P^{CP\text{-}DNP}(^{13}C)$ = 23 % was achieved within a build-up time $\tau_{CP}(^{13}C)$ = 170 s, whereas only $P^{DNP}(^{13}C)$ = 9.5% could be achieved without CP with $\tau_{DNP}(^{13}C)$ = 450 s. The polarization levels $P^{CP\text{-}DNP}(^{13}C)$ and $P^{DNP}(^{13}C)$ obtained at different temperatures are shown in Table 3.1 (1). With the probe design used in our experiments, CP can provide an enhancement $\varepsilon_{CP} > 2$ compared to conventional direct

DNP. The use of CP also decreases the time needed for the polarization to level off to its steady state equilibrium. In the experiment presented in Figure 3.9, an acceleration factor κ_{CP} = 2.6 was obtained.

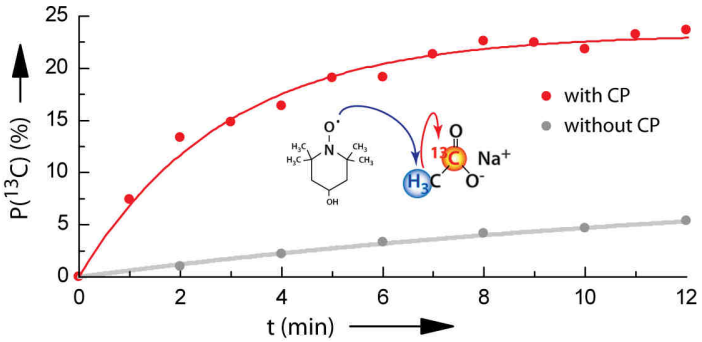

Figure 3.9: DNP build-up curves of the ^{13}C polarization measured without CP (grey curve) and with CP (red curve) monitored with short 5° observation pulses as shown in Figure 3.2.

T (K)	$P^{DNP}(^{1}H)$ (%)	$P^{DNP}(^{13}C)$ (%)	$P^{DNP\text{-}CP}(^{13}C)$ (%)	ε_{CP}
1.2	40	10	23.0	2.3
2.2	24	6	14.6	2.4
3	12	3	7.2	2.4
4.2	8	2	4.4	2.1

Table 3.1: ^{1}H and ^{13}C polarizations as well as the maximal polarizations reached by CP with our solenoid coil design for 3M 1-^{13}C labelled acetate with 30 mM TEMPOL in 100% deuterated water:ethanol (2:1) at B_0 = 3.35 T for different temperatures.

In view of performing rapid dissolution to produce hyperpolarized samples for solution-state NMR, we studied the relaxation behavior of the highly polarized ^{13}C spins immediately after CP at 1.2 K and 4.2 K (Figure 3.10). If the microwave field remains 'on', the polarization $P^{CP\text{-}DNP}(^{13}C)$ returns to the DNP stationary state $P^{DNP}(^{13}C)$. This return to the stationary state is faster than $T_1(^{13}C)$, and close to $\tau_{DNP}(^{13}C)$. When the microwave field is switched 'off' after CP, $P^{CP\text{-}DNP}(^{13}C)$ returns to thermal equilibrium. All relevant time constants are sufficiently long (>100 s even at 4.2 K) to allow one to perform rapid dissolution within a few seconds after CP.

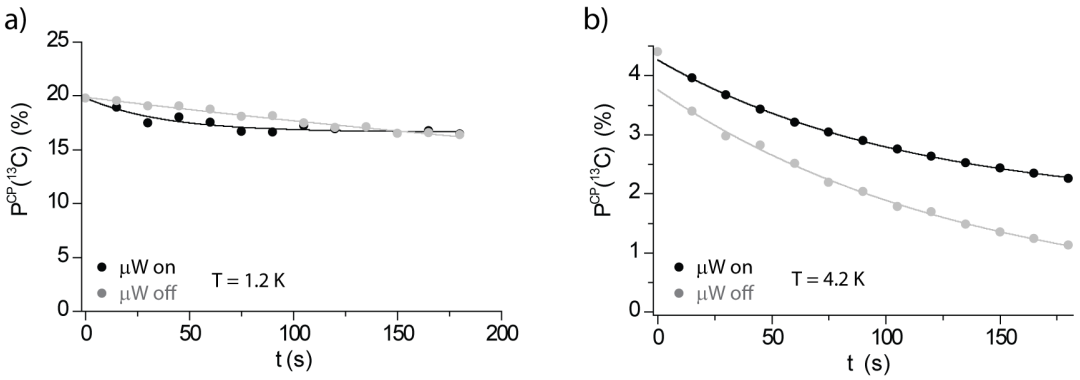

Figure 3.10: Relaxation of the ^{13}C magnetization after CP either with microwave irradiation switched 'on' (black curves) or with microwave irradiation switched 'off' (grey curves), at 1.2 K (**a**) or 4.2 K (**b**).

3.3.2 Cross-polarization at 6.7 T

Experimental reports on low temperature Dissolution-DNP at fields above 3.35 T, *i.e.*, at B_0 = 4.6 T using Trityl (29) and at B_0 = 5 T using TEMPO (30), show substantial improvements in polarization levels achieved by direct DNP, *i.e.*, $P^{DNP}(^{13}C)$ = 35 % at 4.6 T and 15 % at 5 T, albeit at the price of prohibitively long build-up times: $\tau_{DNP}(^{13}C)$ > 2000 s with Trityl at 4.6 T and 1200 s with TEMPO at 5 T. On the other hand, the build-up times are usually much shorter for protons than for carbon-13 when TEMPO is used as polarizing agent (12, 31-33). The combination of high polarizing fields and CP is therefore a good option to transfer the high proton polarization to low-γ nuclei.

The design of our 6.7 T DNP polarizer was adapted from the 3.35 T apparatus described previously (11, 34) by running a superconducting magnet designed for B_0 = 7.05 T (Oxford Instruments) at B_0 = 6.7 T, corresponding to an EPR frequency ν_0(e)= 188 GHz. A microwave source (ELVA) initially operating at 94 GHz (tuning range ±250 MHz, $P_{\mu w}^{max}$ = 400 mW) was coupled to a frequency doubler (VDI / D200) to yield 188 GHz (tuning range ±500 MHz, $P_{\mu w}^{max}$ = 120 mW.) Apart from the tuning and matching circuitry for $\nu_0(^1H)$ = 285.23 MHz and $\nu_0(^{13}C)$ = 71.73 MHz, all other components of the DNP polarizer were kept unchanged. Moreover, we empirically determined the optimal TEMPO radical concentration to be on the order of 50 mM at 6.7 T instead of 30 mM at 3.35 T. Although these simple upgrades may appear straightforward, the improvements in polarization are quite significant.

At 1.2 K and 6.7 T, proton polarization values as high as $P^{DNP}(^1H)$ = 90 % can be readily obtained by microwave irradiation at $\nu_{\mu w}$ = 188.3 GHz, corresponding to the negative optimum of the DNP frequency spectrum, with a short build-up time $\tau_{DNP}(^1H)$ = 150 s. Under the same conditions, the ^{13}C polarization builds up much slowly by direct DNP with $\tau_{DNP}(^{13}C)$ = 1980 s towards a level $P^{DNP}(^{13}C)$ = 36 % (see Table 3.2 and 2.3). With Trityl, it might be possible to achieve higher ^{13}C polarization levels at B_0 = 6.7 T, but the build-up times are likely to be much longer.

T (K)	$P^{DNP}(^1H)$ (%)	$P^{DNP}(^{13}C)$ (%)	$P^{DNP\text{-}CP}(^{13}C)$ (%)	ε_{CP}	$\tau_{DNP}(^{13}C)$	$\tau_{CP}(^{13}C)$	κ_{CP}
1.2	91	36	71	2.0	1980	488	4.0
2.2	60	22.5	43.8	2.0	1010	192	5.2
4.2	25	5.5	15.5	2.8	359	70	5.1

Table 3.2: ^1H and ^{13}C polarizations as well as the maximal polarizations reached by CP with our solenoidal coil design for 3M 1-^{13}C labelled acetate with 50 mM TEMPOL in 100% deuterated water:ethanol (2:1) at B_0 = 6.7 T for different temperatures. The time constants of the direct and CP ^{13}C DNP build-up curves as well as the corresponding acceleration factors κ_{CP} are also reported.

Cross Polarization at 6.7 T was first tested using a solenoid coil design that is not ideal for rapid dissolution. Using the multiple-contact CP sequence shown in Figure 3.5a, it was possible to achieve an unprecedented polarization level of $P^{DNP\text{-}CP}(^{13}C)$ = 71 % within a record build-up time of $\tau_{CP}(^{13}C)$ = 490 s (4). Multiple-contact adiabatic half-passage cross-polarization CP was used at intervals Δ_{CP} = 300 s. To convert the longitudinal magnetization $I_z + S_z$ to the transverse plane $I_x + S_x$, each CP contact comprised two frequency-swept pulses applied simultaneously to both ^1H and ^{13}C channels, with a duration of 150 µs and a constant 40 kHz amplitudes on both channels. The carrier frequencies were swept in a linear fashion from – 100 kHz to the resonances of ^1H or ^{13}C, respectively. A rectangular pulse with a constant 40 kHz amplitude of duration τ_{CP} = 1 ms was applied to the ^1H channel, simultaneously with a ramped pulse applied to the ^{13}C channel with an amplitude that is increasing linearly between 35 and 45 kHz. Finally the two flip-back pulses were applied with frequencies that are swept in the opposite sense as

during the excitation step to bring the magnetization back to $I_z + S_z$. The polarizations obtained by such CP contacts are shown in Table 3.2 for different temperatures.

High polarization levels $P^{DNP\text{-}CP}(^{13}C) > 70\%$ could be achieved using a solenoidal radio-frequency coil that was *not* suitable for rapid dissolution. This coil was therefore replaced by Helmholtz coils (Figure 3.1b). Moreover, the waveguide that was terminated by a horn right above the sample in our initial design, was placed on the side of the cavity in our new design to enable dissolution. Special attention was given to the design of reliable *rf* coils for efficient CP with homogeneous B_1 fields over the entire sample volume. However, because of arcing in superfluid helium at $T = 1.2$ K, the *rf* fields used for CP were limited to 15 kHz each, using 15 and 25 W on the proton and carbon channels, respectively.

The probe was tested on a DNP sample of 1-^{13}C acetate 3M dissolved in D_2O:Ethanol-d_6 (2:1) with 50 mM TEMPOL. With such coil design, $P^{DNP\text{-}CP}(^{13}C) = 45$ %, *i.e.* $\varepsilon_{CP} = 1.7$, could be obtained with a fast build-up time $\tau_{CP}(^{13}C) = 810$ s. The sample was then dissolved with 5 mL of superheated D_2O and transferred in 10 s to a 7.05 T NMR spectrometer for detection. The remaining room temperature signal was estimated to correspond to a polarization $P(^{13}C) \approx 40\%$ (See Figure 3.11). Exactly the same experiment was applied to ^{13}C enriched sodium pyruvate and yielded $P(^{13}C) = 40.5\%$ after dissolution (3).

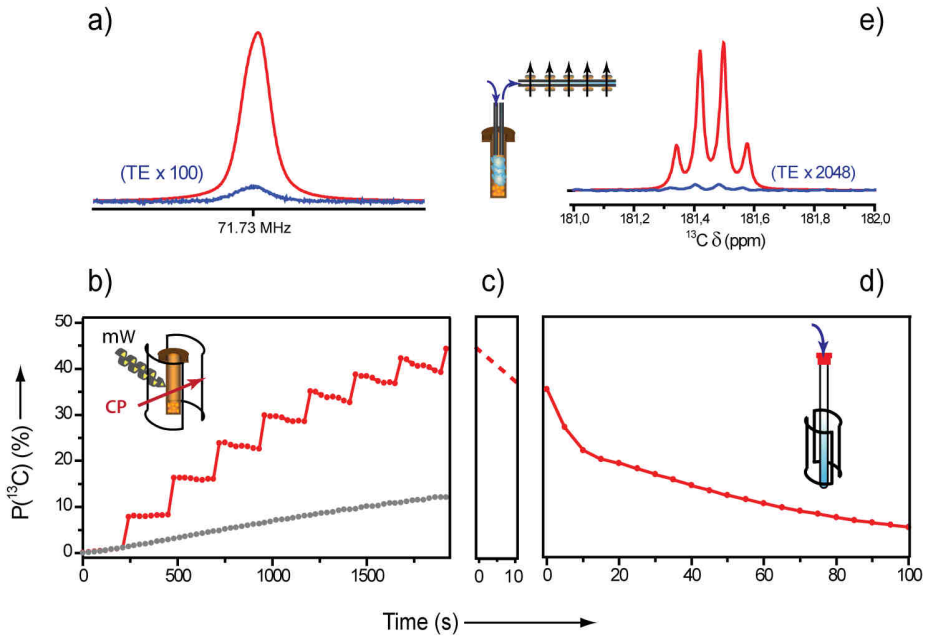

Figure 3.11: **a**) Signals of ^{13}C observed at $T = 4.2$ K and $B_0 = 6.7$ T of 50 µL frozen beads of a 3 M solution of ^{13}C-1 enriched sodium acetate in a deuterated water/ethanol mixture (67:33 v/v) doped with 50 mM TEMPO measured without CP-DNP (blue) at thermal equilibrium (scaled by a factor 100) and with CP-DNP (red) (with $P_{\mu w} = 120$ mW at $\nu_{\mu w} = 188.3$ GHz). **b**) ^{13}C DNP build-up curves with (red) and without (grey) CP measured every 30 s with 5° pulses. Multiple-contact CP was performed every 240 s with the pulse sequence described in Figure 3.5b with $B_1 = 15$ kHz, and a contact time of 1 ms. **c**) The dissolution and transfer process requires $t_{diss} = 10.7$ s. **d**) Relaxation of ^{13}C in solution at *ca*. $T = 300$ K after transfer to a magnetic field $B_0 = 7.05$ T, measured with 5° pulses at 5 s intervals. **e**) Signals of ^{13}C-1 sodium acetate immediately after dissolution (red) and at thermal equilibrium (blue), scaled by a factor 2048.

3.4 Improvements and future developments

3.4.1 CP from solvents to deuterated analytes

Although spectacular enhancement factors can be achieved by D-DNP, applications are inexorably limited by the lifetime of the hyperpolarized magnetization, which is usually determined by the relaxation time T_1. Considerable efforts have been deployed to reduce losses of polarization during sample transfer, in particular to provide access to slow and subtle chemical transformations such as slow metabolic processes. This is of particular interest in the context of metabolic *in-vivo* imaging where more than 60 seconds may be required between dissolution and injection for filtration, pH adjustment, and quality control (35). Whatever paths may be chosen for extending the lifetimes of hyperpolarization, in many cases the mere presence of proton spins in the molecules may impose a severe erosion of the hyperpolarization. Nuclear spin-lattice relaxation driven by intra-molecular dipolar interaction, in particular between a hyperpolarized ^{13}C spin and neighboring ^{1}H spins, even when they are separated by two or more bonds, may offer efficient relaxation pathways. A simple solution to this problem consists in the partial or complete deuteration of the molecule of interest, such as the methyl groups in 3-^{13}C pyruvate (36) or ^{15}N-trimethyglutamine (37), or even the amine group in ^{15}N-glutamine (38). A good example of this approach is the use of ^{15}N-trimethylphenylammonium-d_9 as a platform for designing a variety of hyperpolarized chemical probes, with $T_1(^{15}N)$ exceeding 800 s (39).

Such an approach could at a first glance appear to be incompatible with Cross Polarization. In this Section, it will be shown that, surprisingly, Cross Polarization can transfer magnetization from ^{1}H to ^{13}C even when the molecules are perdeuterated, provided that the concentration of protons in the surrounding glassy solvent is sufficient (5). As a proof of principle, we demonstrate our method for ^{13}C enriched 1-^{13}C pyruvate-d_3, and for the 2-^{13}C and 3-^{13}C isotopologues of pyruvate-d_3 in natural abundance. Many other molecules are expected to benefit from perdeuteration like 5-^{13}C glutamine (40), 1,4-$^{13}C_2$ fumarate (41), 1-^{13}C urea (42), 1-^{13}C DHA (43), or even 2-^{13}C fructose (44).

A 1.5 M solution of sodium 1-^{13}C pyruvate-d_3 containing 50 mM TEMPOL in D_2O:H_2O:glycerol-d_8 (4:1:5) with a ^{1}H concentration of *ca*. 11 M was used. Figure 3.12a shows how the ^{13}C polarization of deuterated pyruvate increased stepwise by multiple-contact CP from remote solvent protons. If a CP contact is established every 5 minutes, the ^{13}C polarization builds up with a time constant $\tau_{CP}(^{13}C)$ = 950 s. This polarization build-up is comparable to the one observed with non-deuterated 1-^{13}C pyruvate ($\tau_{CP}(^{13}C)$ = 990 s) under the same conditions (Figure 12b).

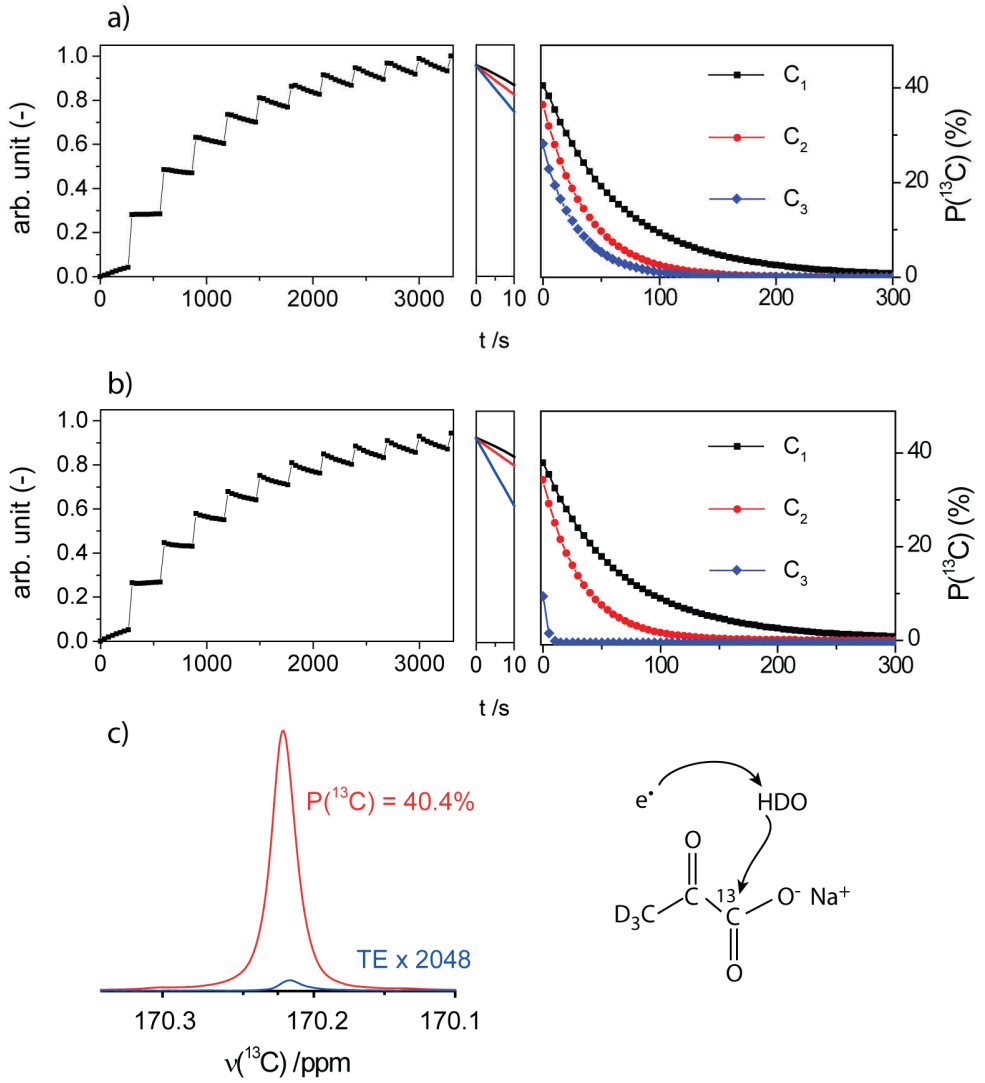

Figure 3.12: Hartmann-Hahn Cross Polarization (CP) experiments performed on (**a**) deuterated and (**b**) non-deuterated 1-^{13}C pyruvate. The left panels show the build-up of the ^{13}C signals, measured every 37.5 s at 1.2 K using 5° pulses. An adiabatic CP contact is established every 5 min. The middle panels show relaxation during dissolution and transfer to a 7 T (300 MHz) NMR spectrometer. The right panels show the polarization decays of ^{13}C of carboxyl (C_1), carbonyl (C_2) and methyl (C_3) groups after dissolution. The signals were measured at T = 300 K with 5° pulses applied at 5 s intervals. **c**) Spectrum of 1-^{13}C pyruvate-d_3 measured 10 s after dissolution showing $P(^{13}C)$ = 40.4 % (red line), compared to a spectrum measured after complete relaxation to thermal equilibrium with 128 pulses with 90° nutation angles, rescaled by a factor 2048 (blue line).

The 1-^{13}C polarization in deuterated pyruvate measured after dissolution and transfer to a 300 MHz NMR spectrometer is slightly higher ($P(^{13}C)$ = 40.4 %) than in its non-deuterated counterpart ($P(^{13}C)$ = 37.9 %). The relaxation times $T_1(^{13}C)$ of 1-^{13}C are almost identical for deuterated and non-deuterated 1-^{13}C pyruvate. On the other hand, 2-^{13}C and 3-^{13}C show significant improvements of $T_1(^{13}C)$ upon deuteration, respectively by a factor 1.15 and 9.75. The obvious reason for this extension of T_1 is the reduction of heteronuclear ^{1}H-^{13}C dipolar relaxation. In addition to the remarkable extension of $T_1(^{13}C)$ of the 3-^{13}C, we observed a significant improvement in nuclear polarization measured 10 s after dissolution. The polarization of the 3-^{13}C was improved by a factor 3 in the deuterated molecules after dissolution,

because the polarization was better preserved during the transfer. Similar improvements are reported in Figure 3.13 for deuterated 1,2-$^{13}C_2$ acetate-d_3 compared to protonated 1,2-$^{13}C_2$ acetate. After dissolution, a polarization of $P(^{13}C)$ = 20% was obtained on the carboxyl group of deuterated acetate and $P(^{13}C)$ = 15% for its deuterated methyl group.

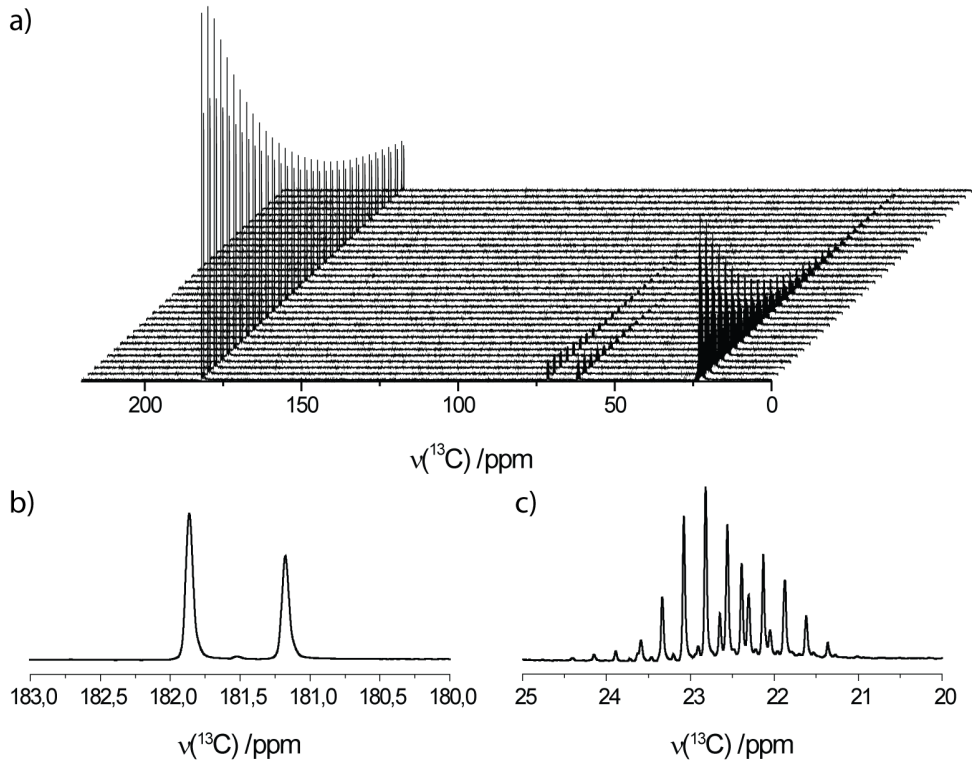

Figure 3.13: **a**) Hyperpolarized ^{13}C NMR spectra of deuterated doubly enriched 1,2-$^{13}C_2$ acetate-d_3 recorded every 5 s after dissolution-DNP, showing the effects of longitudinal relaxation $T_1(^{13}C)$ at 7 T and 300 K. **b**) NMR signals of the carboxyl C_1. **c**) NMR signals of the methyl C_2, revealing asymmetries that are characteristic of very low spin temperatures (45).

3.4.2 CP to other heteronuclei

The use of Cross Polarization in DNP is of course not limited to the transfer of polarization from ^{1}H to ^{13}C. The technique can also be applied to other low-gamma nuclei. Cross Polarization to ^{6}Li under DNP conditions was performed in our group by A. J. Perez-Linde (46). Moreover, at the time of writing, Jonas Milani has built CP-DNP probes designed for ^{29}Si, ^{129}Xe and ^{15}N. Such nuclei were rarely used until now with D-DNP, because of their prohibitively long build-up times and their low polarization values. They appear promising since they exhibit long T_1's. For example $T_1(^{15}N)$ = 800 s was measured in ^{15}N, d_9 trimethylphenylammonium (39).

Moreover, as be shown in Chapter 8, so called Long-Lived States (LLS) can be populated directly at very low spin temperatures (47). Therefore CP under DNP conditions appears to be the best way to create LLS in systems comprising pairs of ^{15}N spins (48) or pairs of ^{13}C spins (49-51).

References

1. Bornet A, Melzi R, Jannin S, & Bodenhausen G (2012) Cross Polarization for Dissolution Dynamic Nuclear Polarization Experiments at Readily Accessible Temperatures 1.2 < T < 4.2 K. *Appl. Magn. Reson.* 43(1-2):107-117.
2. Jannin S, Bornet A, Colombo S, & Bodenhausen G (2011) Low-temperature cross polarization in view of enhancing dissolution Dynamic Nuclear Polarization in NMR. *Chem. Phys. Lett.* 517(4-6):234-236.
3. Bornet A, Melzi R, Perez-Linde AJ, Hautle P, van den Brandt B, Jannin S, & Bodenhausen G (2013) Boosting Dissolution Dynamic Nuclear Polarization by Cross Polarization. *J. Phys. Chem. Lett.* 4(1):111-114.
4. Jannin S, Bornet A, Melzi R, & Bodenhausen G (2012) High field dynamic nuclear polarization at 6.7 T: Carbon-13 polarization above 70% within 20 min. *Chem. Phys. Lett.* 549:99-102.
5. Vuichoud B, Milani J, Bornet A, Melzi R, Jannin S, & Bodenhausen G (2014) Hyperpolarization of Deuterated Metabolites via Remote Cross-Polarization and Dissolution Dynamic Nuclear Polarization. *J. Phys. Chem. B* 118(5):1411-1415.
6. Perez Linde AJ (2010) Application of Cross Polarization Techniques to Dynamic Nuclear Polarization Dissolution Experiments. PhD Thesis (University of Notthingham, Nottingham).
7. Sarkar R, Comment A, Vasos PR, Jannin S, Gruetter R, Bodenhausen G, Hall H, Kirik D, & Denisov VP (2009) Proton NMR of N-15-Choline Metabolites Enhanced by Dynamic Nuclear Polarization. *J. Am. Chem. Soc.* 131(44):16014.
8. Comment A, Jannin S, Hyacinthe JN, Mieville P, Sarkar R, Ahuja P, Vasos PR, Montet X, Lazeyras F, Vallee JP, Hautle P, Konter JA, van den Brandt B, Ansermet JP, Gruetter R, & Bodenhausen G (2010) Hyperpolarizing Gases via Dynamic Nuclear Polarization and Sublimation. *Phys. Rev. Lett.* 105(1).
9. Mieville P, Jannin S, Helm L, & Bodenhausen G (2010) Kinetics of Yttrium-Ligand Complexation Monitored Using Hyperpolarized Y-89 as a Model for Gadolinium in Contrast Agents. *J. Am. Chem. Soc.* 132(14):5006.
10. Ardenkjaer-Larsen JH, Leach AM, Clarke N, Urbahn J, Anderson D, & Skloss TW (2011) Dynamic Nuclear Polarization Polarizer for Sterile Use Intent. *NMR Biomed.* 24(8):927-932.
11. Comment A, van den Brandt B, Uffmann K, Kurdzesau F, Jannin S, Konter JA, Hautle P, Wenckebach WTH, Gruetter R, & van der Klink JJ (2007) Design and performance of a DNP prepolarizer coupled to a rodent MRI scanner. *Concept. Magn. Reson. B* 31B(4):255-269.
12. Kurdzesau F, van den Brandt B, Comment A, Hautle P, Jannin S, van der Klink JJ, & Konter JA (2008) Dynamic nuclear polarization of small labelled molecules in frozen water-alcohol solutions. *J. Phys. D Appl. Phys.* 41(15).
13. Hartmann SR &Hahn EL (1962) Nuclear Double Resonance in Rotating Frame. *Phys. Rev.* 128(5):2042.
14. Pines A, Gibby MG, & Waugh JS (1973) Proton-Enhanced Nmr of Dilute Spins in Solids. *J. Chem. Phys.* 59(2):569-590.
15. Pines A, Waugh JS, & Gibby MG (1972) Proton-Enhanced Nuclear Induction Spectroscopy - Method for High-Resolution NMR of Dilute Spins in Solids. *J. Chem. Phys.* 56(4):1776.
16. Abragam A &Goldman M (1978) Principles of Dynamic Nuclear-Polarization. *Rep. Prog. Phys.* 41(3):395-467.
17. Lurie FM &Slichter CP (1963) Spin Temperature in Nuclear Double Resonance. *Phys. Rev. Lett.* 10(9):403.

18. Rovnyak D (2008) Tutorial on analytic theory for cross-polarization in solid state NMR. *Concepts Magn. Reson. A* 32A(4):254-276.
19. Marks D &Vega S (1996) A theory for cross-polarization NMR of nonspinning and spinning samples. *J. Magn. Reson., Ser. A* 118(2):157-172.
20. Tegenfeldt J &Haeberlen U (1979) Cross Polarization in Solids with Flip-Back of I-Spin Magnetization. *J. Magn. Reson.* 36(3):453-457.
21. Baum J, Tycko R, & Pines A (1985) Broad-Band and Adiabatic Inversion of a 2-Level System by Phase-Modulated Pulses. *Phys. Rev. A* 32(6):3435-3447.
22. Garwood M &DelaBarre L (2001) The return of the frequency sweep: Designing adiabatic pulses for contemporary NMR. *J. Magn. Reson.* 153(2):155-177.
23. Tannus A &Garwood M (1997) Adiabatic pulses. *NMR Biomed.* 10(8):423-434.
24. Kupce E &Freeman R (1995) Adiabatic Pulses for Wide-Band Inversion and Broad-Band Decoupling. *J. Magn. Reson., Ser. A* 115(2):273-276.
25. Hediger S, Meier BH, Kurur ND, Bodenhausen G, & Ernst RR (1994) Nmr Cross-Polarization by Adiabatic Passage through the Hartmann-Hahn Condition (Aphh). *Chem. Phys. Lett.* 223(4):283-288.
26. Lee JS &Khitrin AK (2008) Thermodynamics of adiabatic cross polarization. *J. Chem. Phys.* 128(11).
27. Redfield AG (1969) Nuclear Spin Thermodynamics in Rotating Frame. *Science* 164(3883):1015-&.
28. Batel M, Dapp A, Hunkeler A, Meier BH, Kozerke S, & Ernst M (2014) Cross-polarization for dissolution dynamic nuclear polarization. *Phys. Chem. Chem. Phys.* 16(39):21407-21416.
29. Johanneson H, Macholl S, & Ardenkjaer-Larsen JH (2009) Dynamic Nuclear Polarization of [1-C-13]pyruvic acid at 4.6 tesla. *J. Magn. Reson.* 197(2):167-175.
30. Jannin S, Comment A, Kurdzesau F, Konter JA, Hautle P, van den Brandt B, & van der Klink JJ (2008) A 140 GHz prepolarizer for dissolution dynamic nuclear polarization. *J. Chem. Phys.* 128(24).
31. Gerfen GJ, Becerra LR, Hall DA, Griffin RG, Temkin RJ, & Singel DJ (1995) High-Frequency (140 Ghz) Dynamic Nuclear-Polarization - Polarization Transfer to a Solute in Frozen Aqueous-Solution. *J. Chem. Phys.* 102(24):9494-9497.
32. Hartmann G, Hubert D, Mango S, Morehous.Cc, & Plog K (1973) Proton Polarization in Alcohols at 50 Kg, 1k. *Nucl. Instrum. Methods.* 106(1):9-12.
33. Nicholas DJ, Williams WG, Banks PHT, & Cragg DA (1970) Proton Polarization Measurements at High Magnetic Fields and Low Temperatures. *Nucl. Instrum. Methods.* 87(2):301-&.
34. Comment A, van den Brandt B, Uffmann K, Kurdzesau F, Jannin S, Konter JA, Hautle P, Wenckebach WT, Gruetter R, & van der Klink JJ (2008) Principles of operation of a DNP prepolarizer coupled to a rodent MRI scanner. *Appl. Magn. Reson.* 34(3-4):313-319.
35. Nelson SJ, Kurhanewicz J, Vigneron DB, Larson PEZ, Harzstark AL, Ferrone M, van Criekinge M, Chang JW, Bok R, Park I, Reed G, Carvajal L, Small EJ, Munster P, Weinberg VK, Ardenkjaer-Larsen JH, Chen AP, Hurd RE, Odegardstuen LI, Robb FJ, Tropp J, & Murray JA (2013) Metabolic Imaging of Patients with Prostate Cancer Using Hyperpolarized [1-C-13]Pyruvate. *Sci. Transl. Med.* 5(198).
36. Barb AW, Hekmatyar SK, Glushka JN, & Prestegard JH (2013) Probing alanine transaminase catalysis with hyperpolarized (CD3)-C-13-pyruvate. *J. Magn. Reson.* 228:59-65.
37. Chiavazza E, Viale A, Karlsson M, & Aime S (2013) N-15-Permethylated amino acids as efficient probes for MRI-DNP applications. *Contrast Media & Molecular Imaging* 8(5):417-421.
38. Barb AW, Hekmatyar SK, Glushka JN, & Prestegard JH (2011) Exchange facilitated indirect detection of hyperpolarized (ND2)-N-15-amido-glutamine. *J. Magn. Reson.* 212(2):304-310.

39. Nonaka H, Hata R, Doura T, Nishihara T, Kumagai K, Akakabe M, Tsuda M, Ichikawa K, & Sando S (2013) A platform for designing hyperpolarized magnetic resonance chemical probes. *Nat. Commun.* 4:2411.
40. Gallagher FA, Kettunen MI, Day SE, Lerche M, & Brindle KM (2008) C-13 MR spectroscopy measurements of glutaminase activity in human hepatocellular carcinoma cells using hyperpolarized C-13-labeled glutamine. *Magn. Reson. Med.* 60(2):253-257.
41. Gallagher FA, Kettunen MI, Hu DE, Jensen PR, in't Zandt R, Karlsson M, Gisselsson A, Nelson SK, Witney TH, Bohndiek SE, Hansson G, Peitersen T, Lerche MH, & Brindle KM (2009) Production of hyperpolarized [1,4-C-13(2)]malate from [1,4-C-13(2)]fumarate is a marker of cell necrosis and treatment response in tumors. *Proc. Natl. Acad. Sci. U.S.A.* 106(47):19801-19806.
42. von Morze C, Larson PEZ, Hu S, Keshari K, Wilson DM, Ardenkjaer-Larsen JH, Goga A, Bok R, Kurhanewicz J, & Vigneron DB (2011) Imaging of Blood Flow Using Hyperpolarized [C-13] Urea in Preclinical Cancer Models. *J. Magn. Reson. Imaging* 33(3):692-697.
43. Gallagher FA, Kettunen MI, & Brindle KM (2009) Biomedical applications of hyperpolarized C-13 magnetic resonance imaging. *Prog. Nucl. Magn. Reson. Spectrosc.* 55(4):285-295.
44. Keshari KR, Wilson DM, Chen AP, Bok R, Larson PEZ, Hu S, Van Criekinge M, Macdonald JM, Vigneron DB, & Kurhanewicz J (2009) Hyperpolarized [2-C-13]-Fructose: A Hemiketal DNP Substrate for In Vivo Metabolic Imaging. *J. Am. Chem. Soc.* 131(48):17591-17596.
45. Vuichoud B, Milani J, Chappuis Q, Bornet A, Bodenhausen G, & Jannin S (to be submitted) Spin PolarimetrY for Magnetic Resonance (SPY-MR): measuring absolute spin polarization in Dissolution-DNP experiments.
46. Linde AJP, Bornet A, Milani J, Vuichoud B, Melzi R, Jannin S, & Bodenhausen G (2014) Cross polarization from H-1 to quadrupolar Li-6 nuclei for dissolution DNP. *Phys. Chem. Chem. Phys.* 16(45):24813-24817.
47. Tayler MCD, Marco-Rius I, Kettunen MI, Brindle KM, Levitt MH, & Pileio G (2012) Direct Enhancement of Nuclear Singlet Order by Dynamic Nuclear Polarization. *J. Am. Chem. Soc.* 134(18):7668-7671.
48. Ghosh RK, Kadlecek SJ, Ardenkjaer-Larsen JH, Pullinger BM, Pileio G, Levitt MH, Kuzma NN, & Rizi RR (2011) Measurements of the Persistent Singlet State of N(2)O in Blood and Other Solvents-Potential as a Magnetic Tracer. *Magn. Reson. Med.* 66(4):1177-1180.
49. Marco-Rius I, Tayler MCD, Kettunen MI, Larkin TJ, Timm KN, Serrao EM, Rodrigues TB, Pileio G, Ardenkjaer-Larsen JH, Levitt MH, & Brindle KM (2013) Hyperpolarized singlet lifetimes of pyruvate in human blood and in the mouse. *NMR Biomed.* 26(12):1696-1704.
50. Pileio G, Bowen S, Laustsen C, Tayler MCD, Hill-Cousins JT, Brown LJ, Brown RCD, Ardenkjaer-Larsen JH, & Levitt MH (2013) Recycling and Imaging of Nuclear Singlet Hyperpolarization. *J. Am. Chem. Soc.* 135(13):5084-5088.
51. Laustsen C, Pileio G, Tayler MCD, Brown LJ, Brown RCD, Levitt MH, & Ardenkjaer-Larsen JH (2012) Hyperpolarized singlet NMR on a small animal imaging system. *Magn. Reson. Med.* 68(4):1262-1265.

Chapter 4:

Microwave Frequency Modulation

Monochromatic microwave irradiation of the ESR spectrum of polarizing agents is usually performed in the Dissolution-DNP polarizer. Hovav *et al.* (1) have shown that by using frequency-modulated (rather than monochromatic) microwave irradiation one can improve DNP at 3.35 T in the temperature range 10-50 K. The authors suggested that this *"should be tested in the future also at the 1–2 K temperature range typically used with dissolution DNP".* In this Chapter it will be shown that this prediction was indeed confirmed at lower temperatures and higher fields (1.2 K and 6.7 T). The use of frequency-modulated microwave irradiation under these conditions permits one to decrease the concentration of paramagnetic polarization agents. The technique compensates for the losses of polarization and the deceleration of the build-up rates induced by a reduction of the concentration of radicals. Low electron concentrations allow for more efficient Cross Polarization. Moreover, the life-time of the hyperpolarized magnetization is also prolonged after dissolution under such conditions, which can make a crucial difference, especially if ^{1}H is to be observed, as will be shown in Chapters 5-8.

4.1 Frequency modulation compensates for low radical concentrations

As shown in Chapter 3, Cross Polarization is handicapped by large NMR line-widths and short $T_{1\rho}$. Moreover, ^{13}C relaxation to the DNP steady-state polarization level between CP steps reduces the overall efficiency of Cross Polarization, and thus the maximal ^{13}C polarization achievable. The process could be improved if the electron concentrations could be decreased. Such a reduction of paramagnetic species present would also be of great benefit for the lifetime of the hyperpolarized magnetization after dissolution, as will be shown in Chapter 5-8. Nevertheless, for the DNP process to be efficient, an optimal electron concentration has to be used. High radical concentrations enhance electron-electron dipolar couplings, which enable rapid spectral spin diffusion within the broad inhomogeneous ESR line of TEMPOL. As a consequence, a larger fraction of the electron spins can contribute to the DNP process. If the radical concentration is too low, only a small fraction of the electron spins will contribute to DNP, which will translate into low nuclear spin polarizations and very long build-up times. On the other hand, if the electron spin concentration is too high, the ESR line will tend to be homogeneously broadened well beyond its inhomogeneous width, which will translate into fast build-up rates, but with poor nuclear spin polarizations. In practice, the best radical concentration was found to be around 50 mM at 1.2 K and 6.7 T.

It has been shown recently by Thurber *et al.*(2), Cassidy *et al.* (3), and most recently by Hovav *et al.* (1) that DNP by CE and SE can be greatly improved by using either field-modulated or frequency-modulated microwave irradiation. The same approach is also beneficial at lower temperatures like T = 1.2 K and at a higher magnetic fields such as B_0 = 6.7 T as will be shown below (4). If frequency modulation is used, the fraction of the ESR line where DNP is effective is no longer determined by the radical concentration. The number of DNP-active electrons is increased, and consequently the nuclear enhancement. In fact,

frequency modulation can play a similar role as spectral spin diffusion. More detailed theoretical explanations supported by numerical simulations are given by Hovav *et al.* (1).

To implement frequency modulation, the frequency of the microwave source was controlled directly in the voltage-controlled oscillator unit (VCO) by a constant or modulated voltage (Stanford Research Systems DS345). The voltage source combined with the Elva VCO enables fast (up to 10 MHz) and broad frequency modulation over a range of ± 500 MHz. The microwave frequency typically varies in a sinusoidal fashion according to $\nu_{\mu w}(t) = \langle\nu_{\mu w}\rangle + \frac{1}{2}\Delta\nu_{\mu w}\sin(2\pi f_{mod}t)$, where $\langle\nu_{\mu w}\rangle$ is the average frequency, $\Delta\nu_{\mu w}$ the amplitude of the frequency modulation, and f_{mod} the frequency of this modulation. A schematic description of these parameters is presented in Figure 4.1.

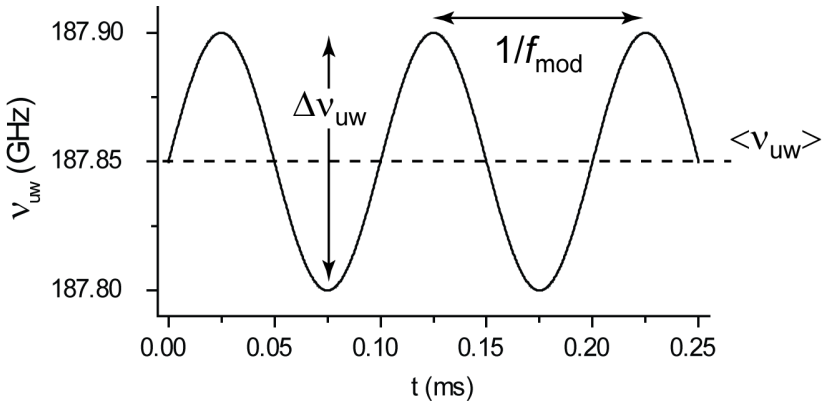

Figure 4.1: Scheme illustrating the frequency modulation method. The microwave frequency typically varies in a sinusoidal fashion according to $\nu_{\mu w}(t) = \langle\nu_{\mu w}\rangle + \frac{1}{2}\Delta\nu_{\mu w}\sin(2\pi f_{mod}t)$, where $\langle\nu_{\mu w}\rangle$ is the average frequency, $\Delta\nu_{\mu w}$ the amplitude of the frequency modulation, and f_{mod} the frequency of modulation.

4.2 Experimental results at 6.7 T and 1.2 K

4.2.1 Frequency-modulated proton build-up curves

Proton DNP was investigated for samples containing 10, 25 and 50 mM TEMPOL, respectively, in a 10:40:50 (v/v/v) H_2O:D_2O:glycerol-d_8 mixture, at T = 1.2 K. The gain in polarization brought about by frequency modulation is modest for high radical concentrations when the ESR spectra are homogeneously broadened, but becomes substantial for low radical concentrations when the ESR line-widths are inhomogeneous. Frequency modulation permits one to increase the proton polarization at low sub-optimal electron concentrations, while simultaneously accelerating the DNP build-up times. Table 4.1 gives the final proton polarization $P(^1H)$ and the corresponding build-up times $\tau_{DNP}(^1H)$ with and without frequency modulation for positive and negative DNP effects, and for three different radical concentrations. The effect of frequency modulation is hardly remarkable at a high radical concentration of 50 mM, but it is much more pronounced as the radical concentration is decreased to 25 or 10 mM. Figure 4.2 shows the effect of microwave frequency modulation on the ^1H DNP build-up behavior for positive or negative DNP in a sample with an electron concentration of 25 mM, performed at the optimal monochromatic frequencies $\nu_{\mu w}$ = 187.85 and 188.3 GHz. The amplitude of the frequency modulation was set to $\Delta\nu_{\mu w}$ = 100 MHz with a modulation frequency f_{mod} = 10 kHz.

[e⁻] (mM)	Modulation	$P^+(^1H)$ (%)	$\tau^+_{DNP}(^1H)$ (s)	$P^-(^1H)$ (%)	$\tau^-_{DNP}(^1H)$ (s)
10	with	14.5*	2600**	-21.1*	2500**
	without	0.9*	n.a.***	-1.2*	n.a.***
25	with	57.3	159 ± 1.8	-60.7	185 ± 2
	without	9.3*	9000**	-29.5	625 ± 11
50	with	61.3	108 ± 1.6	-63.3	152 ± 2
	without	21.9	338 ± 7	-43.7	218 ± 4

Table 4.1: Positive and negative proton polarization and build-up times at T = 1.2 K and B_0 = 6.7 T for different TEMPOL concentrations in a 10:40:50 (v/v/v) H_2O:D_2O:glycerol-d_8 mixture, with and without frequency modulation. Where * DNP maximum was not reached; the polarization shown was achieved after 20 minutes of microwave irradiation. ** Fits have large uncertainties because only the first 20 minutes of the DNP build-up curve were recorded. *** Estimates of the build-up times are not available because of poor fits.

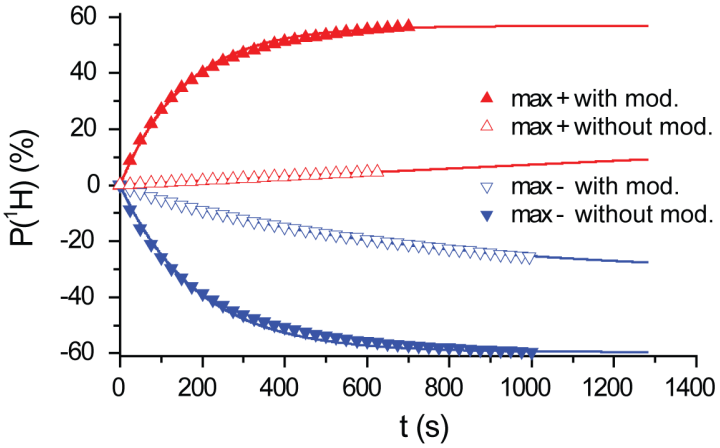

Figure 4.2: Negative (blue symbols) and positive (red symbols) ^{1}H DNP build-up curves measured at T = 1.2 K and B_0 = 6.7 T, with and without frequency modulation, in 3 M 1-^{13}C acetate with 25 mM TEMPOL in a 10:40:50 (v/v/v) H_2O:D_2O:glycerol-d_8 mixture. The optimal frequencies $\nu_{\mu w}$ = 187.85 and 188.3 GHz were set for positive or negative DNP respectively, with a microwave power $P_{\mu w}$ = 87.5 mW. An amplitude $\Delta\nu_{\mu w}$ = 100 MHz was used for frequency modulation.

Figure 4.3 shows a DNP microwave spectrum measured for a sample containing 25 mM TEMPOL. It shows the proton polarization $P(^1H)$ achieved with DNP as a function of the irradiation frequency $\nu_{\mu w}$ with and without frequency modulation. The line-shapes of the DNP microwave spectra are substantially different with or without microwave frequency modulation. The DNP microwave spectrum measured with frequency modulation has positive and negative optima that are roughly separated by the proton Larmor frequency $\nu_0(^1H)$ = 285.23 MHz, which is typical for the Cross Effect. On the other hand, the DNP microwave spectrum measured without frequency modulation, in addition to showing reduced DNP performance, has a width between positive and negative optima reduced to *c.a.* 150 MHz.

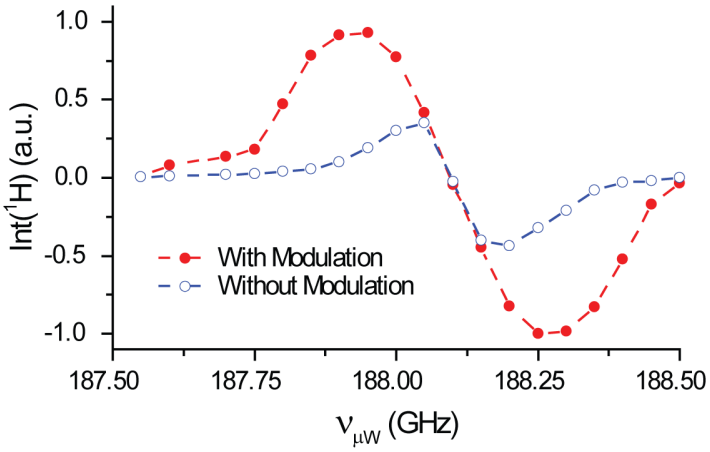

Figure 4.3: Polarization $P(^1H)$ with and without frequency modulation ($\Delta\nu_{\mu w}$ = 100 MHz) for 3 M 1-^{13}C acetate with 25 mM TEMPOL in a 10:40:50 (v/v/v) H_2O:D_2O:glycerol-d_8 mixture, as a function of the (average or monochromatic) microwave frequency.

This change of DNP frequency spectra with free electron concentration was investigated in more detail on samples of 1-^{13}C acetate 3M and 50, 25, or 10 mM TEMPOL in H_2O:D_2O:Glycerol-d_8 (1:4:5) at B_0 = 6.7 T and T = 4.2 K (Figure 4.4a). As the concentration of the polarizing agent is lowered, the difference between the positive and negative DNP optima $\Delta_{DNP}^{max}(^1H)$ and Δ_{DNP}^{max} (^{13}C) decreases. This effect occurs for both for ^{1}H and ^{13}C, but is more visible for the latter nucleus.

The variation of the free electron concentration influences (among other parameters) the electronic spectral diffusion. At higher electronic concentrations, the spectral diffusion between irradiated and non-irradiated electrons should increase the number of DNP-active centers. To see how this affects the shape of the DNP frequency spectra, it is possible to modify Equation 2.4 of Chapter 2, which involved only electrons resonating in a narrow bandwidth near to the applied microwave frequency $\nu_{\mu W}$, determined by the frequency increment of the digitized spectrum $I_{ESR}(\nu_{\mu W})$. In the version of Equation 4.1, the CE DNP spectrum is obtained by summation over irradiation frequencies $\nu_{\mu W}$ over a variable bandwidth $\Delta\nu_{\mu W}$:

$$CE\left(\nu_{\mu W}\right) = a_{CE} \sum_{\nu_{\mu W} \pm \Delta\nu_{\mu W}} \left[I_{ESR}\left(\nu_{\mu W}\right)\left(I_{ESR}\left(\nu_{\mu W} + \nu_0(n)\right) - I_{ESR}\left(\nu_{\mu W} + \nu_0(n)\right)\right)\right] \tag{4.1}$$

The resulting CE DNP frequency spectra calculated using Equations 4.1 with different spectral diffusion bandwidths for ^{1}H and ^{13}C are shown in Figure 4.4b. The effect is less pronounced for ^{1}H than for ^{13}C, but is comparable with our experimental results. Both for ^{1}H and ^{13}C, Δ_{DNP}^{max} becomes larger as $\Delta\nu_{\mu W}$ increases.

One can thus postulate that the modulation of the microwave frequency can be used as a substitute for the electron spectral diffusion when e-e dipole-dipole couplings become smaller at lower concentrations of polarizing agents (larger e-e distances).

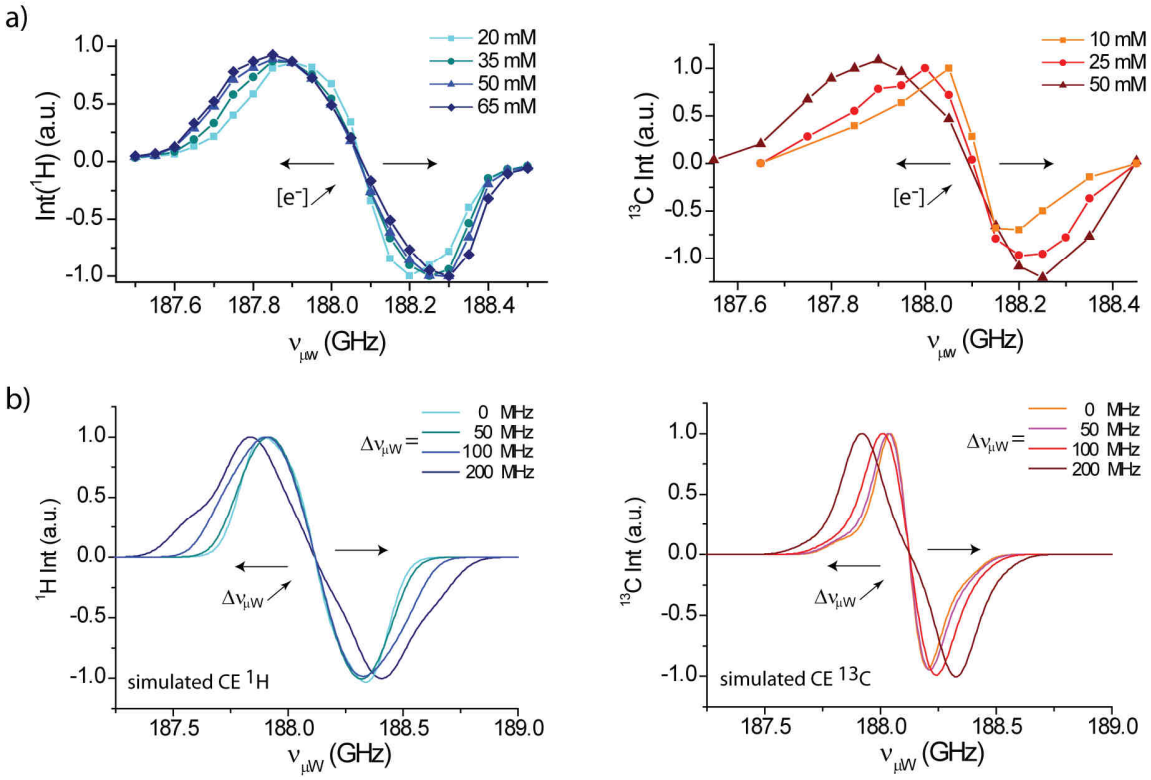

Figure 4.4: **a**) Effect of the electron concentration on the shape of the ^{1}H and ^{13}C DNP spectra. Normalized ^{1}H and ^{13}C DNP spectra of a sample of 3M 1-^{13}C acetate in H_2O:D_2O:Gly-d_8 (1:4:5) polarized at B_0 = 6.7 T and T = 4.2 K, with 20, 35, 50, or 65 mM TEMPOL. **b**) Influence of the electronic spectral diffusion on the shape of the DNP spectra. CE contributiosn calculated with Equations 4.1 for different bandwidths $\Delta\nu_{\mu W}$ for ^{1}H and ^{13}C.

4.2.2 Cross Polarization with low electron concentration

The reduction of the radical concentration, made possible by frequency modulation, makes CP more efficient. Figure 4.5 illustrates this concept by showing that, even though $P(^{1}H)$ slightly decreases when the radical concentration is reduced from 50 to 25 mM, $P(^{13}C)$ after CP is significantly increased. Since $P(^{13}C)$ is obtained from $P(^{1}H)$ by $^{1}H \rightarrow {}^{13}C$ CP, one would not expect such an advantage. However, the improved CP efficiency compensates for the decrease in ^{1}H polarization. Indeed, a decrease in radical concentration results in an extension of nuclear spin-lattice relaxation times, which improves the preservation of hyperpolarized ^{13}C magnetization in-between the CP steps. Additionally, we observed a significant ^{1}H line narrowing in the 1-^{13}C acetate samples at 1.2 K owing to the reduction of paramagnetic line broadening to 35 or 25 kHz for samples with 25 or 10 mM TEMPOL respectively.

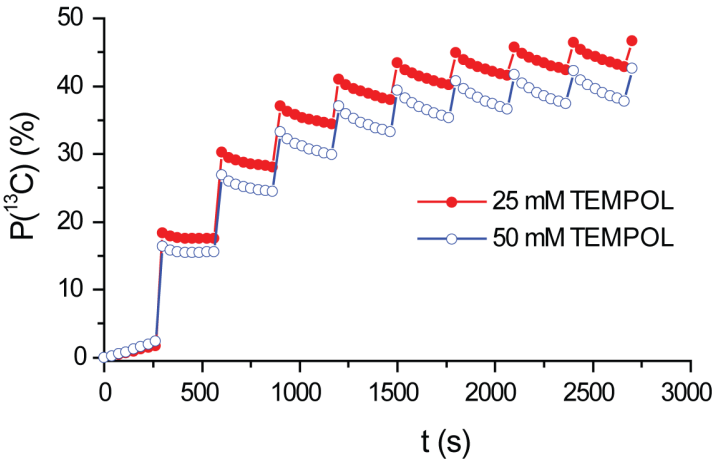

Figure 4.5: DNP build-up curve of the ^{13}C polarization, measured with multiple cross-polarization contacts, for 3 M 1-^{13}C acetate doped with 25 mM TEMPOL with frequency modulation (red filled circles) or 50 mM TEMPOL without frequency modulation (blue empty circles).

The extension of nuclear spin-lattice relaxation times after dissolution is possible when the electron concentration is reduced. This will also improve the preservation of hyperpolarized magnetization during the transfer and the detection of the signal. As it will be shown in the next Chapters, this is of crucial importance, especially when working with protons.

References

1. Hovav Y, Feintuch A, Vega S, & Goldfarb D (2014) Dynamic nuclear polarization using frequency modulation at 3.34 T. *J. Magn. Reson.* 238:94-105.
2. Thurber KR, Yau WM, & Tycko R (2010) Low-temperature dynamic nuclear polarization at 9.4 T with a 30 mW microwave source. *J. Magn. Reson.* 204(2):303-313.
3. Cassidy MC, Chan HR, Ross BD, Bhattacharya PK, & Marcus CM (2013) In vivo magnetic resonance imaging of hyperpolarized silicon particles. *Nat. Nanotechnol.* 8(5):363-368.
4. Bornet A, Milani J, Vuichoud B, Linde AJP, Bodenhausen G, & Jannin S (2014) Microwave frequency modulation to enhance Dissolution Dynamic Nuclear Polarization. *Chem. Phys. Lett.* 602:63-67.

Part B

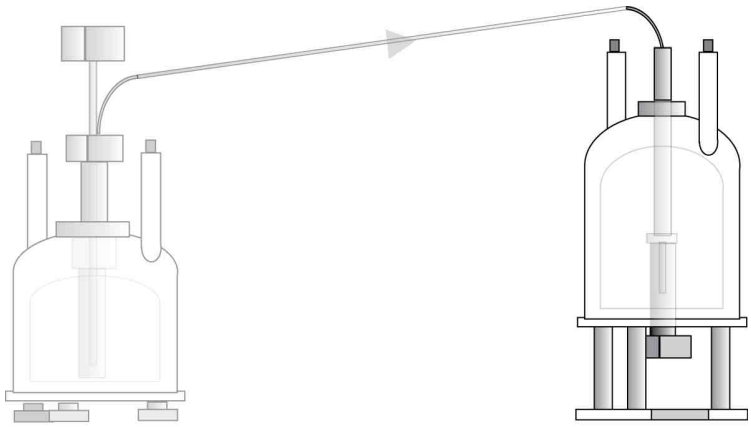

Chapter 5:

DNP enhanced Long-Lived States to study protein-ligand interactions

In this Chapter, I will discuss applications of D-DNP of protons to drug screening using Long-Lived States (LLS). This technique was developed in our group in collaboration with Roberto Buratto (1). In the next Sections, I will first develop the basis of the LLS technique to study protein-ligand interactions without DNP. More advanced applications can be found elsewhere, for example in Reference (2). Then, in Section 5.2, I will focus on the adaptation of the technique to couple it with D-DNP (3). Finally, in Section 5.3, I will quickly introduce some improvements that could be made in the future to render the DNP-LLS method more efficient.

5.1 LLS to study protein-ligand interactions: original experiments without Dissolution-DNP

5.1.1 How to measure dissociation constants with NMR

The functions of a protein are usually expressed by interactions with other biomolecules or smaller ligands, like hormones, substrates, *etc*. Therefore, a fundamental goal in pharmaceutical research and drug development is to find natural or synthetic molecules that interact specifically and strongly with a target biomolecule, promoting or inhibiting its activity.

The binding of a ligand to a protein can be regarded as an equilibrium which results from a balance between association and dissociation events (4). For the simplest case of a protein with a single binding site, the association of a ligand *L* to a receptor protein *P* forming the complex *PL* is described by the equilibrium:

$$P + L \underset{k_{off}}{\overset{k_{on}}{\rightleftharpoons}} PL \tag{5.1}$$

where k_{on} and k_{off} are the kinetic association and dissociation constant, in units of $s^{-1}M^{-1}$ and s^{-1} respectively. The dissociation constant K_D characterizes the thermodynamic equilibrium between the concentrations of the free protein, the free ligand and the protein-ligand complex [*P*], [*L*] and [*PL*]:

$$K_D = \frac{[P]\cdot[L]}{[PL]} = \frac{k_{off}}{k_{on}} \tag{5.2}$$

Studies of binding affinities or the identification of new bioactive substances by screening of libraries of compounds is usually performed using biological assays such as the enzyme-linked immunosorbent assay

(ELISA) (5). Nevertheless, in the last decades, a large variety of physicochemical methods have also been established for this purpose, like isothermal titration calorimetry (6) or surface plasmon resonance (7). NMR spectroscopy techniques have emerged as a powerful approach for the identification of lead compounds in the drug discovery process or for the investigation of protein-ligand interactions (8, 9). NMR methods have the advantage to extend the range of measurable interactions with K_D in the mM range or above, a range that is not well covered by traditional biochemical binding assays.

The general principle of NMR approach is to observe an NMR parameter (that we will call ξ) that changes when the protein and ligand interact (10-13). Theoretically, all spectroscopic NMR parameters may serve as a gauge for binding activity, but only the ones that can be measured easily and with high sensitivity are significant. The object of the NMR observation can be the ligand or the protein. If it is the protein, the parameters that can be monitored are limited to chemical shifts. Moreover, this methodology implies ^{15}N or ^{13}C labelling, well resolved two-dimensional spectra and assignment of the entire protein or at least of its active site. If the ligand is studied, the choice of parameters is broader. It includes longitudinal, transverse and double quantum relaxation, diffusion constants, intermolecular and intramolecular magnetization transfer (14) (NOEs, saturation transfer, Water-LOGSY). Moreover, as protein-ligand complexes are dynamic systems, their exchange rate is of primary importance. For a system in slow exchange (high binding affinity, K_D in the µM range or lower), resolved signals can be recorded for the free protein, the free ligand and the protein-ligand complex and their concentrations can be obtained by integration of their respective signals. Nevertheless, this is difficult in practice because one has to deal with µM signals and complex spectra.

For systems in fast exchange on the NMR time scale, the distribution of species is described in terms of mole fractions of bound (X^{bound}) and free (X^{free}) ligands, and all observed ligand NMR parameters, ξ^{obs}, are given by averages of free and bound parameters, ξ^{free} and ξ^{bound}, weighted by the mole fractions:

$$\xi^{obs} = X^{free}\xi^{free} + X^{bound}\xi^{bound} \qquad (5.3)$$

with $X^{free} = [L]/[L]_0$, $X^{bound} = [PL]/[L]_0$ and the total ligand concentration $[L]_0 = [L] + [PL]$. The details of Equation 5.3 for relaxation rates, adapted from McConnell (15), Luz & Meiboom (16) and Fielding (17), can be found in the supplementary material of Reference (1). Two important approximations must be made in this proof: the saturation approximation must be valid. i.e., $[PL] << [L]_0$, and the fast exchange approximation must be fulfilled, *i.e.*,

$$k_{on} >> k_{off} >> \xi^{free} - \xi^{bound}$$

To illustrate the importance of this approximation, the comparison between the observed values of the relaxation rate $\xi^{obs} = R_1^{obs} = 1/T_1^{obs}$ calculated as a function of the dissociation constant K_D with the fast exchange approximation (Equation 5.3) and without it is shown in Figure 5.1a. If the K_D of the observed ligand is too small, *i.e.*, if the binding is too strong, Equation 5.3 cannot be applied anymore.

Using the definition of K_D and assuming saturation, Equation 5.3 can be rewritten to give an expression of ξ^{obs} that depends only on measurable variables (the details of the derivation are given in supplementary material of Reference (1)):

$$\xi^{obs} = \frac{[P]_0}{K_D + [L]_0}\left(\xi^{bound} - \xi^{free}\right) + \xi^{free} \qquad (5.4)$$

where $[P]_0$ is the total protein concentration. Therefore, to measure K_D, the value of any relevant NMR parameter ξ^{obs} can be measured as a function of the total concentration of the ligand of interest $[L]_0$ while keeping constant the total concentration $[P]_0$ of the protein. ξ^{free} can be measured in an independent experiment with $[P]_0 = 0$. The dissociation constant can then be easily determined by a fit with Equation 5.4 of $\xi^{obs}([L]_0)$, with $[P]_0$ and ξ^{free} as constant and ξ^{bound} and K_D as variable parameters. Rearranging Equation 5.4, one can extract $(\xi^{free} - \xi^{obs})$, which represents the deviation of ξ^{obs} from its free value due to the presence of the protein:

$$\left(\xi^{free} - \xi^{obs}\right) = \frac{[P]_0}{K_D + [L]_0}\left(\xi^{free} - \xi^{bound}\right) \qquad (5.5)$$

This deviation will be large if $(\xi^{free} - \xi^{bound})$, the difference between the values of the parameter in the free and bound states, is large. A few examples of $\xi^{obs}([L]_0/[P]_0)$ calculated with Equation 5.4 for different ξ^{bound}/ξ^{free} ratios are shown in Figure 5.1b.

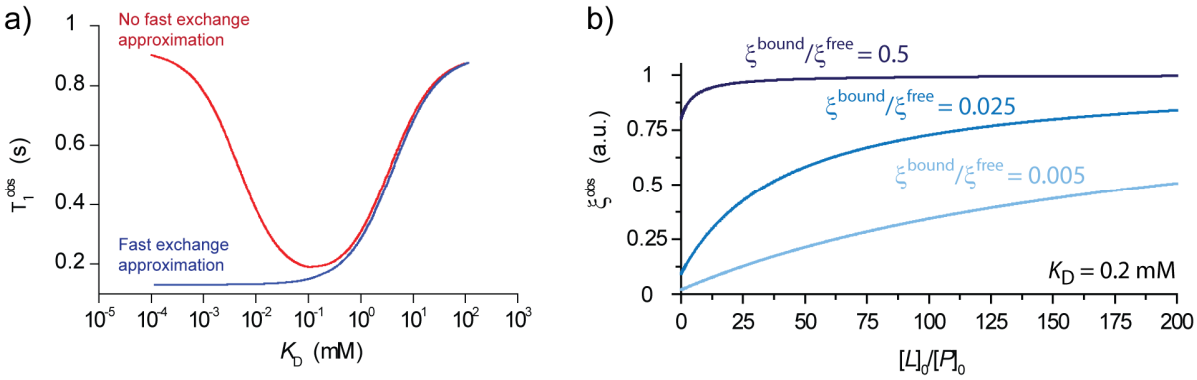

Figure 5.1: **a)** Range of validity of the fast exchange approximation; calculation of the effect of the dissociation constant K_D on $T_1^{obs} = 1/R_1^{obs}$ within the fast exchange approximation (Equation 5.4), (blue) and without invoking the fast exchange approximation ($R_1^{obs} = X^{free}R_1^{free} + X^{bound}\, 1/((R_1^{bound})^{-1} + \tau^{bound})$ (red), with $T_1^{free} = 1$ s, $T_1^{bound} = 0.02$ s; $[L]_0 = 1$ mM, $[P]_0 = 50$ µM; $\tau_b = 1/k_{off}$ the residence time in the bound environment and $k_{on} = 10^8$ s^{-1} M^{-1} (see Reference (1) for the derivation of this equation). **b)** Influence of the deviation of ξ^{bound} from ξ^{free} on ξ^{obs} calculated with Equation 5.4 for different ξ^{bound}/ξ^{free} ratios, with $K_D = 0.2$ mM.

Therefore, the larger $|\xi^{free} - \xi^{bound}|$, the lower the ligand-protein concentration ratio needed to observe a deviation of ξ^{obs} from ξ^{free}. NMR parameters that are strongly influenced by binding to a protein should thus be chosen as probes for K_D measurements.

5.1.2 Introduction to Long-Lived States

So-called Long-Lived States (LLS)(18-20), also known as Singlet States (SS) in isolated two-spin systems, can be used very effectively to investigate protein-ligand interactions (1). Indeed, the protracted lifetimes T_{LLS} of these nuclear spin states are exquisitely sensitive to binding to a protein, giving a dramatic contrast between the lifetimes T_{LLS} of the bound and free forms. Long-Lived States, first described by Levitt and co-workers (21-24), have the unique property that their populations relax with

time constants that can be much longer than longitudinal relaxation time constants (T_{LLS} >> T_1). For pairs of protons, ratios T_{LLS}/T_1 as large as 60 have been observed in R-CH=CH-R' systems. In the case of homonuclear two spin-½ systems, singlet ($|S_0\rangle$) and triplet ($|T_{+1}\rangle$, $|T_0\rangle$, $|T_{-1}\rangle$) states can be constructed by combinations of the four Zeeman product states ($|\alpha\alpha\rangle$, $|\alpha\beta\rangle$, $|\beta\alpha\rangle$, $|\beta\beta\rangle$):

$$
\begin{aligned}
|S_0\rangle &= 1/\sqrt{2}\left(|\alpha\beta\rangle - |\beta\alpha\rangle\right) \\
|T_{+1}\rangle &= |\alpha\alpha\rangle \\
|T_0\rangle &= 1/\sqrt{2}\left(|\alpha\beta\rangle + |\beta\alpha\rangle\right) \\
|T_{-1}\rangle &= |\beta\beta\rangle
\end{aligned}
\qquad (5.6)
$$

Singlet states are anti-symmetric with respect to the permutation of the two spins, whereas the three triplet states are symmetric. As the intra-molecular dipole-dipole (DD) interaction between these two spins is symmetric with respect to the exchange of the two nuclei, it cannot interconvert singlet and triplet populations (20). This interaction is the main relaxation mechanism for spins ½ in liquid state NMR (25). Thus if a population difference between singlet and triplet states is created, only secondary relaxation mechanisms, like external DD, CSA, or paramagnetic relaxation due to species in solution, will be efficient, and the magnetization can be stored for a long time since its relaxation time constant will be longer than T_1.

Measurement of T_{LLS}: LLS pulse sequence

In a system with two magnetically inequivalent spin (IS), $|S_0\rangle$ and $|T_0\rangle$ are not eigenstates of the nuclear spin Hamiltonian, so that the singlet state population is continuously converted to triplet states which rapidly relax. On the other hand, Long Lived States cannot be excited and detected in a two-spin system with magnetically equivalent spins (I_2), as conventional NMR experiments will act similarly on the two spins, and as it has no net magnetization. An LLS pulse sequence is thus divided in three blocks (Figure 5.2a).

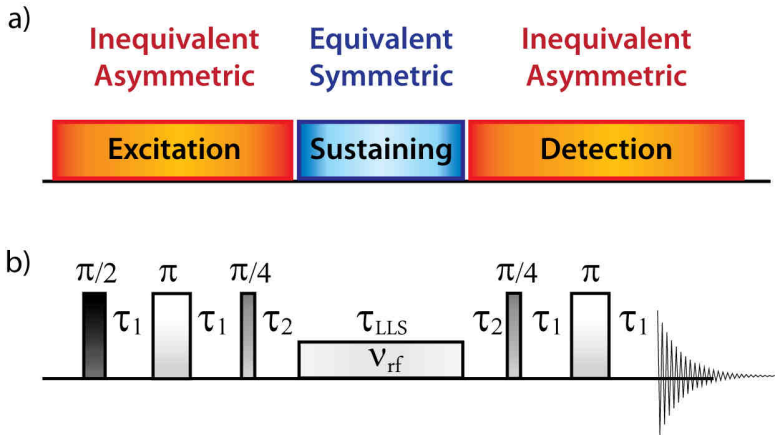

Figure 5.2: Pulse sequence used to excite, sustain and observe LLS: **a)** Schematic view. **b)** Detailed view. The conversion is most efficient if $\tau_1 = 1/4J_{IS}$ and $\tau_2 = 1/2\Delta\nu_{IS}$.

One has (i) to start with a system comprising two non-equivalent spins, and convert via a pulse sequence (22, 26) their Boltzmann equilibrium population into a spin density operator corresponding to a so-called

precursor state, *i.e.*, a state that acquires a long-lived property as soon as the two spins are made equivalent; (ii) preserve the LLS population by temporarily suppressing the effects of the chemical shift difference. This is done in the experiment presented in this chapter by applying a resonant radiofrequency (*rf*) field (22, 24, 27, 28) during a sustaining time τ_{LLS}, with the carrier (ν_{rf}) placed half-way between the chemical shifts of the two spins. The LLS are efficiently sustained if the *rf* field is at least five times stronger than the chemical shift difference between the two spins (29); (iii) finally, the LLS isolation is suspended; the system is again best described as an IS system. A suitable pulse sequence is applied to obtain observable magnetization (26). The lifetime of the LLS can be determined by fitting the signal intensities recorded as a function of τ_{LLS} to the exponential function $\exp(-\tau_{LLS}/T_{LLS})$.

The complete LLS pulse sequence used for the protein-ligand experiment is shown in Figure 5.2b. A detailed description of the sequence using the product operator formalism can be found in Reference (26) as well as in the supplementary material of Reference (1).

5.1.3 LLS to study protein-ligand interactions

It turns out that a protein can be a very good relaxation agent for Long-Lived States. Indeed, a ligand carrying LLS that enters into a binding pocket will experience dipole-dipole interactions with all spins, mainly the protons, of the protein. The correlation time of a bound ligand will also become longer. Finally, the local magnetic fields at the sites of the two protons of the ligand interacting with a protein may also change. Therefore, the average resonance frequency and the chemical shift difference ($\Delta\nu_{IS}$) of the two spins involved in a LLS can differ between L^{free} and L^{bound}. As the sustaining field has to be applied on resonance and with intensity at least 5 times larger than $\Delta\nu_{IS}$, the bound ligand may experience a less efficient sustaining. All these mechanisms added together, this implies that $T_{LLS}^{bound} << T_{LLS}^{free}$. Moreover, as T_{LLS}^{free} is long compared to T_1^{free}, this implies that, compared to other methods, the difference between the free and bound values of T_{LLS} is large. Therefore, LLS constitutes a good choice for an NMR parameter to be studied in view of the determination of K_D.

The measurement of K_D with the LLS technique is limited to weak ligands that carry two inequivalent protons that are relatively isolated from other spins and that represent a source of external dipole-dipole interactions. Nevertheless, as will be shown below, it is easily possible to overcome these two limitations. A ligand can be functionalised with an "LLS tag" and one can use competition methods to study strong binders. To measure K_D, a weak ligand is titrated into a solution containing a fixed concentration of protein. At each concentration, T_{LLS} is measured with the pulse sequence shown in Figure 5.2. With $\xi = R_{LLS} = 1/T_{LLS}$ Equation 5.4 becomes:

$$R_{LLS}^{obs} = \frac{[P]_0}{K_D + [L]_0}\left(R_{LLS}^{bound} - R_{LLS}^{free}\right) + R_{LLS}^{free} \qquad (5.7)$$

The urokinase-type plasminogen activator (uPa), a protein of the trypsin family, was chosen as a target for a test of the LLS method to determine K_D. The first step consists in finding a weak ligand of uPa with two isolated inequivalent protons, where an LLS could be excited. It was shown by phage display (30) using a peptide library and consensus sequence analysis that peptides which bind to uPA must contain at least one arginine residue. As glycine residues in peptides contain two diastereotopic H^{α} protons, it is straightforward to excite LLS in virtually any glycine containing peptide (31). We therefore considered the tripeptide Gly-Gly-Arg (GGR) as a weak ligand for uPa.

In the free ligand *L* = GGR, the lifetime T_{LLS} of the two H^{α} protons in the central glycine was determined to be T_{LLS}^{free} = 8.0 ± 0.2 s at 8 °C and 400 MHz. The ligand was then titrated over a range 0.5 < $[L]_0$ < 10 mM in the presence of $[P]_0$ = 10 µM uPA at 8 °C. The curve in Figure 5.3a was fitted to Equation 5.7, yielding K_D^{weak} = 220 ± 10 µM and T_{LLS}^{bound} = 30 ± 10 ms (as expected T_{LLS}^{bound} << T_{LLS}^{free}). By contrast, as shown in Figure 5.3a, binding has virtually no effect on the longitudinal (spin-lattice) relaxation times T_1 of the same H^{α} protons.

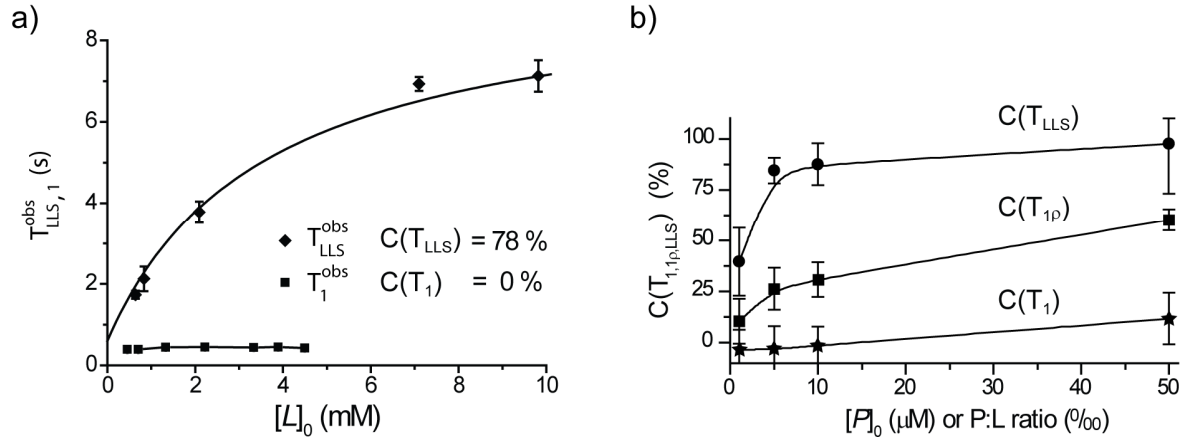

Figure 5.3: **a)** Lifetimes T_{LLS} of Long-Lived States associated with the two H^{α} protons of the central glycine residue of the weak ligand *L* = Glycine-Glycine-Arginine (GGR) and their conventional longitudinal relaxation times T_1 in the presence of $[P]_0$ = 10 µM of the protein uPA, as a function of $[L]_0$ at 8°C and 400 MHz in D_2O. The curve shows a fit of the experimental data to Equation 5.7. **b)** Contrast of life-times T_{LLS}, T_1 and $T_{1\rho}$ of ligands binding to proteins. The experimental contrast $C(T_{LLS})$, $C(T_1)$ and $C(T_{1\rho})$ for T_{LLS} (dots), non-selective $T_{1\rho}$ (squares) and non-selective T_1 (stars) for a solution with a fixed concentration [*L*] = 1 mM of the tripeptide ligand Gly-Gly-Arg (GGR) and a variable trypsin concentration 0.5 µM < $[P]_0$ < 50 µM in D_2O at 8 °C at 11.7 T (500 MHz for protons).

Enhanced contrast of LLS

Following Equation 5.5 and Figure 5.1b, one can define for each parameter ξ a dimensionless parameter to express its contrast for a given $[P]_0/[L]_0$ ratio:

$$C_{\xi} = \left| \frac{\xi_{free} - \xi_{obs}}{\xi_{free} + \xi_{obs}} \right| \tag{5.8}$$

A high contrast implies that a small fraction X^{bound} can be detected by the method*, i.e.,* that the NMR parameter ξ is sensitive to ligand-protein binding. To demonstrate the enhancement of the contrast $C(T_{LLS})$, with respect to the contrast $C(T_1)$ and $C(T_{1\rho})$, binding experiments were carried out for a 1 mM solution of the tripeptide ligand Glycine-Glycine-Arginine (GGR) in the presence of its target protein trypsin in the range 0.5 < [*P*] < 50 µM, using different methods (T_{LLS}, non-selective T_1 and non-selective $T_{1\rho}$). Figure 5.3b shows that the LLS method can work with a protein-ligand ratio that is about 25 times lower than required for the well-known selective $T_{1\rho}$ method, whereas the non-selective T_1 contrast remains below $C(T_1)$ < 10 % even at the highest protein concentration [*P*] = 50 µM.

Spin-pair labelling

A drawback of screening by LLS is that the ligands must carry a pair of non-equivalent spins-½. We therefore developed a synthetic labelling strategy comprising two steps: (i) the identification of a 'spy ligand' that binds weakly to its target protein, and (ii) the functionalization of this ligand by attaching a 'spin-pair label' that can carry LLS. By way of illustration, 3-bromothiophene-2-carboxylic acid ('BT'), which is known to have long lifetimes T_{LLS} (21, 32), was covalently attached to the tripeptide GGR. The resulting spin-pair labelled tripeptide will henceforth be called BT-GGR. The details about the synthesis of BT-GGR can be found in the supplementary material of Reference (3).

Despite some steric effects and long-range dipolar relaxation mechanisms in the spin-pair labelled tripeptide BT-GGR, the two aromatic protons of the bromothiophene group retain a remarkably long lifetime $T_{LLS}^{free}(BT) = 11.7 \pm 0.7$ s. In this particular peptide, the diastereotopic pairs of the α-protons of the two glycine residues of BT-G_1G_2R can also be used to excite LLS, and have lifetimes $T_{LLS}^{free}(G_1) = 10.4 \pm 0.5$ s and $T_{LLS}^{free}(G_2) = 9.3 \pm 0.5$ s. (see Figure 5.4a).

The spin-pair labelled spy ligand L = BT-GGR was added to a solution of $[P]_0 = 25$ µM trypsin over a range $0.5 < [L]_0 < 40$ mM. At each concentration $[L]_0$, the observed relaxation times $T_{LLS}^{obs} = 1/R_{LLS}^{obs}$ of three different pairs of protons (belonging to the bromothiophene group and to the middle and terminal glycines) were measured using the pulse sequence of Figure 5.2. Figure 5.4b shows how the titration curves can be fitted to Equation 5.7. As expected, nearly the same dissociation constants were obtained for the three proton pairs that can sustain LLS in BT-GGR: $K_D(BT) = 0.18 \pm 0.03$ mM, $K_D(G_1) = 0.24 \pm 0.01$ mM, $K_D(G_2) = 0.21 \pm 0.02$ mM. Moreover, the fact that K_D(BT-GGR) is close to K_D(GGR) shows that the spin-pair label does not interfere with the binding. The LLS fitted lifetime of G_2 (*i.e.*, the glycine closest to the arginine) in the bound form ($T_{LLS}^{bound}(G_2) = 16 \pm 1$ ms) is shorter than for the two other LLS sites ($T_{LLS}^{bound}(BT) = 90 \pm 20$ ms, $T_{LLS}^{bound}(G_1) = 110 \pm 40$ ms). This shorter T_{LLS}^{bound} is believed to be due to the fact that the arginine R, and thus also the glycine G_2, enter more deeply into the active site of trypsin.

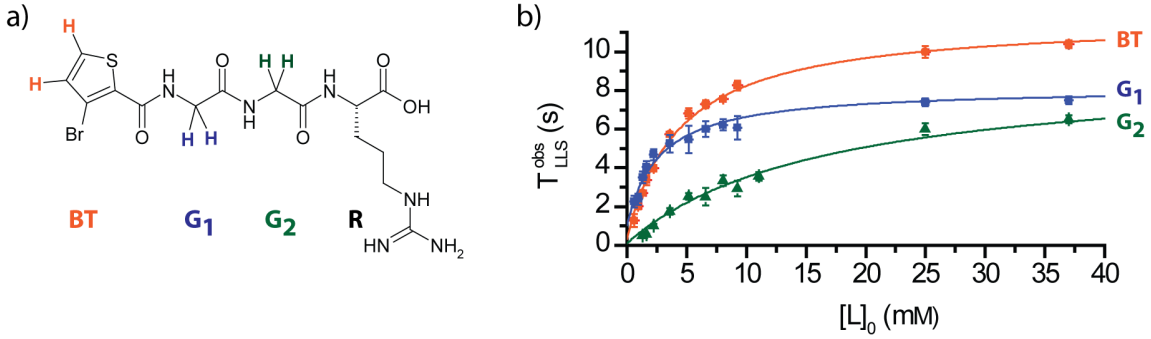

Figure 5.4: **a)** Pairs of protons capable of sustaining LLS in BT-GGR: on bromothiophene BT (orange), on the N-terminal glycine G_1 (blue) and on central glycine G_2 (green), the latter being close to the arginine residue that binds to the protein. **b**) Observed LLS lifetimes of the three proton pairs on the spin-pair labeled tripeptide BT-GGR as a function of the ligand concentration, in the presence of 25 µM trypsin in D_2O at 25 °C and 11.7 T (500 MHz for protons).

The covalent attachment of 'spin-pair labels' such as bromothiophene (BT) permits one to broaden the scope of the LLS screening method to virtually any weak ligand in the fast exchange regime. By way of example, bromothiophene carboxylic acid was attached to the N-terminus of a tripeptide, but other 'spin-pair labels' could be designed. Spy ligands with higher sensitivity to binding could be engineered

with the following features: (i) spy ligands with enhanced T_{LLS}^{free}, (ii) LLS functionalizing groups that are closer to the binding site, (iii) the use of nearly equivalent spins (33). Our labels are far less bulky than chromophores used in fluorescence experiments, and should not induce significant steric impediments to binding.

Competition binding experiments

Once a weak ligand has been identified and characterized by titration, it can be used as a "spy ligand" in competition experiments (34). When a stronger competitor blocks the active site of the protein, the weak spy ligand will no longer have free access to its target (Figure 5.5a). The concentration $[P]_{free}$ of the protein that remains free to bind the weak ligand can be derived from the definition of the dissociation constant K_D^{strong} of the stronger competitor. Here, the approximation that the binding sites are saturated by ligands cannot be made since $[L^{strong}]_0 \approx [P]_0$ (See the supplementary material of Reference (1)):

$$[P]_{free} = [P]_0 - \frac{b - \sqrt{b^2 - 4[P]_0[L^{strong}]_0}}{2} \tag{5.9}$$

where $b = ([P]_0 + [L^{strong}]_0 + K_D^{strong})$ and $[L^{strong}]_0$ is the total concentration of the competitor. To describe the relaxation rate R_{LLS}^{obs} of the weak spy ligand in competition experiments, $[P]_0$ in Equation 5.7 must be replaced by $[P]_{free}$ of Equation 5.9. As the amount of free available protein decreases, the effects of the protein on the lifetime T_{LLS}^{obs} of the weak spy ligand will be less pronounced (See Figure 5.5a).

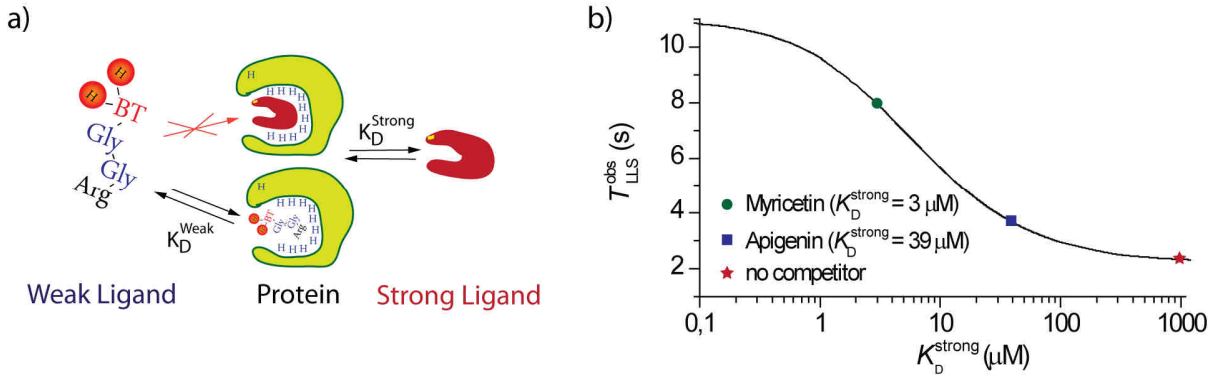

Figure 5.5: **a)** Schematic view of competition experiments. **b)** Influence of a competitor on the LLS lifetime of a weak ligand. LLS lifetimes T_{LLS}^{obs} of the pair of aromatic protons of the bromothiophene spin-pair label BT as a function of the dissociation constant of a competing stronger ligand, calculated using Equation 5.7 and 5.9. The parameters of the weak ligand BT-GGR were obtained from the fit of the data in Figure 5.5b: K_D = 0.2 mM, T_{LLS}^{bound} = 0.1 s, T_{LLS}^{free} = 11 s, $[L]_0$ = 0.5 mM, $[P]_0$ = 25 µM and $[L^s]_0$ = 50 µM. The three points correspond to T_{LLS}^{obs} in the presence of myricetin (K_D^{strong}= 3 µM, dots), apigenin (K_D^{strong} = 39 µM, squares) and in the absence of any competitor (stars) calculated for these conditions.

When stronger ligands are added, the lifetime T_{LLS}^{obs} of the spy ligand gives information about the dissociation constant K_D^{strong} of the competitor. Note that the competitors do not need to contain any spin pairs that can sustain an LLS. Moreover, as the changes in T_{LLS}^{obs} need only be observed for the weak ligand, there are no requirements for the stronger ligands to fulfil the fast-exchange condition. As the strong competitors themselves do not need to be observed directly, their concentration can also be

lowered, typically to the same level as the concentration of the protein, *i.e.* to $[L]_0 \approx [P]_0$, which may typically be in the range of a few µM.

Once the dissociation constant K_D^{weak} of the weak spy ligand and its LLS lifetime in the bound form T_{LLS}^{bound} are known, it is possible to optimize $[L^{strong}]_0$ and $[P]_0$ to rank strong competitors L^{strong} according to their binding strengths. Figure 5.5b shows the calculated T_{LLS}^{obs}(BT) of the bromothiophene protons in BT-GGR if $[P]_0$ = 25 µM and $[L^{strong}]_0$ = 50 µM as function of K_D^{strong}. Under these conditions, T_{LLS}^{obs} changes dramatically between K_D^{strong} = 100 and 0.1 µM. If K_D^{strong} < 0.1 µM, one can detect a large effect on the lifetime T_{LLS}^{obs} of the weak spy ligand, but it is not possible to rank the ligands according to their affinities.

A library of competing ligands can be ranked according to their affinities by observing the LLS signal of the weak spy ligand. Under the conditions shown in Figure 5.5b, one can easily rank competing ligands with great accuracy provided 1 µM < K_D^{strong} <100 µM. Note that the LLS sequence of Figure 5.2 can be used with a single sustaining delay τ_{LLS}. This strategy is compatible with dissolution DNP, as it will be discussed in section 5.2 As T_{LLS}^{obs} of the weak spy ligand is longer in the presence of a stronger competitor, the LLS signal intensity of the spy ligand after a suitably chosen delay τ_{LLS} will be higher. LLS spectra with τ_{LLS} = 3 s were recorded with 0.5 mM BT-GGR, in the presence of $[P]_0$ = 25 µM trypsin with four different competitors, all with $[L^{strong}]_0$ = 50 µM: myricetin (K_D^{strong} = 3 µM), morin (K_D^{strong} = 30 µM), apigenin (K_D^{strong} = 39 µM) (35) and benzamidine (K_D^{strong} = 39 µM) (36). Figure 5.6a shows three of the five LLS spectra, obtained either without competitor, with apigenin, or with myricetin. Figure 5.6b shows the signal intensities of the weak spy ligand BT-GGR in the presence of one of the four competing ligands.

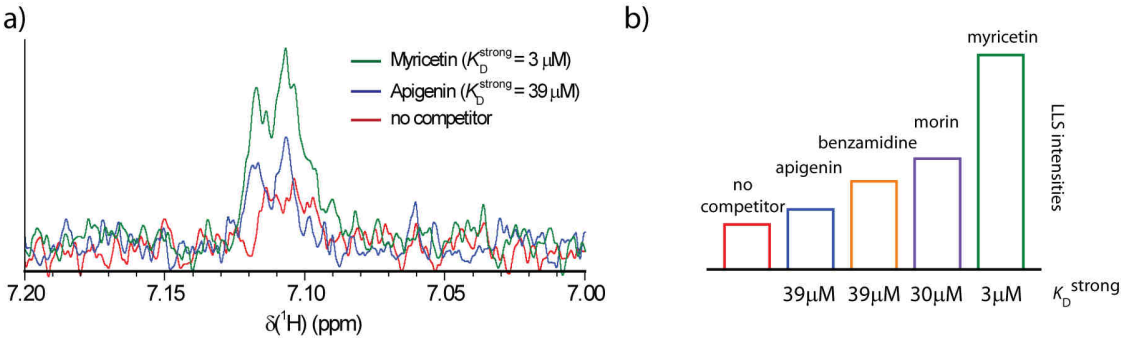

Figure 5.6: **a)** Signals of one of the two aromatic protons of bromothiophene of 0.5 mM of the weak spy ligand BT-GGR in the presence of 25 µM trypsin, using the LLS sequence of Figure 5.2 with a sustaining time τ_{LLS} = 3 s in D_2O at 25 °C and 11.7 T (500 MHz for protons.) (i) In the absence of any competitor (red), (ii) in competition with 50 µM of the intermediate ligand apigenin (blue), and (iii) in competition with 50 µM of the of the stronger ligand myricetin (green). **b)** Peak intensities of one of the aromatic protons of BT-GGR under the same conditions as in **a**, without competitor or in the presence of apigenin, benzamidine, morin or myricetin. The better the binding, the smaller the dissociation constant, and the more intense the LLS signal of the displaced spin-pair labeled spy ligand BT-GGR.

Compared to other NMR screening methods, the LLS method thus offers much improved contrast. For the same ligand concentration (*i.e.,* for the same experimental time), the protein concentrations can be greatly reduced, giving access to poorly soluble protein targets and decreasing the risk of aggregation. When used in competition mode, the LLS method allows one to rank high-affinity ligands using simple 1D experiments.

5.2 Adaptations of LLS protein-ligand experiment to be DNP-compatible

It is clearly desirable to use low concentrations of both proteins and ligands, not only to save expensive materials, but also to avoid protein aggregation and problems with mixtures ('cocktails') in the manner of combinatorial chemistry. The drive towards low ligand concentrations is generally limited by poor sensitivity of NMR. At concentrations [*L*] < 100 µM, NMR spectra with sufficient signal-to-noise ratios require extensive signal averaging. Hyperpolarization of nuclear spins by Dissolution Dynamic Nuclear Polarization (D-DNP) can overcome this problem. The technique has not been very popular for ^{1}H and ^{19}F nuclei so far, because fast T_1 relaxation tends to cause losses of polarization during the transfer from the polarizer to the spectrometer. Enhancements ε_{DNP} up to four orders of magnitudes can be obtained for nuclei with low gyromagnetic ratios, while enhancements $100 < \varepsilon_{DNP} < 1000$ can be achieved for ^{1}H or ^{19}F nuclei (37).

5.2.1 DNP requirements

DNP of protons

Proton hyperpolarization is very suitable for drug screening. Indeed, in comparison to the more conventional D-DNP of ^{13}C, ^{1}H DNP has many unique advantages that make it suitable for such studies. First of all, the fact that no labelling is required is an advantage for the versatility of the method. The requirement of a labelling step that may possibly be challenging from a chemical point of view in the design of the weak spy ligand could make this labelling extremely fastidious, if not impossible. Moreover, as shown in Chapter 2, if a paramagnetic source with a broad ESR line is used, protons can polarize to very high values, especially at high field. Even more importantly, protons polarize with fast build-up time constants, compared to other nuclei. As shown in Section 2.5, $\tau_{DNP}(^{1}H)$ = 70 s at 3.35 T and 1.2 K and $\tau_{DNP}(^{1}H)$ = 150 s at 6.7 T and 1.2 K. This give an essential advantage in the context of drug screening. To be able to test an extensive library of possible competitors, a fast repetition rate is highly desirable.

Nevertheless, ^{1}H D-DNP has a critical disadvantage, compared to ^{13}C DNP. Proton hyperpolarization relaxes back to Boltzmann equilibrium with a short time constant once the DNP sample is dissolved and during the transfer from the polarizer to the detection spectrometer. The development of special strategies is needed to overcome this drawback. The most obvious strategy consists in reducing the transfer time. Bowen and *al.* designed a transfer line where the time that elapses between the dissolution and the first NMR pulse is reduced to 1.2 s (38). The paramagnetic centres needed to polarize the nuclei during the DNP process have a dramatic effect on the relaxation times of these nuclei once dissolved at room temperature, especially at low field. This paramagnetic relaxation can be attenuated by using a magnetic tunnel (39) that protects the transfer line from low field regions by sustaining a field of *ca.* 0.9 T. The radicals can also be quenched by vitamin C (40), or removed from the dissolved solution by precipitation and filtration (See Chapter 7). Finally, the design of molecules with long $T_1(^{1}H)$ is also a good strategy. Of course, all of these solutions can be combined together.

In this context, an LLS-functionalized weak ligand designed as a probe for drug screening can be a good candidate for ^{1}H Dissolution-DNP. Indeed, as the LLS method requires a spin-pair with two isolated protons, they will have a relatively long T_1. Therefore no additional effort is needed to design a ligand that is suitable for D-DNP and to couple drug screening by LLS with hyperpolarization. An alternative strategy, consisting in populating the LLS directly in the polarizer, will be developed in the Section 5.3.2 at the end of this Chapter.

One shot experiments

In order to couple an existing NMR method with Dissolution-DNP, an additional effort is required from the experimentalist. Indeed, as the hyperpolarized magnetization returns to Boltzmann equilibrium, the pulse sequence needs to be adapted to extract the desired information in a single shot. For drug studies by LLS, $[L]_0$ titrations and incrementations of the sustaining time cannot be done. A strategy could consist in detecting a single LLS spectrum of the hyperpolarized weak ligand after a fixed sustaining τ_{LLS} (Figure 5.7). As will be described below, the presence of a strong ligand that interacts with the protein of interest will modify the intensity of the spectrum of the weak ligand. An alternative new sequence that allows the precise measurement of T_{LLS}^{obs} in one shot will also be proposed in Section 5.3.1. Another more challenging example of the adaptation of an existing NMR sequence to D-DNP, called Water-LOGSY in this context, will be developed in Chapter 6.

5.2.2 DNP LLS experiment

Figure 5.7 describes the steps of a DNP LLS experiment that can be used to detect and rank potential strong ligands. The sample loaded in the polarizer will contain only the weak spy ligand in a glass-forming matrix with a paramagnetic species as polarizing agent (e.g., 50 mM TEMPOL). The concentration of the ligand should be chosen with respect to the desired final concentration in the detection spectrometer to compensate for the dilution in the dissolution step (typically by a factor 25-200). Since typical final concentrations $[L]_0$ are in the 10-100 µM range, the DNP sample preparation is facilitated by relatively low analyte concentrations (in the mM range).

Once the proton polarization has reached the desired level, the sample is dissolved and transferred as fast as possible to the detection spectrometer. It is then injected, depending on the objective, **(i)** into a solution of D_2O, **(ii)** into a solution of protein at low concentration (µM range), or **(iii)** into a solution of protein in presence of a potential strong ligand, or a cocktail of ligands to be tested, also in the µM range.

The LLS are excited on the hyperpolarized weak ligand with the sequence shown in Figure 5.7. They are sustained for a fixed delay τ_{LLS}. As will be explained below, this delay can be adjusted as a function of the range of K_D^{strong} that we want to investigate. Then the LLS are converted back to observable magnetization and the remaining signal of the hyperpolarized weak ligand is inspected. The intensity of this signal will be the gauge of the binding strength of the strong ligand(s) present in the solution.

Depending on the conditions, the LLS lifetime of the weak ligand (T_{LLS}^{obs}) will be different, and therefore the signal after the fixed sustaining delay τ_{LLS} will reflect this change, as can be seen in Figure 5.7. The two limits for T_{LLS}^{obs} are determined by experiments **(i)** and **(iii)** (see also Figure 5.5b). If the weak ligand is totally free, it has a long LLS lifetime $T_{LLS}^{obs} = T_{LLS}^{free}$, which translates into an intense signal after the sustaining time τ_{LLS}. On the contrary, if the hyperpolarized weak ligand is injected to a solution containing only its protein target, it will have a short T_{LLS}^{obs}, and thus only a weak magnetization will survive after the LLS experiment. These two limits only have to be tested once for a set of measurements concerning an arbitrary number of potential strong ligands, regardless whether they are mixed as 'cocktails' or as separate solutions.

The characterization of potential strong ligands can then be done with experiments of type **(ii)**. Here, the hyperpolarized weak spy ligand is injected to a solution containing a mixture of the target protein and one or several potential strong ligands. The concentration of L^{strong} is typically the same as $[P]_0$ (in the µM

range), but it can be adapted as a function of the range of K_D^{strong} that one wishes to target. As described in the previous section, if the tested competitor has a strong affinity for the protein, it will block its binding site, and therefore the remaining concentration of free protein that is able to contribute to the relaxation of the LLS of the weak hyperpolarized ligand ($[P]_{free}$ in Equation 5.9) will decrease. With increasing strength of the competitor, T_{LLS}^{obs} of the spy ligand will increase (see Figure 5.5b). The remaining LLS signal of the weak ligand after the sustaining delay τ_{LLS} will thus increase as K_D^{strong} becomes stronger (see Figure 5.7). Therefore, a simple inspection of the LLS spectrum of the hyperpolarized spy ligand permits one to "read out" the strength of the competitor(s) present in the sample in low µM concentrations.

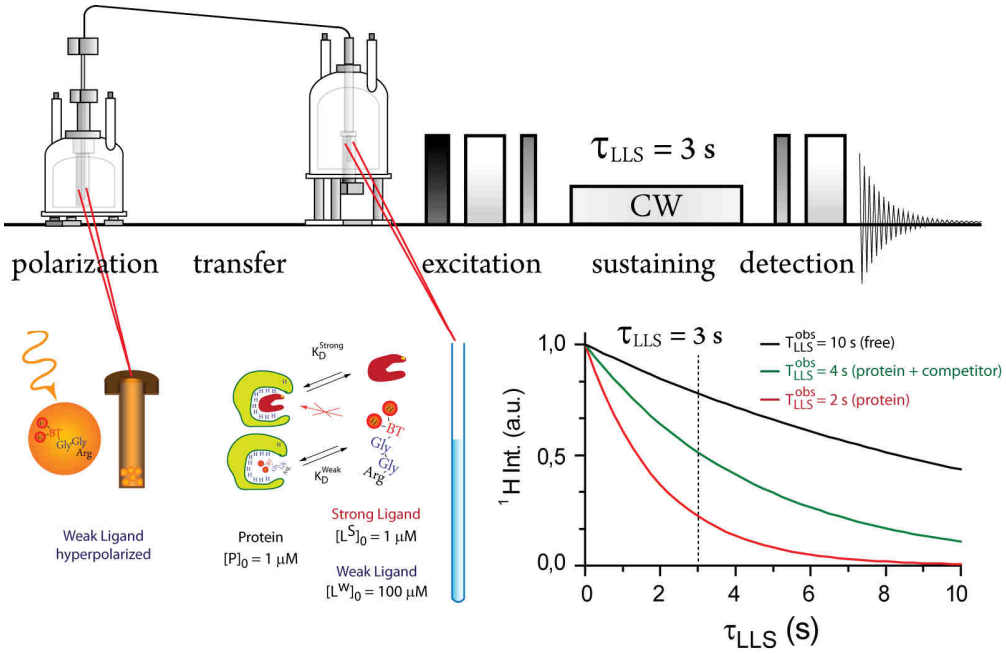

Figure 5.7: Schematic representation of a DNP-LLS experiment. The sustaining delay is fixed to τ_{LLS} = 3 s. The LLS signal intensity varies as a function of τ_{LLS} if T_{LLS}^{obs} = 10 s (solution **(i)**, free ligand, black), T_{LLS}^{obs} = 4 s (solution **(ii)**, protein + competitor, green), T_{LLS}^{obs} = 2 s (solution **(iii)**, only protein, red), see insert of Figure 5.8.

10 mM BT-GGR was dissolved with 25 mM TEMPOL in a glass-forming solvent mixture H_2O:D_2O:DMSO-d_6 (v:v:v = 5:35:60). Five frozen beads (50 µL) of this solution were loaded together with five frozen beads (50 µL) of 3 M ascorbate (40) into a home-built DNP polarizer (41, 42) operating at B_0 = 6.7 T and T = 1.2 K. The sample was irradiated with monochromatic microwaves at a frequency $f_{\mu W}$ = 188.3 GHz and power $P_{\mu W}$ = 100 mW. After about 15 minutes of microwave irradiation, a steady-state proton polarization $P(^1H)$ is reached. The DNP sample can be rapidly dissolved in 0.7 s with 5 mL of hot D_2O (P = 1 MPa, T = 400 K) and transferred to a 11.7 T NMR spectrometer in 4.5 s trough a 'magnetic tunnel' (39) so that B_0 > 0.8 T during transfer, which is particularly important to preserve the polarization of ^1H and ^{19}F nuclei (38). A fraction of 400 µL of the hyperpolarized solution is then injected in *ca*. 2 s into a 5 mm NMR tube containing 250 µL D_2O and, depending on the conditions, 3.65 µM trypsin and 3.65 µM of a competitor such as myricetin. After injection, the final solution has a concentration of 1.4 µM protein, 1.4 µM competitor, and 120 µM hyperpolarized spy ligand BT-GGR. After a 3 s interval to allow for proper mixing, a reference free induction decay is observed in 0.5 s after exciting transverse magnetization with a single 5° pulse to control the quality on the hyperpolarized sample and to normalize the signal intensity

of the spy ligand with respect to its known concentration. This is immediately followed by an LLS sequence as described in Figure 5.7 with a fixed sustaining time τ_{LLS} = 3 s.

The DNP enhancements of the aromatic protons of the spin-pair-labelled spy ligand BT-GGR were on the order of ε_{DNP} = 100 – 200, compared to the Boltzmann equilibrium at 25 °C and 11.7 T (500 MHz for protons). A significant fraction of the proton hyperpolarization was lost during the 10 s interval between dissolution and signal acquisition. A faster sample injection device (38) could reduce the interval to 1.2 s.

Figure 5.8b shows DNP enhanced LLS spectra of (i) 120 µM of the spin-pair-labeled spy ligand BT-GGR in the absence of protein (in black), (ii) the same upon addition of 1.4 µM trypsin (in red), and (iii) the same after further addition of 1.4 µM myricetin as strong competitor (in green).

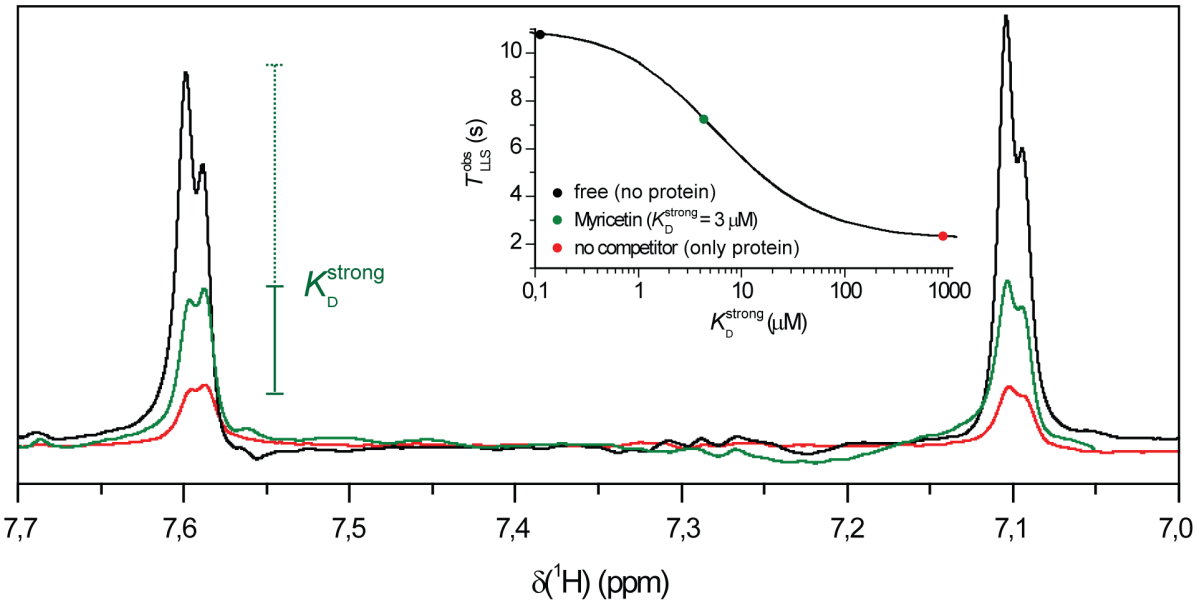

Figure 5.8: DNP enhanced LLS spectra of the two aromatic protons of bromothiophene in 120 µM BT-GGR after a sustaining time τ_{LLS} = 3 s, (i) without protein (black), (ii) in the presence of 1.4 µM trypsin (red), (iii) with 1.4 µM trypsin and 1.4 µM myricetin as strong competitor (green). All spectra were acquired in a single scan in D_2O, at 25 °C and 11.7 T (500 MHz for protons). (**Insert**): Influence of the K_D^{strong} of a competitor on the LLS lifetime of a weak ligand: LLS lifetimes T_{LLS}^{obs} of the pair of aromatic protons of the bromothiophene spin-pair label as a function of the dissociation constant K_D^{strong} of a competing stronger ligand, calculated using Equation 5.7 and 5.9. The parameters of the weak ligand BT-GGR were obtained from the fit of the data in Figure 5.5b: K_D = 0.2 mM, T_{LLS}^{bound} = 0.1 s, T_{LLS}^{free} = 11 s, $[L]_0$ = 0.5 mM, $[P]_0$ = 25 µM and $[L^{strong}]_0$ = 50 µM. The three points correspond to T_{LLS}^{obs} in the absence of protein (black dot), with protein in the absence of any competitor (red dot), and with protein in the presence of myricetin (K_D^{strong}= 3 µM, green dot), calculated for these conditions.

A dramatic decrease of the LLS signal intensity stemming from BT-GGR is observed upon adding trypsin. The contrast defined in Equation 5.8 is $C(T_{LLS})$ = 75 %. Addition of an equimolar amount of the strong competitor myricetin leads to a partial displacement of the spy ligand that can be readily detected by the revival of its LLS signal. Indeed, as shown in the insert of Figure 5.8, T_{LLS}^{obs} of the weak ligand, and thus the signal after the fixed sustaining delay, depends on K_D^{strong} of the competitor (Equation 5.7 and 5.9).

With only 120 µM of the spin-pair-labelled spy ligand BT-GGR, the DNP-enhanced LLS spectrum of Figure 5.8 recorded in a single scan after τ_m = 3 s has a signal-to-noise ratio SNR = 130. Under the same

conditions, but without DNP, an accumulation of 225 transients for about 1 h was necessary in order to reach the same SNR. A DNP-enhanced LLS spectrum of BT-GGR with a concentration as low as 10 µM could be recorded with an SNR = 16. Clearly, DNP allows one to reduce the concentration of ligands, but the protein concentration should not be further decreased. In fact, according to Equation 5.7, the contrast C_{LLS} would decrease if the limit $K_D + [L_0] \approx K_D$ were to be reached. Without DNP, using a 50-fold increase in the ligand concentration (Figure 5.6a), 256 transients had to be accumulated in 100 min to obtain a SNR = 8.

The experimental conditions can be adapted to the primary objective: low concentrations of either protein or ligand, fast throughput, high sensitivity for the displacement by a competitor or high SNR. In Figure 5.8, the conditions were optimized for high SNR and high contrast upon addition of a competitor, albeit at the expense of a slightly higher ligand concentration and longer polarization build-up time. To have a faster throughput, one could polarize at T = 4.2 K and B_0 = 6.7 T, where a proton polarization $P(^1H)$ = 25 % can be reached by DNP in about 2 min (42). The price to pay would be a ~ 3 times lower SNR. Similarly, at T = 1.2 K and B_0 = 3.35 T, like in commercially available DNP polarizers, $P(^1H)$ = 40 % can be reached in about 6 min (43) (See Figure 2.25 of Chapter 2).

5.3 To go further

5.3.1 Single-shot detection sequences

Instead of merely measuring the intensity of the NMR peak after a fixed sustaining delay as in Figure 5.8 , the determination of T_{LLS}^{obs} should give more reliable and precise information about the strength of the binding of a strong competitor. The standard way of measuring LLS relaxation time constants has to be adapted to be compatible with Dissolution-DNP. Indeed, it is not possible to do n complete LLS experiments as in Figure 5.2 with increased sustaining times. One has to get the information in a single shot. The idea is to excite LLS as usual, and to convert only small fractions f of the LLS into observable magnetization at regular intervals, while preserving the largest fraction (1-f).

An additional difficulty must be overcome. Once the sustaining field is interrupted (point b in Figure 5.9), the magnetization is not directly observable and the LLS has to be converted into single quantum coherences by a suitable pulse sequence. This pulse sequence must preserve the unobserved fraction (1-f) and must re-inject it as an LLS precursor for the next sustaining loop (points g or a in Figure 5.9).

In the next section, the sequence developed for this purpose in collaboration with Maninder Singh will be described step by step, using the product operator formalism (44-46). It can be followed in parallel with Figures 5.9 and 5.10.

LLS excitation and sustaining

(a-b): The LLS precursor state $\sigma(a) = 2I_zS_z + ZQ_x$ is excited with the "Sarkar sequence" (while DQ_x is suppressed by a pulsed field gradient) which corresponds to $S_0 - ½(T_{+1} + T_{-1})$ in the singlet-triplet basis STB under CW irradiation (see Equation 8.4 for the basis conversion). During the sustaining of the LLS, the triplet states will equilibrate, hence (without considering LLS relaxation and normalization) $\sigma(b) = S_0 - ⅓(T_{+1} + T_0 + T_{-1})$ in STB under CW irradiation, which corresponds to $\sigma(b) = 2I_zS_z + 2ZQ_x$ in PB when irradiation is interrupted.

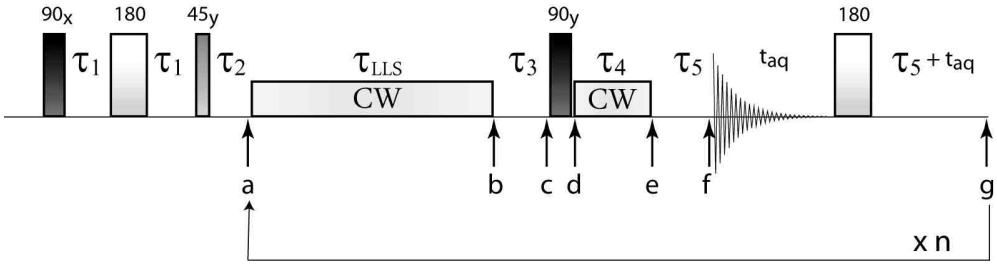

Figure 5.9: Single-shot LLS sequence. The conversion is most efficient if $\tau_1 = 1/4J_{IS}$ and $\tau_2 = 1/2\Delta\nu_{IS}$. An optional gradient can be added during τ_2 to eliminate double quantum coherence. The delay $\tau_3 = \arcsin(f)/(2\pi\Delta\nu_{IS})$ can be adjusted to convert a fraction *f* of the LLS into observable magnetization, and to preserve a fraction (1-*f*) that will be re-injected in the form of an LLS precursor in the next $(n+1)^{th}$ loop, provided $\tau_4 = 1/4J_{IS}$ and $\tau_5 = 1/2\Delta\nu_{IS}$. The evolution of the system described by the product operator formalism can be seen in Figure 5.10.

Partial conversion and detection of LLS

(b-c): To convert only a fraction of LLS into detectable magnetization, we first allow a fraction *f* of $2ZQ_x$ to evolve in τ_3 under the difference of chemical shifts $\Delta\nu_{IS}$ into $2ZQ_y$ (without affecting $2I_zS_z$). Hence $\sigma(c) = 2I_zS_z + 2ZQ_x \cos(2\pi\Delta\nu_{IS}\tau_3) + 2ZQ_y \sin(2\pi\Delta\nu_{IS}\tau_3)$, with $\tau_3 = \arcsin(f)/(2\pi\Delta\nu_{IS})$. The term *f* is the fraction of LLS converted in τ_3 into detectable magnetization (and later allowed to decay) at each point of the single-shot LLS sequence. The delay $\tau_3 = \arcsin(f)/(2\pi\Delta\nu_{IS})$ will thus permit to choose the fraction of the LLS that will be detected ($2ZQ_y$ part of σ(c), in green in Figure 5.10) and the fraction of the LLS that will be preserved and re-injected at the end of the loop ($2I_zS_z + 2ZQ_x$ part, in red in Figure 5.10).

(c-d): Detected part (green in Figure 5.10): a $(90°)_y$ pulse will convert $2ZQ_y = 2I_yS_x - 2I_xS_y$ into detectable single quantum magnetization $\sigma(d)_{det} = (-2I_yS_z + 2I_zS_y)$ where "*det*" stands for the detectable part of σ(d)
The preserved part is shown in red in Figure 5.10: the $(90°)_y$ pulse leaves $2I_zS_z + 2ZQ_x = 2I_zS_z + 2I_xS_x + 2I_yS_y$ unchanged if the fraction lost by conversion into detectable magnetization is not taken into account. $\sigma(d)_{pres} = 2I_xS_x + 2I_zS_z + 2I_yS_y = 2I_zS_z + 2ZQ_x$, where "*pres*" stand for preserved part of $\sigma(d) = \sigma(d)_{det} + \sigma(d)_{pres}$.

Conversion of $\sigma(d)_{det}$ into detectable in-phase magnetization compatible with fast acquisition

At this point, $\sigma(d)_{det}$ would lead to a spectrum with two antiphase doublets if a full FID were acquired. Such a signal acquisition has the advantage that is allows one to separate different species according to frequency, but it is time consuming (about 0.5 s). As we are only interested in the intensity of the peak of a single known weak ligand, a time saving sequence can be implemented. Provided that one uses a filter that selects the magnetization of the weak ligand, it is possible to record only a single point during detection. The detection can thus be shortened to 10-500 µs, albeit as the expense of SNR.
Nevertheless the form of $\sigma(d)_{det}$ is not compatible with fast detection; as only a single point is taken during detection, the antiphase magnetization will not contribute to the signal and averages to zero. It is therefore necessary to convert $\sigma(d)_{det}$ into in-phase magnetization, while preserving $\sigma(d)_{pres}$.

(d-e): Detection: The antiphase magnetization needs to be converted to in-phase magnetization. A τ-π-τ echo is possible. Nevertheless, it is better to let $\sigma(d)_{det} = 2I_zS_y - 2I_yS_z$ evolve via Long-Lived Coherences (LLC) (47, 48) into $\sigma(e)_{det} = I_x - S_x$ under CW irradiation, because the preserved part $\sigma(d)_{pres}$ will be stored in the form of LLS during this delay. The preserved part is $\sigma(e)_{pres} = \sigma(d)_{pres} = 2I_zS_z + 2ZQ_x$.

(e-g): The detected part $\sigma(e)_{det}$ = I_x - S_x evolves during $\tau_5 = 1/(2\Delta\nu_{IS})$ into I_y + S_y . This in-phase magnetization (both terms having the same sign) is detected during t_{aq} (t_{aq} = 10-500 µs) in a single point. The term $2I_zS_z$ of preserved part $\sigma(d)_{pres}$ does not evolve during τ_5 + aq, but the $2ZQ_x$ term does. This term is refocused by inserting a π pulse and a delay $\tau_6 = \tau_5 + t_{aq}$ to give again $\sigma(g)_{pres} = 2I_zS_z + 2ZQ_x$ which can be injected into the next sustaining loop and conserved as LLS during the next τ_{LLS}.

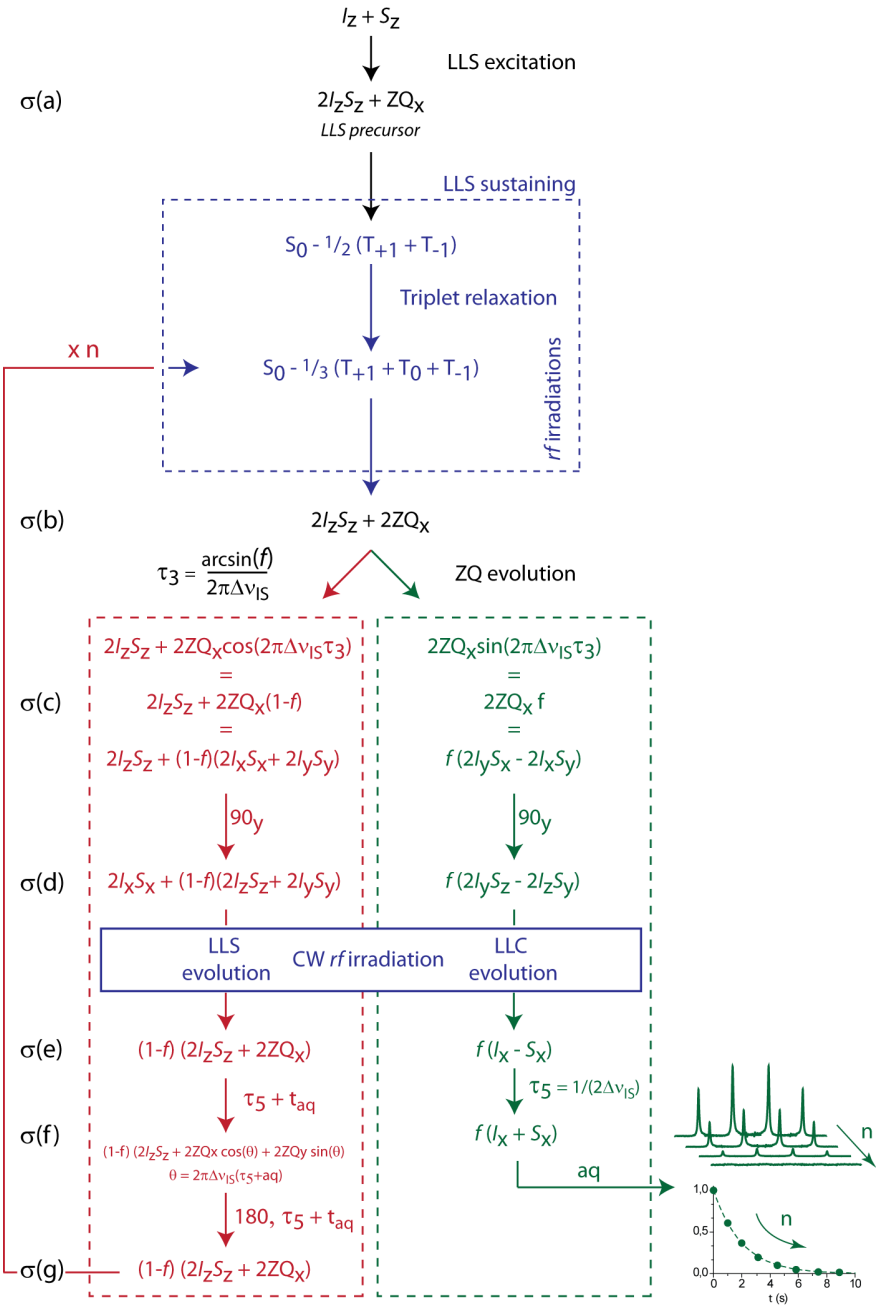

Figure 5.10: Evolution of the magnetization during the Single-Shot LLS sequence in Figure 5.9 described with the product operator formalism. In blue, the system is under resonant *rf* irradiation, which is best described in the singlet-triplet basis (STB). The parallel evolution of the LLS fraction *f* converted into observable magnetization is shown in green, while the evolution of the preserved part is shown in red.

Repetition of the loop for the next LLS point

The sequence starts again for the next LLS point with σ(b') = (1-f) ($2I_zS_z$ +$2ZQ_x$). The loop can be repeated *n* times with a fixed sustaining delay τ_{LLS}. The signal recorded as function of $t = n\tau_{LLS}$ can be fitted to a mono-exponential decay with an apparent relaxation time constant T_{LLS}^*. During each loop *n*, a fraction *f* of the magnetization is destroyed. A procedure must therefore be implemented to obtain T_{LLS} by correcting T_{LLS}^* as it will be developed below.

There is still work in progress for this project at the time of writing this Thesis. The sequence has only been implemented for "slow" acquisition, where a complete FID is recorded in 0.5 s. The fitting procedure has not yet been finalized and no test has been done using the pulse sequence coupled to D-DNP, let alone for experiments on ligands bound to proteins. Only preliminary results are presented below.

The sequence was tested on a 50 mM solution of 2,3-dibromothiophene (BT) in D_2O, with T_{LLS} = 23.4 ± 0.9 s measured with the standard sequence (Figure 5.2). A total of 8 data points, one every 10 seconds, were taken with the Single-Shot LLS sequence, while varying the fraction *f*. When *f* is decreased, a smaller fraction of the LLS magnetization is converted into observable magnetization, and the SNR is reduced. Depending on the fraction *f* of LLS that is converted at each point, the apparent lifetime (T_{LLS}^*) changes. The data recorded with the Single-Shot LLS sequence while incrementing the converted fraction *f* is shown in figure 5.11. As expected, a higher fraction *f* shortens the apparent lifetime T_{LLS}^*.

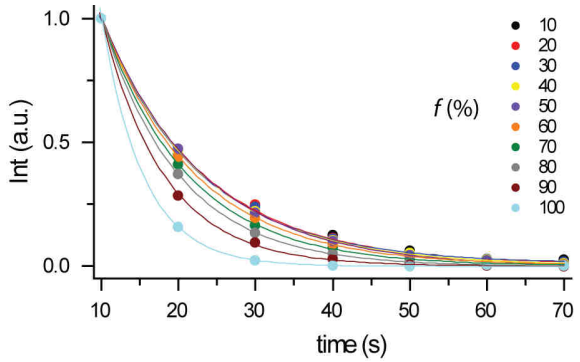

Figure 5.11: Signal intensities measured in a single shot with the sequence described in Figure 5.9 of 50 mM 2,3-bromothiophene (BT) in D_2O at *T* = 298 K and B_0 = 11.7 T (500 MHz for ^{1}H). The interval Δ*t* is set to 10 s and the fraction *f* of LLS converted to observable magnetization at each loop is varied between *f* = 10% and 100%, encoded by different colors.

If the increment τ_{LLS} of the total sustaining interval $n\tau_{LLS}$ is constant, if relaxation within the triplet manifold between points a and b in Figure 5.9 is assumed to be complete, so that σ(b) = $S_0 - \frac{1}{3}(T_{+1} + T_0 + T_{-1})$, and finally if one neglects relaxation during the brief detection intervals, one can describe the LLS decay and the intermittent puncture of the magnetization with:

$$I(t) = a\exp\left(-\frac{t}{T_{LLS}}\right)(1-f)^n \qquad (5.10)$$

Where n = (*t*-Δ*t*)/Δ*t* and Δ*t* = τ_{LLS} + τ_3 + τ_4 + 2(τ_5 + t_{aq}) in each loop. In reality, relaxation cannot be neglected during the acquisition sequence, and it is possible that relaxation within the triplet manifold is

not complete so that σ(b) ≠ S_0 – ⅓(T_{+1} + T_0 + T_{-1}). Therefore, the fraction of the LLS magnetization destroyed during each loop *n* is underestimated. Due to these approximations, *f* is not precisely known. This renders the extraction of the LLS relaxation time rather imprecise. Another strategy has thus to be deigned to correct T_{LLS}^* with the knowledge of the parameters *f* and Δ*t*.

Experimental calibration

Finally, a more straightforward and practically more useful strategy could simply consist in experimentally calibrating a correction factor to convert the apparent rate $R_{LLS}^* = 1/T_{LLS}^*$ into a rate $R_{LLS}^{corr} = 1/T_{LLS}^{corr}$ while taking into account the parameters *f* and Δ*t*, by systematically varying T_{LLS} of the weak ligand under investigation:

$$R_{LLS} = R_{LLS}^* + R_{LLS}^{corr}(f, \Delta t) \tag{5.11}$$

The calibration can be done for a given ligand/protein combination, prior to any hyperpolarized DNP study. T_{LLS} can be varied by incrementing the protein concentration $[P]_0$ or, to reduce expenses, by adding a paramagnetic species like TEMPOL to the solution. The "true" LLS lifetime should be measured by the normal sequence of Figure 5.2 and a correction table can be obtained, measuring T_{LLS}^* with the Single-Shot LLS sequence with variable *f* and Δ*t* for different $[P]_0$ or [TEMPOL] concentrations.

5.3.2 All the way to LLS

The spin-pair label of the weak spy ligand designed to probe protein-ligand interactions could also be used to preserve the hyperpolarized magnetization during the transfer between the polarizer and the detection spectrometer. As will be developed in more detail in Chapter 8, it is also possible to impose symmetry on a system with two magnetically inequivalent spins simply by lowering the main field B_0 (21, 23). If $\Delta\nu_{IS} < J_{IS}$, a triplet-singlet imbalance (TSI) characterized by a singlet order population P_{TSI} with a long lifetime can be isolated. Moreover, as shown by Tayler *et al.* (49), simply by hyperpolarizing a system with two magnetically inequivalent spins, a precursor state for Long-Lived States can be directly populated in the polarizer. As will be developed in Chapter 8, the singlet order population P_{TSI} is proportional to the square of the longitudinal polarization, P_Z achieved by DNP: $P_{TSI} = -P_Z^2/3$.

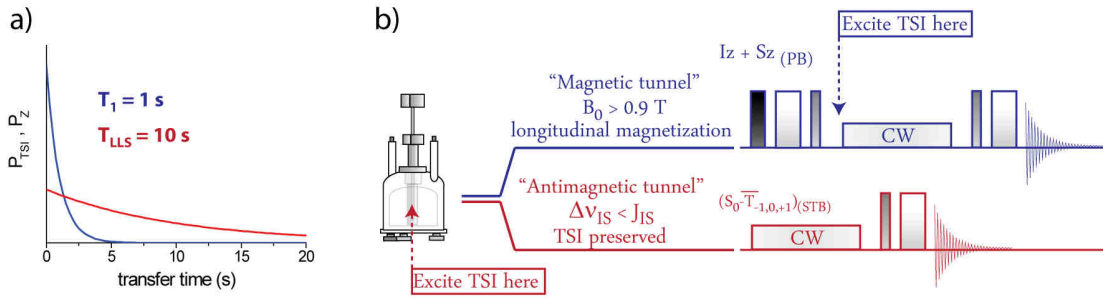

Figure 5.12: **a)** Relaxation of longitudinal (blue) and LLS (red) magnetization during transfer. **b)** DNP-LLS strategies. In red, LLS precursor is excited by DNP and preserved at low field during the transfer. After injection into the spectrometer, the *rf* irradiation starts immediately. The normal path used in this Chapter, where LLS are excited by a pulse sequence in the spectrometer after dissolution, is shown in blue.

Therefore, in the context of DNP-LLS drug screening, an alternative strategy could consist in (i) populate LLS precursor state of the spin-pair label of the weak spy directly by ^{1}H hyperpolarization. In our

conditions, at 6.7 T and 1.2 K, as $P_Z(^1H)$ can be as high as 91%, $P_{TSI} = -P_Z^2/3 = -27\%$ will be close to its theoretical maximum $P_{TSI} = -33\%$. (ii) Once dissolved, the sample is transferred through a low field, or possibly through an iron tube to shield the sample from external fields between the two magnets. At this point, the order will be preserved during the transfer in the form of an LLS. (iii) The sample is then injected into a solution of the target protein and possible competitors that is waiting in the spectrometer. There is no need to excite an LLS precursor state, since one can simple start the resonant *rf* irradiation to isolate the TSI. The detection is the same as for the normal LLS sequence.

Depending on T_1 and T_{LLS} of the spy ligand during the transfer and on the transfer time (see Figure 5.12a), one could choose between two different strategies, *i.e.,* two different points for the excitation of LLS. If T_1 is short, or if the transfer is slow, the LLS could be excited in the polarizer and preserved at low field (so that $\Delta\nu_{IS} < J_{IS}$) during the transfer (in red in Figure 5.12b). If T_1 is sufficiently long, or if the transfer is rapid, the normal path (blue in Figure 5.12b) should be preferred, since P_{TSI} is only proportional to $-P_Z^2/3$.

References

1. Salvi N, Buratto R, Bornet A, Ulzega S, Rentero Rebollo I, Angelini A, Heinis C, & Bodenhausen G (2012) Boosting the sensitivity of ligand-protein screening by NMR of long-lived states. *J. Am. Chem. Soc.* 134(27):11076-11079.
2. Buratto R, Mammoli D, Chiarparin E, Williams G, & Bodenhausen G (2014) Exploring weak ligand-protein interactions by long-lived NMR States: improved contrast in fragment-based drug screening. *Angew. Chem. Int. Ed.* 53(42):11376-11380.
3. Buratto R, Bornet A, Milani J, Mammoli D, Vuichoud B, Salvi N, Singh M, Laguerre A, Passemard S, Gerber-Lemaire S, Jannin S, & Bodenhausen G (2014) Drug screening boosted by hyperpolarized long-lived States in NMR. *ChemMedChem* 9(11):2509-2515.
4. Connors KA (1987) *Binding Constants: The Measurement of Molecular Complex Stability* (Wiley, New York).
5. Friguet B, Chaffotte AF, Djavadiohaniance L, & Goldberg ME (1985) Measurements of the true affinity constants in solution of antigen-antibody complexes by enzyme-linked immunosorbent-assay. *J. Immunol. Methods* 77(2):305-319.
6. Ladbury JE &Chowdhry BZ (1996) Sensing the heat: The application of isothermal titration calorimetry to thermodynamic studies of biomolecular interactions. *Chemistry & Biology* 3(10):791-801.
7. Schuck P (1997) Reliable determination of binding affinity and kinetics using surface plasmon resonance biosensors. *Curr. Opin. Biotechnol.* 8(4):498-502.
8. Pochapsky SS &Pochapsky TC (2001) Nuclear magnetic resonance as a tool in drug discovery, metabolism and disposition. *Curr. Top. Med. Chem.* 1(5):427-441.
9. Wyss DF, McCoy MA, & Senior MM (2002) NMR-based approaches for lead discovery. *Curr Opin Drug Di De* 5(4):630-647.
10. Carlomagno T (2005) Ligand-target interactions: What can we learn from NMR? *Annu. Rev. Biophys. Biomol. Struct.* 34:245-266.
11. Fielding L (2007) NMR methods for the determination of protein-ligand dissociation constants. *Prog. Nucl. Mag. Res. Sp.* 51(4):219-242.
12. Meyer B &Peters T (2003) NMR Spectroscopy techniques for screening and identifying ligand binding to protein receptors. *Angew. Chem.-Int. Edit.* 42(8):864-890.
13. Stockman BJ &Dalvit C (2002) NMR screening techniques in drug discovery and drug design. *Prog. Nucl. Mag. Res. Sp.* 41(3-4):187-231.

14. Ni F (1994) Recent Developments in Transferred Noe Methods. *Prog. Nucl. Magn. Reson. Spectrosc.* 26:517-606.
15. Mcconnell HM (1958) Reaction Rates by Nuclear Magnetic Resonance. *J. Chem. Phys.* 28(3):430-431.
16. Luz Z &Meiboom S (1964) Proton Relaxation in Dilute Solutions of Cobalt(2) + Nickel)2) Ions in Methanol + Rate of Methanol Exchange of Solvation Sphere. *J. Chem. Phys.* 40(9):2686-2692.
17. Fielding L (2003) NMR methods for the determination of protein-ligand dissociation constants. *Curr. Top. Med. Chem.* 3(1):39-53.
18. Levitt MH (2010) Singlet and other states with extended lifetimes. *Encyclopedia of Nuclear Magnetic Resonance*, ed RK Harris RWChichester, UK), Wiley Ed.
19. Levitt MH (2012) Singlet Nuclear Magnetic Resonance. *Annu. Rev. Phys. Chem.* 63:89-105.
20. Pileio G (2010) Relaxation theory of nuclear singlet states in two spin-1/2 systems. *Prog. Nucl. Magn. Reson. Spectrosc.* 56(3):217-231.
21. Carravetta M, Johannessen OG, & Levitt MH (2004) Beyond the T-1 limit: Singlet nuclear spin states in low magnetic fields. *Phys. Rev. Lett.* 92(15):153003.
22. Carravetta M &Levitt MH (2004) Long-lived nuclear spin states in high-field solution NMR. *J. Am. Chem. Soc.* 126(20):6228-6229.
23. Carravetta M &Levitt MH (2005) Theory of long-lived nuclear spin states in solution nuclear magnetic resonance. I. Singlet states in low magnetic field. *J. Chem. Phys.* 122(21).
24. Pileio G &Levitt MH (2009) Theory of long-lived nuclear spin states in solution nuclear magnetic resonance. II. Singlet spin locking. *J. Chem. Phys.* 130(21).
25. Abragam A (1961) *Principles of Nuclear Magnetism* (Oxford University Press).
26. Vasos PR, Sarkar R, & Bodenhausen G (2007) Singlet-state exchange NMR spectroscopy for the study of very slow dynamic processes. *J. Am. Chem. Soc.* 129(2):328-334.
27. Gopalakrishnan K &Bodenhausen G (2006) Lifetimes of the singlet-states under coherent off-resonance irradiation in NMR spectroscopy. *J. Magn. Reson.* 182(2):254-259.
28. Sarkar R, Ahuja P, Moskau D, Vasos PR, & Bodenhausen G (2007) Extending the scope of singlet-state spectroscopy. *Chem. Phys. Chem.* 8(18):2652-2656.
29. DeVience SJ, Walsworth RL, & Rosen MS (2012) Dependence of nuclear spin singlet lifetimes on RF spin-locking power. *J. Magn. Reson.* 218:5-10.
30. Heinis C, Rutherford T, Freund S, & Winter G (2009) Phage-encoded combinatorial chemical libraries based on bicyclic peptides. *Nat. Chem. Biol.* 5(7):502-507.
31. Ahuja P, Sarkar R, Vasos PR, & Bodenhausen G (2009) Diffusion Coefficients of Biomolecules Using Long-Lived Spin States. *J. Am. Chem. Soc.* 131(22):7498.
32. Bornet A, Jannin S, & Bodenhausen G (2011) Three-field NMR to preserve hyperpolarized proton magnetization as long-lived states in moderate magnetic fields. *Chem. Phys. Lett.* 512(4-6):151-154.
33. Tayler MCD &Levitt MH (2011) Singlet nuclear magnetic resonance of nearly-equivalent spins. *Phys. Chem. Chem. Phys.* 13(13):5556-5560.
34. Dalvit C, Flocco M, Knapp S, Mostardini M, Perego R, Stockman BJ, Veronesi M, & Varasi M (2002) High-throughput NMR-based screening with competition binding experiments. *J. Am. Chem. Soc.* 124(26):7702-7709.
35. Checa A, Ortiz AR, de Pascual-Teresa B, & Gago F (1997) Assessment of solvation effects on calculated binding affinity differences: Trypsin inhibition by flavonoids as a model system for congeneric series. *J. Med. Chem.* 40(25):4136-4145.
36. Renatus M, Bode W, Huber R, Sturzebecher J, & Stubbs MT (1998) Structural and functional analyses of benzamidine-based inhibitors in complex with trypsin: Implications for the inhibition of factor Xa, tPA, and urokinase. *J. Med. Chem.* 41(27):5445-5456.

37. Lee Y, Zeng HF, Ruedisser S, Gosser AD, & Hilty C (2012) Nuclear Magnetic Resonance of Hyperpolarized Fluorine for Characterization of Protein-Ligand Interactions. *J. Am. Chem. Soc.* 134(42):17448-17451.
38. Bowen S &Hilty C (2010) Rapid sample injection for hyperpolarized NMR spectroscopy. *Phys. Chem. Chem. Phys.* 12(22):5766-5770.
39. Milani J, Vuichoud B, Bornet A, Mieville P, Mottier R, Jannin S, & Bodenhausen G (2015) A Magnetic Tunnel to Shelter Hyperpolarized Fluids. *Rev. Sci. Instrum.*
40. Mieville P, Ahuja P, Sarkar R, Jannin S, Vasos PR, Gerber-Lemaire S, Mishkovsky M, Comment A, Gruetter R, Ouari O, Tordo P, & Bodenhausen G (2010) Scavenging Free Radicals To Preserve Enhancement and Extend Relaxation Times in NMR using Dynamic Nuclear Polarization. *Angew. Chem. Int. Edit.* 49(35):6182-6185.
41. Comment A, van den Brandt B, Uffmann K, Kurdzesau F, Jannin S, Konter JA, Hautle P, Wenckebach WTH, Gruetter R, & van der Klink JJ (2007) Design and performance of a DNP prepolarizer coupled to a rodent MRI scanner. *Concept. Magn. Reson. B* 31B(4):255-269.
42. Jannin S, Bornet A, Melzi R, & Bodenhausen G (2012) High field dynamic nuclear polarization at 6.7 T: Carbon-13 polarization above 70% within 20 min. *Chem. Phys. Lett.* 549:99-102.
43. Jannin S, Bornet A, Colombo S, & Bodenhausen G (2011) Low-temperature cross polarization in view of enhancing dissolution Dynamic Nuclear Polarization in NMR. *Chem. Phys. Lett.* 517(4-6):234-236.
44. Hore PJ, Jones JA, & Wimperis S (2000) *NMR: The toolkit* (Oxford University Press Inc., New-York).
45. Sorensen OW, Eich GW, Levitt MH, Bodenhausen G, & Ernst RR (1983) Product Operator-Formalism for the Description of Nmr Pulse Experiments. *Prog. Nucl. Magn. Reson. Spectrosc.* 16:163-192.
46. Stait-Gardner T &Price WS (2009) A Physical Interpretation of Product Operator Terms. *Concepts Magn. Reson. A* 34A(6):322-356.
47. Sarkar R, Ahuja P, Vasos PR, & Bodenhausen G (2010) Long-Lived Coherences for Homogeneous Line Narrowing in Spectroscopy. *Phys. Rev. Lett.* 104(5).
48. Sarkar R, Ahuja P, Vasos PR, Bornet A, Wagnieres O, & Bodenhausen G (2011) Long-lived coherences for line-narrowing in high-field NMR. *Prog. Nucl. Magn. Reson. Spectrosc.* 59(1):83-90.
49. Tayler MCD, Marco-Rius I, Kettunen MI, Brindle KM, Levitt MH, & Pileio G (2012) Direct Enhancement of Nuclear Singlet Order by Dynamic Nuclear Polarization. *J. Am. Chem. Soc.* 134(18):7668-7671.

Chapter 6:

DNP-enhanced Water-LOGSY

In this Chapter, I will describe the adaptation to Dissolution-DNP of Water-LOGSY (Water-Ligand Observed via Gradient SpectroscopY), a powerful method used for drug screening. This technique uses the transfer of proton magnetization from water to ligands to report on binding to a protein. This technique, although it is extremely efficient and unambiguous, suffers from low sensitivity. Hyperpolarization of protons can therefore be very useful. The coupling between DNP and Water-LOGSY was explored by Quentin Chappuis during his Master's Thesis under my guidance (1). Further details about the experiments and resulting observations can be found elsewhere (2). Here, I only want to discuss the adaptations of the detection sequence that are required to make it DNP compatible. This example is particularly illustrative of difficulties that can be encountered while trying to couple an established method to hyperpolarization.

6.1 Water-LOGSY experiments

Water-LOGSY (Water-Ligand Observed via Gradient SpectroscopY) (3-6) is a remarkable NMR experiment used to detect interactions of proteins and ligands in solution. The detection of binding by Water-LOGSY relies on the spontaneous transfer of polarization from water to ligands. This transfer can occur via two pathways: via the nuclear Overhauser effect (NOE) or via chemical exchange (4). In the case of NOE, the transfer can occur either directly from the solvent to the ligand or indirectly via the bound protein. The sign of the NOE transfer depends on the rotational correlation time of the molecules involved: rapidly tumbling free ligands have negative enhancements, while slowly tumbling ligand-protein complexes feature positive enhancements. Therefore, the difference between free and bound ligands can be readily and unambiguously identified (4).

In conventional (non-enhanced) Water-LOGSY experiments, the ligands of interest are usually mixed with the target protein in H_2O:D_2O solutions with high proton concentrations (90% or more) to maximize the magnetization transfer from the protons of the solvent to the ligand. The experiment starts with the saturation of all signals apart from the solvent (preparation). A mixing delay allows the transfer of magnetization from the unsuppressed solvent to the analytes (mixing). A detection sequence using solvent suppression is then applied (detection). Inspection of the resulting spectrum and comparison to the same experiment without saturation permits one to detect binding. Positive magnetization transfer occurs in slowly-tumbling protein-ligand complexes, whereas magnetization with an opposite sign is transferred from water to rapidly-tumbling ligands when they cannot bind to the target protein (Figure 6.1).

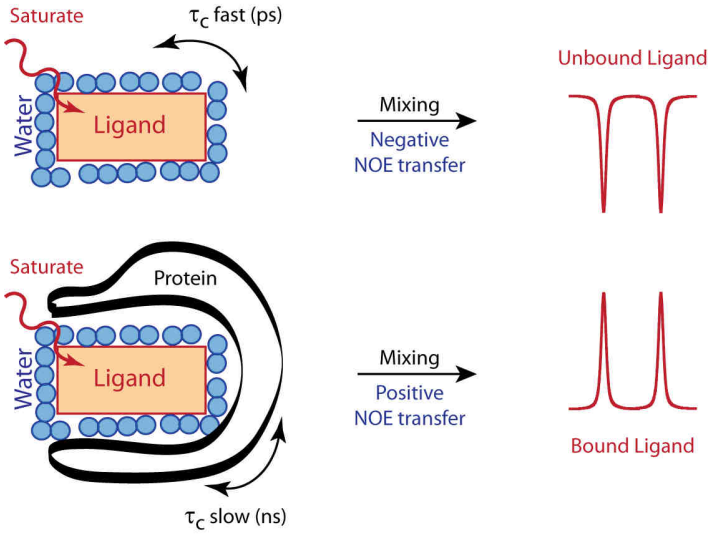

Figure 6.1: Schematic representation of the Water-LOGSY experiment. The large magnetization of bulk water is transferred via NOE and/or chemical exchange during the mixing time to the ligand, which has been saturated during the preparation step. Magnetization transferred from the solvent to a rapidly-tumbling free ligand confers a negative enhancement. Water magnetization which is transferred through a slowly-tumbling protein-ligand complex yields a positive enhancement.

Unfortunately, NMR signals observed in Water-LOGSY are typically 20–30 times weaker than signals in traditional one-dimensional NMR experiments, because only magnetization transferred by NOE's or exchange is detected. Therefore, ligand concentrations on the order of 200 µM are required to obtain a sufficient signal-to-noise ratio in a measurement time of 10 minutes. This concentration exceeds the aqueous solubility of most ligands that can be identified, for example, by High Throughput Screening (HTS). Hyperpolarization of water can thus be used to improve the sensitivity of the experiment. Nevertheless, as will be shown in the next section, the combination of the two techniques will engender some difficulties, and therefore the standard Water-LOGSY protocol needs to be adapted to render the DNP enhanced experiment successful.

6.2 DNP enhanced Water-LOGSY

In a DNP-Water-LOGSY experiment, the protons of water are hyperpolarized by D-DNP and injected into a solution containing a target protein and one or several putative ligands. The subsequent transfer of polarization from hyperpolarized water to the ligands reveals protein-ligand binding properties (Figure 6.2). The hyperpolarization of water is reproducible and robust, since it does not depend on the polarizability and relaxation times of the ligands. Since proteins and ligands can be mixed before injecting hyperpolarized water, protein-ligand equilibria can be probed, even if the kinetics are slow. Moreover, the spontaneous transfer of polarization from water to proteins enables the observation of ^{1}H spectra of proteins with concentrations below 20 µM, and hence a quality control of the protein being screened.

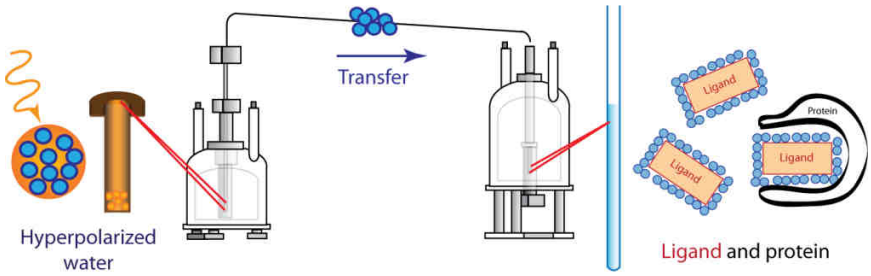

Figure 6.2: Schematic DNP-enhanced Water-LOGSY experiment. Water is polarized in a 200 µL glassy solution of H_2O:Glycerol-d_8 (1:1) with 25 mM TEMPOL to $P(^1H)$ > 38% at B_0 = 6.7 *T* and T = 1.2 K. The sample is then dissolved with 5 mL of superheated D_2O at 450 K and 1 MPa. The sample is transferred in 10 s to the detection spectrometer in a magnetic tunnel (7) keeping the magnetic field above 0.9 T. No scavenging agents (8) are used. 450 µL of hyperpolarized water are injected in an NMR tube containing the ligand of interest in equilibrium with the target protein. The Water-LOGSY detection sequence is then applied. The detection sequence can be repeated, as far as the water polarization can be preserved.

Nevertheless, DNP-Water-LOGSY presents a number of practical problems. First, the protons of hyperpolarized water relax rapidly, requiring special considerations for the preparation of the hyperpolarized solution to achieve the highest possible polarization and slowest relaxation during transfer. Some solutions to this relaxation problem are given in Chapters 5 and 7.

Moreover, in the NMR magnet, large amounts of hyperpolarized water leads to a huge water signal, which causes radiation damping and demagnetization effects that need to be taken into account. Figure 6.3 shows ^1H spectra obtained by non-selective excitation with small angle pulses (0.01°) just after the injection of hyperpolarized water into the spectrometer (2 < $P(^1H)$ < 5%). Right after injection, the width of the proton spectrum exceeds the usual width measured in non-enhanced NMR experiments by several orders of magnitude. This broadening of the hyperpolarized water peak is caused by radiation damping (RD), a feedback phenomenon that leads to a fast return to equilibrium of species that have a large magnetization component in the transverse plane (9, 10). The characteristic time constant of the return of the magnetization via radiation damping is inversely proportional to the gyromagnetic ratio of the nuclei γ, the quality factor of the probe *Q*, and the magnetization M_0 (10):

$$\tau_{RD}^{-1} = 2\pi\gamma Q M_0 \qquad (6.1)$$

Therefore, the detection sequence of DNP-enhanced experiments should avoid excitating the hyperpolarized water signal. Indeed, considering the high polarization reached, even a tiny fraction of the water magnetization that is not aligned with the longitudinal quantization axis could have dramatic radiation damping effects and could causes distortions of the spectrum of the ligands. The scheme should avoid the excitation of transverse magnetization followed by selective defocusing as used in WATERGATE sequences (11, 12). Moreover, at the same time, the water polarization should be preserved as much as possible in order to be able to transfer what remains of it by Water-LOGSY in subsequent scans. Finally, the detection sequence should not cause any phase distortions to allow a reliable interpretation of the LOGSY effect on the ligands.

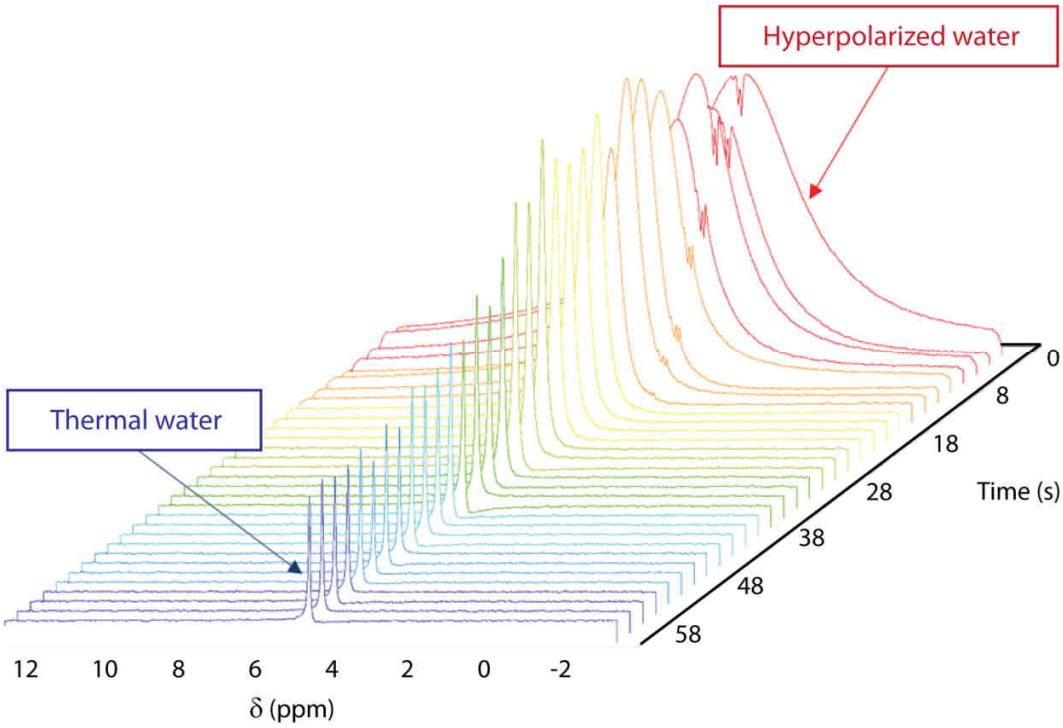

Figure 6.3: Water hyperpolarisation in a DNP-Water-LOGSY experiment. During the experiment, the water magnetisation is monitored by small nutation angles (0.01°), with a repetition time of 2 s. In the first scans, the signal displays a width of several kHz due to radiation damping (Data recorded by Quentin Chappuis).

6.3 DNP-Water-LOGSY detection sequences

Compared to the original Water-LOGSY experiment, the preparation step, where the ligand is normally saturated, can be replaced by the injection of hyperpolarized water (Figure 6.4). Indeed, as the polarization of hyperpolarized water is much larger than the thermal polarization of the ligand, a LOGSY effect will occur during the equilibration of their respective longitudinal magnetization components. Moreover, providing the water magnetization is not destroyed upon the detection, a series of scans can be recorded as long as the water hyperpolarization is not lost through longitudinal relaxation. This series of LOGSY spectra can then be added to improve the SNR (Figure 6.4).

The aim of the DNP-enhanced Water-LOGSY sequence is to observe the signals of the ligands enhanced by the transfer from the hyperpolarized water as long as possible, rather than the signal of water itself. The ideal detection scheme must therefore have the following characteristics. **(i)** It should not result in a significant solvent signal, **(ii)** it should not destroy the solvent polarization, **(iii)** it should excite ligand resonances across the full range of chemical shifts, even close to the solvent resonance, **(iv)** it should result in a clean excitation of the ligand resonances, without any phase errors and intensity losses depending on the offset with respect to the carrier frequency. Three sequences that we developed to allow coupling of DNP and Water-LOGSY are given below.

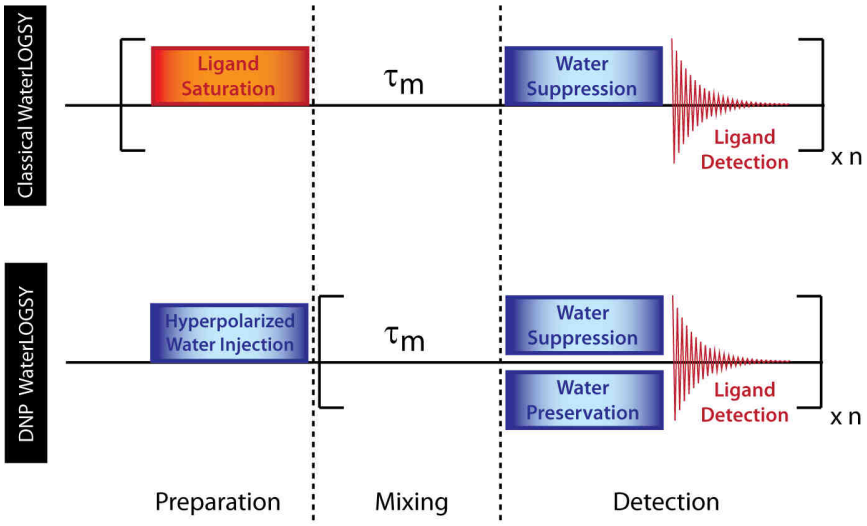

Figure 6.4: Schematic paths of conventional (non-enhanced) and DNP-enhanced Water-LOGSY experiments. In the latter case, the saturation of the ligands in the preparation step is replaced by the injection of hyperpolarized water. Moreover, in the detection step, not only does the water signal need to be suppressed, but its polarization needs to be preserved as well. Indeed, in this case, a series of mixing/detection steps can be recorded, as long as the water magnetization is sufficiently polarized.

6.3.1 Sequence 'A' selective ligand excitation:

The most straightforward solution is to excite only the resonances of the ligands with a shaped selective pulse, and to use a selective refusing pulse flanked by two magnetic field gradients that will only refocus the ligand signals (see Figure 6.5).

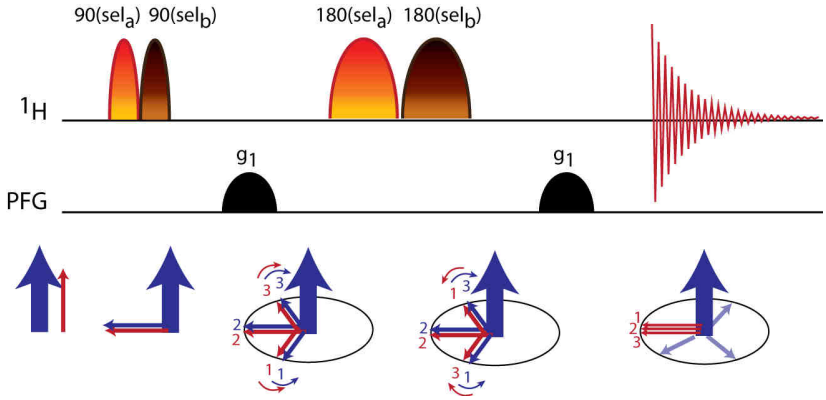

Figure 6.5: Water-LOGSY detection sequence 'A', using selective excitation and selective refocusing of the ligand signal upfield (a, red) and downfield (b, brown) with respect to the resonance frequency of the solvent. Pathway of the magnetization of the solvent (blue arrow) and of the ligands (red arrow) during the course of the echo sequence. The numbers 1, 2, 3 represents species located in regions with different magnetic field intensities generated by the PFG.

In the Bruker library of shaped pulses, we have chosen Pc9 (13) for excitation and Rsnob (14) for inversion. As Pc9 may excite some of the solvent signal even when it is far from resonance, it is necessary to make an echo using pulsed field gradients rather than a simple excitation to dephase the fraction of

the solvent magnetisation that has been unwittingly excited. On the other hand, in contrast to excitation by a Gaussian pulse, refocusing produces signals with identical phase across the entire excited region. Furthermore, we found that the overall sequence does not cause significant losses of solvent magnetisation.

Since this scheme uses selective pulses, it cannot excite the resonance on both sides of the solvent signal at the same time. Two strategies can be used to record both regions of the spectrum in a single scan. One way is to use polychromatic pulses where the carrier frequency is swept during the pulse. Another way is to apply two excitation pulses in quick succession with different carrier frequencies (pulses a and b in Figure 6.5) and, after the defocusing delay, two refocusing pulses. The delays must be set in such a way that the refocusing points are the same for both excitation/refocusing pulses pairs. We chose the second strategy because the results of polychromatic pulses are difficult to predict by simulations. This excitation scheme fulfils almost all the conditions that we have defined: its only drawbacks are that it does not allow exciting resonances close to the solvent and that the pulses calibrations is rather time-consuming.

6.3.2 Sequence 'B' using a selective water flip-back

The goal of this sequence is to avoid the need of applying two selective pulses upfield and downfield with respect to the solvent resonance frequency. Therefore, the sequence starts with a non-selective excitation followed by a selective solvent flip-back pulse (Figure 6.6).

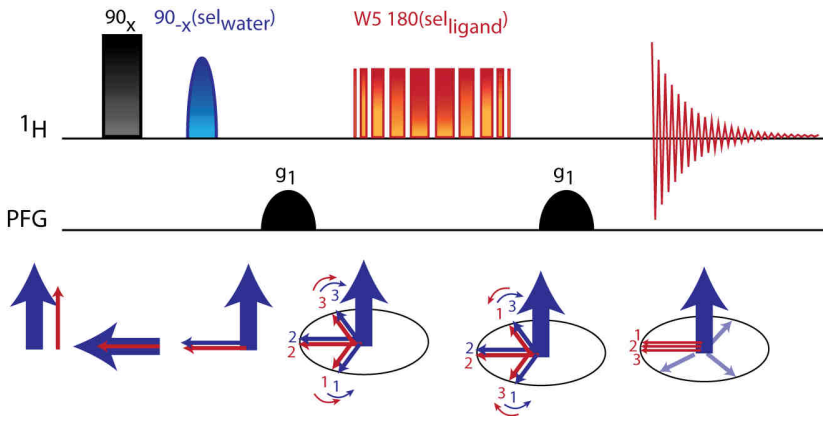

Figure 6.6: Water-LOGSY detection sequence 'B', using non-selective excitation, followed by a selective water flip-back pulse. The remaining solvent magnetization is suppressed using a Watergate W5 (11) scheme. The pathways of the magnetization of the solvent (blue arrows) and of the ligand (red arrows) are shown during the sequence. The number 1, 2, 3 represents species located in regions with different magnetic field intensities generated by the PFG.

At this point, the magnetization vectors of all analytes are excited while the solvent magnetization is returned to the longitudinal axis. The remaining of the sequence only aims at suppressing the residual transverse component of the solvent magnetisation. We used a Watergate W5 composite pulse which consists in a series of ten hard pulses with the following nutation angles: (7.8° – 18.5° – 37.2° – 70° – 134.2° – 134.2° – 70° – 37.2° – 18.5 – 7.8°). This train of hard pulses inverts or refocuses all spins *except* those that fulfil the conditions (11, 12):

$$\nu_0 = \nu_{RF} + k\frac{1}{\tau}, \text{ with } k = 0,1,2,... \quad (6.2)$$

Where ν_0 is the precession frequency of a spin and ν_{RF} is the transmitter frequency. All pulses are separated by the same delay τ. If this delay is short enough, all sidebands lie outside of the relevant spectral range. The transmitter frequency is placed on-resonance with respect to the solvent (k = 0) and, as a consequence, the W5 pulse train refocuses all spins except the solvent magnetisation.

The drawback of this sequence, especially in the context of DNP enhanced polarization of water, is that it requires a selective solvent flip-back pulse. First of all, it is not possible to calibrate this pulse under real conditions with high DNP enhanced water magnetization. Moreover, the water polarization may change slightly from one dissolution 'shot' to another. Therefore the solvent flip-back pulse may not be completely effective.

6.3.3 Sequence 'C' water flip-back using radiation damping

This third sequence takes advantage of the rapid radiation damping caused by the intense magnetization of the DNP enhanced water. The RD effect being very strong, it is possible to simply remove the water flip-back pulse from the sequence in Figure 6.6, and to replace it by a delay allowing the water to return to the longitudinal axis by itself via radiation damping (Figure 6.7). In our instrument, an RD time constant on the order of 200 µs can be estimated (10) from the linewidth of the hyperpolarized water signal of Figure 6.4.

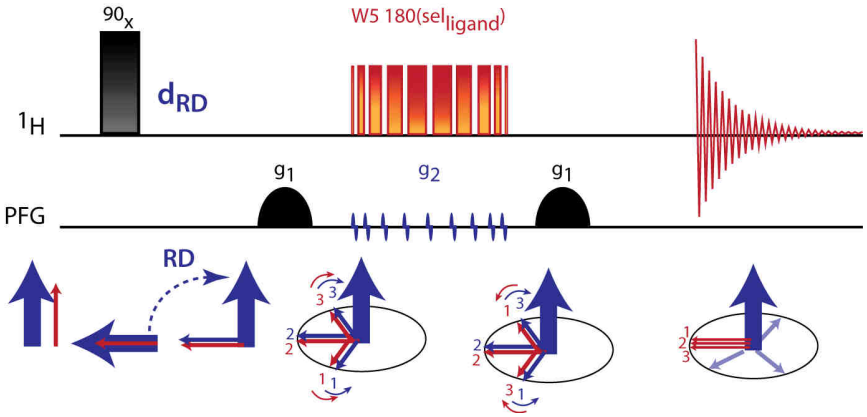

Figure 6.7: Water-LOGSY sequence 'C', using non-selective excitation, followed by a delay d_{RD} long enough to let radiation damping drive the water magnetization back to the z-axis. The remaining water magnetization is suppressed using a Watergate W5 (11) scheme. Small symmetric gradients are applied in-between the W5 pulses to defocus the strong hyperpolarized water magnetization and avoid radiation damping during these intervals. The pathways of the magnetization of the solvent (blue arrows) and of the ligand (red arrows) are shown during the course of the sequence. The number 1, 2, 3 represents species located in regions with different magnetic field intensities generated by the PFG.

A delay d_{RD} of a few milliseconds should be sufficient to allow for the major fraction of the water magnetization to return to the longitudinal axis. Nevertheless, RD might cause adverse effects during the selective W5 refocussing pulse train. If RD is active between the pulses, W5 might fail to leave the water untouched, so that the state of the magnetisation at the end of the refocusing pulse train may become unpredictable. Short pairs of symmetric pulsed field gradients can be applied in each inter-pulse delay τ

of the W5 sequence (g_2 in Figure 6.7). Because of their symmetry they will have no net effect, but as they defocus and refocus the magnetization, the radiation damping caused by the hyperpolarized water becomes less intense. The refocusing by the W5 pulse train should therefore be cleaner. This flip-back method has the advantage of being extremely selective, and, in contrast to shaped selective pulses, does not require any delicate calibration steps.

The sequence of Figure 6.7 was tested on a sample of 6 mM adenosine, 6 mM formate, 2 mM 1-^{13}C acetate and 3 mM 4 aminobenzoic acid in H_2O:D_2O (9:1). For an unpolarised sample, a delay of 70 ms after water excitation is needed to let the magnetization return to the z-axis via radiation damping. If an excitation pulse is applied after this delay, the area of the water peak is 89% of the area after a simple excitation. To test the ability of the sequence of Figure 6.7 to preserve the water magnetization, a small 5° pulse is added at the end. Comparison of the area of the water peak with a simple 5° excitation gives again a ratio of 89%. The spectrum of Figure 6.8 shows that, provided that the ligands do not resonate at frequencies that are too close to the solvent, the sequence of Figure 6.7 preserves the integrity of the peaks of interest, while efficiently eliminating the solvent signals.

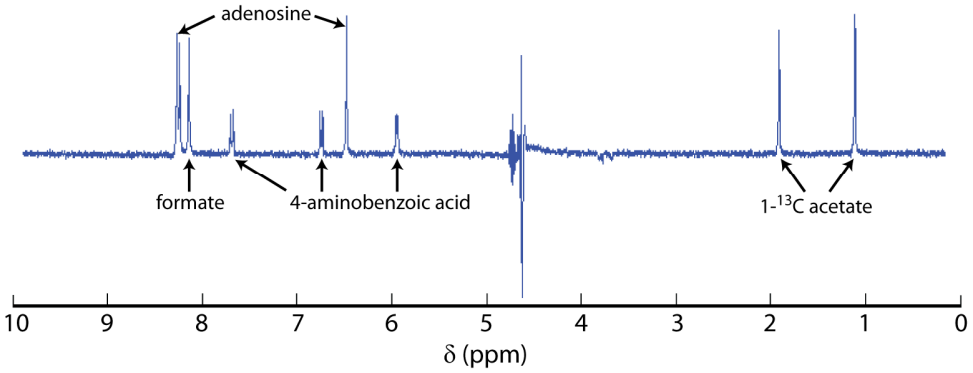

Figure 6.8: Hyperpolarized ^{1}H NMR spectrum of 6 mM adenosine, 6 mM formate, 2 mM 1-^{13}C acetate and 3 mM 4 aminobenzoic acid in H_2O:D_2O (9:1), acquired with the sequence of Figure 6.7 on a 7 T spectrometer (300 MHz for ^{1}H) at 298 K without cryoprobe. The delay d_{RD} is set to 70 ms, the W5 interpulse delay is set to 300 µs. (Data provided by Quentin Chappuis).

6.4 Other improvements needed for DNP-enhanced Water-LOGSY

New sequences were developed to allow one to suppress the solvent peak while preserving the solvent magnetization under non-standard conditions where the polarization is enhanced by DNP. Sequence No 'A' was used successfully by Quentin Chappuis in a DNP-enhanced Water-LOGSY experiment (1, 2) to observe the binding of different ligands to the protein Dot1L, a human histone methyl transferase (15). Even if the detection of the DNP-enhanced Water-LOGSY experiment has been optimized, other steps can still be improved. The most important remaining difficulty resides in the preservation of the hyperpolarized water magnetization during the dissolution and transfer to the detection spectrometer. Indeed, it should be possible to increase the enhancement of the method by at least one order of magnitude by fighting relaxation. Some solutions to this problem will be given in Chapter 7.

References

1. Chappuis Q (2014) The Preparation of Hyperpolarized Water and its Use to Enhance "WATER-LOGSY" Drug Screening. Master Thesis (Ecole Polytechnique Fédérale de Lausanne, Lausanne).
2. Chappuis Q, Milani J, Vuichoud B, Bornet A, Gossert AD, Bodenhausen G, & Jannin S (to be published) Hyperpolarized Water to Reveal Protein-Ligand Interactions
3. Dalvit C (1996) Homonuclear 1D and 2D NMR experiments for the observation of solvent-solute interactions. *J. Magn. Reson., Ser B* 112(3):282-288.
4. Dalvit C, Fogliatto G, Stewart A, Veronesi M, & Stockman B (2001) WaterLOGSY as a method for primary NMR screening: Practical aspects and range of applicability. *J. Biomol. NMR* 21(4):349-359.
5. Dalvit C, Pevarello P, Tato M, Veronesi M, Vulpetti A, & Sundstrom M (2000) Identification of compounds with binding affinity to proteins via magnetization transfer from bulk water. *J. Biomol. NMR* 18(1):65-68.
6. Gossert AD, Henry C, Blommers MJJ, Jahnke W, & Fernandez C (2009) Time efficient detection of protein-ligand interactions with the polarization optimized PO-WaterLOGSY NMR experiment. *J. Biomol. NMR* 43(4):211-217.
7. Milani J, Vuichoud B, Bornet A, Mieville P, Mottier R, Jannin S, & Bodenhausen G (2015) A Magnetic Tunnel to Shelter Hyperpolarized Fluids. *Rev. Sci. Instrum.*
8. Mieville P, Ahuja P, Sarkar R, Jannin S, Vasos PR, Gerber-Lemaire S, Mishkovsky M, Comment A, Gruetter R, Ouari O, Tordo P, & Bodenhausen G (2010) Scavenging Free Radicals To Preserve Enhancement and Extend Relaxation Times in NMR using Dynamic Nuclear Polarization. *Angew. Chem. Int. Edit.* 49(35):6182-6185.
9. Chen JH, Cutting B, & Bodenhausen G (2000) Measurement of radiation damping rate constants in nuclear magnetic resonance by inversion recovery and automated compensation of selective pulses. *J. Chem. Phys.* 112(15):6511-6514.
10. Krishnan VV &Murali N (2013) Radiation damping in modern NMR experiments: Progress and challenges. *Prog. Nucl. Magn. Reson. Spectrosc.* 68:41-57.
11. Furihata K, Shimotakahara S, & Tashiro M (2008) An efficient use of the WATERGATE W5 sequence for observing a ligand binding with a protein receptor. *Magn. Reson. Chem.* 46(9):799-802.
12. Liu ML, Mao XA, Ye CH, Huang H, Nicholson JK, & Lindon JC (1998) Improved WATERGATE pulse sequences for solvent suppression in NMR spectroscopy. *J. Magn. Reson.* 132(1):125-129.
13. Kupce E &Freeman R (1994) Wide-Band Excitation with Polychromatic Pulses. *J. Magn. Reson., Ser. A* 108(2):268-273.
14. Kupce E, Boyd J, & Campbell ID (1995) Short Selective Pulses for Biochemical Applications. *J. Magn. Reson., Ser B* 106(3):300-303.
15. Okada Y, Feng Q, Lin YH, Jiang Q, Li YQ, Coffield VM, Su LS, Xu GL, & Zhang Y (2005) hDOT1L links histone methylation to leukemogenesis. *Cell* 121(2):167-178.

Chapter 7:

New strategies to bypass paramagnetic relaxation after polarization

As shown in Chapters 5 and 6, an important part of the magnetization built by DNP can be sacrificed by relaxation during the transfer between the polarizer and the detection spectrometer, as well as during the course of the enhanced experiment. This is particularly true for protons. An improvement up to one order of magnitude in the SNR could be expected if this relaxation was reduced. In this Chapter, I will first show that the main contribution to relaxation in a D-DNP experiment comes from the presence of free electrons of the polarizing agent dissolved concomitantly with the hyperpolarized sample. I will then present a new strategy, developed in collaboration with the groups of Prof. Lyndon Emsley and Prof. Christophe Copéret, that allows to retain the free radicals molecules in the polarizer while the DNP-enhanced analytes flow to the detection spectrometer (1).

7.1 Paramagnetic relaxation at low field

The paramagnetic species have a kind of bipolar comportment along the course of a Dissolution-DNP experiment. On one hand, during the polarization build-up process in the polarizer, they have a beneficial role, as free electrons are at the origin of the high polarization transmitted to the nuclei. On the other hand, during both dissolution, transfer and detection steps, they can be the source of dramatic losses of polarization. This has two consequences for any hyperpolarized experiment: less polarization can be available and the time window at disposition for measurement is shortened. As developed in Chapters 5 and 6, paramagnetic species are particularly handicapping, if not lethal, for hyperpolarized nuclei like ^{1}H.

Moreover, as shown by Bryant and co-workers in studies of translational motion in the vicinity of paramagnetic nitroxides (2, 3), paramagnetic relaxation is extremely efficient at low field. The following data, particularly illustrative of this low field effect, are kindly shared by Dr Pascal Mieville and Jonas Milani, who studied in our group the relaxation induced by polarizing agents in the context of Dissolution-DNP (4, 5). The relaxation of a system of spins ½ is the sum of the contribution of three main mechanisms: the internuclear dipole-dipole interactions (DD), the chemical shift anisotropy (CSA) and the paramagnetic interactions (electron-nuclei dipolar interactions). In Figure 7.1a, the contribution of these three mechanisms is calculated for the protons of a small molecule in presence of 2.5 mM of electrons, at different magnetic fields, according to References (6) for R_1^{DD} and R_1^{CSA} and (2-4) for R_1^{param}. It can be clearly seen that, at low magnetic field (below 0.1 T), the paramagnetic contribution becomes dominant.

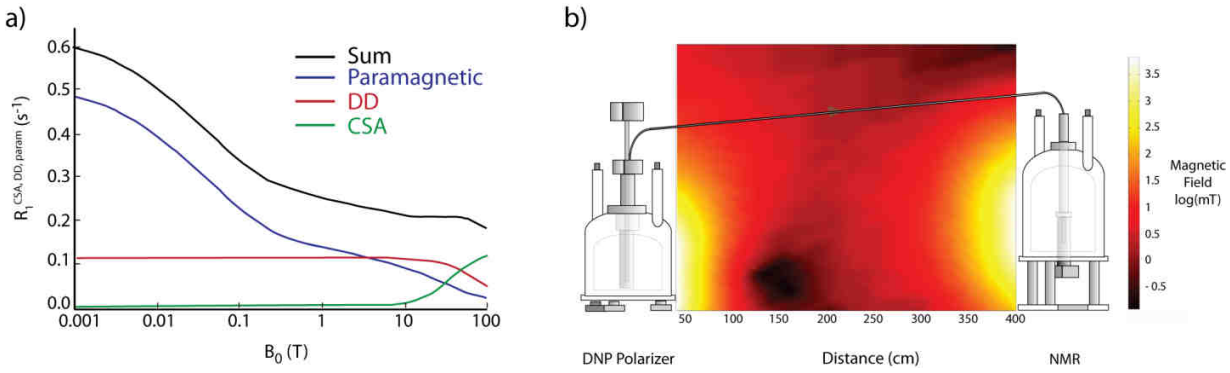

Figure 7.1: **a)** Illustration of the contributions of different relaxation mechanisms as a function of the B_0 field. The contributions of the CSA (green), the internuclear DD interactions (red) and the paramagnetic interactions (blue) are calculated according to References (2-4, 6). (Data provided by Jonas Milani) **b)** Magnitude of the static field measured in the plane between an unshielded 6.7 T Oxford Instruments Ox2 ODX polarizer (left) and an unshielded WB magnet of a Bruker 300 MHz NMR spectrometer (right). (Data shared with Jonas Milani (5)).

As an illustration, the ^{13}C spin-lattice relaxation rates of a 3 M solutions of 1-^{13}C acetate were measured at different fields in non-degased D_2O (**ii**), with the addition of 0.25 mM of TEMPOL (**i**), and with the addition of 50 mM sodium ascorbate (**iii**) (7) using a custom build shuttle relaxometer (4) (Figure 7.2a). Proton R_1's were measured in the same condition on a sample of bromothiophene carboxylate (5) (Figure 7.2b). As ascorbate is a reducing agent that quenches TEMPOL, as well as paramagnetic dioxygen, the difference between curves **(i)** and **(iii)** in Figure 7.2 reports the contribution of R_1^{param}. The paramagnetic relaxation increases drastically below 0.1 T, both for ^1H and ^{13}C, even at TEMPOL concentration 10-20 times lower than in D-DNP conditions.

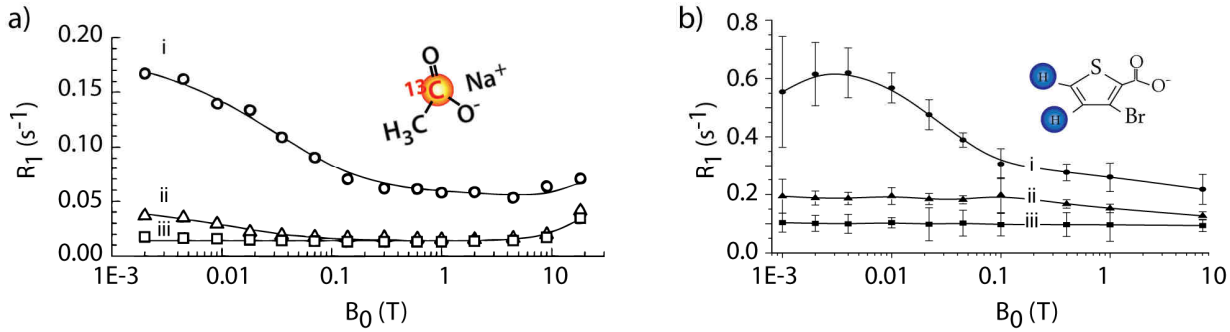

Figure 7.2: **a)** (Δ) Spin–lattice relaxation rates $R_1(^{13}C) = 1/T_1(^{13}C)$ in 3 M 1-^{13}C labeled acetate in non-degassed D_2O as a function of B_0 over the range 2 mT < B_0 < 18.8 T; (○) the same after addition of 2.5 mM TEMPOL; and (□) after adding 30 mM ascorbate to scavenge the radicals. (Data provided by with Pascal Mielville (4)) **b)** $R_1(^1H)$ of bromothiophene carboxylate under the same conditions as in **a**. (Data shared with Jonas Milani (5)).

The two examples of Figure 7.2 are representative of the exacerbated relaxation at low magnetic field during a Dissolution-DNP experiment. Indeed, apart from unique system based on dual centre magnet (8), during the transfer step, the hyperpolarized solution is no longer immersed in the magnetic field of the polarizer, and not yet sheltered by the field of the detection magnet, and thus exposed to very low magnetic field region (mT range) for a time period varying from seconds (9) to minutes (10). The exact magnetic field pattern experienced by the hyperpolarized fluid in our laboratory was mapped systematically with a triple-axis Hall probe (11) and is shown in Figure 7.1b (5). Most of the transfer

therefor goes through a relatively low field, on the order of B_0 = 1 mT. With our magnet configuration, the sample can even travel through a zone where the field is inverted (black area in Figure 7.1b)

Paramagnetic relaxation is efficient as well inside the polarizer during the dissolution procedure. Many critical phenomena, especially for ^{1}H, could occur. During the docking of the dissolution stick to the DNP sample holder, this last one is lifted above the liquid helium bath, *i.e.* to a region of lower field (See Figure 7.3b). As shown in Figure 7.3a, the ^{1}H relaxation rate of a frozen DNP sample (1-^{13}C acetate 3M with 50 mM TEMPOL in D_2O:Glycerol-d_8 1:1) becomes extremely fast while decreasing the field. Moreover, the dissolution stick initially at room temperature may slightly heat up the solid sample before the arrival of the hot water, which may cause faster relaxation. Furthermore, in the first hundreds of milliseconds of dissolution, while the hyperpolarized solution is pushed out of the polarizer, the local radical concentration is still high, which is problematic, as the paramagnetic relaxation efficiency is proportional to the free electron concentration.

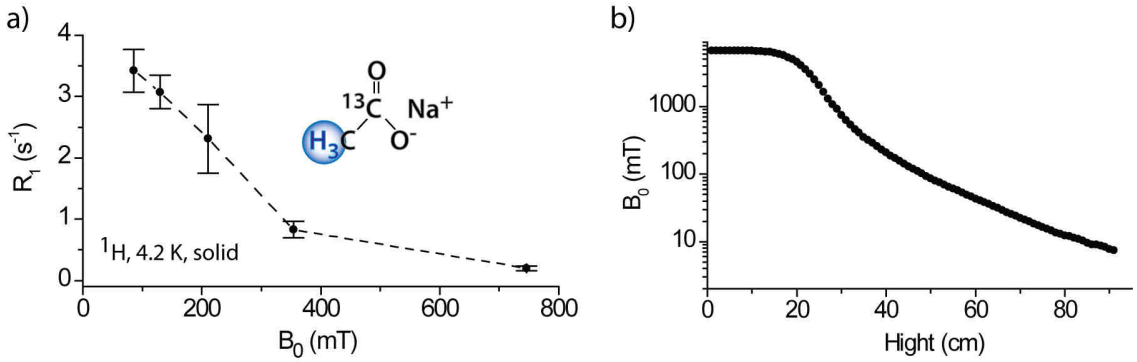

Figure 7.3: **a)** Proton relaxation rates R_1(^{1}H) measured in a solid DNP sample of 3 M 1-^{13}C acetate with 50 mM TEMPOL in D_2O:Glycerol-d_8 (1:1) at 4.2 K as function of the field above the centre of our 6.7 T DNP polarizer. **b)** Magnitude of the magnetic field measured along the vertical z-axis above the centre of our 6.7 T polarizer (Data shared with Jonas Milani (5)).

To avoid losses induced by the polarizing agent that no long serve any functions, it is therefore a good strategy to try to eliminate the radical as soon as possible. For some radicals, such as trityls, separation can be achieved by solvent extraction (12), or precipitation by a jump in pH followed by mechanical filtration (13). For TEMPO with its derivatives, quenching with sodium ascorbate (vitamin C) can convert nitroxide radical into diamagnetic species trough reduction (7). However, for quantitative and rapid quenching, ascorbate must be used in excess, and remaining ascorbate may affect the analyte or sensitive components present in the NMR or MRI system, such as enzymes (14-16). Furthermore, the presence of potentially non-innocent additional products arising from the polarizing agent is obviously undesirable for in vivo MRI experiment. In the next Section, a method to produce pure hyperpolarized solution free of radical, glassing and reducing agents will be developed.

7.2 Hybrid Polarizing Solids (HYPSO)

A new generation of hybrid polarizing solids (called HYPSO) was developed in collaboration with the group of Prof. Lyndon Emsley and Prof. Christophe Copéret to perform DNP efficiently while avoiding paramagnetic relaxation (1). The strategy consists in the incorporation of TEMPO radicals in a mesostructured silica matrix. The powder can then be wetted with a solution containing molecules of

interest for MRS or MRI (for example metabolites) that will fill the pore channels of the material via incipient wetness impregnation (Figure 7.4). DNP can then be performed as usual at low temperatures. During dissolution, HYPSO will be physically retained by simple filtration in the cryostat of the DNP polarizer and a pure hyperpolarized solution will be collected within a few seconds. The resulting solution that contains the pure substrate will be free from any paramagnetic or toxic pollutants and ready for in-vivo infusion.

7.2.1 Sample preparation

One approach to obtain a solution free of radical would require an efficient solid polarizing matrix, which could then be easily separated from the solution. In order to maximize the polarization produced in such heterogeneous systems, it is crucial to avoid polarization losses via radical-radical interactions; the challenge being to control both the radicals density and distribution onto the solid. In this field, immobilization of radicals on silica gels or thermo-responsive polymers (17-19) has been reported for room temperature Overhauser DNP of liquid water. Mesostructured hybrid organosilica materials with immobilized polarizing agents were initially developed for MAS-DNP (20) and reported good enhancements. The same approach was optimized for D-DNP. In order to immobilize the polarizing agent, mesoporous materials are prepared via a Sol-Gel process. In the first generation of materials (HYPSO-1.0), The TEMPO moieties are covalently bound to the silica surface through propylamide linkers ($O_{1.5}Si(CH_2)_3$–NHCO–TEMPO) (Figure 7.4). The polarizing agents are homogeneously distributed along the pore channels of the silica matrix. The detail of the synthesis can be found in the supplementary material of Reference (1) and (20).

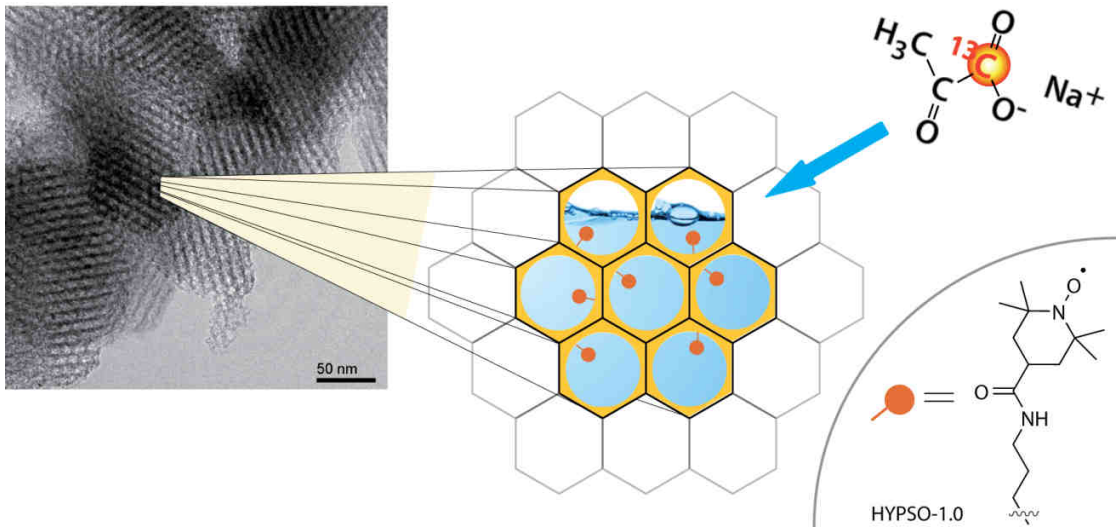

Figure 7.4: Schematic representation of the HYPSO strategy. The solution containing the analyte to be hyperpolarized is impregnated in a mesoporous silica material which contains polarizing agents (red dots) that are covalently attached to its surface. The transmission electron microscopy image (taken with a Philips CM30 TEM operating at 300 kV) shows the porous structure of the material.

The material can then be wetted with a solution containing the molecule to be hyperpolarized. The pores will be filled by incipient wetness impregnation (Figure 7.4). HYPSO can be impregnated with up to ~1.8 mL/g corresponding to a complete filling of the pores (~1.0 mL/g) as well as the additional inter-grain volumes (~0.8 mL/g). The high porosity of HYPSO gives it a weightless aspect. Its effective filling factor amounts to $\eta = V_{solution}/V_{total} = 0.85$.

7.2.2 DNP on HYPSO

Once HYPSO is impregnated with a solution of interest, routine DNP can readily be performed in a standard manner by microwave irradiation of the polarizing agent ESR transition. The proton polarization obtained by DNP at T = 1.2 K and B_0 = 6.7 T using HYPSO-1.0 depends on the electron concentrations and shows a broad optimum around 88 µmol.g^{-1}, which roughly corresponds to an electron concentration of 49 mM in the pores, close to the optimal value of 50 mM that is normally used in D_2O:glycerol-d_8 mixtures. The proton build-ups of a solution of 3 M 1-^{13}C acetate in D_2O loaded in 100 mg of material are shown in Figure 7.5. At T = 4.2 K, $P(^1H)$ = 7.5% and $\tau_{DNP}(^1H)$ = 30 s and at 1.2 K, $P(^1H)$ = 49.3% and $\tau_{DNP}(^1H)$ = 130 s. This is lower that standard polarization reached in the same conditions with normal DNP solutions. The build-ups are also not fully mono-exponentials, which mean that some diffusion occurs, and that the polarizing agent is not perfectly homogeneously distributed. A better control of the distribution of the TEMPO functionalities (for example mimicking the statistical Poisson distribution in frozen glassy matrices) within the material may lead to further improved efficiency.

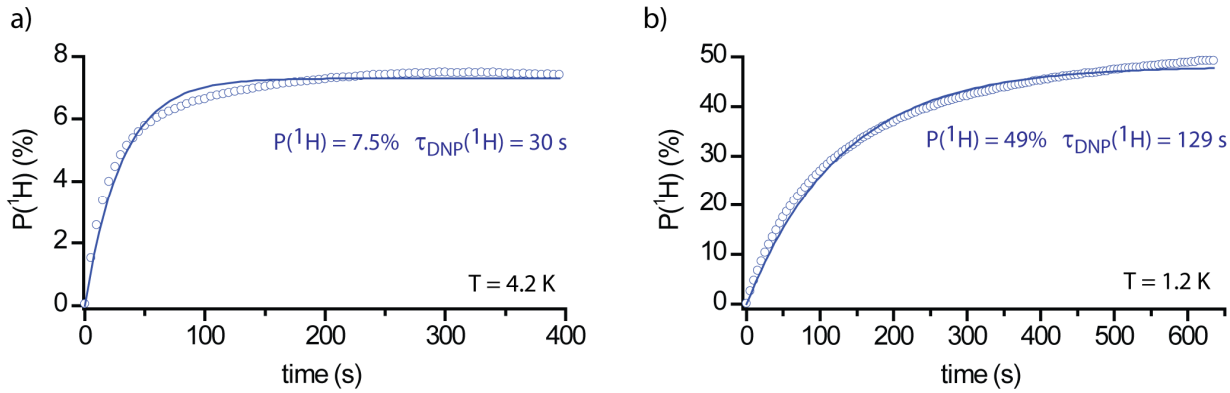

Figure 7.5: Build-up plots of the polarization $P(^1H)$ of 180 µL of a 3 M acetate solution in D_2O impregnated in 100 mg of HYPSO-2.0 at B_0 = 6.7 T at (**a**) T = 4.2 K, and **(b)** T = 1.2 K. The lines show fits to monoexponential functions.

Another important feature of dissolution-DNP with HYPSO is that no glassing agents such as glycerol or DMSO are required, regardless of the target material to be polarized. Apart from some specific cases, such as for neat pyruvic acid, where the analyte spontaneously forms a glass upon freezing, the addition of glass-forming agents is mandatory in numerous Dissolution-DNP experiments. This can be avoided with HYPSO. This feature can be seen in Figure 7.6 where the DNP build-up of $P(^1H)$ at 4.2 K of a pure H_2O:D_2O (1:9) solution impregnated in the HYPSO material is compared with the build-up of $P(^1H)$ in a solution of a glass forming mixture H_2O:D_2O:DMSO-d_6 (1:3:6) under the same conditions. Indeed, as the polarizing agents are attached to the HYPSO material, there is no risk for them to be repelled to the edge of crystals that might form upon freezing.

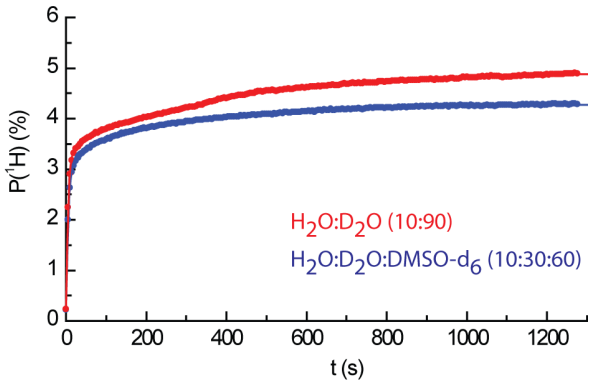

Figure 7.6: Build-up plots of the polarization $P(^1H)$ of 40 µL pure H_2O:D_2O (1:9) (red) or glassy H_2O:D_2O:DMSO-d_6 (1:3:6) (blue) impregnated in 24 mg of HYPSO-1.0 at B_0 = 6.7 T and T = 4.2 K.

A polarization $P(^{13}C)$ = 36 % can be reached via Cross-Polarization in 3 M 1-^{13}C pyruvate in H_2O:D_2O (1:9) (see Figure 7.7a) using a HYPSO-2.0 material obtained by an improved synthesis, using a different linker to attach TEMPO, *via* a click reaction between alkyne-TEMPO and azidopropyl moieties of the material. Furthermore, such materials allow access to a broad range of solid polarizing matrices, for instance, with silica materials containing trityl radicals. Preliminary results with a first generation of materials with 16 µmol trityl per gram (HYPSO-1.2) yield $P(^{13}C)$ = 15% after 2 hours, indicating that it should be possible to obtain about 25% when the asymptotic value is reached (see Figure 7.7b).

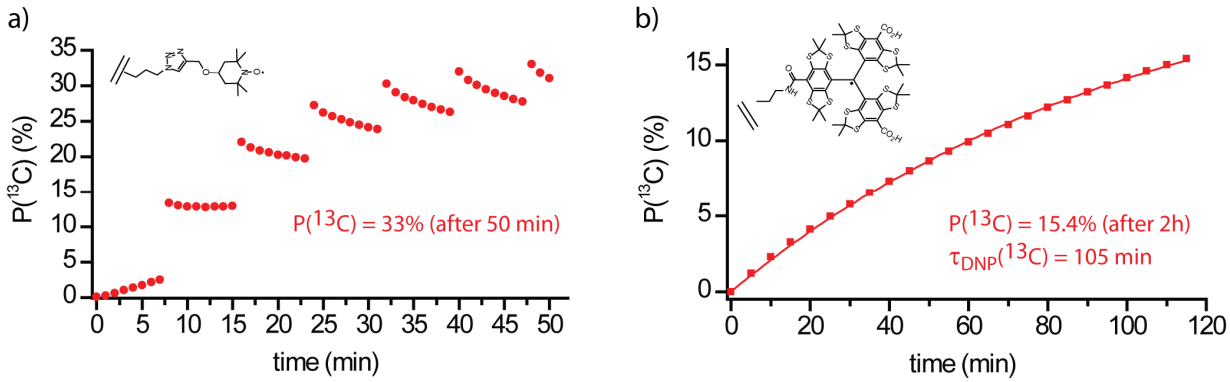

Figure 7.7: **a**) Build-up plots of the polarization $P(^{13}C)$ during multiple-contact cross-polarization ($^1H \rightarrow {}^{13}C$ CP at 7.5 min intervals) with microwave irradiation, obtained for 20 mg of HYPSO-2.0 (containing ? 41 µmol/g radical) impregnated with 36 µL of a 3 M solution of 1-^{13}C pyruvate in D_2O. A polarization $P(^{13}C)$ > 30% is reached in 32.5 min. **b**) Direct ^{13}C DNP performed on 20 mg of HYPSO-1.2 (with 16 µmol/g radical) impregnated with a 36 µL of a 3 M solution of 1-^{13}C pyruvate in D_2O. A modest polarization $P(^{13}C)$ = 15% is only achieved after 2 hours with a time constant $\tau_{DNP}(^{13}C)$ = 105 ± 3 min, apparently towards an asymptotic value $P(^{13}C)^{max}$ = 23 %.

7.2.3 Filtration of HYPSO upon dissolution

Once the polarization of the analyte has reached the desired level, the solution should be separated from the HYPSO matrix containing the paramagnetic centres that contribute to relaxation after dissolution. The idea is to wash the pores of the material with the dissolution solvent and thus to expel the target material or analyte, while retaining the solid HYPSO by filtration. This crucial step has to be carried out as close as possible to the centre of the polarizing magnet where the magnetic field is

intense. For example, a filtration along the transfer line, beyond the stray field of the magnet, would be catastrophic in term of paramagnetic relaxation. Indeed, in this case the hyperpolarized solution could stay in the pores of the material, therefore in close contact with highly concentrated unpaired electrons in a low field region. A good solution consists in mounting a cellulose filter at the bottom of the dissolution stick, *i.e.*, at the top of the DNP sample holder during dissolution.

Dissolution is subsequently performed by injecting 5 mL of superheated water. The polarizing agents remain attached to the surface of the mesopores during dissolution, due to their covalent linkage with the silica matrix. The solution is in practice easily expelled from HYPSO by injecting hot water under pressure (T_{diss} = 450 K, P_{diss} = 1 MPa) as it is usually done for regular frozen glassy DNP samples. The resulting slurry is then forced by pressurized hot water with a helium pressure of P_{push} = 6 MPa through a home built cellulose fiber filter mounted just above the DNP sample holder, as near as possible to the center of the 6.7 T magnetic field of the polarizer. The hyperpolarized solution is then transferred to the detection spectrometer. As an example, the hyperpolarized 1-^{13}C pyruvate signal was measured at 7 T with an enhancement factor ε_{DNP} = 32500 compared to its thermal equilibrium signal after complete relaxation (Figure 7.8). Such enhancement attests for a polarization $P(^{13}C)$ = 25.3 %. The polarization decays with $T_1(^{13}C)$ = 49.4 ± 0.4 s, which is typical of a pure D_2O solution of 1-^{13}C-pyruvate without any free radicals.

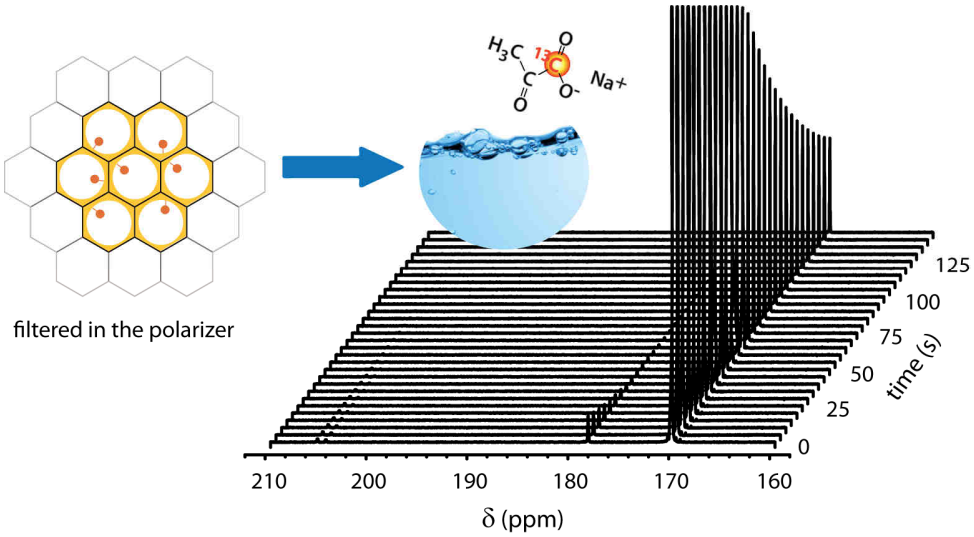

Figure 7.8: NMR spectra of 1-^{13}C pyruvate hyperpolarized with HYPSO-1.0 measured every 5 s with a nutation angle of 5° at 7 T (300 MHz for protons) and 298 K.

As a proof of general applicability, the same experiment was also performed on fumarate (with $P(^{13}C)$ = 19.9 % for both carbonyl carbons) and on the dipeptide Alanine-Glycine (with $P(^{13}C)$ = 15.0 % and $P(^{13}C)$ = 13.6 % for the Alanine carbonyl carbon and the Glycine carboxyl carbon respectively).

D-DNP can thus be performed very efficiently using the HYPSO family of polarizing agents. The sample preparation is carried out without glassing agents to provide pure hyperpolarized solutions (no radical contamination), which can easily be separated from the polarizing solids using standard filters. The efficiency of these solid polarization matrices is the result of the controlled incorporation of a homogeneous distribution of radicals along the pore channels of a highly porous mesostructured

material. Although already shown here with pyruvate, acetate, fumarate, and a dipeptide (Alanine-Glycine), the approach should be applicable to a broad range of molecules that can be hyperpolarized by D-DNP.

References

1. Gajan D, Bornet A, Vuichoud B, Milani J, Melzi R, van Kalkeren HA, Veyre L, Thieuleux C, Conley MP, Gruning WR, Schwarzwalder M, Lesage A, Coperet C, Bodenhausen G, Emsley L, & Jannin S (2014) Hybrid polarizing solids for pure hyperpolarized liquids through dissolution dynamic nuclear polarization. *Proc. Natl. Acad. Sci. U. S. A.* 111(41):14693-14697.
2. Borah B &Bryant RG (1981) Nmr Relaxation Dispersion in an Aqueous Nitroxide System. *J. Chem. Phys.* 75(7):3297-3300.
3. Polnaszek CF &Bryant RG (1984) Nitroxide Radical Induced Solvent Proton Relaxation - Measurement of Localized Translational Diffusion. *J. Chem. Phys.* 81(9):4038-4045.
4. Mieville P, Jannin S, & Bodenhausen G (2011) Relaxometry of insensitive nuclei: Optimizing dissolution dynamic nuclear polarization. *J. Magn. Reson.* 210(1):137-140.
5. Milani J, Vuichoud B, Bornet A, Mieville P, Mottier R, Jannin S, & Bodenhausen G (2015) A Magnetic Tunnel to Shelter Hyperpolarized Fluids. *Rev. Sci. Instrum.*
6. Kowalewski J &Mäler L (2006) *Nuclear spin relaxation in liquids theory, experiments, and applications* (Taylor & Francis, New-York).
7. Mieville P, Ahuja P, Sarkar R, Jannin S, Vasos PR, Gerber-Lemaire S, Mishkovsky M, Comment A, Gruetter R, Ouari O, Tordo P, & Bodenhausen G (2010) Scavenging Free Radicals To Preserve Enhancement and Extend Relaxation Times in NMR using Dynamic Nuclear Polarization. *Angew. Chem. Int. Edit.* 49(35):6182-6185.
8. Leggett J, Hunter R, Granwehr J, Panek R, Perez-Linde AJ, Horsewill AJ, McMaster J, Smith G, & Kockenberger W (2010) A dedicated spectrometer for dissolution DNP NMR spectroscopy. *Phys. Chem. Chem. Phys.* 12(22):5883-5892.
9. Bowen S &Hilty C (2010) Rapid sample injection for hyperpolarized NMR spectroscopy. *Phys. Chem. Chem. Phys.* 12(22):5766-5770.
10. Nelson SJ, Vigneron D, Kurhanewicz J, Chen A, Bok R, & Hurd R (2008) DNP-hyperpolarized C-13 magnetic resonance metabolic imaging for cancer applications. *Appl. Magn. Reson.* 34(3-4):533-544.
11. Schott C, Popovic RS, Alberti S, & Tran MQ (1999) High accuracy magnetic field measurements with a Hall probe. *Rev. Sci. Instrum.* 70(6):2703-2707.
12. Harris T, Bretschneider C, & Frydman L (2011) Dissolution DNP NMR with solvent mixtures: Substrate concentration and radical extraction. *J. Magn. Reson.* 211(1):96-100.
13. Ardenkjaer-Larsen JH, Leach AM, Clarke N, Urbahn J, Anderson D, & Skloss TW (2011) Dynamic Nuclear Polarization Polarizer for Sterile Use Intent. *NMR Biomed.* 24(8):927-932.
14. Lee Y, Heo GS, Zeng HF, Wooley KL, & Hilty C (2013) Detection of Living Anionic Species in Polymerization Reactions Using Hyperpolarized NMR. *J. Am. Chem. Soc.* 135(12):4636-4639.
15. Lee Y, Zeng HF, Mazur A, Wegstroth M, Carlomagno T, Reese M, Lee D, Becker S, Griesinger C, & Hilty C (2012) Hyperpolarized Binding Pocket Nuclear Overhauser Effect for Determination of Competitive Ligand Binding. *Angew. Chem. Int. Edit.* 51(21):5179-5182.
16. Lee Y, Zeng HF, Ruedisser S, Gosser AD, & Hilty C (2012) Nuclear Magnetic Resonance of Hyperpolarized Fluorine for Characterization of Protein-Ligand Interactions. *J. Am. Chem. Soc.* 134(42):17448-17451.

17. Dollmann BC, Junk MJN, Drechsler M, Spiess HW, Hinderberger D, & Munnemann K (2010) Thermoresponsive, spin-labeled hydrogels as separable DNP polarizing agents. *Phys. Chem. Chem. Phys.* 12(22):5879-5882.
18. Gitti R, Wild C, Tsiao C, Zimmer K, Glass TE, & Dorn HC (1988) Solid Liquid Intermolecular Transfer of Dynamic Nuclear-Polarization - Enhanced Flowing Fluid H-1-Nmr Signals Via Immobilized Spin Labels. *J. Am. Chem. Soc.* 110(7):2294-2296.
19. McCarney ER &Han S (2008) Spin-labeled gel for the production of radical-free dynamic nuclear polarization enhanced molecules for NMR spectroscopy and imaging. *J. Magn. Reson.* 190(2):307-315.
20. Gajan D, Schwarzwalder M, Conley MP, Gruning WR, Rossini AJ, Zagdoun A, Lelli M, Yulikov M, Jeschke G, Sauvee C, Ouari O, Tordo P, Veyre L, Lesage A, Thieuleux C, Emsley L, & Coperet C (2013) Solid-Phase Polarization Matrixes for Dynamic Nuclear Polarization from Homogeneously Distributed Radicals in Mesostructured Hybrid Silica Materials. *J. Am. Chem. Soc.* 135(41):15459-15466.

Chapter 8:

Hyperpolarized Equivalent Long-Lived States ("HELLS")

In this Chapter, I will discuss a more common combination of Long-Lived States and Dissolution-DNP than the one developed in Chapter 5. In the experiment of Chapter 5, DNP enhanced LLS were used as a probe and information about ligand binding was extracted from the observation of their relaxation rates. Here, I will treat the use of Long-Lived States to preserve the hyperpolarized magnetization. Up to now, several methods were developed to convert DNP enhanced polarization into singlet order. The great majority of these rely on various manipulations of spins after the hyperpolarization step, inducing difficulties, like extra hardware, pulse sequences or waste of time. An exception arose from the group of Malcolm Levitt. In their cleaver experiment (1), they proved that singlet spin order in two coupled inequivalent spins can be made directly available if the polarization is high, without extra manipulations. In my opinion, providing that high polarization can be reached (at high field for ^{1}H and by Cross-Polarization for heteronuclei), this will be the preferred way to excite LLS in future Dissolution-DNP experiments, because the simpler, the better.

In this Chapter, I will introduce an experimental procedure that was developed to show that singlet order can also be populated by D-DNP in molecules with magnetically equivalent spins (2).

8.1 LLS to sustain hyperpolarization

8.1.1 Different attempts to combine DNP and LLS

As shown in Section 1.2.2 of Chapter 1, one of the specificities of Dissolution-DNP consists in the physical separation between the apparatus for polarization and detection, and therefore the need of rapid transfer of the hyperpolarized sample. This transfer, sometimes poetically called *voyage*, can be performed either manually or by means of a pneumatic system. During the voyage, the hyperpolarized molecules experience low magnetic fields (sometimes as low as the earth's field, or even below), which have detrimental effects on the enhanced polarization. This is one of the reasons why Dissolution-DNP has been most useful for nuclear spins with long T_1, such as the isolated low-gamma quaternary ^{13}C spin in 1-^{13}C pyruvic acid (3, 4). On the other hand, apart from some exotic experiments (5, 6), ^{1}H spins have hardly ever been exploited by D-DNP as their short T_1's rapidly drive the hyperpolarization back towards Boltzmann equilibrium. The most straightforward way to fight relaxation consist in speeding up the transfer. Bowen *et al.* (7) have developed a fast injection device where the interval between dissolution and detection is reduced to 1.2 s. As described in Chapter 6, an effective alternative consists in the elimination of paramagnetic polarizing agents, by reduction (8), extraction (9), precipitation (10) or by the use of hybrid polarizing solids (HYPSOs) with radicals incorporated in silica material (11). A magnetic tunnel (12) can also be used to protect the transfer line from low magnetic field regions.

Another possible strategy to take advantage of the large ^{1}H hyperpolarization that can be obtained under our experimental conditions consists in storing the magnetization in the form of Long-Lived States (LLS) (13, 14). In recent years, several successful studies combining D-DNP with Long-Lived States (1, 15-21) have shown that hyperpolarized magnetization can be converted into LLS with extended lifetimes T_{LLS} >> T_1. As introduced in Chapter 5, in a pair of equivalent spins ½, the singlet state S_0 = (|αβ⟩-|βα⟩)/ √2 is largely disconnected from the triplet states T_{+1} = |αα⟩, T_0 = (|αβ⟩+|βα⟩)/ √2 and T_{-1} = |ββ⟩ because relaxation mechanisms that are symmetric with respect to spin exchange (such as the dipole-dipole interaction between the two spins) cannot induce singlet-triplet transitions (22-24). Therefore, if a triplet-singlet population imbalance (TSI) is prepared by any means, it is likely to be long-lived. I use the expression TSI in analogy to the A/E imbalance (AEI) recently described for methyl groups by Benno Meier *et al.*(25).

Nevertheless, most experiments where D-DNP is combined with LLS (15-19) rely on *rf* pulses sequences to prepare the LLS *after* the transfer of the hyperpolarized sample to the detection magnet. As a result, extensive relaxation occurs during the transfer. Moreover, these additional manipulations may be difficult to implement. They may take valuable time or require extra hardware. However, Tayler and co-workers (1) have shown that LLS order can be directly populated before the transfer by D-DNP for the two inequivalent ^{13}C spins in 1,2-$^{13}C_2$-pyruvic acid. In their experiment, they demonstrated that a singlet-triplet population imbalance could be created directly by hyperpolarization, *i.e.,* without any extra manipulations of the sample. The amount of TSI, P_{TSI}, that can be created will depend on the nuclear polarization reached, as will be shown in the next section.

8.1.2 Direct enhancement of nuclear singlet order by hyperpolarization

For non-interacting spins-½, by definition of polarization, P_Z = (n_α-n_β)/(n_α+n_β) so that if n_α+n_β = 1, one obtains P_Z = (n_α-n_β). Thus for the normalized population of each energy level we have: P_Z = n_α-(1- n_α), hence n_α=(1+ P_Z)/2; and, likewise, n_β=(1- P_Z)/2. For a pair of inequivalent spins-½ in a strong magnetic field, the eigenstates are given by product states of the form:|$\alpha_1\alpha_2$⟩ = |α_1⟩|α_2⟩, |$\alpha_1\beta_2$⟩ = |α_1⟩|β_2⟩,| $\beta_1\alpha_2$ ⟩ = |β_1⟩|α_2⟩, |$\beta_1\beta_2$⟩ = |β_1⟩|β_2⟩. The populations of these states are given by the products of the populations of the non-interacting nuclei:

$$\begin{aligned} n_{\alpha 1\alpha 2} &= n_{\alpha 1}n_{\alpha 2} = (1+P_Z)(1+P_Z)/4 \\ n_{\beta 1\alpha 2} &= n_{\alpha 1}n_{\beta 2} = (1+P_Z)(1-P_Z)/4 \\ n_{\alpha 1\beta 2} &= n_{\beta 1}n_{\alpha 2} = (1-P_Z)(1+P_Z)/4 \\ n_{\beta 1\beta 2} &= n_{\beta 1}n_{\beta 2} = (1-P_Z)(1-P_Z)/4 \end{aligned} \qquad (8.1)$$

We thus have the following density matrix σ in the product basis (PB), which is the eigenbasis for a weakly coupled IS spin system, with diagonal elements or populations that can be arranged in the form of a vector:

$$\sigma_{PB} = \begin{pmatrix} n_{\alpha\alpha} \\ n_{\alpha\beta} \\ n_{\beta\alpha} \\ n_{\beta\beta} \end{pmatrix} = \frac{1}{4}\begin{pmatrix} (1+P_Z)(1+P_Z) \\ (1+P_Z)(1-P_Z) \\ (1-P_Z)(1+P_Z) \\ (1-P_Z)(1-P_Z) \end{pmatrix} \qquad (8.2)$$

We can define the traceless deviations of the populations $\Delta\sigma = \sigma - E$:

$$\Delta\sigma_{PB} = \begin{pmatrix} \Delta n_{\alpha\alpha} \\ \Delta n_{\alpha\beta} \\ \Delta n_{\beta\alpha} \\ \Delta n_{\beta\beta} \end{pmatrix} = \frac{1}{4}\begin{pmatrix} (1+P_Z)(1+P_Z) \\ (1+P_Z)(1-P_Z) \\ (1-P_Z)(1+P_Z) \\ (1-P_Z)(1-P_Z) \end{pmatrix} - \frac{1}{4}\begin{pmatrix} 1 \\ 1 \\ 1 \\ 1 \end{pmatrix} = \frac{1}{4}\begin{pmatrix} 2P_Z + {P_Z}^2 \\ -{P_Z}^2 \\ -{P_Z}^2 \\ -2P_Z + {P_Z}^2 \end{pmatrix} \tag{8.3}$$

The deviations of populations from the fully saturated state as function of the nuclear Zeeman polarization P_Z, calculated using Equation 8.3 for each eigenstate are shown in Figure 8.1a.

If the two spins *I* and *S* are made equivalent, the density operator is better expressed in a singlet-triplet basis (STB), the eigenbasis of an I_2 system (see Equation 5.6). The transformation from the PB to the symmetry-adapted STB can be done using the conversion matrix (see supplementary material of Reference (26)):

$$\Phi_{PB} = V\Phi_{STB}V^{-1}, \text{ with } V = V^{-1} = \begin{pmatrix} 1 & & & \\ & 2^{-1/2} & 2^{-1/2} & \\ & 2^{-1/2} & -2^{-1/2} & \\ & & & 1 \end{pmatrix} \tag{8.4}$$

Here, since $\Delta n_{\alpha\beta} = \Delta n_{\beta\alpha}$, (and thus also $n_{\alpha\beta} = n_{\beta\alpha}$), it can be easily seen using Equation 8.2, 8.3 and 8.4 that $\Delta\sigma_{PB} = \Delta\sigma_{STB}$ (and hence $\sigma_{PB} = \sigma_{STB}$) with the following diagonal elements:

$$\left(\Delta n_{\alpha\alpha}, \Delta n_{\alpha\beta}, \Delta n_{\beta\alpha}, \Delta n_{\beta\beta}\right) = \left(\Delta n_{T+1}, \Delta n_{T0}, \Delta n_{S0}, \Delta n_{T-1}\right) = \frac{1}{4}\left(2P_Z + P_Z^2, -P_Z^2, -P_Z^2, -2P_Z + P_Z^2\right) \tag{8.5}$$

P_{TSI}, defined as the mean triplet-singlet population difference, can be calculated from the elements of Equation 8.5:

$$P_{TSI} = \Delta n_{S0} - \frac{1}{3}\left(\Delta n_{T+1} + \Delta n_{T0} + \Delta n_{T-1}\right) = -\frac{P_Z^2}{3} \tag{8.6}$$

The TSI will thus result from the depletion of $n_{\alpha\beta}$ and $n_{\beta\alpha}$ by hyperpolarization. The negative sign arises since a strong polarization will deplete the singlet state. Figure 8.1b shows the normalized triplet-singlet population imbalance as a function of the nuclear Zeeman polarization according to Equation 8.6.

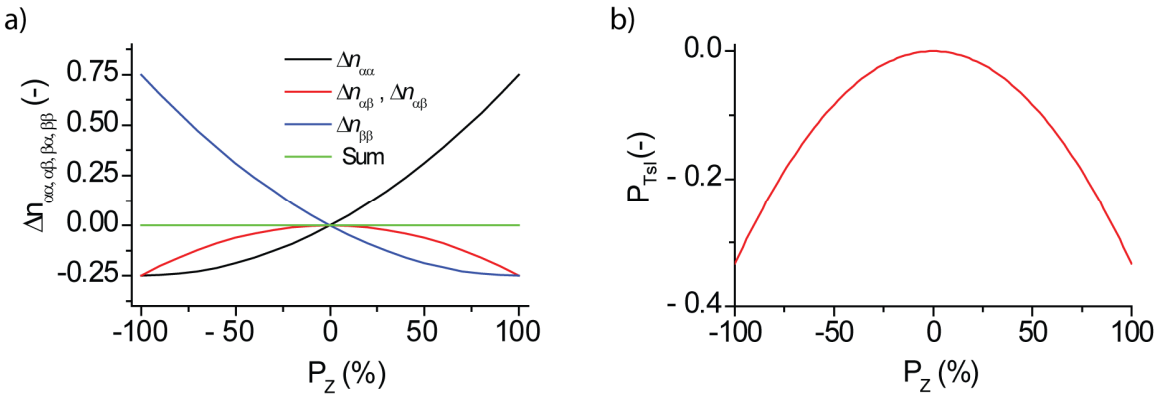

Figure 8.1: **a)** Deviations of populations from the fully saturated state for each eigenstate αα (black), αβ (red), βα (red) and ββ (blue) as function of the nuclear Zeeman polarization P_Z calculated using Equation 8.3 **b)** Normalized triplet-singlet population imbalance as a function of the nuclear Zeeman polarization according to Equation 8.6.

Therefore, provided a high spin polarization can be reached by D-DNP, say P_Z = 50%, a significant amount of singlet order, in this example P_{TSI} = - 8.33%, can be created directly without any *rf* pulses. In the case where P_Z = 91% can be achieved, one obtains P_{TSI} = - 28%. Such high levels of polarization can indeed be prepared directly by DNP for ^{1}H at B_0 = 6.7 T and T = 1.2 K and indirectly for ^{13}C or other nuclei via Cross Polarization from ^{1}H (27).

In this Chapter, I will demonstrate that a TSI can also be efficiently populated by D-DNP in a pair of *magnetically equivalent* ^{1}H spins, and that this TSI is preserved in the liquid state after dissolution for a long time T_{TSI}. This type of LLS will be referred to as Hyperpolarized Equivalent Long-Lived States (HELLS)(2).

8.2 Imposing or breaking symmetry in LLS experiments

The experimental challenge of any study of Long-Lived States consists in manipulating the symmetry of the spin system involved, since the magnetic equivalence needs to be lifted both during excitation and detection but preserved during storage. In this context, two possible scenarios are: 1) in most experiments described so far, the symmetry is imposed on an otherwise inequivalent two-spin system during the storage period only, or 2), like in the present experiment, the symmetry of an inherently equivalent two-spin system is broken during both excitation and detection (See Figure 8.2).

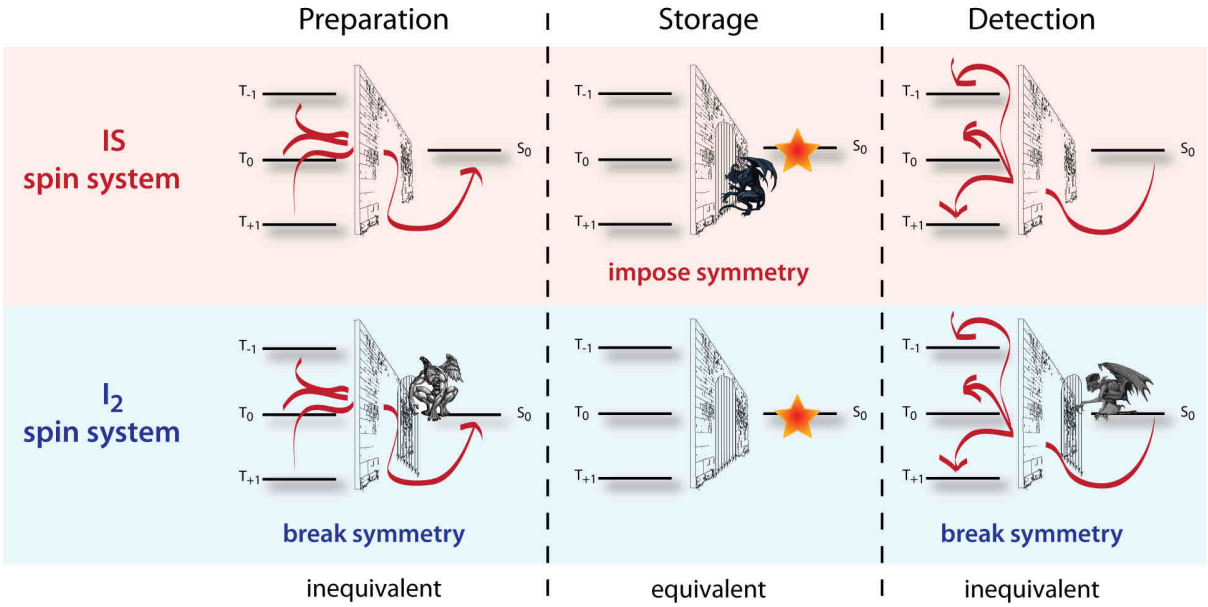

Figure 8.2: Schematic representation of experimental LLS scenarios where the symmetry is either imposed during the storage phase on an inequivalent IS spin system (upper part) or where the symmetry of an equivalent I_2 spin system is broken during the excitation and the detection (lower part).

If one starts with an inequivalent two-spin system, a precursor state, *i.e.,* a state that acquires a long-lived property as soon as the two spins are made equivalent during the storage interval, can be prepared, normally by suitable *rf* pulse sequences, or directly by hyperpolarizing the sample (1). The symmetry can then be imposed on the precursor state, either by *rf* irradiation (28, 29), by adiabatic transport to low fields (18, 30) or by chemical reactions (16). Alternatively, a compromise can be found by using systems containing nearly equivalent spins (31) where the singlet and triplet states are only weakly mixed, but where their admixture can be augmented by suitable pulse sequences to induce a magnetization-to-singlet (M2S) conversion for the excitation, reversed by a singlet-to-magnetization (S2M) conversion prior to detection.

Para-hydrogen (32-34) offers a good example of nuclear singlet order in a molecule with two equivalent spins. The singlet state of H_2 can be produced at low temperatures (typically 40 K) in the presence of a paramagnetic catalyst which allows singlet-triplet inter-conversion by lifting the symmetry of H_2 near the catalytic surface. The singlet spin state of H_2 has the lowest energy, primarily determined by the quantization of its rotational state, and therefore is predominantly populated at low temperatures. This leads to the creation of a large TSI, compared to H_2 in Boltzmann equilibrium at room temperature. *Para*-H_2 is not magnetically active and therefore cannot be observed directly by NMR, but it can be converted into observable signals through an asymmetric hydrogenation reaction where the two protons stemming from *para*-H_2 become inequivalent.

8.3 HELLS experiments

The goal of this study was to demonstrate experimentally that it is possible to populate by DNP a triplet-singlet imbalance (TSI) in a system with two magnetically equivalent spins and that this TSI can be stored after dissolution in liquid state. As can be seen in Figure 8.2, even if the storage is straightforward, an

experimental complication arises when working with LLS in equivalent spin systems: the symmetry of the molecule has to be lifted during the excitation and detection phase. The HELLS experiment was designed to verify the postulate that the symmetry is broken under DNP conditions (in a static solid at low temperature in the presence of free electrons); but in order to detect a signal, a "de-symmetrization" step has to be added. Fumarate was chosen as test molecule with equivalent spins, and we used the enzymatic conversion of fumarate into malate to reveal the TSI sealed in the form of unobservable Long-Lived States in fumarate.

8.3.1 Energy levels and flow of populations during HELLS experiments

Preparation of a triplet-singlet imbalance under DNP conditions

For efficient D-DNP, the samples usually consists of frozen glassy solids containing typically 10-50 mM polarizing agents such as TEMPOL in addition to the molecules of interest. In our experiments, the molecule of interest shall possess two spins *I* and *S* that are magnetically equivalent in solution, but that are inequivalent in the frozen state in moderate magnetic fields since they are exposed to slightly different environments and therefore experience different chemical shifts because of chemical shift anisotropies (CSA) and different inter-nuclear as well as electron-nuclear dipolar couplings. Given that freezing to low temperatures lifts the equivalence, the energy levels are better expressed in the product basis (PB). At T = 1.2 K and B_0 = 6.7 T, the proton Boltzmann polarization without DNP is P_Z = 0.57% see Equation 1.7). Therefore, as shown in Equation 8.3, the deviations of the diagonal elements of the density matrix from the demagnetized state, $\Delta\sigma = \sigma - E$, will be ($\Delta n_{\alpha\alpha}$, $\Delta n_{\alpha\beta}$, $\Delta n_{\beta\alpha}$, $\Delta n_{\beta\beta}$) = ¼ ($2P_Z + P_Z^2$, $-P_Z^2$, $-P_Z^2$, $-2P_Z + P_Z^2$) = (0.003, 0, 0, -0.003). Assuming for simplicity that DNP could confer a Zeeman polarization P_Z = 100%, only the lowest energy level $|\alpha\alpha\rangle$ would be populated by hyperpolarization, so that ($\Delta n_{\alpha\alpha}$, $\Delta n_{\alpha\beta}$, $\Delta n_{\beta\alpha}$, $\Delta n_{\beta\beta}$) = (0.75, -0.25, -0.25, -0.25) (see Figure 8.3a: TSI Preparation and Figure 8.1a). For a Zeeman polarization P_Z = 91%, that can readily be achieved experimentally, one obtains ($\Delta n_{\alpha\alpha}$, $\Delta n_{\alpha\beta}$, $\Delta n_{\beta\alpha}$, $\Delta n_{\beta\beta}$) = (0.66, -0.2, -0.2, -0.25).

Storage of triplet-singlet imbalance at low or high field

As soon as the polarized sample is heated and dissolved, chemical shift anisotropies (CSA) and dipolar couplings are averaged out, so that the spins *I* and *S* become magnetically equivalent. The density operator can therefore better be expressed in the singlet-triplet basis (STB). As the energy levels αβ and βα remain equally populated (see Figure 8.1a), one obtains $\Delta\sigma_{PB} = \Delta\sigma_{STB}$ with the diagonal elements of Equation 8.5. As shown in Equation 8.6, the triplet-singlet population imbalance $P_{TSI} = -P_z^2/3$. The TSI can be stored indifferently at low or high magnetic field (for example in a magnetic tunnel (12)). During the storage period, the populations of the three triplet states will equilibrate, *i.e.*, the deviations of the populations of the three triplet levels will average out because of dipole-dipole relaxation to give:

$$\left(\Delta n_{T+1}\right)' = \left(\Delta n_{T0}\right)' = \left(\Delta n_{T-1}\right)' = \frac{1}{3}\left(\Delta n_{T+1} + \Delta n_0 + \Delta n_{T-1}\right) = \frac{1}{4}\frac{P_Z^2}{3} \qquad (8.7)$$

Since the singlet should not be affected by dipole-dipole relaxation, the triplet-singlet imbalance in principle remains equal to $P_{TSI} = -P_Z^2/3$ (see Figure 8.3b: TSI Storage).

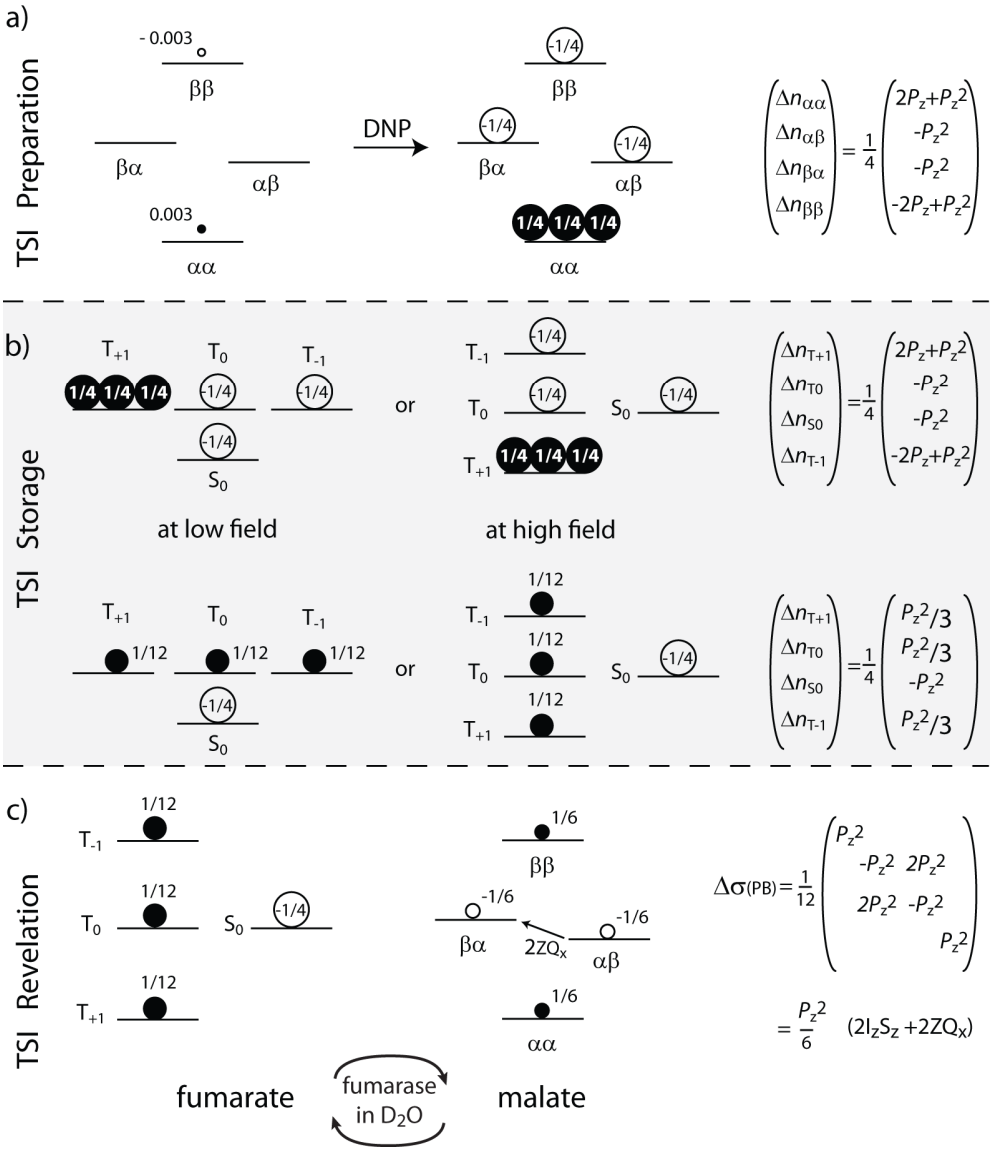

Figure 8.3: Schematic deviations of the populations with respect to the fully saturated state Δσ = σ - E among the energy levels of the two protons of fumarate ***a)*** (left) in the polarizer at 6.7 T and 1.2 K without DNP at Boltzmann equilibrium ($P_z(^1H)$ = 0.57%) and (right) after DNP polarization to the theoretical limit $P_z(^1H)$ = 100%, ***b)*** during the transfer, which may go through low magnetic fields or through a magnetic tunnel to sustain a higher field, ***c)*** in the detection magnet, typically at 7 T and 300 K, where the spins are made inequivalent by an enzymatic conversion. In each scheme, the deviations of the diagonal elements from the demagnetized state Δσ = σ - E are given as a function of the polarization P_z. In (*c*), the off-diagonal elements of the density matrix (zero-quantum coherences) are also shown.

Revelation of the triplet-singlet imbalance

The sample is then transferred to the NMR or MRI magnet for detection. The system of two equivalent spins can then be transformed (chemically or enzymatically) into a system of two *in*equivalent spins, so that the 'sealed' hyperpolarization can be 'revealed' by conversion into observable magnetization. If the

reaction is fast and goes to completion, one can convert Δσ from the STB to the PB, using the suitable base transformation in Equation 8.4 (26, 35):

$$\Delta\sigma_{PB} = V\Delta\sigma_{STB}V^{-1} = \frac{1}{12}\begin{pmatrix} P_Z^2 & & & \\ & -P_Z^2 & 2P_Z^2 & \\ & 2P_Z^2 & -P_Z^2 & \\ & & & P_Z^2 \end{pmatrix} \tag{8.8}$$

The resulting density matrix $\Delta\sigma_{PB}$ shown in Equation 8.8 can be expressed as a superposition of longitudinal two-spin order and zero-quantum coherences (their matrix representations in the product basis can be found in Appendix 9.2 of Reference (36)) (see Figure 8.3c: TSI Revelation):

$$\Delta\sigma_{PB} = \frac{P_Z^2}{6}\left(2I_zS_z + 2ZQ_x\right) \tag{8.9}$$

Therefore, after the symmetry-breaking reaction, an NMR pulse sequence that convert $2I_zS_z + 2ZQ_x$ into observable magnetization is needed to reveal the TSI created by DNP. Ideally, this sequence should reject other terms, like single quantum magnetization that may be present because of incomplete polarization in step (*a*) or relaxation in step (*b*). If these two conditions are fulfilled, the detection of a signal will unambiguously constitute a proof of the creation of a triplet-singlet imbalance (TSI) in molecules with magnetically equivalent spins by hyperpolarization, which is only possible if the symmetry of the molecule is lifted during the DNP process in the polarizer.

8.3.2 Slow fumarate to malate enzymatic conversion: problems and solutions

To test the HELLS experiment, we chose the two equivalent protons of fumarate as a receptacle of triplet-singlet imbalance. The symmetry of the molecule can be lifted by the enzymatic conversion of fumarate into malate by fumarase in D_2O (see insert of Figure 8.4).

Enzymatic reactions are not instantaneous, and do not necessarily lead to a complete conversion into the product. Figure 8.4 shows an example of the conversion of fumarate into malate by fumarase under conditions that can be combined with D-DNP. The steady-state concentrations are only reached after 25 minutes. This has important implications for our experiment. In fact, a highly polarized state $\Delta\sigma = 2I_zS_z + 2ZQ_x$ is indeed produced instantaneously in malate whenever fumarate molecules carrying a TSI undergo an enzymatic conversion, but the ZQ_x term immediately starts evolving under the difference of chemical shifts, and therefore rapidly dephases and averages to zero as the reaction goes on. Furthermore, the hyperpolarized TSI of fumarate, once it is transferred to malate and converted into longitudinal two-spin order and zero-quantum coherence as shown in Equation 8.9, will tend to relax to thermal Boltzmann equilibrium by efficient relaxation mechanisms.

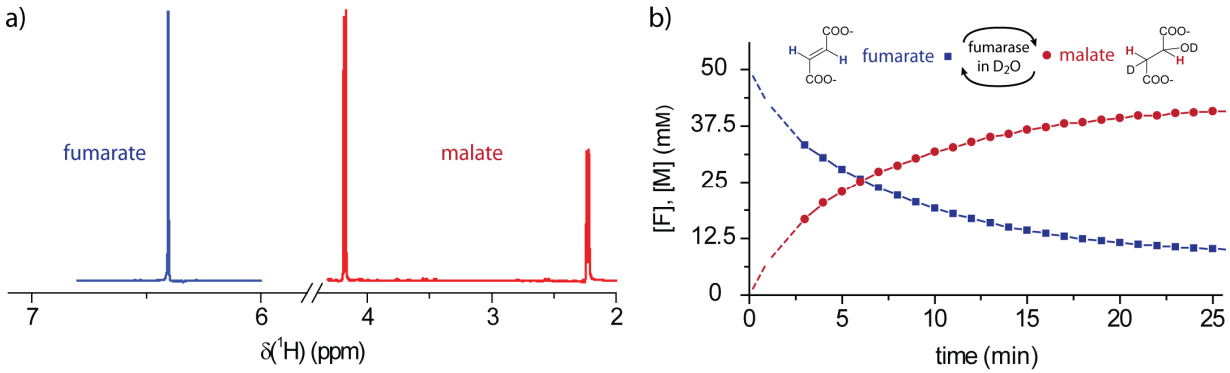

Figure 8.4: ***a)*** Proton NMR spectrum of fumarate and malate. ***b)*** Enzymatic conversion of fumarate into malate by fumarase at 300 K monitored by integration of the conventional ^{1}H NMR signals of the two species. The nuclear polarizations are in thermal Boltzmann equilibrium, without resorting to DNP. A volume of 4 µL of a 5.8 mg/mL solution of fumarase (*i.e.*, 10 units) was injected into 500 µL of a 50 mM fumarate solution at pH 8 in a buffer of 25 mM TRIS and 200 mM NaCl.

To counter these two problems, it is however possible to sustain the LLS of malate by so-called 'high field' methods (24, 26, 28) like in the LLS sequence used in Chapter 5, *e.g.*, by applying an *rf* irradiation half-way between the two chemical shifts (either by applying a continuous-wave (CW) irradiation, or, if desired, a WALTZ-16 pulse train) (29), thus preserving as much as possible the full $\Delta\sigma = 2I_zS_z + 2ZQ_x$ state. This strategy allows one to slow down relaxation of $2I_zS_z$ and prevent dephasing of ZQ_x. For the two inequivalent protons in malate, we thus determined T_{LLS} = 6 s at B_0 = 7 T and T = 298 K. Moreover, the use of WALTZ-16 pulse trains has the advantage of wiping out any single-quantum magnetization that does not arise from HELLS. A conventional LLS detection sequence, *e.g.*, the second half of the 'Sarkar sequence'(26) (Figure 8.5) can finally be used to transform $\Delta\sigma = 2I_zS_z + 2ZQ_x$ into observable magnetization.

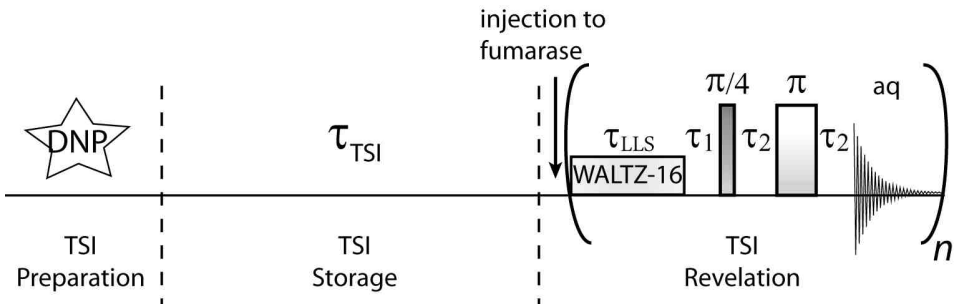

Figure 8.5: Timing of a HELLS experiment. The protons of fumarate are hyperpolarized at 6.7 T and 1.2 K. The hyperpolarized sample is then dissolved and stored in a holding chamber at high field during a delay τ_{TSI}. Finally hyperpolarized fumarate is injected into a solution containing fumarase which will start the enzymatic conversion from fumarate into malate. Concurrently, a WALTZ-16 pulse train is applied with an *rf* amplitude ν_1 = 3 kHz during the delay τ_{LLS}. The remainder of the detection pulse sequence is identical to the second half of the sequence described in Section 5.1.2. The conversion of the LLS into observable magnetization is most efficient when $\tau_1 = 1/4J_{IS}$ and $\tau_2 = 1/2\Delta\nu_{IS}$ (in malate J_{IS} = 10.4 Hz and $\Delta\nu_{IS}$ = 960 Hz at 300 MHz.) The detection scheme can be repeated *n* times.

After dissolution, the hyperpolarized solution containing fumarate that carries the triplet-singlet imbalance (TSI) is transferred to a holding chamber just above the NMR tube to determine its lifetime T_{TSI}

during a variable pre-injection delay τ_{TSI}. The fumarate solution is then injected into a solution containing fumarase to start the conversion of fumarate into malate, accompanied by a conversion of the TSI of fumarate into an LLS of malate. A WALTZ-16 pulses train is applied during a delay τ_{LLS} with the carrier half-way between the chemical shifts of the two protons of malate in order to make these two protons effectively equivalent. As will be developed in the next Section, this "accumulation delay" τ_{LLS} has to be optimized to maximize the signal observed. This optimization has to take into account the slow enzymatic conversion of the TSI stored in fumarate into malate and the fast relaxation of malate magnetization. The detection scheme can be repeated *n* times, bearing in mind that the LLS on malate is replenished during each sustaining interval τ_{LLS} by enzymatic conversion of fumarate that carries a slowly relaxing TSI.

8.3.3 Optimization of malate accumulation time

Since the lifetime of the LLS of malate (T_{LLS}^{M} = 6 s at 300 MHz if the *rf* amplitude of the CW field is ν_1 = 3 kHz) is short compared to the enzymatic transformation timescale, the time τ_{LLS} (see Figure 8.5) allocated for the LLS to accumulate in malate before it is converted into observable signals needs to be carefully optimized. The concentrations [*F*] and [*M*] of fumarate and malate can be described by pseudo first-order kinetics:

$$\begin{cases} \dfrac{d[F](t)}{dt} = -k_{FM}[F](t) + k_{MF}[M](t) \\ \dfrac{d[M](t)}{dt} = -k_{MF}[M](t) + k_{FM}[F](t) \end{cases} \tag{8.10}$$

where [*F*](t) and [*M*](t) are the concentrations of fumarate and malate, k_{FM} and k_{MF} are the *apparent* kinetic constants of the overall enzymatic conversion of fumarate into malate and vice-versa, without considering the details of the Michaelis-Menten mechanism.

The temporal evolution of the expectation value P_{LLS}^{M} in malate arising from the conversion of fumarate under *rf* irradiation can be obtained solving the rate equations:

$$\begin{cases} \dfrac{dP_{TSI}^{F}(t)}{dt} = -\left(k_{FM} + R_{TSI}^{F}\right)P_{TSI}^{F}(t) + k_{MF}P_{LLS}^{M}(t) \\ \dfrac{dP_{LLS}^{M}(t)}{dt} = -\left(k_{MF} + R_{LLS}^{M}\right)P_{LLS}^{M}(t) + k_{FM}P_{TSI}^{F}(t) \end{cases} \tag{8.11}$$

where P_{TSI}^{F} and P_{LLS}^{M} are the expectation values of the triplet-singlet imbalance in fumarate and the long-lived state in malate, and R_{TSI}^{F} and R_{LLS}^{M} are their relaxation rates.

The 'apparent' rate constants k_{FM} and k_{MF} can be obtained by fitting the signal amplitudes in Figure 8.4*b* to the rate equations 8.10. One can then predict, by solving the rate equations 8.11, the temporal evolution of P_{TSI}^{F} in fumarate in the presence of 10 units of enzyme, as well as P_{LLS}^{M} of malate obtained by the conversion of the TSI of fumarate into an LLS of malate that relaxes with R_{LLS}^{M} (Figure 8.6). These curves were obtained by assuming that T_{TSI}^{F} = 60 s for fumarate (based on preliminary observations discussed below), and using the experimentally determined time constant T_{LLS}^{M} = 6 s for malate. According to Figure 8.6, the optimal delay to maximize the conversion of the TSI of fumarate into LLS of

malate is 10 s. Thus one should wait τ_{LLS} = 10 s while sustaining the LLS by a suitable *rf* field before attempting to convert the LLS of malate into observable magnetization. The alternation of *rf* irradiation intervals and signal observation can be repeated *n* times. During each interval τ_{LLS} the LLS of malate will be replenished by the enzymatic conversion of the slowly relaxing TSI of fumarate. The decay of the magnetically silent TSI of fumarate will be indirectly reflected in the decay of the malate signal as *n* increases. Moreover, it can be seen in Figure 8.6b that only *ca*. 1% of the HELLS of fumarate is transferred to malate during each loop *n* = 1, 2, … , *N*.

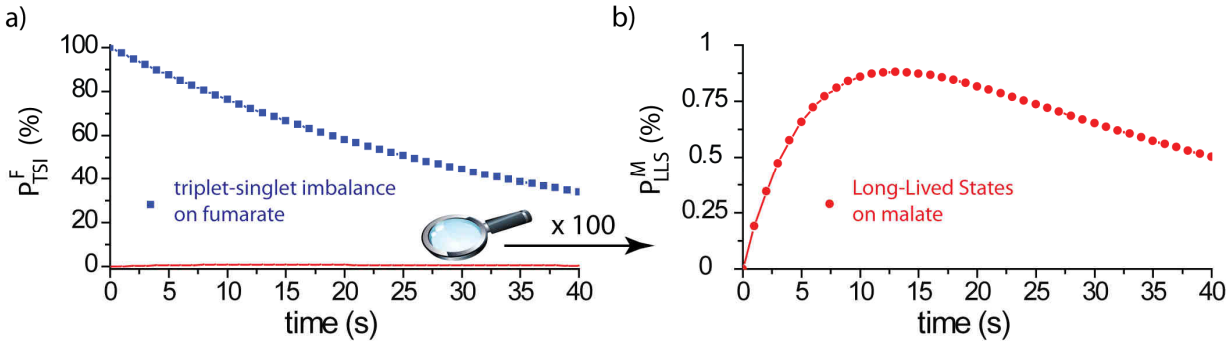

Figure 8.6: Temporal evolution of the (unobservable) triplet-singlet imbalance (P_{TSI}) of fumarate **(*a*)** and of the signal of malate **(*b*)** obtained by numerical solution of Equation 8.11 with T_{TSI}^F = 60 s and T_{LLS}^M = 6 s, and the apparent forward and backward rate constants k_{MF} = 4.5 10^{-4} s^{-1} and k_{FM} = 3.7 10^{-4} s^{-1} = 0.825 k_{MF} optimized by fitting the curves in Figure 8.4 with Equation 8.10. The vertical scale was increased 100 times in (*b*) to show the malate signal, which is barely visible as (-•-) in (*a*) because of the slow rate of the enzymatic conversion.

8.3.4 Results

A sample comprising 10 frozen pellets of 10 µL each of 0.5 M fumarate with 50 mM TEMPOL was hyperpolarized by monochromatic microwave irradiation at B_0 = 6.7 T and *T* = 1.2 K for about 20 min. The sample was then dissolved, together with 10 frozen pellets of 10 µL each of 3 M sodium ascorbate in D_2O (8), with 5 mL D_2O at 400 K and 1.0 MPa, and transferred in 4.5 s to a holding chamber just above the magnetic center of a 7 T NMR (300 MHz) spectrometer, where the static field is B_{hold} > 6.5 T. After a pre-injection delay 1 < τ_{TSI} < 60 s that allows one to assess the lifetime T_{TSI} of the triplet-singlet imbalance (P_{TSI}) of hyperpolarized fumarate in the holding chamber, the solution was injected into a 5 mm NMR tube containing fumarase to start the conversion of fumarate into malate, and concomitantly to transfer the TSI of fumarate into an LLS on malate. The latter was sustained by a WALTZ-16 pulse train with an *rf* amplitude ν_1 = 3 kHz. The sequence of Figure 8.5 was then used to convert the LLS of malate into observable magnetization.

Figure 8.7d shows four spectra of malate acquired at 7 s intervals (*N* = 4 loops, each comprising a sustaining interval τ_{LLS} = 6 s and an acquisition time, *aq*, of 1 s) after the injection of hyperpolarized fumarate into the NMR tube containing fumarase. In this case, the pre-injection delay τ_{TSI} = 1 s where the fumarate was kept in the holding chamber was negligible compared to T_{TSI}^F. Since the enzymatic conversion is relatively slow, the signals of Figure 8.7d arise from the conversion of a small fraction of fumarate into malate (*ca.* 1% every 7 s, according to Figure 8.6b). To be more precise, taking into account the dissolution (100 µL frozen DNP sample containing 0.5 M fumarate diluted by 5mL of D_2O), the triplet-singlet polarization after relaxation (P_{TSI} = $-P_z^2/3$ = -27.6% for the best possible polarization $P_z(^1H)$ = 91%), the slow enzymatic conversion and the limited quantum yield (ca. 50%) of the conversion of the LLS into single quantum coherence during the detection sequence, the signal detected without

cryoprobe in Figure 8.7d corresponds to a malate concentration of 7 µM. The signal is thus quite intense, even if the SNR appears modest.

The decay of the malate signal with increasing n reflects (*i*) the decay of the unobservable TSI of fumarate with a time constant T_{TSI}^{F} due to its relaxation (believed to be very slow), (*ii*) the consumption of fumarate with a time constant $1/k_{FM}$ due to its enzymatic conversion into malate, and (*iii*) the decay of the LLS of malate with a time constant T_{LLS}^{M} = 6 s (Figure 8.6a) However, it appears risky to extract an estimate of T_{TSI}^{F} from numerical fits of a single decay.

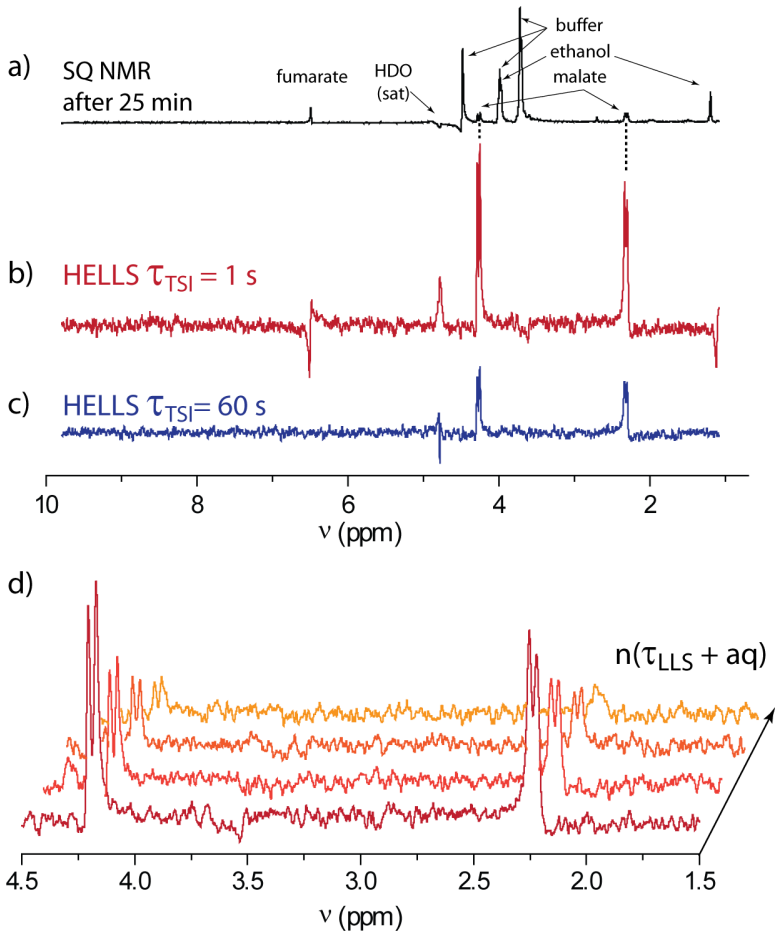

Figure 8.7: ***a***) Conventional NMR spectrum excited by a 90° pulse 25 min after injection of fumarate into a solution containing fumarase, when the enzymatic reaction has reached a steady state and the hyperpolarization (both P_{TSI}^{F} in fumarate and P_{LLS}^{M} in malate) has decayed to thermal equilibrium. Note the signals of fumarate, malate, ethanol and buffer. The HDO peak was attenuated by pre-saturation with a selective pulse with an rf amplitude of 75 Hz and a duration of 5 s. ***b***) Spectrum of malate (without significant stopover in the holding chamber since τ_{TSI} = 1 s << T_{TSI}^{F}) recorded with the sequence of Figure 8.5, shortly after injection (n = 1) into a solution containing fumarase in the 7 T NMR system. ***c)*** Spectrum of malate recorded after keeping the hyperpolarized fumarate for τ_{TSI} = 60 s in the holding chamber at B_0 > 6.5 T prior to injection into the fumarase solution. ***d***) The first four spectra of malate acquired with n = 1, 2, 3 and 4 at intervals of 7 s using the sequence in Figure 8.5 (τ_{TSI} = 1 s, τ_{LLS} = 6 s, acquisition time 1 s) showing that P_{LLS}^{M} is replenished through the enzymatic reaction.

The lifetime T_{TSI}^{F} can be estimated more accurately by repeating the entire experiment after keeping the fumarate that carries the hyperpolarized TSI in the holding chamber during a longer pre-injection delay

τ_{TSI} = 60 s. Although it is challenging to reproduce the experiment under identical conditions, we were able to observe that the remaining signal of malate after τ_{TSI} = 60 s was reduced by a factor of *ca*. 3.5 (Fig 8.7b,c), implying that $T_{TSI}^{F} \approx 50$ s. This is somewhat shorter than the lifetime T_{TSI} = 270 s reported by Zhang *et al.* (37) for deuterated dimethyl maleate produced by addition of *para*-H_2 onto deuterated dimethyl acetylene dicarboxylate. This discrepancy may be due to the presence of dissolved paramagnetic triplet oxygen in the superheated water used in our dissolution experiments, or to the presence of some residual TEMPOL radicals since its reduction by ascorbate may not be quantitative. Because the WALTZ-16 pulse train destroys magnetization arising from any sources other than HELLS, single-quantum terms arising either from D-DNP or from a partial return to thermal Boltzmann equilibrium are wiped out (compare Figure 8.7b,c with Figure 8.7a). The detected signals can therefore unambiguously be traced back to the TSI of fumarate prepared by D-DNP, stored in the holding chamber for a time τ_{TSI}, and converted into LLS of malate by the enzyme. The remaining peaks of fumarate and HDO in the spectrum of Figure 8.7b probably stem from hyperpolarized single-quantum magnetization that has not been fully saturated by the WALTZ-16 pulse train and was brought into the active volume of the *rf* coil by convection.

The HELLS experiment proves that a pure triplet-singlet imbalance (TSI) can be readily created by D-DNP in a system that contains two spins that are magnetically equivalent in solution. Once dissolved, this imbalance displays a lifetime T_{TSI} that is much longer than the longitudinal relaxation time T_1. This is believed to be the first proof of principle of the creation of Hyperpolarized Long-Lived States for equivalent spins (HELLS) by D-DNP. Such a long-lived spin order can readily be used to monitor a slow enzymatic process of biochemical relevance, but may find applications in other areas of magnetic resonance such as imaging (MRI) where hyperpolarization by D-DNP has become a technique of choice to enable metabolic imaging, and where short lifetimes of hyperpolarized molecules are usually a major limitation. As fumarate plays a crucial role in the Krebs cycle, it may be of interest for *in-vivo* studies as it has been demonstrated to be a probe for cellular necrosis (38). The HELLS methodology could be applied to more challenging molecules containing magnetically equivalent pairs of spins, such as CH_2RR', CH_2Cl_2, and possibly H_2O as discussed in the next Section.

8.4 To go further: *para*-water

An ongoing project in our group that was started by Dr. Nicola Salvi and is now coordinated by Daniele Mammoli, is to render the singlet state in *para*-H_2O accessible to indirect NMR observation. The term *para*-water is used by analogy to *para*-hydrogen. The *para*- and *ortho*- forms of H_2O can be separated in molecular beams (39), and *para*-water can be prepared if it is trapped in C_{60} cages (40). Parallel strategies are developed in our group to lift the symmetry of the water molecule and allow one to excite and observe a triplet-singlet imbalance, for example by adsorption of water vapor to a chiral surface, by hydration of gypsum or by rapid chemical addition of H_2O to chloral CCl_3CHO.

It appeared that freezing H_2O in aprotic solvent under DNP conditions could be a good method to lift the symmetry of the two protons either through intermolecular dipole-dipole interactions (41) or through the anisotropy of their chemical shifts (42). Indeed, it can be seen in the proton spectra of H_2O diluted in DMSO-d_6 doped with TEMPO and frozen at *ca.* 1.2 K in a field of 6.7 T (Figure 8.8) that the degeneracy of the two spins is lifted. As a result, the anti-symmetric *para*-state is mixed with the central triplet state, and singlet/triplet inter-conversion can occur. As shown in this Chapter, hyperpolarization of proton spins by DNP can indeed create a precursor state characterized by a singlet-triplet imbalance. In Figure 8.8b a proton spectrum excited by a 1^o pulse is recorded every 50 s after starting irradiation with a

resonant microwave field. The spectrum in Figure 8.8a corresponds to a modest ^{1}H polarization, close to Boltzmann equilibrium at 1.2 K, while Figure 8.8c corresponds to the highest polarization that could be reached by microwave irradiation. The rising polarization is accompanied by a growing asymmetry of the spectra due to the increasing population of the lowest-lying state.

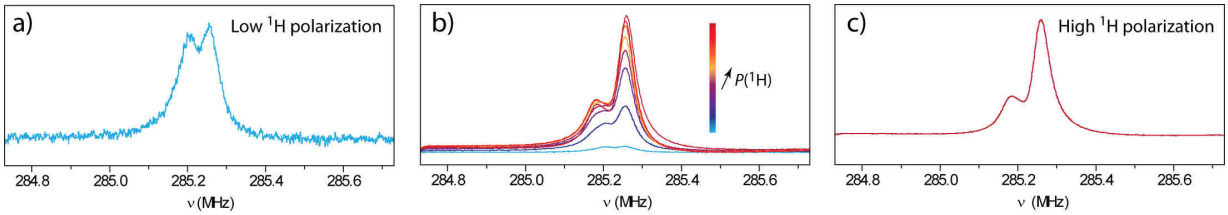

Figure 8.8: Proton spectra of 20 % H_2O diluted in 80 % DMSO-d_6 with 50 mM TEMPOL at 6.7 T and 1.2 K **a)** at low (Boltzmann) polarization, **b)** recorded every 50 s with 100 mW µW irradiation at 187.7 GHz, **c)** at maximal DNP polarization.

The expressions of Equations 8.2 and 8.3 can be rewritten in terms of superpositions of the population operators I_Z, S_Z, $2I_ZS_Z$ and E (36):

$$\sigma_{PB} = \frac{P_Z}{2}\left(I_Z + S_Z\right) + \frac{P_Z^{\,2}}{2} 2I_ZS_Z + E \tag{8.12}$$

$$\Delta\sigma_{PB} = \frac{P_Z}{2}\left(I_Z + S_Z\right) + \frac{P_Z^{\,2}}{2} 2I_ZS_Z \tag{8.13}$$

The presence of the two-spin order term explains the growing asymmetry in the spectra of Figure 8.8 as the nuclear Zeeman polarization increases.

At high polarization levels, the expressions in Equation 8.12 and 8.13 will correspond to a triplet-singlet imbalance once the spins become equivalent after dissolution. Hyperpolarized *para*-H_2O should in principle be long-lived. Nevertheless, the excitation of TSI of the two magnetically equivalent spins in water is only the first step in the quest for observing *para*-water. The problem of rapid proton exchange, the presence of some paramagnetic polarizing agents during storage, and the need to lift the symmetry for detection represent additional challenges.

The HELLS experiment presented in this Chapter was originally designed to obtain experimental evidence that a long-lived triplet-singlet imbalance can be created in a system with two equivalent spins, as occur in H_2O, while circumventing the difficulty of proton exchange that cannot occur in fumarate, when the sample is frozen and hyperpolarized under DNP conditions. Thus, to finish this last chapter, I could site the good words of Dr. Takuya Segawa: "*Para*-(d)ice can be created out of HELLS".

References

1. Tayler MCD, Marco-Rius I, Kettunen MI, Brindle KM, Levitt MH, & Pileio G (2012) Direct Enhancement of Nuclear Singlet Order by Dynamic Nuclear Polarization. *J. Am. Chem. Soc.* 134(18):7668-7671.

2. Bornet A, Ji X, Mammoli D, Vuichoud B, Milani J, Bodenhausen G, & Jannin S (2014) Long-Lived States of Magnetically Equivalent Spins Populated by Dissolution-DNP and Revealed by Enzymatic Reactions. *Chem. Eur. J.* 20(51):17113-17118.
3. Day SE, Kettunen MI, Gallagher FA, Hu DE, Lerche M, Wolber J, Golman K, Ardenkjaer-Larsen JH, & Brindle KM (2007) Detecting tumor response to treatment using hyperpolarized C-13 magnetic resonance imaging and spectroscopy. *Nat. Med.* 13(11):1382-1387.
4. Karlsson M, Jensen PR, Duus JO, Meier S, & Lerche MH (2012) Development of Dissolution DNP-MR Substrates for Metabolic Research. *Appl. Magn. Reson.* 43(1-2):223-236.
5. Buratto R, Bornet A, Milani J, Mammoli D, Vuichoud B, Salvi N, Singh M, Laguerre A, Passemard S, Gerber-Lemaire S, Jannin S, & Bodenhausen G (2014) Drug screening boosted by hyperpolarized long-lived States in NMR. *ChemMedChem* 9(11):2509-2515.
6. Harris T, Szekely O, & Frydman L (2014) On the Potential of Hyperpolarized Water in Biomolecular NMR Studies. *J. Phys. Chem. B* 118(12):3281-3290.
7. Bowen S &Hilty C (2010) Rapid sample injection for hyperpolarized NMR spectroscopy. *Phys. Chem. Chem. Phys.* 12(22):5766-5770.
8. Mieville P, Ahuja P, Sarkar R, Jannin S, Vasos PR, Gerber-Lemaire S, Mishkovsky M, Comment A, Gruetter R, Ouari O, Tordo P, & Bodenhausen G (2010) Scavenging Free Radicals To Preserve Enhancement and Extend Relaxation Times in NMR using Dynamic Nuclear Polarization. *Angew. Chem. Int. Edit.* 49(35):6182-6185.
9. Harris T, Bretschneider C, & Frydman L (2011) Dissolution DNP NMR with solvent mixtures: Substrate concentration and radical extraction. *J. Magn. Reson.* 211(1):96-100.
10. Ardenkjaer-Larsen JH, Leach AM, Clarke N, Urbahn J, Anderson D, & Skloss TW (2011) Dynamic Nuclear Polarization Polarizer for Sterile Use Intent. *NMR Biomed.* 24(8):927-932.
11. Gajan D, Bornet A, Vuichoud B, Milani J, Melzi R, van Kalkeren HA, Veyre L, Thieuleux C, Conley MP, Gruning WR, Schwarzwalder M, Lesage A, Coperet C, Bodenhausen G, Emsley L, & Jannin S (2014) Hybrid polarizing solids for pure hyperpolarized liquids through dissolution dynamic nuclear polarization. *Proc. Natl. Acad. Sci. U. S. A.* 111(41):14693-14697.
12. Milani J, Vuichoud B, Bornet A, Mieville P, Mottier R, Jannin S, & Bodenhausen G (2015) A Magnetic Tunnel to Shelter Hyperpolarized Fluids. *Rev. Sci. Instrum.*
13. Levitt MH (2010) Singlet and other states with extended lifetimes. *Encyclopedia of Nuclear Magnetic Resonance*, ed RK Harris RWChichester, UK), Wiley Ed.
14. Levitt MH (2012) Singlet Nuclear Magnetic Resonance. *Annu. Rev. Phys. Chem.* 63:89-105.
15. Vasos PR, Comment A, Sarkar R, Ahuja P, Jannin S, Ansermet JP, Konter JA, Hautle P, van den Brandt B, & Bodenhausen G (2009) Long-lived states to sustain hyperpolarized magnetization. *Proc. Natl. Acad. Sci. U.S.A.* 106(44):18469-18473.
16. Warren WS, Jenista E, Branca RT, & Chen X (2009) Increasing Hyperpolarized Spin Lifetimes Through True Singlet Eigenstates. *Science* 323(5922):1711-1714.
17. Ahuja P, Sarkar R, Jannin S, Vasos PR, & Bodenhausen G (2010) Proton hyperpolarisation preserved in long-lived states. *Chem. Commun.* 46(43):8192-8194.
18. Bornet A, Jannin S, & Bodenhausen G (2011) Three-field NMR to preserve hyperpolarized proton magnetization as long-lived states in moderate magnetic fields. *Chem. Phys. Lett.* 512(4-6):151-154.
19. Laustsen C, Pileio G, Tayler MCD, Brown LJ, Brown RCD, Levitt MH, & Ardenkjaer-Larsen JH (2012) Hyperpolarized singlet NMR on a small animal imaging system. *Magn. Reson. Med.* 68(4):1262-1265.
20. Marco-Rius I, Tayler MCD, Kettunen MI, Larkin TJ, Timm KN, Serrao EM, Rodrigues TB, Pileio G, Ardenkjaer-Larsen JH, Levitt MH, & Brindle KM (2013) Hyperpolarized singlet lifetimes of pyruvate in human blood and in the mouse. *NMR Biomed.* 26(12):1696-1704.

21. Pileio G, Bowen S, Laustsen C, Tayler MCD, Hill-Cousins JT, Brown LJ, Brown RCD, Ardenkjaer-Larsen JH, & Levitt MH (2013) Recycling and Imaging of Nuclear Singlet Hyperpolarization. *J. Am. Chem. Soc.* 135(13):5084-5088.
22. Carravetta M &Levitt MH (2005) Theory of long-lived nuclear spin states in solution nuclear magnetic resonance. I. Singlet states in low magnetic field. *J. Chem. Phys.* 122(21).
23. Pileio G (2010) Relaxation theory of nuclear singlet states in two spin-1/2 systems. *Prog. Nucl. Magn. Reson. Spectrosc.* 56(3):217-231.
24. Pileio G &Levitt MH (2009) Theory of long-lived nuclear spin states in solution nuclear magnetic resonance. II. Singlet spin locking. *J. Chem. Phys.* 130(21).
25. Meier B, Dumez JN, Stevanato G, Hill-Cousins JT, Roy SS, Hakansson P, Mamone S, Brown RCD, Pileio G, & Levitt MH (2013) Long-Lived Nuclear Spin States in Methyl Groups and Quantum-Rotor-Induced Polarization. *J. Am. Chem. Soc.* 135(50):18746-18749.
26. Sarkar R, Vasos PR, & Bodenhausen G (2007) Singlet-state exchange NMR spectroscopy for the study of very slow dynamic processes. *J. Am. Chem. Soc.* 129(2):328-334.
27. Bornet A, Melzi R, Perez-Linde AJ, Hautle P, van den Brandt B, Jannin S, & Bodenhausen G (2013) Boosting Dissolution Dynamic Nuclear Polarization by Cross Polarization. *J. Phys. Chem. Lett.* 4(1):111-114.
28. Carravetta M &Levitt MH (2004) Long-lived nuclear spin states in high-field solution NMR. *J. Am. Chem. Soc.* 126(20):6228-6229.
29. Sarkar R, Ahuia P, Moskau D, Vasos PR, & Bodenhausen G (2007) Extending the scope of singlet-state spectroscopy. *Chem. Phys. Chem.* 8(18):2652-2656.
30. Carravetta M, Johannessen OG, & Levitt MH (2004) Beyond the T-1 limit: Singlet nuclear spin states in low magnetic fields. *Phys. Rev. Lett.* 92(15):153003.
31. Tayler MCD &Levitt MH (2011) Singlet nuclear magnetic resonance of nearly-equivalent spins. *Phys. Chem. Chem. Phys.* 13(13):5556-5560.
32. Bowers CR &Weitekamp DP (1987) Para-Hydrogen and Synthesis Allow Dramatically Enhanced Nuclear Alignment. *J. Am. Chem. Soc.* 109(18):5541-5542.
33. Eisenschmid TC, Kirss RU, Deutsch PP, Hommeltoft SI, Eisenberg R, Bargon J, Lawler RG, & Balch AL (1987) Para Hydrogen Induced Polarization in Hydrogenation Reactions. *J. Am. Chem. Soc.* 109(26):8089-8091.
34. Gloggler S, Colell J, & Appelt S (2013) Para-hydrogen perspectives in hyperpolarized NMR. *J. Magn. Reson.* 235:130-142.
35. Nagashima K &Velan SS (2013) Understanding the Singlet and Triplet States in Magnetic Resonance. *Concepts Magn. Reson. A* 42(5):165-181.
36. Hore PJ, Jones JA, & Wimperis S (2000) *NMR: The toolkit* (Oxford University Press Inc., New-York).
37. Zhang YN, Soon PC, Jerschow A, & Canary JW (2014) Long- Lived 1H Nuclear Spin Singlet in Dimethyl Maleate Revealed by Addition of Thiols. *Angew. Chem. Int. Ed.* 53(13):3396-3399.
38. Gallagher FA, Kettunen MI, Hu DE, Jensen PR, in't Zandt R, Karlsson M, Gisselsson A, Nelson SK, Witney TH, Bohndiek SE, Hansson G, Peitersen T, Lerche MH, & Brindle KM (2009) Production of hyperpolarized [1,4-C-13(2)]malate from [1,4-C-13(2)]fumarate is a marker of cell necrosis and treatment response in tumors. *Proc. Natl. Acad. Sci. U.S.A.* 106(47):19801-19806.
39. Kravchuk T, Reznikov M, Tichonov P, Avidor N, Meir Y, Bekkerman A, & Alexandrowicz G (2011) A Magnetically Focused Molecular Beam of Ortho-Water. *Science* 331(6015):319-321.
40. Beduz C, Carravetta M, Chen JYC, Concistre M, Denning M, Frunzi M, Horsewill AJ, Johannessen OG, Lawler R, Lei XG, Levitt MH, Li YJ, Mamone S, Murata Y, Nagel U, Nishida T, Ollivier J, Rols S, Room T, Sarkar R, Turro NJ, & Yang YF (2012) Quantum rotation of ortho and para-water encapsulated in a fullerene cage. *Proc. Natl. Acad. Sci. U.S.A.* 109(32):12894-12898.

41. Eisendrath H, Stone W, & Jeener J (1978) Nmr of Protons in Gypsum .1. Experimental Proof of Existence of 4 Thermodynamic Invariants. *Phys. Rev. B* 17(1):47-53.
42. Modig K &Halle B (2002) Proton magnetic shielding tensor in liquid water. *J. Am. Chem. Soc.* 124(40):12031-12041.

Conclusions

The original objective of Dissolution-DNP has now become a reality. Real-time imaging of tumors in human patients acquired while following the metabolism of hyperpolarized 1-^{13}C pyruvate was successfully achieved in 2013 (1). This great success in medical imaging should push forward the entire research in Dissolution-DNP. Indeed, even if extremely important, D-DNP is not limited to metabolic imaging of hyperpolarized 1-^{13}C pyruvate. The method can be used in combination with a variety of other NMR or MRI methods, using an extensive variety of different molecules and enhanced nuclei.

As shown in this Thesis, looking slightly outside the box can actually improve the content of the box. DNP research was initially oriented to optimize ^{13}C polarization. In this context, the polarization of protons was widely regarded as undesirable, since it would attenuate the ^{13}C hyperpolarization through a leakage effect, as described in Chapter 2. Therefore, radicals with narrow EPR lines were preferred. As shown in Chapter 3, the use of radicals with broad lines, like TEMPO, combined with hyperpolarization of ^{1}H, can be beneficial for the magnetization of heteronuclei. Indeed, protons have the property that they can be polarized by DNP to higher values and with shorter build-up times than other nuclei like ^{13}C. The addition of a doubly resonant *rf* coil inside the polarizer permits one to transfer the highly abundant ^{1}H magnetization to other nuclei via Cross Polarization, a standard and well-known NMR technique. Moreover, for conventional direct ^{13}C D-DNP, the polarizing field was rarely increased beyond 3.35 T. Indeed, even if it is possible to reach larger ^{13}C polarizations at higher fields, the long build-up time constants of direct ^{13}C polarization become prohibitive. On the contrary, when working with protons, increasing the field turns out to be an advantage. The polarization can be as high as $P(^{1}H)$ = 90% at 6.7 T and 1.2 K, while the build-up time constants remain short enough ($\tau_{DNP}(^{1}H)$ = 150 s under the same conditions). Therefore, combining proton polarization at high field with Cross-Polarization, it was possible to reach a record polarization $P(^{13}C)$ = 70% within an extremely short build-up time of 20 min in 1-^{13}C pyruvate (2).

Cross Polarization does not only improve the DNP of carbon-13 labelled pyruvate, but also of other molecules, like glucose, urea, fumarate or butyrate, for example. This is true even if the molecule is deuterated, as the CP transfer can be performed from the protons of the solvents (3). Moreover, CP from hyperpolarized protons can enhance any low gamma nuclei, like ^{15}N, ^{6}Li, ^{29}Si or ^{129}Xe, providing that the doubly resonant coil is tuned. These nuclei unpopular so far for D-DNP, because of their low polarization and excessively long build-up times, should now become accessible.

Highly and rapidly available protons polarization can be observed directly after dissolution as well. High throughput combined with natural abundance are indeed two key advantages. The main obstacle that has to be overcome is the fast relaxation of the ^{1}H magnetization once the sample is dissolved. Paramagnetic species, which are necessary for DNP to occur, contribute strongly to relaxation during the sample transfer, at low field and at room temperature, and during the observation of the enhanced signals. Numerous approaches to avoid paramagnetic relaxation have already been proposed, like, for example, precipitation and filtration (4), reduction with ascorbate (5), or the use of a magnetic tunnel during the transfer to avoid low field regions (6). In the course of the present Thesis, two alternative strategies were proposed. The modulation of the microwave frequency during the polarization step allows one reducing by a factor two the electron concentration needed to perform efficient DNP (7). This reduction is also beneficial after dissolution, lowering the concentration of the paramagnetic

species. It was also shown that it is possible to obtain a hyperpolarized solution without any paramagnetic species by covalently attaching the free radicals to mesoporous silica materials (referred to as HYPSO) and by filtering these particles in the polarizer while the enhanced analytes are transferred to the spectrometer for detection (8).

The use of so-called Long-Lived States (LLS) (9) to preserve hyperpolarized magnetization is also perfectly adapted to D-DNP. Using variable techniques, it is possible to populate such LLS in systems with two coupled spins. These LLS will be insensitive to nuclear dipole-dipole relaxation, and therefore relax slowly to Boltzmann equilibrium. It was shown by Levitt and co-workers (10) that it is possible to populate LLS in inequivalent spin systems, without any other manipulation, simply by going to a high polarization, for example using DNP. In this Thesis, it was demonstrated that it is as also possible to populate LLS in systems with two equivalent spins under DNP conditions inside the polarizer (11). Regarding the high polarization needed, the combination of the transfer of hyperpolarized ^{1}H magnetization via Cross-Polarization and LLS to low-gamma nuclei like ^{13}C or ^{15}N should surely be explored in the near future. Moreover, the use of HYPSO polarization materials should also be a good option in this context to avoid paramagnetic relaxation, which strongly affects Long-Lived States.

As said in the preamble, the field of Dissolution-DNP is driven by metabolic imaging of prostate cancer, but is by far not limited to this application. Especially with the help of Cross-Polarization, any NMR active nucleus in any molecule can be polarized by D-DNP to high values in a short build-up time. The range of possible applications is then only limited by the inspiration of the experimentalist. One can think for example of monitoring chemical reactions(12), *in vitro* enzymatic studies (13), or *in cellulo* metabolic experiments (14). In this Thesis, two applications in the context of drug screening were proposed. Hyperpolarized Long-Lived States were used to probe protein-ligand interactions(15). The Water-LOGSY technique was also studied, especially problems associated with the management of highly polarized water (16).

References

1. Nelson SJ, Kurhanewicz J, Vigneron DB, Larson PEZ, Harzstark AL, Ferrone M, van Criekinge M, Chang JW, Bok R, Park I, Reed G, Carvajal L, Small EJ, Munster P, Weinberg VK, Ardenkjaer-Larsen JH, Chen AP, Hurd RE, Odegardstuen LI, Robb FJ, Tropp J, & Murray JA (2013) Metabolic Imaging of Patients with Prostate Cancer Using Hyperpolarized [1-C-13]Pyruvate. *Sci. Transl. Med.* 5(198).
2. Jannin S, Bornet A, Melzi R, & Bodenhausen G (2012) High field dynamic nuclear polarization at 6.7 T: Carbon-13 polarization above 70% within 20 min. *Chem. Phys. Lett.* 549:99-102.
3. Vuichoud B, Milani J, Bornet A, Melzi R, Jannin S, & Bodenhausen G (2014) Hyperpolarization of Deuterated Metabolites via Remote Cross-Polarization and Dissolution Dynamic Nuclear Polarization. *J. Phys. Chem. B* 118(5):1411-1415.
4. Ardenkjaer-Larsen JH, Leach AM, Clarke N, Urbahn J, Anderson D, & Skloss TW (2011) Dynamic Nuclear Polarization Polarizer for Sterile Use Intent. *NMR Biomed.* 24(8):927-932.
5. Mieville P, Ahuja P, Sarkar R, Jannin S, Vasos PR, Gerber-Lemaire S, Mishkovsky M, Comment A, Gruetter R, Ouari O, Tordo P, & Bodenhausen G (2010) Scavenging Free Radicals To Preserve Enhancement and Extend Relaxation Times in NMR using Dynamic Nuclear Polarization. *Angew. Chem. Int. Edit.* 49(35):6182-6185.
6. Milani J, Vuichoud B, Bornet A, Mieville P, Mottier R, Jannin S, & Bodenhausen G (2015) A Magnetic Tunnel to Shelter Hyperpolarized Fluids. *Rev. Sci. Instrum.*

7. Bornet A, Milani J, Vuichoud B, Linde AJP, Bodenhausen G, & Jannin S (2014) Microwave frequency modulation to enhance Dissolution Dynamic Nuclear Polarization. *Chem. Phys. Lett.* 602:63-67.
8. Gajan D, Bornet A, Vuichoud B, Milani J, Melzi R, van Kalkeren HA, Veyre L, Thieuleux C, Conley MP, Gruning WR, Schwarzwalder M, Lesage A, Coperet C, Bodenhausen G, Emsley L, & Jannin S (2014) Hybrid polarizing solids for pure hyperpolarized liquids through dissolution dynamic nuclear polarization. *Proc. Natl. Acad. Sci. U. S. A.* 111(41):14693-14697.
9. Levitt MH (2012) Singlet Nuclear Magnetic Resonance. *Annu. Rev. Phys. Chem.* 63:89-105.
10. Tayler MCD, Marco-Rius I, Kettunen MI, Brindle KM, Levitt MH, & Pileio G (2012) Direct Enhancement of Nuclear Singlet Order by Dynamic Nuclear Polarization. *J. Am. Chem. Soc.* 134(18):7668-7671.
11. Bornet A, Ji X, Mammoli D, Vuichoud B, Milani J, Bodenhausen G, & Jannin S (2014) Long-Lived States of Magnetically Equivalent Spins Populated by Dissolution-DNP and Revealed by Enzymatic Reactions. *Chem. Eur. J.* 20(51):17113-17118.
12. Jensen PR, Meier S, Ardenkjaer-Larsen JH, Duus JO, Karlsson M, & Lerche MH (2009) Detection of low-populated reaction intermediates with hyperpolarized NMR. *Chem. Commun.* (34):5168-5170.
13. Miclet E, Abergel D, Bornet A, Milani J, Jannin S, & Bodenhausen G (2014) Toward Quantitative Measurements of Enzyme Kinetics by Dissolution Dynamic Nuclear Polarization. *J. Phys. Chem. Lett.* 5(19):3290-3295.
14. Meier S, Karlsson M, Jensen PR, Lerche MH, & Duus JO (2011) Metabolic pathway visualization in living yeast by DNP-NMR. *Mol. Biosyst.* 7(10):2834-2836.
15. Buratto R, Bornet A, Milani J, Mammoli D, Vuichoud B, Salvi N, Singh M, Laguerre A, Passemard S, Gerber-Lemaire S, Jannin S, & Bodenhausen G (2014) Drug screening boosted by hyperpolarized long-lived States in NMR. *ChemMedChem* 9(11):2509-2515.
16. Chappuis Q, Milani J, Vuichoud B, Bornet A, Gossert AD, Bodenhausen G, & Jannin S (to be published) Hyperpolarized Water to Reveal Protein-Ligand Interactions

Appendix

Annex to Chapter 2: Mathematica and Matlab notebooks

SE CE shape of DNP spectrum

```
clear all; close all;

%% 1 Setup

 % 1.2 ESR
 watESR=1;             %chooses ESR shape 1=3Gaussienne, 2=Raw Data
 maille=5*10^-3;       %en GHz

 % 1.3 Saturation
 v1=5*10^3*2*pi;       %en Hz*2pi = rad/s
 T1e=0.1;              % en s

 % 1.4 SE CE
 fuWint=[187 189];
 v01H=285*10^-3;       %en GHz
 v013C=71.25*10^-3;

 % 1.5 Electron Spin Diffusion
 lwe=100*10^-3;        % linewidth/2 of spin packet in GHz      >--lwe--fuw--lwe--<


%% 2 Build ESR spectrum (large)
fuWL=(186:maille:190)';
x=size(fuWL);suWL=x(1,1);clear x;

if watESR==1
v=[187.884 188.1188 188.3255]; a=[0.2042 0.8626 0.2339]; dv=0.2256;
sigma=dv/(2*(2*log(2))^0.5);

y(:,1)= a(1,1)*1/(sigma*(2*pi)^0.5).*exp(-0.5*((fuWL-v(1,1))/sigma).^2); %3 gaussienne
y(:,2)= a(1,2)*1/(sigma*(2*pi)^0.5).*exp(-0.5*((fuWL-v(1,2))/sigma).^2);
y(:,3)= a(1,3)*1/(sigma*(2*pi)^0.5).*exp(-0.5*((fuWL-v(1,3))/sigma).^2);
LESR(:,1)=y(:,1)+y(:,2)+y(:,3);
LESR=LESR/sum(LESR);                                    %normalize the area under the peak to 1
clear y v a dv sigma;
end

if watESR==2
load ESR;                                               %load ESR data

iuW=(min(ESR(:,1)):maille:max(ESR(:,1)))';
x=size(iuW);siuW=x(1,1);clear x;
iESR = interp1(ESR(:,1),ESR(:,2),iuW,'spline');         %interpolate
iESR=iESR/max(iESR);iESR=iESR-min(iESR);                %normalize and baseline

LESR=zeros(suWL,1);                                     %feed interpol data in larger freq window
f1=find(fuWL==iuW(1,1));
LESR(f1:f1+siuW-1,1)=iESR;

clear f1 ESR iESR iuW siuW
end

%% 3 Saturation

s=pi*v1^2*T1e;

for i=1:suWL
  SLESR(i,1)=LESR(i,1)/(1+s*LESR(i,1)/(maille*10^9*2*pi));
```

```
                    %LESR normalized par unit of maille (in s/rad)
end
clear s v1;

%% 4 SE CE

fuW=[fuWint(1,1):maille:fuWint(1,2)]';
x=size(fuW);suW=x(1,1);clear x;

f=find(fuWL==fuWint(1,1));                          %line index in fuWL where fuW start
v1Hs=round(v01H/maille);
v13Cs=round(v013C/maille);

for i=1:suW
    SE1H(i,1)=SLESR(f+v1Hs,1)-SLESR(f-v1Hs,1);
    CE1H(i,1)=SLESR(f,1)*(LESR(f+v1Hs,1)-LESR(f-v1Hs,1));

    SE13C(i,1)=SLESR(f+v13Cs,1)-SLESR(f-v13Cs,1);
    CE13C(i,1)=SLESR(f,1)*(LESR(f+v13Cs,1)-LESR(f-v13Cs,1));
    f=f+1;
end

clear f v1Hs v13Cs;

%% Electron Spin Diffusion

nlwe=lwe/maille;

f1=find(fuWL==fuWint(1,1));f2=find(fuWL==fuWint(1,2));

LSE1H=zeros(suWL,1);LCE1H=zeros(suWL,1);LSE13C=zeros(suWL,1);LCE13C=zeros(suWL,1);
LSE1H(f1:f2,1)=SE1H(:,1);LCE1H(f1:f2,1)=CE1H(:,1);
LSE13C(f1:f2,1)=SE13C(:,1);LCE13C(f1:f2,1)=CE13C(:,1) ;     % Larger SE, CE spectrum

for i=1:suW
   DSE1H(i,1)=sum(LSE1H(f1-nlwe:f1+nlwe,1));
   DCE1H(i,1)=sum(LCE1H(f1-nlwe:f1+nlwe,1));

   DSE13C(i,1)=sum(LSE13C(f1-nlwe:f1+nlwe,1));
   DCE13C(i,1)=sum(LCE13C(f1-nlwe:f1+nlwe,1));
   f1=f1+1;
end

clear f1 f2 LSE1H LCE1H LSE13C LCE13C nlwe lwe;
```

CE rate equations

CE Model 1 (no SD electronic or nuclear): Positive (DQ) Polarization

```
ClearAll["Global`*"]

Pn=0.006;
Pe=0.98;

f0=3/31;
fi=5/31;
Ne=1;
Ne0=Ne*f0;NeD=Ne0 25 fi;Nn=NeD*25;

TMw=5; (*10000 cut uW*)
T1e=1;
TCE=0.001;
T1n=1000;

WMw=1/TMw;W1e=1/T1e;WCE=1/TCE;W1n=1/T1n;

sol2=NDSolve[ { e1b'[t] == -WMw e1b[t]+W1e (1+Pe) e1a[t]- W1e(1-Pe) e1b[t]
                           +WCE e1a[t]e2b[t]nb[t]-WCE e1b[t]e2a[t]na[t],
                e1a'[t] == -e1b'[t],
                e2b'[t] == W1e (1+Pe) e2a[t]- W1e (1-Pe) e2b[t]
                           -WCE e1a[t]e2b[t]nb[t] +WCE e1b[t]e2a[t]na[t],
```

```
                e2a'[t] == -e2b'[t],
                nb'[t]  == W1n (1-Pn) na[t]- W1n (1+Pn) nb[t]
                           -WCE  e1a[t]e2b[t]nb[t]+WCE e1b[t]e2a[t]na[t],
                na'[t]  == -nb'[t],
                e1b[0]==Ne0 (1+Pe)/2,e1a[0]==Ne0 (1-Pe)/2,
                e2b[0]==NeD (1+Pe)/2,e2a[0]==NeD (1-Pe)/2,
                nb[0]==Nn (1-Pn)/2,na[0]==Nn (1+Pn)/2},
                {e1b,e1a,e2b,e2a,nb,na},{t, 2000}];

PlotA=[(
        Evaluate[{na[t]}/.sol2]-Evaluate[{nb[t]}/.sol2])
        /(Evaluate[{na[t]}/.sol2]+Evaluate[{nb[t]}/.sol2])*100, {t,0,2000},PlotRange→All] ;

del={1,10,50,100,200,250,350,500,750,1000,1250,1500,1750,2000};
Datn1=(nb[del]/.sol2)[[1]];Datn2=(na[del]/.sol2)[[1]];DatPn=(Datn2-Datn1)/(Datn2+Datn1)*100;
PlotB=ListPlot[{Join[Transpose[{del,DatPn}]]},PlotRange->{{0,2000},{0,100}},PlotStyle→{Red}];

Show[PlotA,PlotB]
```

CE Model 1 (no SD electronic or nuclear): Negative (ZQ) Polarization

```
ClearAll["Global`*"]

Pn=0.006;
Pe=0.98;

f0=3/31;
fi=5/31;
Ne=1;
Ne0=Ne*f0;NeD=Ne0 25 fi;Nn=NeD*25;

TMw=5; (*10000 cut uW*)
T1e=1;
TCE=1;
T1n=1000;

WMw=1/TMw;W1e=1/T1e;WCE=1/TCE;W1n=1/T1n;

sol2=NDSolve[ { e1b'[t] == -WMw e1b[t] +WMw e1a[t]+W1e (1+Pe) e1a[t]- W1e (1-Pe) e1b[t]
                           +WCE e1a[t]e2b[t]na[t]-WCE e1b[t]e2a[t]nb[t],
                e1a'[t] == -e1b'[t],
                e2b'[t] == W1e (1+Pe) e2a[t]- W1e (1-Pe) e2b[t]
                           -WCE e1a[t]e2b[t]na[t] +WCE e1b[t]e2a[t]nb[t],
                e2a'[t] == -e2b'[t],
                nb'[t]  == W1n (1-Pn) na[t]- W1n (1+Pn) nb[t]
                           +WCE  e1a[t]e2b[t]na[t]-WCE e1b[t]e2a[t]nb[t],
                na'[t]  == -nb'[t],
                e1b[0]==Ne0 (1+Pe)/2,e1a[0]==Ne0 (1-Pe)/2,
                e2b[0]==NeD (1+Pe)/2,e2a[0]==NeD (1-Pe)/2,
                nb[0]==Nn (1-Pn)/2,na[0]==Nn (1+Pn)/2},
                {e1b,e1a,e2b,e2a,nb,na},{t, 2000}];

Plot[(
      Evaluate[{na[t]}/.sol2]-Evaluate[{nb[t]}/.sol2])
      /(Evaluate[{na[t]}/.sol2]+Evaluate[{nb[t]}/.sol2])*100, {t,0,2000},PlotRange→All]
```

CE Model 2 (with SD nuclear): Positive (DQ) Polarization

```
ClearAll["Global`*"]

Pn=0.006;
Pe=0.98;

f0=3/31;
fi=5/31;
Ne=1;
Ne0=Ne*f0;NeD=Ne0 25 fi;Nnc=NeD*25;Nnb=NeD*125;

TMw=0.1; (*10000 cut uW*)
T1e=1;
TCE=0.01;
T1nc=25;
T1nb=1000;
TSDn=10000;
```

```
WMw=1/TMw;W1e=1/T1e;WCE=1/TCE;W1nc=1/T1nc;W1nb=1/T1nb;WSDn=1/TSDn;

sol2=NDSolve[ { e1b'[t]==  -WMw e1b[t] +WMw e1a[t]+W1e (1+Pe) e1a[t]- W1e (1-Pe) e1b[t]
                           +WCE e1a[t]e2b[t]ncb[t]-WCE e1b[t]e2a[t]nca[t],
                e1a'[t]==  -e1b'[t],
                e2b'[t] ==  W1e (1+Pe) e2a[t]- W1e (1-Pe) e2b[t]
                           -WCE  e1a[t]e2b[t]ncb[t] +WCE e1b[t]e2a[t]nca[t],
                e2a'[t]==  -e2b'[t],
                ncb'[t]==  W1nc (1-Pn) nca[t]- W1nc (1+Pn) ncb[t]
                           -WCE  e1a[t]e2b[t]ncb[t]+WCE e1b[t]e2a[t]nca[t]
                           +WSDn nca[t]nbb[t]-WSDn ncb[t]nba[t],
                nca'[t]==  -ncb'[t],
                nbb'[t]==  W1nb (1-Pn) nba[t]- W1nb (1+Pn) nbb[t]
                           -WSDn nca[t]nbb[t]+WSDn ncb[t]nba[t],
                nba'[t]==  -nbb'[t],
                e1b[0]==Ne0 (1+Pe)/2,e1a[0]==Ne0 (1-Pe)/2,
                e2b[0]==NeD (1+Pe)/2,e2a[0]==NeD (1-Pe)/2,
                ncb[0]==Nnc (1-Pn)/2,nca[0]==Nnc (1+Pn)/2,
                nbb[0]==Nnb (1-Pn)/2,nba[0]==Nnb (1+Pn)/2},
                {e1b,e1a,e2b,e2a,ncb,nca,nbb,nba},{t, 2000}];

PlotAc=Plot[(Evaluate[{nca[t]}/.sol2]-Evaluate[{ncb[t]}/.sol2])
             /(Evaluate[{nca[t]}/.sol2]+Evaluate[{ncb[t]}/.sol2])*100,
{t,0,1000},PlotRange->{{0,1000},{0,100}}];

PlotAb=Plot[(Evaluate[{nba[t]}/.sol2]-Evaluate[{nbb[t]}/.sol2])
             /(Evaluate[{nba[t]}/.sol2]+Evaluate[{nbb[t]}/.sol2])*100,{t,0,1000},
PlotRange->{{0,1000},{0,100}}];

Show[PlotAc,PlotAb]
```

Model 3 Polarize nucleus 1 through nucleus 2

```
ClearAll["Global`*"]

Pn2=0.006;
Pn20=1;
Pn1=0.006/4;
Pe=0.98;

f0=3/31;
fi=5/31;
Ne=1;
Ne0=Ne*f0;NeD=Ne0 25 fi;Nn=NeD*25;Nn2=NeD*7;

T1e=1;
WCE1=1/1;
WCE2=1/4;
T1n1=1000;
T1n2=2000;

W1e=1/T1e;W1n1=1/T1n1;W1n2=1/T1n2;

sol2=NDSolve[ { e1b'[t]==W1e (1+Pe) e1a[t]- W1e (1-Pe) e1b[t]
                         +WCE1 e1a[t]e2b[t]n1b[t]-WCE1 e1b[t]e2a[t]n1a[t]
                         +WCE2 e1a[t]e2b[t]n2b[t]-WCE2 e1b[t]e2a[t]n2a[t],
                e1a'[t]==-e1b'[t],
                e2b'[t]==W1e (1+Pe) e2a[t]- W1e (1-Pe) e2b[t]
                         -WCE1 e1a[t]e2b[t]n1b[t]+WCE1 e1b[t]e2a[t]n1a[t]
                         -WCE2 e1a[t]e2b[t]n2b[t]+WCE2 e1b[t]e2a[t]n2a[t],
                e2a'[t]==-e2b'[t],
                n1b'[t]==W1n1 (1-Pn1) n1a[t]- W1n1 (1+Pn1) n1b[t]
                         -WCE1 e1a[t]e2b[t]n1b[t]+WCE1 e1b[t]e2a[t]n1a[t],
                n1a'[t]==-n1b'[t],
                n2b'[t]==W1n2 (1-Pn2) n2a[t]- W1n2 (1+Pn2) n2b[t]
                         -WCE2 e1a[t]e2b[t]n2b[t]+WCE2 e1b[t]e2a[t]n2a[t],
                n2a'[t]==-n2b'[t],
                e1b[0]==Ne0 (1+Pe)/2,e1a[0]==Ne0 (1-Pe)/2,
                e2b[0]==NeD (1+Pe)/2,e2a[0]==NeD (1-Pe)/2,
                n1b[0]==Nn2 (1-Pn1)/2,n1a[0]==Nn2 (1+Pn1)/2,n2b[0]==Nn (1-Pn20)/2,
                n2a[0]==Nn (1+Pn20)/2},
                {e1b,e1a,e2b,e2a,n1b,n1a,n2b,n2a},{t, 2000}];

del={1,10,50,100,200,250,350,500,750,1000,1250,1500,1750,2000};
Datn1=(n1b[del]/.sol2)[[1]];Datn2=(n1a[del]/.sol2)[[1]];DatPn=(Datn2-Datn1)/(Datn2+Datn1)*100;

PlotA=Plot[(Evaluate[{n1a[t]}/.sol2]-Evaluate[{n1b[t]}/.sol2])
```

```
            /(Evaluate[{n1a[t]}/.sol2]+Evaluate[{n1b[t]}/.sol2])*100,{t,0,2000},PlotRange→All];
PlotB=ListPlot[{Join[Transpose[{del,DatPn}]]},PlotRange→All,PlotStyle→{Red}];
Show[PlotA,PlotB]
```

Remerciements

Avant toute chose, je voudrais remercier tous les membres de mon jury de thèse, **Mathilde Lerche**, **Joost Lohman**, **Lyndon Emsley** et **Sandrine Gerber-Lemaire**, qui ont accepté de donner de leur temps pour lire et juger ce travail. Ce sont peut-être les seules personnes à être arrivées jusqu' à cette page, donc, merci.

Je voudrais exprimer toute ma reconnaissance à **Geoffrey Bodenhausen**, mon directeur de thèse. On dit souvent qu'à la fin d'un PhD, les thésards n'ont qu'une envie, fuir au plus loin l'ignoble tyran qui, jour après jour, fit de leur thèse un enfer sur terre. Pour moi, ce fut tout le contraire. Chaque jour de ma thèse a été un petit bonheur. J'ai pu travailler de manière totalement libre et indépendante, tout en pouvant compter sur l'entier soutien de Geoffrey en cas de besoin. Merci beaucoup à lui pour ces quatre années.

Un énorme merci aussi à **Sami Jannin**, mon co-directeur de thèse. Il faudrait un deuxième volume à ce travail intitulé ''*Des innombrables vertus de Sami Jannin en science et ailleurs, un voyage aller-et-retour*'' pour exprimer tout le mal que je pense de lui ! Non seulement, il a une maîtrise totale de son champ de recherche, mais le plus impressionnant est son intérêt et son savoir-faire dans une multitude de domaines annexes, ainsi que les connections instantanées qu'il fait entre ceux-ci. Cela étant dit, sa plus grande qualité est son envie et sa capacité de communiquer son savoir. Pour moi, il est l'image de ce que devrait être un vrai scientifique. Merci pour tout. Cette thèse n'aurait pas été possible sans toi. J'espère que je n'ai pas été trop pénible.

Je voudrais exprimer toute ma gratitude à **Puneet Ahuja** et **Riddhiman Sarkar**, mes deux mentors en RMN, qui m'ont formé à cette technique et qui m'ont montré les vraies valeurs de la recherche scientifique. Merci de m'avoir aidé avec **Paul Vasos** lors de mes premiers pas dans le groupe.

Merci aux vieux de la vielle qui étaient là lors de mes débuts en RMN (tout est relatif, maintenant je crois que c'est moi le vieux du labo). Merci à **Takuya ''Tak'' Segawa** qui a commencé avec moi à J = 0, mais qui est parti définitivement plus vite. Je pense que j'ai toujours une énorme ardoise envers **Veronika Vitzthum** et **Marc Caporini** en ce qui concerne les rosés consommés sur la terrasse du Motel des Pierrettes. Je suis très reconnaissant à **Nicola Salvi** de m'avoir accompagné à Disney World. Merci aussi à **Simone Ulzega** et à **Bikash Baishya**. Enfin, un énorme merci à **Diego Carnevale** pour le quench de gyrotron le plus drôle du monde.

Pas un spectre présenté dans cette thèse n'aurait été possible sans l'aide de **Martial Rey** qui a soigné jour après jour nos spectromètres. Je lui souhaite de merveilleuses parties de golf durant sa retraite en Valais (bien sûr). Le service RMN est de toute façon entre de très bonnes mains avec **Pascal**, **Anto** et **Vlado.** Merci aussi à tous les collaborateurs de notre corridor qui, non seulement rendent notre vie plus facile, mais sont aussi des collègues géniaux. Merci à **Donald, Fredo** et **Patrick**, à **Annelise, Gladys, Benjamin** et **Giovani** au magasin ainsi qu'à **Laure, Daniel** et **Francisco** en MS.

Une thèse de doctorat est souvent perçue comme une quête personnelle et solitaire. C'est totalement faux. Le travail dans un groupe de recherche scientifique c'est avant tout un joyeux mélange de discussions, d'engueulades et de collaborations, où chacun apporte ses compétences propres aux projets en cours. De plus, on a l'impression du dehors que toutes ces réflexions très sérieuses se font de manière concentrée, avec des figures très graves, en blouse blanche autours d'un ordinateur surpuissant. J'ai

jamais eu d'idée géniale dans ces conditions, mais je promets que je vais essayer. En vrai, toutes ces idées compliquées sont le fruit d'intenses réflexions avachis dans des canapés, à boire des cafés (beaucoup de cafés) en dégustant de délicieux gâteaux préparés par Pavel mais aussi en buvant des pichets à Sat ou des quadruples Pastis au Motel des Pierrettes, ainsi que de la Limonette au Noël du magasin. Quelques théories ont aussi sûrement germé en mangeant du cochon à la St-Martin à Grandfontaine, en faisant des barbacs au Bordu ou de la grimpe à Chavornay. Tout ça pour dire que tout le charme de la recherche scientifique disparaîtrait sans groupe de recherche scientifique. Je voudrais d'abord faire tout plein de bisous à la Mafia Romande : à **Quentin Chapppuis**, le seul rasta à avoir réussi à me trainer dans un concert de reggae (c'est quand même trop lent) ; **Jonas Milani**, constructeur devant l'éternel de tunnels magnétiques, mais aussi de probes DNP, de sticks de dissolutions et sniper de bouchons de laser ; et enfin **Basile Vuichoud**, qui surpasse son net handicap génétique d'être né Vaudois par son éternel optimisme ainsi que par sa capacité quasi christique à transformer les prix de poster en bières. Un grand merci à la Mafia Latine; à **Roberto Buratto**, **Daniele Mammoli** et **Estel Canet**, avant tout pour leurs ouverture d'esprit culinaire (personnellement j'aurais pas tenté la Pineapple Pizza, mais ils l'ont fait), ainsi que pour leur très grand vins. Merci également à **Xiao Ji** qui a quand même testé la fondue, la St-Martin et le concours de vins, à **Pavel Kaderavek** pour les délicieux gâteaux cités plus haut, à **Srinivas Chintalapalli** et **Maninder Singh** et à **AJ Perez-Linde** pour ses éclairages sur l'histoire espagnole et sur les probes. Finalement, bienvenue au groupe des méchants du LRM'A' à **Aaron Rossini** et à **Arthur Pinon**.

Je suis aussi extrêmement redevable envers toutes les personnes avec qui j'ai collaboré durant cette thèse. Merci à ''Maestro'' **Alessandro**, à **Imma** et à **Lisa** du groupe **Heinis**, à **Solène Passemard** et **Aurélien Laguerre** du groupe **Gerber**, à **Florian de Nanteuil**, à **Roberto Melzi** de Bruker et à **David Gajan** du groupe **Emsley**.

Un très grand merci à **Béatrice Bliesener-Tong** pour avoir géré ma très légère allergie à l'administration. Grâce à sa gestion experte, le labo roule tout seul (et les voyages pour les conférences sont toujours très bien organisés). Merci aussi à **Anne Lene Odegaard** pour les mêmes raisons mais au niveau de l'école doctorale.

Toutes mes pensées vont bien sûr à **Miss Clara M.**, **Miss Nikita**, **Miss Xénia**, **Miss Simone** et **Miss Banana Probe**, sans qui ce travail aurait été impossible.

Merci aussi aux potes du master, à **Sandra, Yvan, Marion, Delphine, Florian, Bruna et Charline**, pour les bières à Sat, le fameux triptyque burger, Johannis de l'AUVAL et ska-punk à Balelec ainsi que les soirées chasse super bien organisées.

Je voudrais exprimer toute ma gratitude au meilleur colloc' du monde, **Alban**, qui entre une mise en espace musicale, un groove en 777-9311 à la batterie et un peu de théorie quantique des champs relativistes confectionne des desserts hors du commun (en fait il a seulement regardé, mais c'était quand même très bon), ainsi qu'à ses joyeux compagnons qui ont rendu la vie dans cet appart bien sympathique.

Finalement, je voudrais dédier cette thèse à **Papamaman** qui m'ont soutenu tout le temps, dans tous mes projets, sans aucune condition. En réfléchissant à ces remerciements, je me rends compte que votre éducation et votre implication m'ont forgé tel que je suis, quelqu'un capable d'apprécier tous les petits bonheurs de la vie. A aucun moment je n'aurais pu écrire cette thèse sans vous. Merci.

Curriculum Vitae

Personal Data

Name : BORNET Aurélien
Date of birth : 22.11.1985
Nationality : Swiss

Address : Bermouche 1997 Haute-Nendaz
Cell phone : 078 868 27 18
Telephone : 027 288 50 62
e-mail : aurelien.bornet@epfl.ch
aurelien.bornet@gmail.com

Education

Ph.D Thesis student and research assistant of Prof. G. Bodenhausen 2010-Present
Laboratory of Biomolecular Magnetic Resonance (LRMB), EPFL

Master of Science (M.Sc.) in Molecular and Biological Chemistry 2008-2010
Ecole Polytechnique Fédérale de Lausanne

Bachelor of Science (B.Sc.) in Chemistry 2005-2008
Ecole Polytechnique Fédérale de Lausanne

Maturité Fédérale 2000-2005
Lycée Collège des Creusets, Sion

Projects/Internships

Laboratory of Therapeutic Proteins and Peptides (LPPT), EPFL 06.2010-09.2010
Internship : Peptide inhibitors of uPA
Knowledge in production, purification and characterisation of proteins, and in peptides synthesis

Laboratory of Biomolecular Magnetic Resonance (LRMB), EPFL 02.2010-04.2010
Internship : Long Lived Coherences in NMR

Teaching Experiences

EPFL Teaching Assistant 2010-Present
Undergraduate chemistry laboratory courses
Experimental molecular sciences course for master students – NMR
Intensive module of basic and advanced NMR for PhD students
Guidance of two PhD Swiss/Indian exchange projects
Guidance of two Master theses

Competencies

Languages

French : Mother tongue
English : Advanced, B2 (CECR)
German : Basic knowledge, A2 (CECR)

Computer skills

Bruker pulse programming, Matlab, Adobe Illustrator, MS Office Suite

Interests

In winter I like to snowboard in the 4-Vallées domain. In summer I like to read, cook and taste wines from Valais in my garden.

Publications

1) **Bornet, A.**, Ji, X., Mammoli, D., Vuichoud, B., Milani, J., Bodenhausen, G., & Jannin, S. Long-Lived States of Magnetically Equivalent Spins Populated by Dissolution-DNP and Revealed by Enzymatic Reactions. *Chem. Eur. J.* **20**,17113-17118 (2014).

2) Buratto, R., **Bornet, A.**, Milani, J., Mammoli, D., Vuichoud, B., Salvi, N., Singh, M., Laguerre, A., Passemard, S., Gerber-Lemaire, S., Jannin, S., & Bodenhausen, G. Drug Screening Boosted by Hyperpolarized Long-Lived States in NMR. *ChemMedChem* **9**,2509-2515 (2014).

3) Gajan, D., **Bornet, A.**, Vuichoud, B., Milani, J., Melzi, R., van Kalkeren, H.A., Veyre, L., Thieuleux, C., Conley, M.P., Gruning, W.R., Schwarzwalder, M., Lesage, A., Coperet, C., Bodenhausen, G., Emsley, L., & Jannin, S. Hybrid polarizing solids for pure hyperpolarized liquids through dissolution dynamic nuclear polarization. *Proc. Natl. Acad. Sci. U.S.A.* **111**,14693-14697 (2014).

4) Miclet, E., Abergel, D., **Bornet, A.**, Milani, J., Jannin, S., & Bodenhausen, G. Toward Quantitative Measurements of Enzyme Kinetics by Dissolution Dynamic Nuclear Polarization. *J. Phys. Chem. Lett.* **5**,3290-3295 (2014).

5) **Bornet, A.**, Milani, J., Vuichoud, B., Linde, A.J.P., Bodenhausen, G., & Jannin, S. Microwave frequency modulation to enhance Dissolution Dynamic Nuclear Polarization. *Chem. Phys. Lett.* **602**,63-67 (2014).

6) Vuichoud, B., Milani, J., **Bornet, A.**, Melzi, R., Jannin, S., & Bodenhausen, G. Hyperpolarization of Deuterated Metabolites via Remote Cross-Polarization and Dissolution Dynamic Nuclear Polarization. *J. Phys. Chem. B* **118**,1411-1415 (2014).

7) Linde, A.J.P., **Bornet, A.**, Milani, J., Vuichoud, B., Melzi, R., Jannin, S., & Bodenhausen, G. Cross polarization from H-1 to quadrupolar Li-6 nuclei for dissolution DNP. *Phys. Chem. Chem. Phys.* **16**,24813-24817 (2014).

8) **Bornet, A.**, Melzi, R., Linde, A.J.P., Hautle, P., van den Brandt, B., Jannin, S., & Bodenhausen, G. Boosting Dissolution Dynamic Nuclear Polarization by Cross Polarization. *J. Phys. Chem. Lett.* **4**,111-114 (2013).

9) Jannin, S., **Bornet, A.**, Melzi, R., & Bodenhausen, G. High field dynamic nuclear polarization at 6.7 T: Carbon-13 polarization above 70% within 20 min. *Chem. Phys. Lett.* **549**,99-102 (2012).

10) Chinthalapalli, S., Bornet, A., Segawa, T.F., Sarkar, R., Jannin, S., & Bodenhausen, G. Ultrahigh-Resolution Magnetic Resonance in Inhomogeneous Magnetic Fields: Two-Dimensional Long-Lived-Coherence Correlation Spectroscopy. *Phys. Rev. Lett.* **109** (2012).

11) Salvi, N., Buratto, R., **Bornet, A.**, Ulzega, S., Rebollo, I.R., Angelini, A., Heinis, C., & Bodenhausen, G. Boosting the Sensitivity of Ligand-Protein Screening by NMR of Long-Lived States. *J. Am. Chem. Soc.* **134**,11076-11079 (2012).

12) **Bornet, A.**, Melzi, R., Jannin, S., & Bodenhausen, G. Cross Polarization for Dissolution Dynamic Nuclear Polarization Experiments at Readily Accessible Temperatures 1.2 < T < 4.2 K. *Appl. Magn. Reson.* **43**,107-117 (2012).

13) **Bornet, A.**, Milani, J., Wang, S.T., Mammoli, D., Buratto, R., Salvi, N., Segawa, T.F., Vitzthum, V., Mieville, P., Chinthalapalli, S., Perez-Linde, A.J., Carnevale, D., Jannin, S., Caporini, M., Ulzega, S., Rey, M., & Bodenhausen, G. Dynamic Nuclear Polarization and Other Magnetic Ideas at EPFL. *Chimia* **66**,734-740 (2012).

14) Jannin, S., **Bornet, A.**, Colombo, S., & Bodenhausen, G. Low-temperature cross polarization in view of enhancing dissolution Dynamic Nuclear Polarization in NMR. *Chem. Phys. Lett.* **517**,234-236 (2011).

15) **Bornet, A.**, Ahuja, P., Sarkar, R., Fernandes, L., Hadji, S., Lee, S.Y., Haririnia, A., Fushman, D., Bodenhausen, G., & Vasos, P.R. Long-Lived States to Monitor Protein Unfolding by Proton NMR. *Chem. Phys. Chem.* **12**,2729-2734 (2011).

16) **Bornet, A.**, Jannin, S., Konter, J.A., Hautle, P., van den Brandt, B., & Bodenhausen, G. Ultra High-Resolution NMR: Sustained Induction Decays of Long-Lived Coherences. *J. Am. Chem. Soc.* **133**,15644-15649 (2011).

17) **Bornet, A.**, Jannin, S., & Bodenhausen, G. Three-field NMR to preserve hyperpolarized proton magnetization as long-lived states in moderate magnetic fields. *Chem. Phys. Lett.* **512**,151-154 (2011).

18) Sarkar, R., Ahuja, P., Vasos, P.R., **Bornet, A.**, Wagnieres, O., & Bodenhausen, G. Long-lived coherences for line-narrowing in high-field NMR. *Prog. Nucl. Magn. Reson. Spectrosc.* **59**,83-90 (2011).

19) Segawa, T.F., **Bornet, A.**, Salvi, N., Mieville, P., Vitzthum, V., Carnevale, D., Jannin, S., Caporini, M.A., Ulzega, S., Vasos, P.R., Rey, M., & Bodenhausen, G. Extending Timescales and Narrowing Linewidths in NMR. *Chimia* **65**,652-655 (2011).

20) **Bornet, A.**, Sarkar, R., & Bodenhausen, G. Life-times of long-lived coherences under different motional regimes. *J. Magn. Reson.* **206**,154-156 (2010).

Patents

1) G. Bodenhausen, **A. Bornet**, & N. Salvi, EPFL, Determination of binding properties of first chemical compound to second chemical compound between free dissociated state and a bound associated state involves measuring nuclear magnetic resonance, Patent numbers WO2013079106-A1; EP2786165-A1.

2) S. Jannin, A.G. Gianotti, J. Lohman, F. Engelke, R. Melzi, **A. Bornet** & G. Bodenhausen, EPFL - Bruker Switzerland AG, Method of producing hyperpolarized material used in nuclear magnetic resonance and magnetic resonance imaging applications, involves preparing target material, and preparing dissolved material from target material, Patent numbers US2013274111-A1; WO2013153101-A1.

3) S. Jannin**, A. Bornet**, & G. Bodenhausen, EPFL - Bruker Switzerland AG, Nuclear magnetic resonance spectroscopy method for e.g. hyperpolarized sample, involves reconverting magnetization into long lived coherences after observation interval by irradiating sample with radiofrequency-field, Patent numbers EP2523012-A1; US2012286782-A1; US8633697-B2; EP2523012-B1 .

Conference Papers

1) Bornet, A., Jannin, S. & Bodenhausen, G. *Three-field NMR to preserve hyperpolarized proton magnetization as long-lived states in moderate magnetic fields* Euromar (2011) Frankfurt (Germany) (**Poster**)

2) Bornet, A., Jannin, S., Konter, J.A., Hautle, P., van den Brandt, B. & Bodenhausen, G. *Ultra High-Resolution NMR: Sustained Induction Decays of Long-Lived Coherences* Third International Symposium on Dynamic Nuclear Polarization (2011) Lausanne (Switzerland) (**Poster**)

3) Bornet, A., Jannin, S. & Bodenhausen, G. *Three-field NMR to preserve hyperpolarized proton magnetization as long-lived states in moderate magnetic fields* Third International Symposium on Dynamic Nuclear Polarization (2011) Lausanne (Switzerland) (**Poster**)

4) Bornet, A., Jannin, S. & Bodenhausen, G. *Low-temperature Cross Polarization in View of Enhancing Dissolution Dynamic Nuclear Polarization* Lorentz Center Workshop on Hot Topics in Spin-Hyperpolarization (2012) Leiden (Netherland) (**Presentation**)

5) Bornet, A., Chinthalapalli, S., Segawa, T., Sarkar, R., Jannin, S. & Bodenhausen, G. *Ultra High-Resolution NMR in Inhomogeneous Magnetic Fields: Two-Dimensional Long-Lived Coherence Correlation Spectroscopy* Experimental Nuclear Magnetic Resonance Conference (2012) Miami (USA) (**Presentation**)

6) Bornet, A., Buratto, R., Salvi, N., Ulzega, S., Rentero Rebollo, I., Angelini, A., Heinis, C., & Bodenhausen, G. *Boosting Sensitivity of Ligand-Protein Screening by NMR of Long-Lived States* SCS Fall Meeting (2012) Zürich (Switzerland) (**Poster**)

7) Bornet, A., Chinthalapalli, S., Segawa, T., Sarkar, R., Jannin, S. & Bodenhausen, G. *Ultra High-Resolution NMR in Inhomogeneous Magnetic Fields: Two-Dimensional Long-Lived Coherence Correlation Spectroscopy* Euromar (2012) Dublin (Ireland) (**Poster**)

8) Bornet, A., Salvi, N., Mammoli, D., Milani, J., Perez-Linde, A.J., Mieville, P., Jannin, S., & Bodenhausen, G *Long-Lived States and other Tricks to Preserve Hyperpolarized Magnetization in Dissolution DNP* COST Workshop WG 3 (2013) Bad Hofgastein (Austria) (**Presentation**)

9) Bornet, A., Melzi, R., Perez-Linde, A.J., Jannin, S., Hautle, P., van den Brandt, B., & Bodenhausen, G. *$^{1}H \rightarrow {}^{13}C$ Cross-Polarization for Dissolution-DNP at 6.7 T and 1.2 K* Fourth International Symposium on Dynamic Nuclear Polarization (2013) Helsinor (Dennmark) (**Presentation**)

10) Bornet, A., Buratto, R., Mammoli D., Milani, J., Vuichoud, B., Jannin, S., & Bodenhausen, G. *DNP Enhanced Long-Lived States to Performdrug Screening by ^{1}H NMR* COST Workshop (2014) Lymington (UK) (**Presentation**)

11) Bornet, A., Buratto, R., Mammoli D., Milani, J., Vuichoud, B., Jannin, S., & Bodenhausen, G. *Hyperpolarized Long-Lived States to Performdrug Screening by ^{1}H NMR* Euromar (2014) Zürich (Switzerland) (**Poster**)

Awards and Grants

Best Teaching Prize in 2012 from the Section of Chemistry and Chemical Engineering at EPFL

Chemistry Travel Award in 2012 from the Swiss Academy of Sciences and the Swiss Chemical Society